ISTITUTO NAZIONALE DI FISICA NUCLEARE
Laboratori Nazionali di Frascati

FRASCATI PHYSICS SERIES

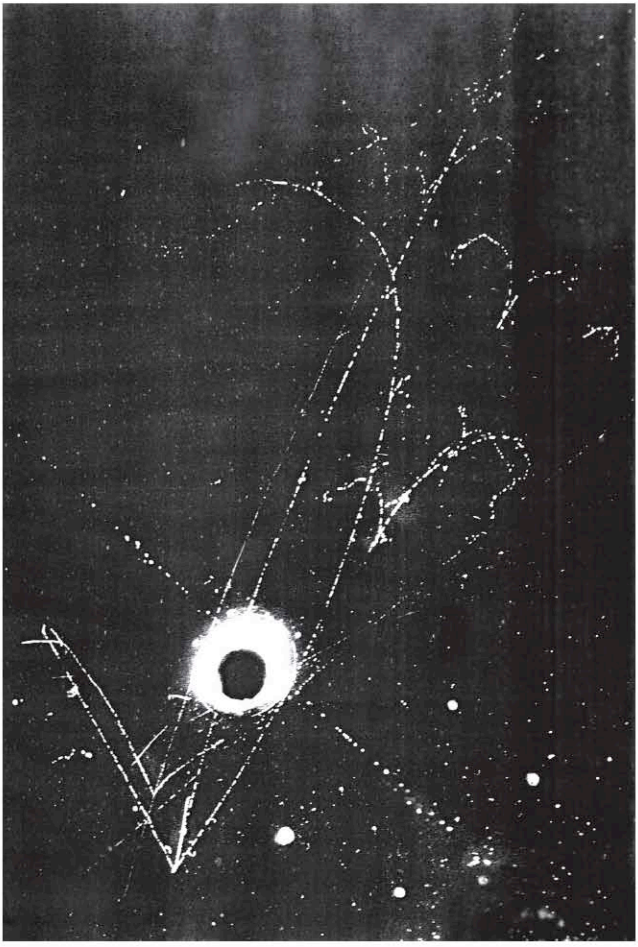

Proceedings of the Fourth International Workshop on

FRONTIER SCIENCE 2005
NEW FRONTIERS IN SUBNUCLEAR PHYSICS

Editors
A. Pullia, M. Paganoni

Proceedings of the Fourth International Workshop on

FRONTIER SCIENCE 2005
NEW FRONTIERS IN SUBNUCLEAR PHYSICS

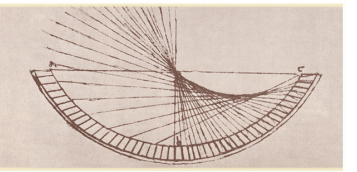

FRASCATI PHYSICS SERIES

Series Editor
Stefano Bianco

Technical Editor
Luigina Invidia

Cover:
First detection of a c → s decay, Gargamelle, 1974 ($\nu_\mu N \rightarrow \mu^- e^+ \nu_e \Lambda^o$)

Volume XL

Istituto Nazionale di Fisica Nucleare – Laboratori Nazionali di Frascati
Divisione Ricerca – SIS – Ufficio Pubblicazioni
P.O. Box 13, I–00044 Frascati (Roma) Italy
email: sis.publications@lnf.infn.it

FRASCATI PHYSICS SERIES

Proceedings of the Fourth International Workshop on
FRONTIER SCIENCE 2005
NEW FRONTIERS IN SUBNUCLEAR PHYSICS

ISBN–88–86409–46–X

Printed in Italy
by Poligrafica Laziale
P.le della Stazione 4/6, 00044 Frascati

FRASCATI PHYSICS SERIES

Volume XL

Proceedings of the Fourth International Workshop on

FRONTIER SCIENCE 2005
NEW FRONTIERS IN SUBNUCLEAR PHYSICS

Editors
A. Pullia, M. Paganoni

Dipartimento di Fisica "G. Occhialini"
Università di Milano-Bicocca, Italia
September 12 –17, 2005

International Advisory Committee

Since 2002

J.–J. Aubert	*IN2P3*
J. Butler	*Fermilab*
J. Dorfan	*SLAC*
E. Iarocci	*INFN*
L. Maiani	*CERN*
H. Sugawara	*KEK*
A.N. Skrinsky	*Novosibirsk*
A. Wagner	*DESY*
M. Witherell	*Fermilab*

Since 2003

A. Bialas	*Krakow University*
P. Cvitanovic	*Atlanta University*
M. Gell-Mann	*Santa Fe University*
L. Kadanoff	*Chicago University*
S. Kauffman	*Santa Fe University*
S. Lovejoy	*Montreal University*
G. Nicolis	*Bruxelles University*
G. Parisi	*Roma "La Sapienza"*
I. Procaccia	*Rehovot University*

Since 2004

S. Bertolucci	*INFN*
P. Carlson	*KTH Stockholm*
P. Fleury	*Ecole Polytechnique*
N. Gehrels	*NASA GSFC*
J. Ormes	*NASA GSFC*
M. Panasyuk	*Moscow University*
G. Setti	*INAF*
S. Ting	*MIT Boston*
A. Wolfendale	*Durham University*

Since 2005

U. Amaldi	*TERA*
E. Fiorini	*Univ. Milano-Bicocca*
D. Haidt	*DESY*
D. Perkins	Univ. *Oxford*
R. Petronzio	*INFN*
D. Treille	*CERN*
G. Veneziano	*CERN*

Steering Commitee

G. Casati	*Como University*
F.L. Fabbri	*INFN Frascati*
G. Pancheri	*INFN Frascati*
S. Ratti	INFN Pavia

Organizing Committee

M. Calvi	*Univ. Milano-Bicocca*
C. Matteuzzi	*INFN Milano*
M. Paganoni	*Univ. Milano-Bicocca (Co-Chair)*
S. Penati	*Univ. Milano-Bicocca*
A. Pullia	*Univ. Milano-Bicocca (Co-Chair)*
E. Previtali	*INFN Milano*
S. Ragazzi	*Univ. Milano-Bicocca*
N. Redaelli	*INFN Milano*
A. Zaffaroni	*Univ. Milano-Bicocca*

Scientific Secretary

T. Tabarelli	*Univ. Milano-Bicocca*

Secretariat

P. Fornari	*Univ. Milano-Bicocca*
S. Galimberti	*Univ. Milano-Bicocca*
A. Mangano	*Univ. Milano-Bicocca*

PREFACE

This Conference is the fourth of a series of Conferences named "Frontier Science". Each conference focuses on one topic, selected from among the most lively subjects in nuclear and sub-nuclear physics, astrophysics, mathematics, theoretical physics, earth science, instrumentation, electronics, computing, and others. The conference consists of plenary sessions devoted in part to invited talks by senior scientists and in part to selected presentations by young researchers, and a poster session. Each year special awards and credits are given to relevant contributions presented by young researchers.

This year the Conference – with an attendance of more than 100 people from 10 countries - was dedicated to the most recent developments in Subnuclear Physics with a special focus on the status and perspectives of scientific programs at large accelerators.

This field concerns the study of the fundamental laws of the Nature through the observation of the matter at his smallest scales, by the detection of the products of the collisions of very high energy partcles. The vitality of the field is witnessed by the large number of experiments in progress and planned, like – just to mention some - the general purpose experiments CMS and ATLAS at the proton proton collider LHC, the BABAR and BELLE detectors at the beauty factories, the CDF and D0 collaborations at the Tevatron.

Moreover, the need of advanced technologies both for the accelerators and the detectors requires a close interaction with technological industries providing a very fruitful exchange of expertise and know-how.

An additional mission of the series of these Conferences is to convey the importance of the field identified as a frontier in modern science to the general public. An open public lecture in Italian was given by Ugo Amaldi on the most recent advances in hadron therapy.

We warmly thank the session chairpersons and all the speakers for their contribution to the scientific success of the Conference.

The Conference was sponsored and supported by the Department of Physics of the University of Milano-Bicocca, the Italian Istituto Nazionale di Fisica Nucleare (INFN) and the Eurotech Company.

We wish to thank the International Advisory Committee members for their valuable scientific advice and support all along the course of the conference organization.

Special thanks go to all the people involved in the Conference organization: We are particularly grateful to Anna Mangano, Paola Fornari and Stefano Galimberti and to the Promoest for their valuable help in preparing and dealing with all the logistics and for the day-by-day assistance.

Finally, our special thank goes to Luigina Invidia, of the Servizio Informazione Scientifica of the Frascati Laboratories, for the technical editing of these Proceedings.

The book is available in electronic format at http://www.lnf.infn.it/sis/frascatiseries
http://www.roma2.infn.it/iwfs04/iwfs.html

June 2006 Antonino Pullia and Marco Paganoni

FrontierScience Awards

The Frontier Science Organizing Committee, to encourage and promote the participation of young researchers to the event, has presented a number of selected young physicists with a FrontierScience Award for the best poster.

A vote cast by all the attendees during the poster session has evaluated all the poster contributions on the basis of the scientific relevance, clearness and originality.

The awarded researchers are, ex-aequo:

Alessandra Retico *(University of Pisa and INFN, Italy)*

Paola Solevi *(University of Milano and INFN, Italy)*

CONTENTS

SESSION I – LHC PHYSICS AND DETECTORS (I)

F. Maltoni	Standard Model Physics at LHC
M. Mangano	Beyond the Standard Model Physics at LHC
F. Piccinini	Monte Carlo event generators for the LHC
T. Boccali	The first days at CMS
M. Limper	Physics with the first events at ATLAS
R. Bellan	Vector fusion at CMS
C. Rovelli	Search for the Higgs in the WW channel at CMS
T. Lari	Search for supersymmetry with early ATLAS data
G. Lehmann	Tests of the ATLAS Trigger and data acquisition system
P. Govoni	The calibration challenge for the CMS electromagnetic calorimeter

Frascati Physics Series Vol. XL (2006), pp. 3
Frontier Science 2005, New Frontiers in Subnuclear Physics
Milano, 12-16 September, 2005

STANDARD MODEL PHYSICS AT LHC

F. Maltoni
CERN, Geneva, Switzerland

Written contribution not received

Frascati Physics Series Vol. XL (2006), pp. 5-12
Frontier Science 2005, New Frontiers in Subnuclear Physics
Milano, 12-16 September, 2005

BEYOND THE STANDARD MODEL PHYSICS AT THE LHC

Michelangelo L. Mangano
CERN, PH-TH, 1211 Geneva 23, Switzerland

Abstract

I briefly review here the main motivations to expect physics beyond the Standard Model to appear at the LHC, and present some possible exciting scenarios.

1 Introduction

We are approaching the start of LHC data taking with a very clear picture of our world: all phenomena observed in the laboratory are consistent and well described by the Standard Model (SM). All of the elements in this picture, with the exception of the sector driving the electroweak symmetry breaking (EWSB), have been observed and their properties measured. The observation of the Higgs boson will complete the SM spectrum, and our attention will move to a deeper layer in our understanding of the universe. There are in

fact several questions which the SM cannot address, or to which it provides the wrong answer: Why 3 families of quarks and leptons? What is the origin of the particle mass hierarchies, and in particular why neutrinos are so much lighter than the others? Why is there a matter-antimatter asymmetry in the Universe? What is the origin of dark matter (DM)? Of dark energy? Is there a grand unification of forces? Why is gravity so weak? Why do we live in 3+1 dimensions? All of the above questions can be classified under a smaller number of headings: what is the origin of EWSB? What is the origin of flavour? How do quantum mechanics and gravity merge into a consistent and calculable theory? Most likely a better understanding of the origin of EWSB will also shed light on the issue of flavour and its ramifications (neutrino masses, CP violation). It is reasonable to expect that the LHC should be able to trigger significant advances on at least the problem of EWSB, and that these advances will point to a more clear direction for the future of HEP. In this short review I will justify this expectation, and discuss some plausible discovery scenarios for the LHC.

2 EWSB after LEP and Tevatron

The Tevatron and LEP's heritage is a strong confirmation of the SM, and at the same time an apparent paradox [1)], illustrated in the following paragraphs. Electroweak precision tests and the value of the top mass are consistent with a rather light Higgs mass: $m_H = 91\,^{+45}_{-32}$ GeV; EW radiative corrections in the SM, integrated up to a scale Λ, shift the bare value of m_H by:

$$\begin{aligned} \delta m_H^2 &= \frac{6G_F\Lambda^2}{\sqrt{2}\pi^2}\,(m_t^2 - \frac{1}{2}m_W^2 - \frac{1}{4}m_Z^2 - \frac{1}{4}m_H^2) \\ &\sim (115\ \text{GeV})^2\,\left(\frac{\Lambda}{400\ \text{GeV}}\right)^2 . \end{aligned} \tag{1}$$

The integration in principle can extend up to very large values of Λ, where new particles may appear, changing eq. (1). As Λ gets significantly larger than 400 GeV, however, the presence of a counterterm (CT) should be assumed, to ensure that the overall value of m_H is consistent with its bounds. This CT can be interpreted as a low-energy manifestation of the physical mechanisms which, at some scale $\overline{\Lambda}$, modify eq. (1). Ensuring that the residual of the cancellation between eq. (1) and the CT is in the 100 GeV range, however, forces a fine

tuning which becomes more and more unbelievable as Λ grows. Assuming that no new physics appears before the GUT scale of 10^{16} GeV leads to a level of fine tuning of 10^{-28}. By and large theorists believe that this is unlikely enough to call for the existence of new physics at scales in the range of 1–few TeV, so as to maintain the fine tuning to within $O(10^{-3})$. This belief however clashes (and this is where the paradox arises) with the staggering agreement between EW data and the SM. The inclusion of generic new physics, parameterized in terms of low-energy effective couplings between the SM particles, and the analysis of the effects induced on EW observables, set lower limits to the scale $\overline{\Lambda}$ in the range of 5-10 TeV [2], at the extreme limit of the fine-tuning window. The solution to the paradox could only be obtained with new physics which cancels the large radiative contributions to m_H and, at the same time, manages to leave all other EW parameters and observables unaffected. Supersymmetry (SUSY) provides one such example! The cancellation of large loop effects between SM particles and their SUSY partners modifies eq. (1) and leads to an upper limit on m_H, given in a simplified approximation here:

$$m_H^2 \lesssim m_Z^2 + \frac{3G_F\, m_t^4}{\sqrt{2}\pi^2} \log\left(\frac{m_{\tilde{t}}^2}{m_t^2}\right) \tag{2}$$

where $m_{\tilde{t}}^2$ is the average squared mass of the two stop states. At the same time, the structure of the theory is such that indeed generic choices of the SUSY parameters, consistent with current experimental limits on new particles, lead to negligible effects in the EW observables. In the minimal realization of SUSY (MSSM), when eq. (2) is improved with 2-loop and non-logarithmic corrections, the experimental limit on m_H pushes however the scale of SUSY in the TeV domain. Once again this is at the edge of being acceptable as a "natural" solution to the fine-tuning problem, and for many theorists the room left for SUSY is becoming too tight. As a result, new scenarios for EW symmetry breaking, particularly some with looser upper limits on the Higgs mass compared to the MSSM, have been proposed (as reviewed in [1]). Some of these ideas lead to rather artificial structures, where the problem of the Higgs naturalness is shifted to slightly higher scales, via the introduction of a new sector of particles around the TeV. Few of them offer the appeal of Supersymmetry, with its clear predictions (calculability), and connections with the other outstanding problems of the Standard Model (Dark Matter, Flavour, CP violation). In most cases, new phenomena within the reach of

the LHC are bound to appear. Little Higgs models, for example, predict the existence of heavy top-like quarks, and of new heavy gauge bosons (W' and Z'). Extra-dimensional, or Higgsless models, predict strong WW scattering at about 1 TeV, and Kaluza-Klein like excitations starting from the TeV scale.

While these alternative scenarios could take longer to be identified experimentally at the LHC, the SUSY framework provides a strong and appealing physics case for a possible early discovery, and therefore should be given maximum priority in the planning for the first LHC data analyses. SUSY is in fact expected to manifest itself with abundant and striking signals, such as the production of multijets with large missing transverse energy ($\not\!\!E_T$), multileptons (possibly same-charge), or prompt photons with large $\not\!\!E_T$. Because of rates, background levels, and nature of the observables, searches for SUSY are expected to be less demanding from the experimental point of view than the quest for the Higgs in the $m_H < 140$ GeV range. In addition, SUSY provides a natural candidate for dark matter, namely the lightest neutralino χ_1^0, the neutral SUSY partner of the photon, Z and of the Higgs. Proving the direct link between dark matter and SUSY would be, perhaps even more than the Higgs discovery, the flagship achievement of the LHC! Last but not least, an early detection of SUSY could immediately provide clear directions to the field of experimental high-energy physics, and allow a robust planning for future facilities.

The large value of m_H shows that room is getting very tight now for SUSY, at least in its *minimal* realizations. This makes the case for an early observation of SUSY at the LHC quite compelling. Should SUSY be discovered at the LHC, via any of the above observables, physicists would face the necessary and ambitious task of understanding the origin of its breaking, which is the source of the multitude of parameters characterizing any SUSY model: the spectrum of sparticle masses, their mixings, and their couplings. To get clues on the mechanism of SUSY breaking should therefore be a crucial goal of the LHC, as well as of any planning for future HEP programmes.

3 The role of flavour physics

Flavour phenomena provide a crucial testbench for most BSM theories [4]. This has been true also for the development of the SM, which was tailored to accommodate $K^0 - \bar{K}^0$ mixing, FCNC and the prediction of charm, CP

violation. In the SM the key element is the GIM mechanism:

$$A(s\bar{d} \to Z/\gamma) \propto (m_t/m_W)^2 \lambda^5 \tag{3}$$

where λ is the Cabibbo angle. In absence of GIM cancellations (as would happen in generic extensions of the SM, like Supersymmetry with arbitrary squark mass matrices), the Cabibbo suppression is absent, and the mass factors reflect the masses of the new particles circulating in the loops. In the case of Supersymmetry, the mass factor is proportional to the mass splittings between squarks of the different generations. Essential probes of the flavour structure of theories BSM are given, for example, by the four very rare decays of kaons: $K^+ \to \pi^+ \nu\bar{\nu}$, $K_L^0 \to \pi^0 \nu\bar{\nu}$ and $K_L^0 \to \pi^0 \ell^+ \ell^-$, with $\ell = e, \mu$, as well as by the rare decays of B mesons: $B_{d,s} \to \ell^+ \ell^-$. Accuracies at the level of 10% in the determination of these BR would provide essential inputs in the study of the flavour structure of any new physics model.

The discovery of Supersymmetry or other new phenomena at the LHC will dramatically increase the motivation for searches of new phenomena in flavour physics. While there is no guarantee that any deviation from the SM will be found, the existence of physics BSM will demand and fully justify these studies: we'll be measuring the properties of something which we know exists, as opposed to frustratingly looking for "we don't know what" as we are unfortunately doing today!

The B physics studies at the LHC and at the B-factories will find therefore a natural complement in a revived and strengthened K physics programme, as well as in new studies of the charm sector and searches for Lepton Flavour Violation (LFV) phenomena. All of these studies will be an essential component of the programme leading to the complete clarification of the nature of the new phenomena to be observed at the LHC.

4 Dark Matter

The evidence for the existence of dark matter is very strong today, with the new recent findings from studies of structure formation and CMB fluctuations. It is important to realize that, whatever its origin, the existence and properties of DM must be encoded somewhere in the Lagrangian of HEP. So it is "our" problem to find out what it is, and not the astrophysicists' problem. From our point of view, the main ingredients of DM are: a stable weakly interacting

particle, with mass vs annihilation rates such as to decouple during the Big Bang from the other states at the appropriate time and with the appropriate density. It so happens that the required numerics works out to match the expected behaviour of particles with mass $O(100\ \mathrm{GeV})$ and weak coupling:

$$\sigma \sim \frac{\alpha_W^2}{M_W^2} \ . \tag{4}$$

It is unavoidable to speculate that the origin of DM is directly linked to the phenomena responsible for EWSB. It is therefore not surprising that most alternative approaches to EWSB (little Higgs, extra-dimensions, Higgsless theories) provide a possible DM candidate. The mass vs coupling relations are inherited by the link to EWSB and the stability is associated to discrete symmetries (like SUSY's R parity). In the case of extra-dimensions, for example, DM could originate from the first photon or neutrino Kaluza-Klein mode. Once again: it is a crucial goal of the future in HEP to firmly establish the true nature of DM, and the hunt might optimistically end already during the first running of the LHC!

5 A dream scenario for HEP at the time of the LHC

I shall outline here a dream scenario, in which an early detection of new physics signals at the LHC drives a chain-reaction of observations and discoveries, and motivates measurements to be performed with a multitude of experiments both at the high and low-energy end of the spectrum. In this scenario, all the topics reviewed before acquire a primary role in exploring in full the parameters and features of the new physics.

Let me therefore assume that the LHC will give indications of a gluino in the TeV mass range (for example in the multijet plus $\not\!\!E_T$ final state). Measurements of the kinematics of these events will provide a determination of the mass of gluinos, and will possibly lead to a separation between gluinos and squarks. Several measurements will then follow: the identification of charginos and neutralinos, with a determination of their masses. The determination of the parameters of the neutralino could establish the neutralino as the particle responsible for dark matter. The relation between the gluino mass and the mass of the charginos and neutralinos will provide important information to select the structure of the SUSY breaking mechanism. Additional informa-

tion will come from other properties of the final states: for example, if hard photons are detected, and the missing energy is associated to very light particles, then scenarios such as gauge-mediated SUSY breaking are favoured. In this case the neutralino is unstable (and therefore could not be held responsible for dark matter), and decays to a photon and a light gravitino (which would therefore become the first detected particle in the quantum spectrum of gravity!). Further studies should focus on the identification of individual squarks, and in particular on the identification and mass determination of the stop and sbottom, together with the mass splitting between the two separate states of each squark. The slepton spectrum can be explored either through the direct production of sleptons (via e.g. DY-like processes), or through their emission during the chain decays of charginos and neutralinos. Their masses can be measured, and the relation between their masses and those of squarks will provide additional information on the structure of SUSY breaking. The detection of the Higgs boson, and of the additional Higgs particles present on SUSY models, will allow to verify the mass relations involving the Higgs, the stop and $\tan\beta$. This study will be complemented by the study of the ttH and bbH couplings, e.g. via the detection of ttH and bbH associated production. To the extent that the masses are low enough, the ILC will provide a unique facility to carry out a good fraction of the above measurements with excellent precision.

The LHC will complement the studies of high-mass phenomena with the observation of rare decays of B mesons, for example $B_{d,s} \to \mu^+\mu^-$.Super B-factories will contribute to the high-accuracy determination of the CP violation asymmetries for modes such as $B \to \phi\psi$ or $B \to \phi K_S$, possibly exposing the underlying contributions due to b and s squarks. The knowledge of the gluino and squark masses gained from the direct measurements at the LHC, will allow to start extracting the squark mixing parameters, and verify the possible consistency with flavour mixing scenarios such as those motivated by SUSY-GUT neutrino models. A more complete exploration of the flavour structure of SUSY will benefit from a new generation of rare kaon decay experiments, which will detect and measure the four golden modes: $K^+ \to \pi^+\nu\bar{\nu}$, $K_L^0 \to \pi^0\nu\bar{\nu}$ and $K_L^0 \to \pi^0\ell^+\ell^-$. In addition, it will be mandatory to search for possible flavour-changing effects in the lepton sector, such as $\mu \to e\gamma$, $\mu \to 3e$, $\tau \to \mu\gamma$, $\tau \to 3\ell$, $\mu \to \tau$ transitions. These measurements could cross-correlate with the

predictions of neutrino-mass models. The presence of SUSY could provide new sources of CP violation, for example in the Higgs sector, or in the gluino or chargino/neutralino couplings. These sources of CP violation could be exposed already at the LHC, but would likely appear as electric dipole moments, either in the neutron (if present in the gluino sector) or in the leptons (if present in the weak gauge fermion sector). Last but not least, the LHC will be the first "top factory", collecting top quark pairs at a Hz-like rate. The t-W-b vertex will be studied in great detail, and FCNC decays such as $t \to Zc$ or $t \to \gamma c$ will be probed at the level of 10^{-5}.

6 Conclusions

The necessity for extensions of the SM is justified both on the basis of theoretical arguments (the hierarchy problem, the flavour structure, the quantization of gravity) and on the basis of the experimental evidence (DM, BAU, neutrino masses). Most theoretical arguments establish a link between EWSB and at least some of the theoretical and experimental motivations for BSM phenomena. It is therefore very likely that the LHC, by detecting the Higgs boson and beginning the study of its properties, will shed the first light on these new phenomena. Several of the BSM schemes under discussion, such as Supersymmetry, would lead to direct and independent signals, which could be detectable prior to the Higgs discovery, thanks to clearer signatures. In several scenarios a full clarification of the new phenomena will require input from a large variety of experiments in addition to the LHC ones. The diversification of the experimental programmes will be a big bonus, and lead to a great boost of various activities world-wide.

References

1. R. Barbieri, arXiv:hep-ph/0410223.

2. R. Barbieri and A. Strumia, Phys. Lett. B **462** (1999) 144; R. Barbieri, A. Pomarol, R. Rattazzi and A. Strumia, Nucl. Phys. B **703** (2004) 127.

3. N. Arkani-Hamed and S. Dimopoulos, JHEP **0506** (2005) 073; G. F. Giudice and A. Romanino, Nucl. Phys. B **699** (2004) 65.

4. A. J. Buras, arXiv:hep-ph/0505175.

Frascati Physics Series Vol. XL (2006), pp. 13-20
Frontier Science 2005, New Frontiers in Subnuclear Physics
Milano, 12-16 September, 2005

MONTE CARLO EVENT GENERATORS FOR THE LHC

Fulvio Piccinini
INFN Sezione di Pavia and Dipartimento di Fisica Nucleare e Teorica, via Bassi 6, I-27100, Pavia, Italy

Abstract

A review on the state of the art of Monte Carlo event generators for high energy hadronic collisions is presented, with emphasis on recent theoretical developments and on the requirements posed by the LHC physics program.

1 Introduction

The last few years have seen a very intense activity in improving existing Monte Carlo tools and developing new ones, in view of the ongoing Tevatron run II analysis and of the LHC start up. Two aspects make of the LHC a completely new machine with respect to Tevatron: the increase of a factor of $\mathcal{O}(10^3)$ in luminosity and the increase of a factor of ten in the available center of mass energy. The first item makes of the LHC a particle factory with statistics much larger than any other machine built up to now. With such a statistics, the

ultimate goal of Standard Model (SM) physics at LHC should be an absolute error of about 15 MeV and 1 GeV for M_W and $m_{\rm top}$ respectively, and a relative precision on $m_{\rm H}$ of the order of 0.1%. In view of these peculiarities, the uncertainties in theoretical predictions could become a limiting factor in extracting information from data analysis. The large center of mass energy should allow the production of new heavy particles, which decay leaving signatures characterized by large jet multiplicities. In order to control the backgrounds to such final states, we need reliable theoretical calculations for multi-jet final states. This signals the importance of higher-order corrections, which are by far dominated by QCD radiation. However, for some precision observables, also electroweak corrections will become important. For instance in Drell Yan, the precise W-mass determination with the foreseen accuracy requires the inclusion of $\mathcal{O}(\alpha)$ electroweak and higher-order photonic corrections. We have already now dedicated programs treating electroweak corrections [1].

In this contribution I will concentrate on QCD Monte Carlo programs, by reviewing the features of the three general classes: Monte Carlo integrators, Parton Shower event generators and Multi-parton Monte Carlo event generators. Last section will be devoted to reviewing recent progress in combining the good features from different classes of programs. Comprehensive and detailed reviews on Monte Carlo event generators for LHC can be found in Ref. [2], where also an exhaustive account of references can be found.

2 Monte Carlo integrators

To this class belong all programs able to calculate cross sections and distributions numerically, the numerical integrations being performed with the Monte Carlo algorithm. Thanks to the flexibility of the Monte Carlo procedure, such programs can give predictions for arbitrary event selections, but only partonic final states are generated. They provide events with flat distribution on the phase space weighted with the matrix element of the process under consideration. For this reason they are also called "generators of weighted events". The typical use of a Monte Carlo integrator is to obtain predictions in fixed order perturbation theory beyond leading order. At present, the techniques are well established to build next-to-leading (NLO) Monte Carlo integrators. The cross section or any other observable distribution is obtained as the sum of the tree-level contribution coherently summed to the one-loop virtual corrections to the

process $2 \to n$, plus the real contribution $\sigma(2 \to n+1)$, where the emission of an additional gluon is considered. The knowledge of NLO corrections is important to test the theoretical uncertainty of the calculations by studying their stability against variations of the renormalisation and factorisation scales. Monte Carlo programs able to treat arbitrary event selections can be used to test the validity of the $K-$factors (defined inclusively as σ_{NLO}/σ_{LO}) at the level of distributions, where different bins can receive different corrections. Even if they are very important tools, Monte Carlo integrators have several limitations: 1) while they work nicely in describing the effects of hard radiation, they fail in the region of soft/collinear singularities, where pure perturbative calculations are unreliable. The accuracy of the calculations can be increased in certain regions of phase space implementing resummed calculations, which are however valid for one observable at a time. Recent work has been devoted to the study of new automatized resummation algorithms [3]; 2) some multiparton final states will be important at LHC (for instance $pp \to t\bar{t}b\bar{b}$ for Higgs physics). In this case multiparton final state NLO virtual QCD corrections are necessary for a NLO Monte Carlo program, which is however beyond the present technical possibilities. Standard techniques for the evaluation of virtual corrections can not be applied to processes with many (possibly massive) partons in the final states. Several groups are working on this problem, investigating new seminumerical methods to calculate virtual corrections with arbitrary external legs [4]; 3) the essential ingredient of any NLO calculations, namely virtual and real corrections, display strong cancellations on the phase space, with the virtual part becoming negative. This prevents a probabilistic interpretation of the elastic event and consequently the generation of unweighted events, which would be distributed in the phase space according to the theory and with unity weight, and would be very useful for detector simulations. These shortcomings allow to introduce the next class of Monte Carlo programs, the Parton Shower Event Generators.

3 Parton Shower Monte Carlo Event Generators

The key ingredient of this class of programs is the parton-shower technique, which allows to generate higher order corrections starting from a simple (tipically $2 \to 1$ or $2 \to 2$) process. The parton-shower technique is a numeric Monte Carlo solution of the DGLAP evolution equations, which allows the calcula-

tion of QCD (and also QED) higher order radiative corrections in the region of collinear parton branching and/or soft gluon emission. The subsequent parton emission is a stochastic Markov process in which successive values of the evolution variable Q, the momentum fraction z and the azimuthal angle ϕ are generated (allowing for kinematics reconstruction). With this method, leading logarithms are automatically resummed to all orders of perturbation theory. The process of showering is completely factorized over the kernel amplitude, making the Parton Shower event generators general-purpose tools, which provide in a natural way unweighted events. Supplementing the showered events with some model of hadronisation, the Parton Shower event generators allow to describe the complete history of the hadron-hadron interaction, from initial state radiation, hard scattering, showering, hadronization, to final state hadrons and leptons, including the underlying event (beam remnants, collisions between other partons in the hadrons and collisions between other hadrons in the colliding beams). All these stages, apart from the hard subprocess, are process independent. The great advantages of Parton Shower event generators are their universality and the possibility of providing an exclusive description of the events, i.e. the complete information for every particle is recorded. For these reasons they are invaluable tools for detector simulations and they are so widespread among the experimental community. In view of the LHC era, where simulation and data analysis become more and more complex and involve an increasing number of users, transparency and maintenance of the codes start to become an important issue. For this reasons, a number of new codes are being developed within the object oriented framework of the `C++` language.

4 Merging NLO calculations with Parton Shower Event Generators

While Parton Shower event generators describe correctly the radiation in the soft/collinear regions, with automatic resummation of leading logarithmic terms, they fail to describe hard wide-angle radiation because of the approximation in the matrix elements with additional radiation and, as a consequence, the cross sections are correct at Leading Order (LO). During last years, many efforts have been dedicated to the problem of interfacing complete NLO calculations with Parton Shower Event Generators. This program would have several positive features, such as:
1) the normalisations accurate at NLO;

2) the hard tails of the distributions correct as in NLO calculations;
3) soft/collinear emissions treated as in Parton Shower event generator, i.e. automatic resummation of the leading logarithms;
4) soft matching between soft/collinear and hard regions without double counting;
5) generation of unweighted exclusive events.

A potential drawback could be the presence of negative weights. A concrete realization of this program is `MC@NLO` [5], which implements many relevant processes for LHC physics.

5 Multiparton Monte Carlo Event Generators

The previous strategy of merging NLO calculations with Parton Shower Monte Carlo programs is not feasible at present for arbitrary multiparton processes. For such final states, even the calculation of exact LO matrix elements can be a very difficult task, due to the very large number of Feynman diagrams involved. A further difficulty is given by the complex peaking behaviour in the phase space rendering the numerical integration a non trivial task. Recently, thanks to helicity amplitude or completely numerical algorithms and computer power, several matrix element event generators have been constructed. They can generate partonic weighted and unweighted events. The strategy to describe real final states with hadrons is to pass the unweighted event samples to the Parton Shower Monte Carlo for further showering and hadronization. This kind of modularity (generate events with one program and further use them with another one) has been facilitated by means of the so called Les Houches Accords [6]. During the workshop MC4LHC held at CERN in 2003 [7], there has been an intensive activity aimed at validating the accuracy of the programs through several tuned comparisons.

6 Matching partonic event generators to Parton Shower

The procedure mentioned above of interfacing matrix element unweighted events with Parton Shower is not free of ambiguities. In order to generate partonic events, one needs to implement cuts at the partonic level. They are unphysical, in the sense that the final jet cross-section should be independent of their choice. Moreover, the same configuration of a final state with n jets can be

obtained from different partonic configurations with $n+m$ partons, which gives rise to double counting. The general problem of matching multiparton matrix element calculations with parton showers has been extensively studied in the literature and for e^+e^- collisions a solution (CKKW) has been proposed and tested on LEP data [8], which avoids double counting and shifts the dependence on the resolution parameter beyond next-to-leading logarithmic (NLL) accuracy. The method consists in separating arbitrarily the phase-space regions covered by matrix element and parton shower, and use, for *all* parton multiplicities, vetoed parton showers together with reweighted tree-level matrix elements by means of suitable Sudakov form-factor combinations. The extension of the procedure to hadronic collisions has been proposed in ref. [9]. Recent detailed results of the implementation of the procedure with the programs `HERWIG`, `PYTHIA` and `SHERPA` have been presented in ref. [10]. In the case of hadronic collisions there is a certain degree of arbitrariness, such as the choice of the Sudakov form factors, the choice of the scale of α_s (LO or NLO), the treatment of the highest-multiplicity matrix element, the choice of the clustering scheme, the use of flavour or colour information to define the tree and the related reweighting factors, the treatment of gauge bosons. All these uncertainties entail that a large degree of tuning on the data (possibly process-dependent) will be needed, and further work remains to be done to find what the correct prescriptions are. A systematic uncertainty of the order of 30% has been estimated in ref. [10]. An independent realization, based on cone algorithms, has been proposed by M.L. Mangano [11]. The procedure is implemented in `ALPGEN v2.1` [12].

7 Summary

The last few years have seen intensive efforts in the development of methods to update existing Monte Carlo simulation programs or write new ones, in order to meet the requirements posed by the LHC: very high statistics for all SM processes studied up to now and presence of multi-jet final states. In this contribution a review of the three general classes of simulation codes (Monte Carlo integrators, Parton Shower event generators and Multi-parton event generators) has been presented. After a discussion of the good features and limitations of each approach, the techniques recently studied to merge different classes have been illustrated, namely NLO calculations with Parton Shower

event generators on one hand and Multiparton matrix element generators with Parton Shower simulation packages on the other hand. While the field is very active with the approaching of the LHC startup, the programs and methods already available are being validated against the fresh Tevatron run II data.

References

1. U. Baur, S. Keller and D. Wackeroth, Phys. Rev. **D59** 013002 (1999); C.M. Carloni Calame et al., Phys. Rev. **D69** 037301 (2004); JHEP **0505** 019 (2005); Acta Phys. Polon **B35** 1643 (2004); W. Placzek and S. Jadach, Eur. Phys. J. **C29** 325 (2003).

2. M. Dobbs et al., `hep-ph/0403100`; `hep-ph/0403045`.

3. A. Banfi, G. Salam and G. Zanderighi, JHEP **0503** 073 (2005).

4. A. Ferroglia et al., Nucl.Phys. **B650** 162 (2003); W.T. Giele and E.W.N. Glover, JHEP **0404** 029 (2004); R.K. Ellis, W.T. Giele and G. Zanderighi, `hep-ph/0508308`.

5. S. Frixione, B.R. Webber, JHEP **0206** 029 (2002); `hep-ph/0207182`; `hep-ph/0307146`; `hep-ph/0309186`; `hep-ph/0402116`; S. Frixione, P. Nason, B.R. Webber, JHEP **0308** 007 (2003); S. Frixione et al. `hep-ph/0512250`.

6. E. Boos et al., `hep-ph/0109068`; W. Giele et al., `hep-ph/0204316`.

7. Workshop on "MC tools for the LHC", CERN, 7 July - 1 August 2003.

8. S. Catani et al., JHEP **0111** (2001) 063; L. Lönnblad, JHEP **0205** 046 (2002); R. Kuhn et al., `hep-ph/0012025`; F. Krauss, R. Kuhn and G. Soff, J. Phys. G **26** L11 (2000).

9. F. Krauss, JHEP **0208** 015 (2002).

10. S. Mrenna and P. Richardson, JHEP **0405** 040 (2004); F. Krauss et al., Phys. Rev. **D70** 114009 (2004), Phys. Rev .**D72** 054017 (2005); A. Schälicke and F. Krauss, JHEP **0507** 018 (2005); T. Gleisberg et al., Phys. Rev. **D72** 034028 (2005).

11. M.L. Mangano, talk given at the "Monte Carlo Tuning Working Group", FNAL, 29-30 April 2003.

12. M.L. Mangano et al., JHEP **0307** 001 (2003).

Frascati Physics Series Vol. XL (2006), pp. 21-24
Frontier Science 2005, New Frontiers in Subnuclear Physics
Milano, 12-16 September, 2005

THE FIRST DAYS AT CMS

Tommaso Boccali
Scuola Normale Superiore and INFN Sezione di Pisa
Piazza dei Cavalieri 7, 56126 Pisa, Italy

Abstract

I describe the current understanding of the commissioning procedure of the CMS [1)] detector at LHC, starting from the precalibration obtained before the beams. The first few pb^{-1} are expected to improve sensibly the performance of all the subdetectors, and allow a commissioning for physics before the achievement of LHC high luminosity running.

1 Introduction

With the current LHC schedule, the first run with colliding beams in LHC is expected on August 2007, with an instantaneous luminosity ranging between $10^{28} - 10^{31}$ $\text{cm}^{-2}s^{-1}$ and an integrated luminosity collected of $10 - 100$ pb^{-1}. The first Physics run is instead scheduled starting from April 2008, with nominal low luminosity 2 10^{33} $\text{cm}^{-2}s^{-1}$ and up to 10 fb^{-1} collected.

2 CMS Commissioning - before colliding beams

The CMS detector configuration will be different for these two run periods: during the first one, the Pixel Tracking system will not be present, and the ECAL endcap will not be installed. Moreover, the RPC and CSC Muon systems will have limited eta coverage, with RPC chambers only up to $\eta = 1.6$ and CSC electronics up to $\eta = 2.1$. The DAQ [2)] system will be operation, but only one slice of L1 will be installed, with a limit in the L1 output set to 12.5 kHz and a design 100 Hz HLT rate on disk.

All the subdetectors will be precalibrated at least to some extent before and during installation; this can be achieved

- without signal sources: in lab the basic functionalities and the noise level can be checked; tracker μstrip detectors will have overgone deep and long testing at different temperatures, and a broken strip map will be available;
- with radioactive sources: ECAL crystals can be calibrated with 1 MeV gammas from ^{60}Co at the level of 5%;
- with cosmic rays: these provide high momentum straight tracks, very practical for alignment studies. Unfortunately, the tracks cover only the barrel region, and need a special RPC trigger. In any case, the rate is about 2 kHz in the muon system, and scales down to 50 Hz for tracks impinging the tracker;
- with beam-halo muons: they consist in a machine induced background, present also with only one beam circulating, and are very energetic (TeV level) horizontal tracks, synchronous with LHC bunches. The rate in the endcap Muon system is 1 kHz, which reduces to 200 Hz for the tracker system (which still needs a special low radius trigger, hopefully provided by TOTEM). These muons are very useful for initial endcap alignment;
- with beam-gas tracks: these are fixed target like events, in which a 7 TeV proton interacts with nucleons, resulting in a 115 GeV cms energy. The events present multiple tracks, mostly in the forward region, with a low p_T which can give triggering issues. Moreover, only the first tracker layers are reached due to the bending in the magnetic field.

As explained, all these configurations need some special and non standard settings, like special triggers or time synchronizations different from the *pp* run ones.

3 CMS Commissioning - with colliding beams

In 2007, the most important tasks to be performed are time alignment (with respect to LHC collisions), geometrical alignment (for tracking devices), and calibrations (mostly for calorimeters). Before LHC interactions, relative timing can only be determined by geometrical constraints and cable length; during the collisions, the timing at 1 ns can be obtained for tracker detectors by maximizing signals on each of them.

Spatial alignment is especially critical due to the very high resolution of the devices, which in the case of Pixel Tracker detectors reach 10 μm. CMS can rely on three different means for detector alignment: hardware constraints and measurements during construction, alignment with laser and with physics events. The construction precision for the silicon tracker is measured before integration with a precision at the level of 15 μm for detectors substructures (layers, petals...), and at the level of 100 μm with a continuously monitored laser system, but only for a few detectors. This system serves to monitor the stability between different structures and as a link between Tracker and Muon systems. During physics runs, the large number of (high p_T)tracks available can be used in a global fit to detector positions; with a reasonable number of tracks, a 10 μm resolution should be possible. Unfortunately, the absence of the Pixel system in the pilot run probably limits the alignment to what can be obtained with the first two means, with a 20% worsening on the Z mass resolution, for example.

In the Muon system, the multiple scattering for tracks with $p_T < 100$ GeV in the iron does not require a resolution on the single hit of any better than 200 μm, which can be obtained only with hardware constraints and laser systems.

The intercalibration of ECAL response is a major task for the CMS commissioning. Starting from the 5% with lab measurements, a 2% calibration level can be readily obtained (in a few days time) with minumum bias events and equalization of the response with ϕ. The design 0.5% in the constant term of the energy resolution instead needs probably more data, specifically

$W \to e\nu$ and $Z \to ee$, and an aligned tracking system. In 10 pb^{-1}, only 10^5 W and 15000 Z decays are available, not sufficient for the calibration of the 75000 crystals.

The trigger system in the 2007 pilot run should present a nominal L1 trigger, apart from the eta coverage and the reduced 12.5 kHz rate. Concerning HLT, the absence of the Pixel system will probably limit its application for physical studies. Moreover, since the priority is detector commissioning and understanding, the HLT table will be focused on calibration, allowing minimum bias events, high p_T single electrons, muons and gammas, and jets with high E_T. No official decision has been taken, but these "easy" objects should allow a timely commissioning of the various subdetectors, at the expenses of a physics program which would be in any case difficult to fulfil. In principle, already in 10 pb^{-1} more $t\bar{t}$ are produced than in any previous experiment, but the absence of a Pixel system and thus of a reliable b-tagging does not allow any measurements [3].

4 Conclusions

During the first LHC Pilot run, scheduled in 2007, the CMS Collaboration will undergo the commissioning of the various CMS subdetectors,in order to reach design performance. The pilot run will probably not be sufficient for a proper Tracker alignment and ECAL calibration, which will be reached only during the 2008 physics run, with the final detector configuration including Pixels and ECAL endcap. Physics will probably have to wait for 2008, when the full performance of the CMS detector should be available.

References

1. The CMS Collaboration, "The Compact Muon Solenoid TDR", CERN/LHCC 94-38 (1994).

2. The CMS Collaboration, "Data Acquisition and High Level Trigger TDR", CERN/LHCC 2002-26.

3. The CMS Collaboration, "The CMS Physics TDR", to be published.

Frascati Physics Series Vol. XL (2006), pp. 25–30
Frontier Science 2005, New Frontiers in Subnuclear Physics
Milano, 12-16 September, 2005

PHYSICS WITH THE FIRST EVENTS IN ATLAS

Maaike Limper
NIKHEF, Kruislaan 409, 1098 SJ Amsterdam, The Netherlands

Abstract

During an initial period of proton-proton collisions at the LHC, the ATLAS detector will be commissioned using well known physics channels. ATLAS will start with measurements of minimum bias events and standard model processes to understand the physics in 14 TeV hadron collisions. Top quark analysis in ATLAS will help to improve the detector performance. Only then early LHC discoveries such as the detection of the first SUSY signals can be made.

1 Introduction

The ATLAS detector is one of two general purpose experiments that will study $\sqrt{s}$=14 TeV proton-proton collisions of the Large Hadron Collider that is currently being built at CERN, Geneva. The luminosity of the LHC will be 10^{33} $\mathrm{cm}^{-2}\mathrm{s}^{-1}$ during its first three years of operation and finally it is designed to

reach 10^{34} $cm^{-2}s^{-1}$. The high center of mass energy and luminosity at the LHC will allow the possibility of discovering the Higgs particle, SUSY particles or maybe even other new physics.
At the end of 2007 a pilot run of the LHC is scheduled to take place, providing ATLAS with its first collisions. In 2008 the LHC will start to run at a luminosity of 10^{33} $cm^{-2}s^{-1}$ for a period of 8 months. The ATLAS detector is currently under construction and should be ready at the start of LHC collisions

2 First measurements with physics

Huge event samples of known standard model processes will be recorded during the first period of LHC collisions. The cross-sections and properties of these processes will be measured. Using this data ATLAS can assess the performance of its detectors without relying on simulation.
The decay of the well known Z^0-boson will be the basis of many studies. Z^0 decays to muons can be used to calibrate and align the muon spectrometer, while Z^0 decays to electrons similarly helps to set the absolute scale in the electromagnetic calorimeters in ATLAS. The absolute jet energy scale can be improved with Z+jet events, or with the hadronic decay of the W in $t\bar{t}$ events. Also the trigger performance needs to be understood well, without relying on simulation. This can be done using minimum bias events, QCD jets with various energy thresholds and single and dilepton samples.

2.1 minimum bias and underlying event

The bulk of the parton interactions at the LHC will be soft interactions (low momentum transfer), which can only be described by non-perturbative phenomenological models. These so called soft interactions play an important role in minimum bias events and the underlying event.
The underlying event consists of all event activity except the hard scattering partons. The underlying event contains a soft component from remaining soft interaction of beam-beam remnants and a hard component from the initial and final state radiation, from color strings stretching between the underlying event and the highest-pt jet, and hard interactions of beam-beam remnants.
Soft interactions are not yet well understood as is shown by predictions for minimum bias and underlying event at LHC energies [2)] using two different

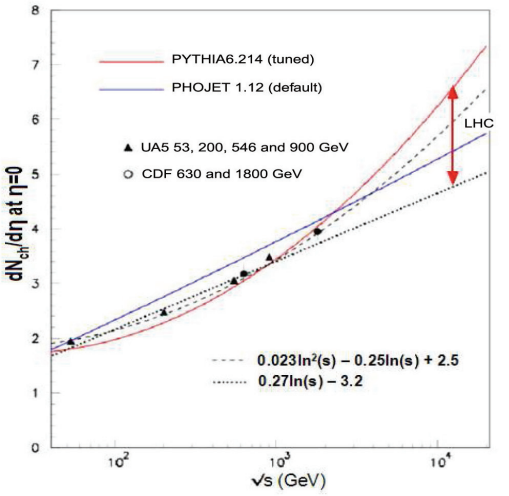

Figure 1: *Charged particle density at* $\eta = 0$ *for a wide range of* $\sqrt{s}$*. The theoretical uncertainty in* $\frac{dN_{ch}}{d\eta}$ *at LHC energy is indicated*

Monte Carlo event generators, PYTHIA and PHOJET. The results obtained with this MC generators disagree by ∼30% in minimum bias charged particle multiplicity distributions (see figure 1), and by a factor ∼2 for underlying event distributions.
These multiplicities in minimum bias can be measured in the ATLAS detector by counting tracks in the inner tracker, requiring only a few thousand events. The particle multiplicities in the underlying event are measured by counting tracks in a region transverse of a high P_t jet.
Minimum bias and underlying event will need to be measured to understand the occupancy, pile-up and backgrounds in the ATLAS detector.

2.2 $t\bar{t}$ analysis with the first collisions in ATLAS

At a luminosity of $10^{33} cm^{-2} s^{-1}$, approximately one $t\bar{t}$-pair will be produced every second in ATLAS, giving excellent statistics to improve measurements of the top quark properties, as well as the opportunity to use the top quark for calibration studies. The top-quark decays into a W-boson and a b-quark, and the W can then decay into either a pair of quarks or a lepton and a neutrino.

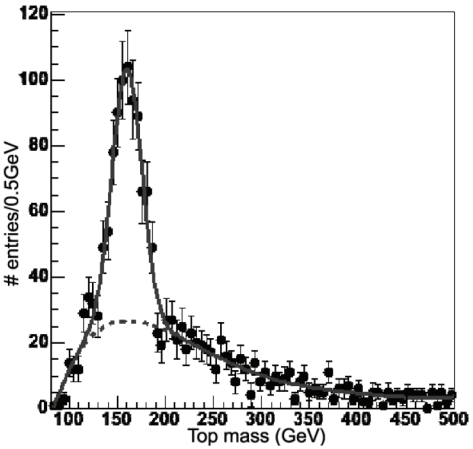

Figure 2: *Top mass measurement using simulated data equivalent to one week of data-taking at a luminosity* $10^{33} cm^{-2} s^{-1}$ *with* M_{top}*= 175 GeV (dashed line indicates fitted background)*

The semi-leptonic decay, where one W decays into jets and the other W decays into leptons, provides the best analysis opportunity for studying $t\bar{t}$ production. The top sample will contain b-jets that can be used to train and improve the b-tagging algorithms. The well known W mass can be used to calibrate the energies of the jets from the hadronic W decays in the top sample. The measurement of missing transverse energy carried by neutrinos passing through the detector can be calibrated by reconstructing the leptonic top.
A study is made of the analysis of semi-leptonic $t\bar{t}$ decays without using the b-tag [3]. The analysis requires the reconstructed W-mass to lie within 10 GeV of the currently known value of the W-mass. A signal of background ratio with the W+4jet background of 1.77 is found with this analysis. Figure 2 shows the result of the analysis using an amount of simulated events that would be equivalent to one week of data-taking at $10^{33} cm^{-2} s^{-1}$ luminosity.
Top will be an important background channel for a lot of "new physics" and therefore needs to be understood well.

3 Model-independent SUSY searches

One possible scenario for early discovery of new physics at ATLAS would be the discovery of supersymmetry. Supersymmetry at a TeV-scale would provide an attractive extension of the Standard Model [4]. Squarks and gluino's with masses of around 1 TeV are produced by the strong interaction and, if they exist, they are copiously produced at the LHC, giving the chance to find SUSY quickly.
In SUSY models conserving R-parity, squarks and gluinos will generally decay through a chain of lighter SUSY-particles. An unmistakable signature for such a decay would be events with high energy jets and leptons, plus missing energy, that is carried away by the lightest SUSY particle at the end of the decay chain. This signature is summed up by the "effective mass" which is defined as $M_{eff} = E_t^{miss} + \Sigma P_t$ (sum over up to 4 high P_t jets)
Figure 3 shows the effective mass for TeV scale SUSY events and the relevant background for events including one high P_t lepton, as found in a study with simulated data [5]. The presence of SUSY follows from the excess over the background in the high regions of the effective mass. Understanding of the fake missing transverse energy in the detector will be vital to understand the effective mass and to discover/exclude the existence of SUSY. Top will be a dominant background in this channel and needs to be well understood before attempting this measurement, as a top background not well under control could mimic the signal from supersymmetry.

4 Conclusions

LHC will provide ATLAS with $\sqrt{s} = 14$ TeV proton-proton collisions, allowing the study of a new energy regime in hadron physics. The ATLAS detector should be well prepared for the first collisions in 2007, which can then be used to improve the performance of the detector. The analysis of $t\bar{t}$ in ATLAS will help to understand and calibrate b-tagging, missing energy and the absolute jet-scale in the detector. The detector performance and the background processes will need to be understood well to allow for discoveries such as the existence of SUSY.

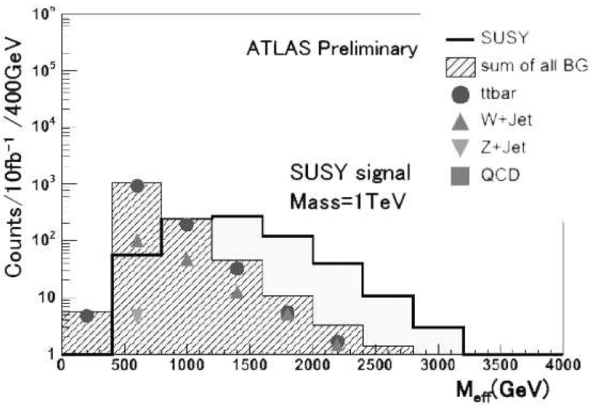

Figure 3: *Result of TeV scale SUSY search in the one-lepton mode, using 10 fb^{-1} of simulated data.)*

References

1. Fabiola Gianotti and Michelangelo Mangano, LHC physics the first one-two years, CERN-PH-TH/2005-072, hep-ph/0504221 (2005).

2. A. Moraes, C. Buttar and I. Dawson, Prediction for Minimum Bias and the Underlying Event at LHC energies, ATL-PHYS-PUB-2005-007 (2005).

3. Ivo van Vulpen, Commissioning with Top events, talk given at ATLAS physics workshop, Rome (2005).

4. I.Hinchliffe, F.E. Paige, G. Polesello, E. Richter-Was, Precision SUSY Measurements with ATLAS: Introduction and Inclusive Measurements, ATLAS-PHYS-No-107, LBNL-40900.

5. S. Asai, Standard Model Backgrounds of SUSY Search, talk given at ATLAS physics workshop, Rome (2005).

Frascati Physics Series Vol. XL (2006), pp. 31-36
Frontier Science 2005, New Frontiers in Subnuclear Physics
Milano, 12-16 September, 2005

VECTOR BOSON FUSION AT CMS

R. Bellan
University of Torino and INFN, Torino, Italy

Abstract

The processes of boson-boson scattering and of Higgs production in boson-boson fusion hold the key to Electroweak Symmetry Breaking (EWSB). A study at parton level of the process $q_1 q_2 \rightarrow q_3 q_4 q_5 q_6 l\nu$ was done. Kinematics cuts were studied to enhance the signal over the background ratio. Different Monte Carlo (MC) programs were used, showing the need of a complete calculation at $O(\alpha^6_{QED})$ for a correct description of the process. A preliminary study of the feasibility of the exploration of this process in the CMS experiment, using a simplified simulation of the detector, was performed. The results are encouraging suggesting that, after about 100 fb^{-1} of data taking at LHC, the energy-scale region above 1 TeV could be explored.

1 Introduction

The *longitudinally polarized*[1] vector bosons fusion process ($V_LV_L \rightarrow V_LV_L$) can probe the EWSB with or without the assumption of the Higgs mechanism. In absence of the Higgs boson the Standard Model (SM) predicts that the scattering amplitude of the $V_LV_L \rightarrow V_LV_L$ process violates the unitarity at about 1.2 TeV. As a consequence the differential cross-section $\mathrm{d}\sigma/\mathrm{M}_{inv}(V_LV_L)$ will deviate from the SM prediction at high values of M_{inv}(VV). Otherwise, if the Higgs boson exists, the $\mathrm{d}\sigma/\mathrm{M}_{inv}(V_LV_L)$ spectrum will show a resonance at $\mathrm{M}_{inv}(V_LV_L)$=m_H.

The studies described in this paper were done considering the semileptonic final state.

2 Studies at Parton Level

The vector boson fusion (VVF) at LHC leads to a six fermion final state. Therefore the MC programs should include all the diagrams for the reaction $q_1q_2 \rightarrow q_3q_4q_5q_6ll$ as the VVF diagrams alone are not gauge invariant [1)]. Different processes like top-top production, which can be rejected by an adequate definition of the signal, as well as V_LV_T and V_TV_T scattering, which is the *irreducible background*, contribute to this final state.

The definition of the signal and a comparison of different MC generators were studied.

2.1 The definition of the signal

A detailed definition of the signal is given in ref. [2)]. It allows to reject the top-top and single top background and the final states with three vector bosons. Furthermore two on-shell Vs are required in the final state. In fig.1 the effects of these cuts are shown for the m_H = 500 GeV and the no-Higgs scenario. The signal amounts to 23% of the total cross-section of the process $q_1q_2 \rightarrow q_3q_4q_5q_6l\nu$.

[1]The longitudinal polarization of the vector bosons arises when the bosons acquire their masses and the symmetry $\mathrm{SU}_L(2)\otimes\mathrm{U}_Y(1)$ is breaking.

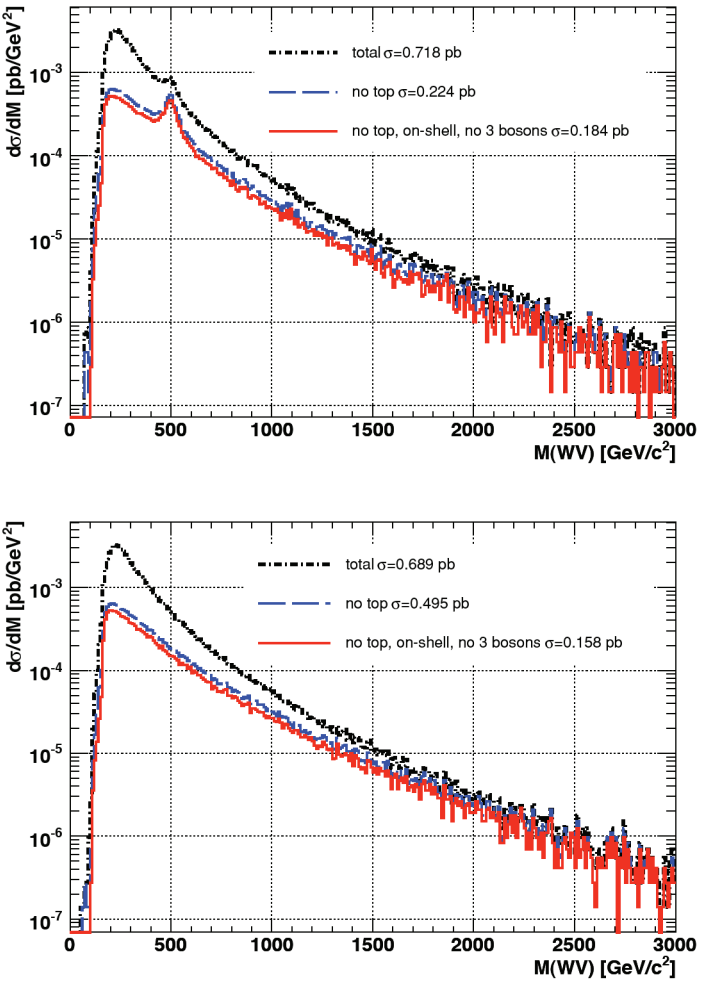

Figure 1: *Differential cross section as a function of the invariant-mass of the two central quarks and the two leptons for the* $qq \to q_F q_B qq\mu\nu$ *process. Top:* $m_H = 500$ *GeV; bottom: no-Higgs scenario.*

2.2 Comparisons of different MC generators

A wide set of MC codes is available, but not all of them are adequate for the simulation of the VVF processes. PHASE [3] was developed as a generator dedicated to the study of processes with six fermion in the final state at LHC. The computation takes into account all the diagrams $2f \to 6f$ at the order $O(\alpha^6_{QED})$ and all the polarizations of the particles.

A comparison between MC generators using different approximations and PHASE was performed for the channel $qq \to q_F q_B qq\mu\nu$.

PHASE-PYTHIA. The *PYTHIA* [4] generator uses the EVB Approximation [5], considering only longitudinally polarized vector bosons. The difference with PHASE is huge over all the invariant-mass spectrum for both the $m_H = 500$ GeV and the no-Higgs scenario (fig.2).

PHASE-MadGraph. The *MadGraph* [6] generator was used to simulate the process through the production and the decay of the final vector bosons[2], which are produced with the zero-width approximation. MadGraph can produce all the polarizations of the vector bosons. The agreement between MadGraph and PHASE's spectra is better than 20% for both the $m_H = 500$ GeV and the no-Higgs scenario (fig.2).

3 Studies with CMS Fast Simulation

Two channels were studied using *PYTHIA* and the *CMS Fast Simulation* [7]:

- $pp \to \mu\mu jjjj$ [8] through the processes $pp \to V_L V_L jj \to Z_L Z_L jj \to \mu\mu jjjj$ and $pp \to Z_L W_L jj \to Z_L W_L jj \to \mu\mu jjjj$.
- $pp \to \mu\nu jjjj$ [9] through the process $pp \to V_L V_L jj \to W_L W_L jj \to \mu\nu jjjj$.

The studies were done for high Higgs masses ($m_H = 500$ GeV and $m_H = 1000$ GeV) and for the no-Higgs scenario. Simulation of background events was also included [10]. A good resolution (estimated using MC info) on the most important observables was obtained. In particular the resolution on the energy scale of the process $M_{inv}(VV)$ is 4% in the $pp \to \mu\mu jjjj$ channel and

[2]MadGraph can simulate the complete process $2f \to 6f$, but for the comparison it was used in the production and decay approximation

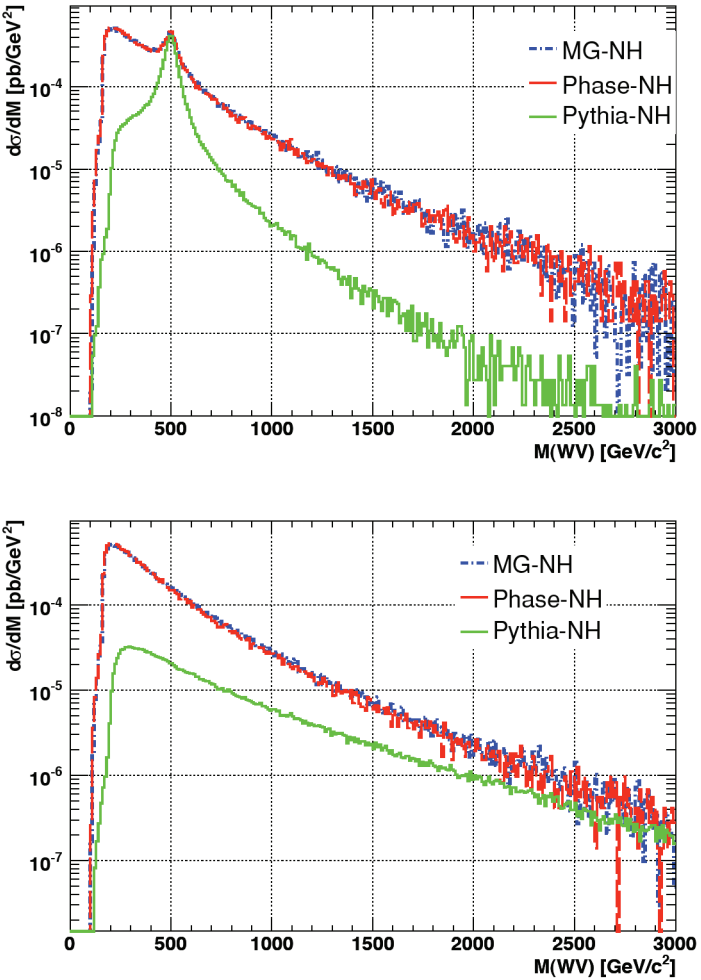

Figure 2: *Differential cross section as a function of the invariant-mass of the two central quark and the two leptons. (Top: $m_H = 500$ GeV; bottom: no-Higgs scenario).*

8% in the $pp \to \mu\nu jjjj$ channel. The resulting background rejection is greater than 99% while the signal efficiency reaches 30% for the $jjjj\mu\mu$ channel and 50% for the $jjjj\mu\nu$ channel.

4 Summary

Electroweak Symmetry Breaking can be probed through the VVF with the CMS detector at LHC. The signal reconstruction and the background rejection algorithms have been successfully tested with the Fast Simulation. Further studies with the Full simulation of the CMS detector are in development.

5 Acknowledgements

I would like to acknowledge all the organizers of *Frontier Science 2005* for their kind hospitality.

References

1. E. Accomando *et al*, DFTT 14/2005.
2. S. Bolognesi, Diploma Thesis, Università degli Studi di Torino (2005).
3. E. Accomando *et al*, DFTT 09/2005.
4. T. Sjöstrand *et al*, Comp. Phys. Comm. **135**, 238 (2001).
5. I. Kuss, Phys. Rev. D **55**(11), 7165 (1997).
6. F. Maltoni and T. Stelzer, hep-ph/0208156.
7. S. Abdullin, A. Khanov and N. Stepanov, CMS TN/94-180.
8. R. Bellan, Diploma Thesis, Università degli Studi di Torino (2004).
9. G. Cerminara, Diploma Thesis, Università degli Studi di Torino (2003).
10. N. Amapane *et al*, HERA-LHC Workshop proceedings (2005).

Frascati Physics Series Vol. XL (2006), pp. 37–40
Frontier Science 2005, New Frontiers in Subnuclear Physics
Milano, 12-16 September, 2005

SEARCH FOR THE HIGGS BOSON IN THE WW DECAY CHANNEL AT CMS

Chiara Rovelli
Università di Milano-Bicocca and INFN Milano
LLR, Ecole Polytechnique - Palaiseau

Abstract

The existence of the Higgs boson is one of the main unsolved questions in particle physics today. In this paper the decay channel $H \rightarrow WW \rightarrow 2l2\nu$ for the Standard Model Higgs is discussed. Simulation studies show it is one of the main discovery channels in the mass range 155-180 GeV at LHC.

1 Introduction

The existence of the Higgs boson is one of the main unsolved questions in particle physics today. The direct search at LEP suggests the lower mass limit m_H >114.4 GeV/c^2 at 95% confidence level [1]. Precision electroweak measurements give the 95% CL upper limit of m_H <219 GeV/c^2 [2].
The Higgs decay in 2 Ws and then into 2 charged leptons and 2 neutrinos is expected to be one of the main discovery channels in the mass range between $2m_W$ and $2m_Z$ at LHC [3]. In this mass region the Higgs boson decays almost exclusively in 2 Ws and the process has high cross section. The two neutrinos

in the final state anyway make the reconstruction of a mass peak not possible, therefore both a good signal over background ratio and full backgrounds control are necessary. Despite the high branching ratio, the channel is one of the most challenging at LHC.

2 Signal and backgrounds

The final state of the $H \to WW \to 2l2\nu$ signal is characterized by two isolated leptons plus large missing energy due to the two undetected neutrinos. The cross section times the W leptonic branching ratio at next to leading order ranges from 0.6 pb to 2.4 pb in the Higgs mass range between 120 GeV/c^2 and 200 GeV/c^2. NLO corrections are important and they largely increase the cross section. The Higgs branching ratio in two Ws is nearly one for Higgs masses around 170 GeV/c^2.

The main backgrounds are the continuum WW production and two top quark production mechanisms, $t\bar{t}$ and Wtb.

The non resonant WW production is the main irreducible background. The NLO cross section for $q\overline{q} \to WW$ times the branching ratio is 11.7 pb, with a K-factor around 1.6 at LHC [4]. The application of a constant K-factor is not fully correct since it does not take into account that NLO corrections are larger for high p_T Ws. The $gg \to WW$ process also contributes to the total cross section [5]. It is suppressed by a factor $O(\alpha_S^2)$ with respect to $q\overline{q} \to WW$ but its contribution is enhanced by the large gluon flux at LHC. Besides it becomes more relevant after the cuts which are commonly employed to improve the signal over background ratio.

The $t\bar{t}$ production has a large cross section at LHC, $\sigma^{NLO} \times BR(W \to l\nu) = 86$ pb. The presence of additional particles in the final state makes its reduction with a jet veto quite efficient. The same holds for the single top production $gb \to Wtb$. The full NLO computations for this process have become recently available and the cross section at NLO is $\sigma^{NLO} \times BR(W \to l\nu) = 3.4$ pb [6].

Other background sources are the continuum vector bosons productions ZZ and WZ. The W+jet production is also a dangerous background due to the large cross section if a jet is misidentifed as a lepton.

3 The search strategy

A set of selections can be exploited to separate the signal from the background on the basis of the kinematical differences among them.
Events are selected if two relatively central, isolated and high p_T leptons are reconstructed. A lower cut on the dilepton mass is imposed to cut away backgrounds from b-resonances and the two leptons are also required not to be consistent with a Z decay.
The backgrounds from $t\bar{t}$ and Wtb productions are reduced by vetoing events which contain a central high p_T jet.
The most difficult background to be kept under control is the WW production. The W^+W^- spin correlations and the stucture of the W decay result in a distinctive signature for the WW pair which is produced in the Higgs decay. For Higgs masses below $\sim$200 GeV/c^2 the opening angle between the two charged leptons in the plane transverse to the beam is small. An upper limit on it can be therefore imposed to improve the signal over background ratio.
For the remaining events the p_T spectra of the two leptons are analysed in the 'signal' and in the 'background' region and mass dependent selections are defined. More details can be found in [3)]

4 Observability in CMS

The method discussed above has been applied to study the sensitivity of the futur CMS experiment [7)] to the $H \rightarrow WW$ channel [8)]. Results include the WW, $t\bar{t}$ and Wtb backgrounds only. No systematic uncertainty has been considered.
In figure 1 the required luminosity to have a 5 standard deviations statistical significance signal is shown in a wide range of Higgs masses. This channel can be considered the best discovery channel in the mass range between roughly 155 and 180 GeV/c^2 at LHC. High significance can be anyway obtained over a larger range of masses.
Despite the absence of a mass peak, the kinematical variables spectra can be usefully exploited to separate the different mass hypothesis. Constraints on the Higgs mass with an accuracy of some GeV can be also put.
A detailed study of the channel with a full simulation of the CMS detector will allow to get a more realistic estimate of the CMS sensitivity with the inclusion of both theoretical and experimental systematics.

5 Conclusions

The Higgs boson decay mode $H \rightarrow WW$ has been shown to give promising results at the LHC. Simple experimental criteria allow to separate the signal

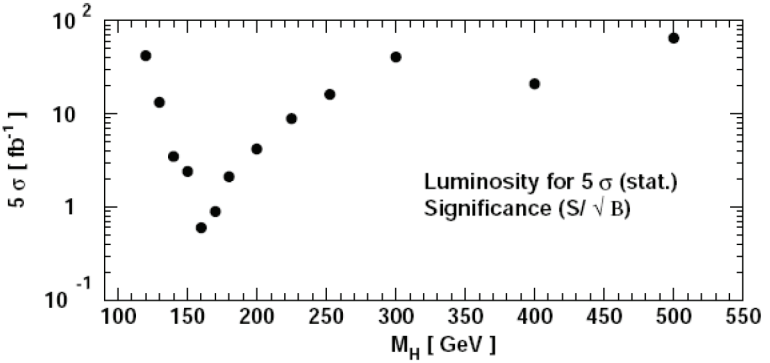

Figure 1: *The required luminosity to obtain a 5 standard deviations statistical significance signal in the channel* $H \rightarrow WW \rightarrow 2l2\nu$ *for* $120\ GeV/c^2 < m_H < 500\ GeV/c^2$ [8].

from the background with a 5-10 σ significance with an integrated luminosity of about 5 fb^{-1} only. This channel is the best discovery one at LHC in the mass range between $2m_W$ and $2m_Z$. High significance can be also obtained over a wide range of masses.

References

1. LEP Collaborations, Phys. Lett. B**565**, 61 (2003).
2. The LEP Electroweak Working Page, http://lepewwg.web.cern.ch/LEPEWV
3. M.Dittmar *et al*, Phys. Rev. D**55**, 167 (1997).
4. S.Frixione, Nucl. Phys. B**410**, 280 (1993).
5. T.Binoth *et al*, JHEP **0503** 065 (2005).
6. J.Campbell *et al*, hep-ph/0506289, to be published.
7. CMS Technical Proposal, CERN LHCC/94-38.
8. M.Dittmar *et al*, CMS NOTE-1997/083.

Frascati Physics Series Vol. XL (2006), pp. 41-44
Frontier Science 2005, New Frontiers in Subnuclear Physics
Milano, 12-16 September, 2005

SEARCH FOR SUPERSYMMETRY WITH EARLY ATLAS DATA

T. Lari
Università di Milano, Dipartimento di Fisica and INFN, Sezione di Milano
On behalf of the ATLAS Collaboration

Abstract

The potential of the ATLAS experiment to discover and study the signals expected from the production of Supersymmetric particles with the first few fb^{-1} of data delivered by the LHC is illustrated.

1 Introduction

One of the main purposes of the LHC collider is the search for Supersymmetry [1]. If Supersymmetry exists at the electroweak scale, it could hardly escape detection at the LHC. The center-of-mass energy of 14 TeV extends the search for SUSY particles up to masses of 2.5 to 3 TeV/c^2 [2].

In the context of the mSUGRA framework with R-parity conservation, scalar quarks and gluinos are expected to dominate the production cross section. Their decay into the Lightest Supersymmetric Particle (LSP), which es-

capes detection, produce an excess of events with multijets, missing energy, and isolated leptons final states compared to the SM expectations. If squarks and gluinos are lighter than about 1 TeV, as implied by naturalness arguments, this signature would be observed with high statistical significance already during the first year of running at the initial LHC luminosity of 10^{33} cm^{-2}s^{-1}.

In the next session, we present the ATLAS strategy to observe the production of SUSY particle through an excess of events with hard jets and large missing energy, a method to measure the top background using data, and the reconstruction of specific decays of Supersymmetry particles.

2 Search for Supersymmetry with ATLAS

The distribution of effective mass, defined as the sum of the missing energy and the transverse momentum of 4 leading jets, is reported in the left plot of Fig. 1 [3] for events which pass the following selections: one isolated lepton (electron or muon) with $p_T > 10$ GeV, $E^T_{MISS} > 100$ GeV, at least one jet with $p_T > 100$ GeV, at least four jets with $p_T > 50$ GeV, transverse sfericity larger than 0.2, transverse mass between lepton and missing energy vector larger than 100 GeV. The most relevant Standard Model processes which contribute to this signature ($t\bar{t}$, W+jets, Z+jets, and multi-jet QCD production) were simulated using ALPGEN [4] (version 1.33) for the hard process, PYTHIA [5, 6] (version 6.2) for emission of soft collinear gluons and hadronization, and ATLFAST [7] to parametrize the detector response. The distribution from Supersymmetric events is reported for LHC Point 2 [2] which has a squark and gluino masses of about 1 TeV. The number of events in the plot correspond to 10 fb^{-1} of integrated luminosity.

At large effective masses the contribution from Supersymmetry is much larger than the statistical error on the Standard Model background event rate. The SUSY/SM ratio is better than in the 0-lepton channel, and the dominant background is from top pair production, which is expected to be known with a smaller systematic error than the other SM backgrounds.

In the right plot of Fig. 1 [3] it is shown that the contribution to the missing energy distribution from $t\bar{t}$ events (dark grey histogram) can be reliably estimated using data (points with error bars) without any bias from the presence of Supersymmetry (the light grey histogram, obtained for mSUGRA Point 5a). This analysis was performed using the detailed simulation of the

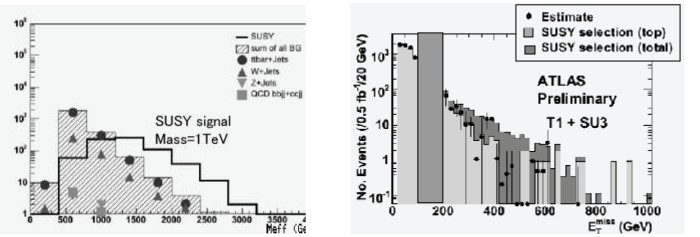

Figure 1: *Left: distribution of effective mass for the events passing the analysis cuts described in the text. The contributions from mSUGRA Point 2 and Standard Model processes are reported. The statistic corresponds to 10 fb^{-1} of data and the fast simulation of the ATLAS detector was used. Right: distribution of transverse missing energy for mSUGRA Point 5a (light grey histogram) and the $t\bar{t}$ background (dark grey histogram) for a statistic of 0.5 fb^{-1} and using the detailed simulation of ATLAS. The points are the measurement of the top contribution from the data.* [3)]

detector, and the statistics is 0.5 fb^{-1}.

The measurement of the $t\bar{t}$ contribution was performed as follows. Events with at least 20 GeV of missing energy, 4 jets with $p_T > 40$ GeV and one isolated lepton were selected (no use of b-tagging was made). A kinematics compatible with the decay of two top quarks (in semileptonic channels) was required, subtracting events from the sidebands of the top mass selection window in order to subtract combinatorial background. The resulting E^T_{MISS} distribution was normalized to the SUSY analysis selection in the range 100-200 GeV (where the contribution from Supersymmetry is expected to be small) and used to get the top contribution at large missing energy.

While an excess of events with large missing energy and jets with high transverse energy will be an hint of the presence of non-SM physics, the existence of Supersymmetry will be more firmly estabilished when the masses and decays of the new particles will be measured. The two body decay chain $\chi_2^0 \to \tilde{l}^{\pm} l^{\pm} \to l^{\pm} l^{\pm} \chi_1^0$ is particularly promising, as it leads to a very sharp edge in the distribution of the invariant mass of the two leptons, which measures

$$M(\text{edge}) = m(\chi_2^0)\sqrt{1 - m^2(\tilde{l})/m^2(\chi_2^0)}\sqrt{1 - m^2(\chi_1^0)/m^2(\tilde{l})} \qquad (1)$$

Combinations of leptons and jets can be used to get other mass relations. Data produced with the detailed detector simulation for the mSUGRA Point 5a

demonstrates that several kinematical edges would be visible with a statistics of 5 fb^{-1} for this particular mSUGRA point [8]. The dilepton edge would be measured to be 100.3 ± 1.1 GeV.

3 Conclusions

The potential of the ATLAS experiment to discover and study Supersymmetry with the first few fb^{-1} of data was discussed. In most model, a clear excess of events over the Standard Model contribution would be observed, and the first kinematical edges, measuring mass relations between Supersymmetric particles, would be reconstructed.

References

1. H.P. Nilles, Phys. Rev. **110**, 1 (1984).
2. The ATLAS Collaboration, Atlas Detector and Physics Performance TDR, CERN/LHCC-99-15 (1999).
3. S. Asai (for the ATLAS SUSY WG), Standard Model Backgrounds of SUSY search, presentation at the 4th ATLAS Physics workshop, Rome, 6-11 June 2005.
4. M.L. Mangano *et al.*, JHEP **0307**, 001 (2003).
5. T. Sjöstrand et al., Comp. Phys. Comm. **135**, 238 (2001).
6. T. Sjöstrand et al., PYTHIA 6.2: physics and manual, hep-ph/0108264 (2001).
7. E. Richter-Was, D. Froidevaux and L. Poggioli, ATLFAST 2.0 a fast simulation package for ATLAS, ATLAS note, ATL-PHYS-98-131.
8. M. Biglietti et al., Full Supersymmetry Simulation for ATLAS in DC1, ATLAS note, ATL-PHYS-2004-011.

Frascati Physics Series Vol. XL (2006), pp. 45-50
Frontier Science 2005, New Frontiers in Subnuclear Physics
Milano, 12-16 September, 2005

TESTS OF THE ATLAS TRIGGER AND DATA ACQUISITION SYSTEM

G. Lehmann Miotto
CERN, PH-ATD Department, Geneva, Switzerland
On behalf of the ATLAS TDAQ Group

Abstract

The complexity of the Trigger and Data AcQuisition (DAQ) systems at LHC experiments has required a long phase of prototyping both for software and hardware technologies. The development of the core aspects of the DAQ for ATLAS is now well advanced and large effort is put into the validation of the performance and the scalability of the most crucial components. This paper presents the results obtained on two testbeds used to verify the functionality and performance of the read out system and the run control.

1 Introduction

The ATLAS experiment [1)] at the Large Hadron Collider (LHC) [2)] is scheduled to start taking data in 2007. The high center of mass energy (14 TeV) and bunch crossing frequency (40 MHz) of the LHC as well as the large amount

of data produced by ATLAS ($\sim 2\ MB$ formatted data per event) require the design of a performant Data AcQuisition (DAQ) system with powerful online event selection capabilities [3) 4)]. The online rejection of events is mandatory in order to reduce the data read out from the detector and put to mass storage to a manageable amount ($\sim 200\ MB/s$). In this paper we will briefly describe the mechanism by which interesting Physics events are selected as well as the architecture of the DAQ. We will then present the results obtained on two testbeds which serve to validate data taking performance and run control aspects of the Trigger and DAQ.

2 The Event Selection System and DAQ Architecture

The ATLAS experiment has been designed to cover the physics in proton-proton collisions with a centre-of-mass energy of 14 TeV at LHC. The online event-selection strategy has to define the proper criteria to cover efficiently the physics programme foreseen for ATLAS, while at the same time providing the required reduction in event rate. In order to guarantee optimal acceptance to new physics, an approach based on emphasizing the use of inclusive criteria for the online selection has been taken, i.e. having signatures mostly based on single- and di-object high-p_T triggers. Here 'high-p_T' refers to objects such as charged leptons with transverse momenta above $O(10)\ GeV$.

The online selection system is organized in three levels. The first trigger level (LVL1) will carry out a rate reduction from 40 MHz down to at most 100 kHz. The second level trigger (LVL2) will reduce the rate by another two orders of magnitude, and the Event Filter (EF) will bring down the data-recording rate to 100 Hz approximately. The DAQ is responsible for formatting, moving and storing the data in such a way that the selection algorithms can perform their task and finally for putting the accepted events to mass storage.

The LVL1 trigger is based on a system of purpose-built hardware processors which analyse multiple events in parallel to avoid the introduction of dead time and sustain the bunch crossing rate of 40 MHz. It uses only information from the calorimeters and some muon detectors, with coarse granularity, to perform the selection, and passes information on to the LVL2 trigger about the areas of the detector which contained interesting features for an event, the so called Regions of Interest (RoI).

The raw data produced at each bunch crossing are kept on on-detector buffers for as long as the LVL1 does not issue an LVL1 accept signal. Only then data are read-out, formatted, and put into Read Out Buffers (ROBs). In ATLAS there are 1600 ROBs. ROBs are housed in groups of three on custom build PCI cards, the ROBINs [5]. ROBINs are installed into commercial rack mounted computers, called Read Out Systems (ROS). Each ROS contains four ROBIN cards, thus 12 ROBs. The function of the ROS is to provide event fragments on demand from the next trigger levels and to store them for as long as it is requested.

The other two trigger levels are based on software running on commercial computer farms. The LVL2 trigger has a decision latency of $\sim 10\ ms$ per event. Several hundreds of software processes will perform data analysis in parallel, to sustain the event rate without introduction of dead time. They will use a sequence of highly optimized trigger selection algorithms which operate on only a fraction (typically $\sim 2\%$) of the event data. The RoI information received by the LVL1 enables the LVL2 algorithms to select precisely the region of the detector, i.e. the ROBs, in which the interesting features reside and therefore to request to the ROSs a limited amount of data for analysis. Events rejected by the LVL2 will be immediately deleted from the ROBs, while the accepted ones will be gathered by the event building system (EB), formatted, deleted from the ROBs and finally passed on to the EF. The EF disposes of an average event treatment time of $\sim 1\ s$ and operates on the complete event. Several thousands of software processes will perform the filtering in parallel, to sustain the LVL2 accept rate. Compared to LVL2, more sophisticated reconstruction and trigger algorithms and more complete and detailed calibration information are used to make the selection. Events not selected by the EF are deleted and those accepted are passed to mass storage.

3 Validation of the Read Out System Performance

As already outlined in the previous section, the ROS is a central element in the ATLAS DAQ architecture. It has to be capable of receiving and storing event fragments at up to 100 kHz and to dispatch the requested data to the LVL2 and to the EB.

The requirements on the output performance of the ROS are not straight forward to determine, since the size of data fragments varies strongly from

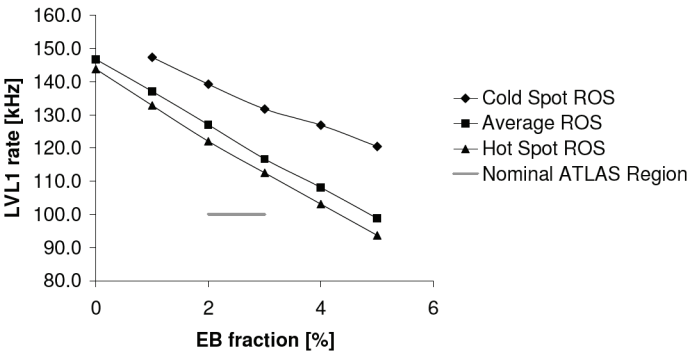

Figure 1: *Sustained LVL1 accept rate as a function of the LVL2 accept rate. The behaviour of all ROSs will lie within the band enclosed between a hot-spot and the cold-spot ROS curve. The grey line indicates the expected ATLAS region.*

detector to detector, the LVL2 requests only a fraction of the data and the output to the EB depends on the rejection power of LVL2. Computer models have been used to infer the maximum performance required depending on the part of the detector the ROS is connected to and the LVL2 behaviour. Three types of ROS have been identified and labeled 'hot-spot', 'average' and 'cold-spot'. Fig. 1 shows the sustained LVL1 accept rate (which corresponds to the ROS event input rate) as a function of the event building (EB) rate (which corresponds to the LVL2 accept rate). It should be noted that in the real experiment the LVL1 accept rate will never go beyond 100 kHz, since this value is determined by the read-out electronics capabilities of the detectors. Also, studies performed with LVL2 algorithms show that the expected EB rate will vary between $2-3\%$. In these conditions the ROS is already capable of satisfying the final ATLAS requirements.

4 Validation of the Run Control system on a Large Scale Testbed

Another aspect of a data acquisition system, which is as crucial as its data taking performance, is the ability to control and configure all elements of the experiment, ranging from the detector modules, to all computers and trigger

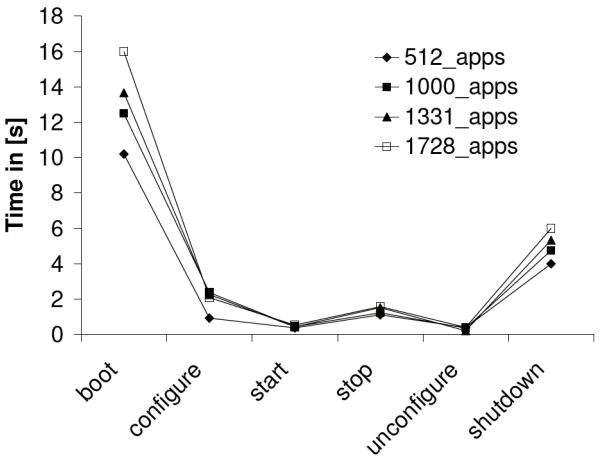

Figure 2: *Time needed to boot and shutdown all DAQ and trigger processes and to perform the transitions within the run control finite state machine. Each transition consists of multiple commands which are being distributed over the network.*

algorithms. In ATLAS there will be in the order of 2000 interconnected computers running $O(10000)$ software processes. To validate this aspect of the DAQ, the exclusive use of a very large computer cluster has been obtained by the DAQ group at CERN for a few weeks. Up to 700 machines were made available to test the performance and scaling behaviour of the run control system. Fig. 2 shows the results obtained: the most time consuming operation are the 'boot' and 'shutdown', which correspond to the moment in which all software processes are launched and terminated, respectively. The other transitions complete in a negligible amount of time. These results show that already today the dispatching of run control commands is very fast. It should be noted nevertheless that in these measurements the real data taking and trigger applications were substituted by light-weight emulators. It is expected that the configuration time will grow to several minutes once the configuration of real detector hardware and analysis algorithms will be included. Also stopping a run will take longer than what was measured here, since time will be needed for all buffered events to go through the DAQ and event selection system.

5 Conclusions

In this paper we have shown how different aspects of a complex system such as the ATLAS Trigger and DAQ can be tested prior to the implementation of the final system at the experiment site. Performance tests on the ROS indicate that this crucial component can safely deliver the nominal readout rates foreseen for the ATLAS experiment. Another set of tests have been carried out on a large computer cluster emulating the farm which will be put in place for the DAQ and trigger. The tests consisted in performing all run control operations on up to 700 machines with $\sim$ 2000 processes. Also in this case the results have shown that the design and implementation of the mechanisms for starting and stopping processes and for distributing run control commands match the expectiations. Despite the fact that these tests are not conclusive for the validation of the complete trigger and DAQ chain, they are essential for its detailed comprehension and debugging. The good results are a step in the right direction towards data taking in 2007.

6 Acknowledgements

The authors would like to thank the Information and Technology department of CERN for having made a large scale computer cluster available for the run control tests.

References

1. ATLAS Collaboration, http://atlas.web.cern.ch/Atlas/index.html
2. LHC, http://lhc.web.cern.ch/lhc/
3. ATLAS Collaboration, ATLAS First-Level Trigger Technical Design Report, CERN/LHCC/98-14 (1998)
4. ATLAS Collaboration, ATLAS High-Level Trigger Data Acquisition and Controls Technical Design Report, CERN/LHCC/2003-022 (2003)
5. B. Green et al., ATLAS Trigger/DAQ RobIn Prototype, IEEE Trans. Nucl. Sci. **51**, 2004, pp. 465-469.

Frascati Physics Series Vol. XL (2006), pp. 51–56
Frontier Science 2005, New Frontiers in Subnuclear Physics
Milano, 12-16 September, 2005

THE CALIBRATION CHALLENGE FOR THE CMS ELECTROMAGNETIC CALORIMETER

P. Govoni
Università di Milano-Bicocca and INFN
on behalf of the CMS-ECAL group

Abstract

To fully exploit its Physics reaches, the lead tungstate crystals Electromagnetic Calorimeter of CMS (ECAL) has to be calibrated with high accuracy. The benchmark is the discovery channel H$\rightarrow \gamma\gamma$ decay. A complete set of protocols for the calibration has been foreseen, that apply from the production level up to the data taking period. Measurements of the crystals properties, of the response to cosmic rays and to known energy electrons, as well as detailed studies of well known standard model Physics channels during the data taking will guarantee the needed accuracy.

Introduction

CMS is one of the multi-purpose experiments that will take data at the LHC proton proton collider.
Its electromagnetic calorimeter (ECAL) will be composed of about 80.000

$PbWO_4$ scintillating crystals, covering an η range running from 0 to 2.5 by means of a barrel (till η=1.49) and two endcaps. Crystals in the barrel are read out by means of Avalanche PhotoDiodes (APD), while in the barrel the scintillating light is detected by Vacuum PhotoTriodes (VPT).
Every single crystal shows a response different from the others, because of differences in the crystal light yield, in the APD gain and in the readout electronics chain gain. Among these, the light yield affects the more the non-uniformity of the crystals response, with a distribution among the crystals with an RMS $\simeq$ 8%.
To let the detector perform uniform measurements over all its coverage region, the crystals response will be equalized to an absolute energy scale. This target will be attained by means of a twofold procedure: the alignment of all the crystals response to a common scale (the inter-calibration) and the determination of the actual energy scale of the detector once aligned (the absolute calibration).
The precision of the calibration procedure is defined by the need of discovering low mass Higgs in the golden channel H$\rightarrow \gamma\gamma$.
The calibration cofficients will depend on the particle crossing the ECAL detector, because of the different shape of the showers generated inside the crystals (i.e. electrons and photons). Besides this, the calibration coefficients could depend on the reconstruction algorithm adopted for the energy reconstruction (for example, whether the energy of a fixed window of crystals around the most energetic one is computed, ore a dynamic clustering procedure depending on the energy deposit is implemented).

1 The pre-calibration

Several calibration protocols have been envisaged, both before and during the CMS data taking. An overview of the ECAL barrel calibration strategies is given, while for the ECAL endcaps similar techniques will be applied.
The most precise measurement of the inter-calibration coefficients before the data taking is performed by exposing single components of the ECAL barrel, the super-modules, to a known energy electrons beam [1)]. A mechanical holding structure aligns the super-modules with respect to the beam in such a way to mimic the CMS geometry and the electrons reach the crystals as if they were generated in the CMS nominal interaction vertex.

Testbeam measurements have been performed during the years 2003 and 2004 and show a precision in the calibration coefficients determination at the order of 0.5%. Figure 1 shows the distribution of the inter-calibration coefficients as measured during the 2004 testbeam: its distribution is at the level of 8%, as expected.

Unfortunately, due to the tight CMS schedule, it will not be possible to

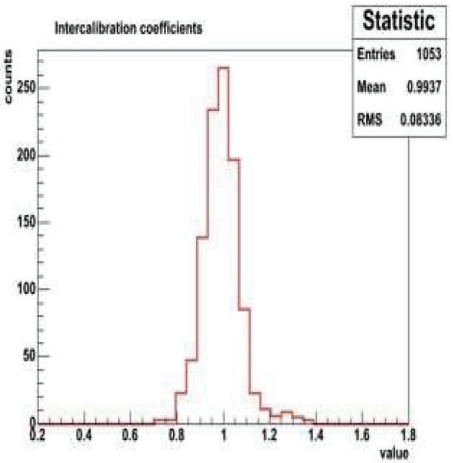

Figure 1: The calibration coefficients distribution as measured during the 2004 testbeam by means of 120 GeV electrons.

put all the super-modules on a testbeam.

However, before any testbeams, all the crystals, the APDs and the electronics components have been characterized by means of laboratory measurements. The crystals light yield is measured, together with their longitudinal trasnmission, in regional centers at CERN and in Roma; the gain of every single APD is calculated from the actual low voltage supply amplitude and the electrioncs chain gain has been measured for each channel.
The composition of these effects provides the first pre-calibration of the detector, with a precision at the level of 4% [2]. Figure 2 shows the distribution of the ratio between the intercalibration coefficients measured at the testbeam and the ones calculated by means of the laboratory measurements.

Another procedure that will be applied to all the super-modules profits of the cosmic muons, that interact as m.i.p. in the crystals [3]. By increasing the APD gains by a factor of 4 to improve the signal-to-noise ratio and by bending the super-modules with an angle of 10 degrees with respect to the horizontal plane, it is possible to measure enough muons crossing the crystals parallel to their axis. Such particles, triggered by means of scintillating planes, are selected by means of a veto procedure on the neighbouring crystals energy. With no need on any tracking devices the muons signal is enough to measure the calibration coefficients with a precision ranging from 1% to 3%, depending on the position of the crystals in the super-module. Figure 3 shows the correlation plot of testbeam inter-calibration coefficients with the ones calculated with preliminary cosmics data.

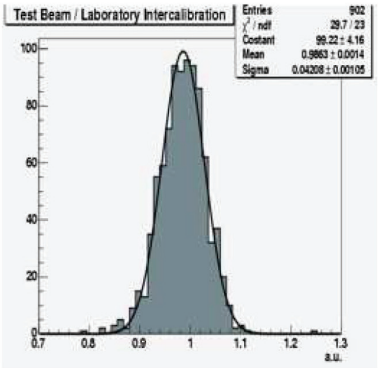

Figure 2: Ratio between the testbeam inter-calibration coefficients and the ones obtained from laboratory measurements

2 The *in situ* calibration

Once the CMS detector will be installed and will start taking data, the calibration precision will be increased by means of *in situ* procedures based on Physics channels.

A first inter-calibration will be reached by exploting the ϕ symmetry of the CMS detector [4]. In each one of the 120 single-crystal rings forming the ECAL barrel the energy deposit due to minimum bias events and jet events is assumed to be the same because of the detector symmetry. This constraint allows to inter-calibrate all the rings of crystals separately with a precision of 2% within few hours. Figure 4 shows preliminary results attaiened by means of a full simulation study [ ]. The alignment of the crystal rings with respect to a physical energy scale wil be performed by studying different decay channels, such as the $Z \rightarrow e^+e^-$ one.

The reconstruciton of the Z mass itself will be used as a constraint to set the calibration coefficients in such a way to best measure the well known M_Z [6]. Event by event, the calibration coefficients are changed accordingly to the difference between the reconstructed Z mass and the known one, until the procedure converges to their actual value. A precision at the level of 1% within few days is expected.

Once the CMS Tracker will be well aligned, the calibration will be performed by comparing its momentum measurement for isolated electrons to the corresponding measurement of ECAL [5]. Studies have been performed on a fully simulated $W^{\pm} \rightarrow e^{\pm}\nu$ dataset, that corresponds to the main source of isolated electrons during the data taking.

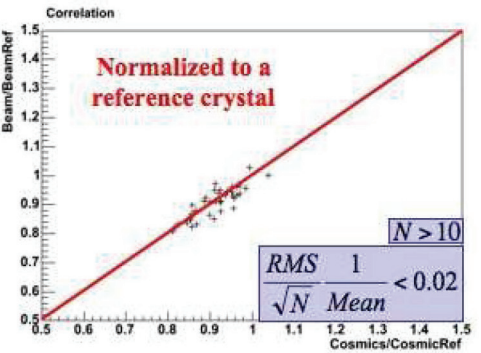

Figure 3: The correlation plot of the testbeam (vertical axis) inter-calibration coefficients with the ones calculated with preliminary cosmics data (horizontal axis)

Both an event by event based procedure and an algorithm based on a χ^2 minimization have been implemented and tested. The studies show that a precision at the level of 0.4% in the central region of the barrel and 1.3% in its forward regions can be achived within few months of data taking at low luminosity (see figure 5).

It will be possible to perform measures and hence calculate and apply the calibration coefficients provided that the crystals response does not change in time. This is not the case, because of the irradiation effects on the crystals transparency that take place during the LHC cycles. To cope with these variations, a laser system will deliver a pulsed signal to each crystal and the response of the data acquisition chain with respect to a fixed reference will be used to correct for the transparency variations.

3 Conclusions

The energetic resolution of the CMS ECAL detector critically depends on the precision at which its single channels will be calibrated. A complete set of protocols has been foreseen, that apply from the production level up to the data taking period, and this guarantees to reach a constant term in the energetic resolution varying from 0.4% in the central region of the detector, up to 1.3% where the material in front of the sub-detector is thicker and the particles loose more energy.

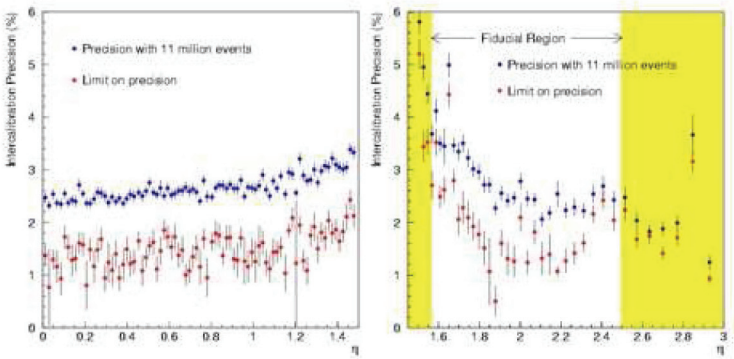

Figure 4: The precision in the ϕ simmetry inter-calibration, as calculated by means of a complete simulation of the CMS detector response to minumum bias events, at low luminosity ($2 \times 10^{33}\text{cm}^{-2}\text{s}^{-1}$)

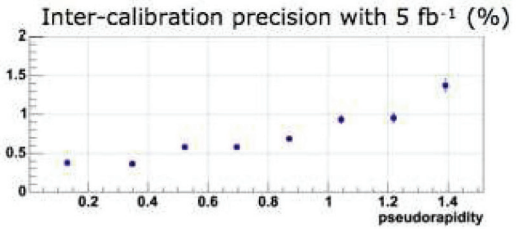

Figure 5: The precision attainable with respect to the η coordinate after an intergrated luminosity of 5 fb^{-1} by studying isolated electrons

References

1. F. Cavallari *et al.*, CMS RN 2004/002
2. L. Barone *et al.*, CMS RN 2004/005
3. T. Camporesi *et al.*, CMS NOTE 2005/023
4. D. I. Futyan, CMS NOTE 04/007
5. L. Agostino *et al.*, CMS NOTE 2006/021
6. P. Meridiani *et al.*, CMS NOTE 2006/039

SESSION II – LHC PHYSICS AND DETECTORS (II)

Frascati Physics Series Vol. XL (2006), pp. 59–70
Frontier Science 2005, New Frontiers in Subnuclear Physics
Milano, 12-16 September, 2005

THE LHC GENERAL PURPOSE DETECTORS

Philippe Bloch
CERN, PH Department, Geneva, Switzerland

Abstract

We present the main characteristics of the two large, general purpose detectors ATLAS and CMS, which will start operation in 2007 at the LHC.

1 Introduction

The prime motivation of the LHC is to discover the nature of electroweak symmetry breaking. The Higgs mechanicsm is the currently favoured mechanism. However, there are alternatives that invoque new symmetries, such as Supersymmetry, or new constituents or forces. The TeV is believed to be the ideal energy scale to study this potential wide range of physics.

The cross sections of the discovery channels are very small, typically less than 1 pb, and the branching ratios into useful decay modes can be as low as

10^{-3}. A very high accelerator luminosity is therefore required. The selection of the rare events among a large background imposes strong requirements on the detector performance. These harsh conditions, together with the requirement to reduce on-line the billion interactions/s to 100 events/s for storage, have created unprecedented challenges in the design and construction of the detectors.

This paper focuses on the two multipurpose detectors ATLAS and CMS which are being assembled at CERN and will start operation in 2007. After a short review of the physics and the experimental requirements, we will present how the two collaborations have addressed these challenges, often in a different but complementary way.

2 Physics requirements

At the LHC, the Standard Model Higgs provides a good benchmark to test the performance of a General Purpose Detector. The current lower limit on the mass of the Higgs boson from LEP is 114.5 GeV. Fully hadronic final states dominate the branching ratios but unfortunately these cannot be used to discover the Higgs boson at the LHC due to the large QCD backgrounds. Hence the search is conducted using final states containing isolated leptons and photons. In the mass interval 114-130 GeV the two-photon decay is the most promissing channel. The natural width of the Higgs boson is small (≈ 10 MeV) and the width of a signal will be entirely dominated by the instrumental two-photon mass resolution. An excellent photon energy and a good angular resolution are therefore needed. In addition, a correct localization of the primary interaction vertex, π^0 rejection and efficient photon isolation are required.

If the Higgs mass is larger than 130 GeV, the Higgs boson should be detectable via its decay into two Z bosons (one of them may be virtual), resulting in 4 isolated leptons in the final state. The detector requirements can be summarized as a good dimuon (or di- electron) mass resolution, implying good momentum resolution for low momenta, and a large geometric acceptance up to pseudorapidity $|\eta| = 3$.

In the region $700 < m_H < 1000$ GeV the reactions likely to provide the clearest signals involve neutrinos and/or jets from W or Z decays. Hence, good missing E_T and di-jet mass resolution will be important. In the case were the Higgs is produced by W fusion, the signal/background ratio can be enhanced

by using tagging jets emitted in the high rapidity ($3 < |\eta| < 5$) region, where hadronic calorimetry is therefore required.

Searches for physics beyond the Standard Model put further requirements. The search for new, massive heavy vector bosons imposes a momentum resolution that is sufficient to unambiguously determine the charge of leptons up to 1 TeV in the region $|\eta| < 2$. Many final states contain undetected particles, leading to significant missing E_T, and abundance of b-jet or τ-jet production. Hence, efficient b/τ-jet tagging and triggering on τ's are important.

3 Experimental Challenges

The main LHC parameters in the proton proton mode, at $\sqrt{s} = 14$ TeV, are a luminosity of $10^{34}\text{cm}^{-2}\text{s}^{-1}$ and a bunch crossing interval of 25 ns, corresponding to an inelastic event rate of 8×10^8 interactions per second and ≈ 20 superimposed events per crossing. Thus, the products of an interaction under study may be confused with those of other interactions in the same bunch crossing (pileup). This effect can be reduced by using highly granular detectors with good and fast time response, giving low occupancy, at the expense of having a very large number (more than 10^7) of detector elements.

The high particle fluxes emanating from the interaction region lead to high radiation levels (fluences up to 10^{17}n/cm^2 and doses up to 10^7 Gy) requiring radiation hard detectors and front-end electronics. In some cases, the radiation levels impose a special environment for long term viability: for example, the Silicon sensors used in the central trackers must be run at low temperature ($-10°$C) to limit the leakage current and avoid reverse annealing. The radiation damage deteriorates often the performance and may induce time-dependent variations. Finally, the induced activity restricts the possibility of access and maintenance, requiring a long term reliability similar to what is asked for satellite experiments.

A major R&D effort was therefore necessary during the last 15 years to select and develop detectors and electronics that could operate reliably at the LHC.

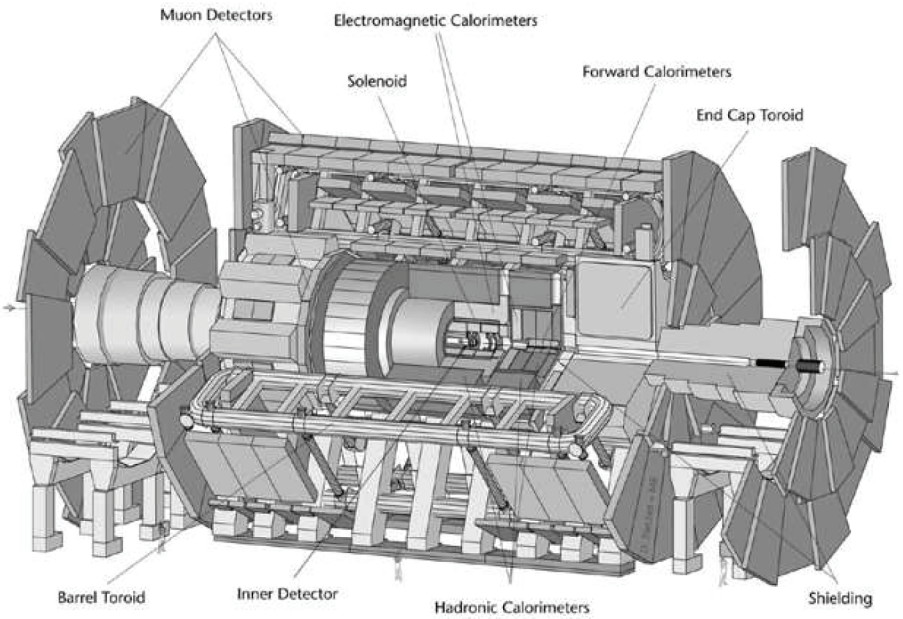

Figure 1: *The ATLAS detector. The total length is 46 m, the diameter 25 m and the weight 7000 t.*

4 The ATLAS [1)] and CMS [2)] detectors

4.1 General layout and magnetic field configuration

Sketches of the ATLAS and CMS detectors are shown in Figure 1 and 2 respectively. They both exhibit the typical 'onion' structure of a 4π colliding beam detector. From inside to outside, one finds

- the inner tracker, to precisely measure the charged particles produced in the collision. The tracker is embedded in a constant magnetic field parallel to the beam axis, in order to measure the curvature and therefore the momentum of the particles,
- the electromagnetic calorimeter, made of high Z material, which absorbs

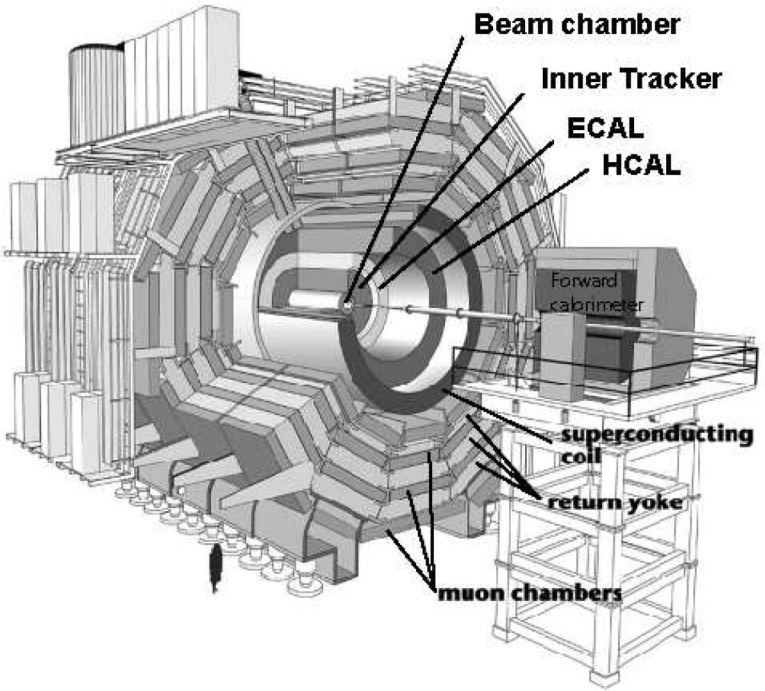

Figure 2: *The CMS detector. The total length is 21.6 m, the diameter 15 m and the weight 12500 t.*

electrons and photons. It allows a precise measurement of their position and energy,

- the hadronic calorimeter, which absorbs and measures the energy of the charged and neutral hadrons. After this detector remain only the weakly interacting particles, i.e. muons and neutrinos,

- finally, the muon system, measuring the curvature of the muons in a magnetic field.

Both detectors comprise a Barrel part, closed by two endcaps. However, ATLAS and CMS differ strongly (in particular in size) because they have chosen a different field configuration for the muon system.

In ATLAS, the magnet configuration uses large superconducting air-core toroids consisting of independent coils arranged with an eight-fold symmetry. Toroids have the property that the transverse momentum resolution is constant over a wide range of pseudo-rapidity. In an air-core toroid, a good stand alone momentum resolution can be reached as long as the product BL^2 (B being the magnetic field and L the tracking length) is large enough. Two drawbacks of the toroidal configuration are:

- the bending does not take place in the transverse plane and hence benefit cannot be drawn from the precise knowledge of the beam-beam crossing point (20 μm at LHC), and
- an additional 2T solenoid is needed to provide field for the inner tracker.

The sagitta, s, for a track of momentum p in a uniform magnetic field is given by $s = \frac{0.3BL^2}{8p}$. In the case of ATLAS, where B = 0.6 T, L= 4.5 m, the sagitta has to be measured with a precision of 50 μm. For a muon system as large as in ATLAS, precision of this nature presents special challenges of spatial and alignment precision.

In CMS, a large BL^2 is obtained using a high field solenoid (4T). The bending, which takes place in the transverse plane, starts at the primary vertex. For tracks that pass through the end of the solenoid, the momentum resolution worsens, but the effect can be attenuated by choosing a favourable length/radius ratio. Centrally produced muons are measured three times: in the inner tracker, after the coil and in the return flux. As shown in Fig. 3, in the stand alone mode (no inner tracking) the momentum resolution is limited by multiple scattering to $\approx 6\%$ below 400 GeV/c and therefore worse than for the ATLAS stand-alone muon sytem. However, in the combined mode (inner tracking + muon system), the CMS momentum resolution is better, in particular because one uses the property that after the yoke the track points back to the interaction point to improve the momentum measurement inside the inner cavity. Note also that the CMS muon system requires a less precise sagitta measurement (≈ 100 μm).

Both magnets are nearing completion: the eight ATLAS coils have been recently installed in the experimental cavern. The cold mass of the CMS coil has been inserted in its cryostat and will be cooled down early 2006.

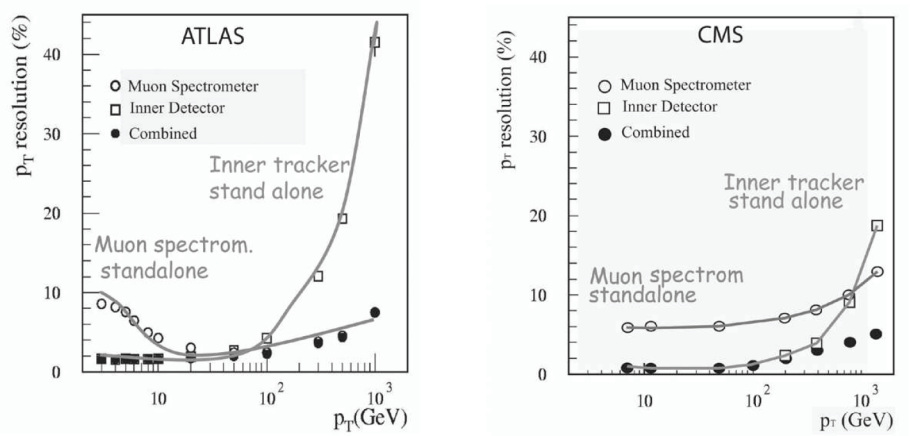

Figure 3: *The muon momentum resolution at* $\eta = 0.1$ *for ATLAS (left) and CMS (right).*

4.2 Inner Tracking

Both ATLAS and CMS detectors contain pixel detectors, placed closest to the interaction vertex where the particle flux is the highest. The typical size of a pixel is 125 μm $\times$ 125 μm. The occupancy of a pixel element is very low, even at high luminosity (10^{-4}). Furthermore, the pixel detectors allow one to reconstruct secondary vertices from B meson decays.

For the larger radii, ATLAS and CMS have adopted a different strategy (Fig 4):

- In ATLAS, the intermediate region at radii between 25 and 50 cm is equipped with silicon microstrip detectors, with a total area of 60 m^2 which provide only 4 precision space points in the barrel region and 9 points in the endcaps on each side. The silicon microstrip detectors are surrounded by straw-tubes, with transition radiation capability for electron identification (TRT), that provide a continuous tracking with many, but less precise, points per track.

- In CMS, the full volume is equipped with Si microstrip detectors providing precision space points. In the barrel region, at radii between 20 and 115 cm, the track is measured with 10 precision points. The forward

region has nine micro-strip layers in each of the two End-Caps. The total area of the silicon detectors is 220 m^2, about two orders of magnitude larger than in previous experiments.

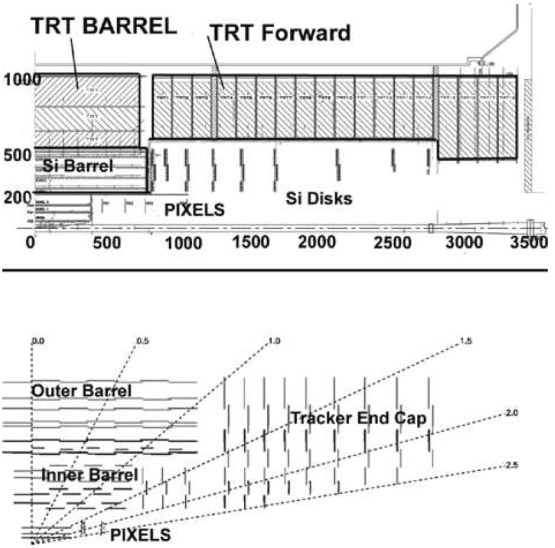

Figure 4: *Layout of the ATLAS (top) and CMS (bottom) inner trackers.*

4.3 Calorimeters

4.3.1 Electromagnetic calorimeters

The best performance in terms of energy resolution is only possible using homogeneous calorimeters such as inorganic scintillating crystals. CMS has chosen lead tungstate (PbWO4) scintillating crystals. These crystals have a short radiation length (0.89 cm), are fast and radiation hard. However, the low light yield requires use of photo-detectors with intrinsic gain that can operate in a magnetic field; silicon avalanche photo-diodes (APDs) have been chosen for the barrel crystals and vacuum phototriodes for the endcap crystals. The calorimeter comprises over 75000 crystals, with a granularity of $\Delta\eta\Delta\phi = 0.016 \times 0.016$ in the Barrel. The sensitivity of both the crystals and the APD response to

temperature changes requires a very good temperature stability (a stability of 0.02°C has been achieved in the test beam). An other difficulty is that the radiation damage modifies slightly the crystal transparency, which is monitored with a laser light injection system. In the 2004 test beam running, the energy resolution has been measured to be $\frac{\sigma(E)}{E} = \frac{0.033}{\sqrt{(E)}} \oplus \frac{0.12}{E} \oplus 0.004$ (E in GeV). More than half of the crystals have already been delivered and mechanically assembled.

ATLAS (Fig. 5) is using a lead/liquid argon sampling calorimeter (LAr). The absence of internal amplification of charge results in a stable calibration over long periods of time. The flexibility in the size and the shape of the charge collecting electrodes allows high granularity both longitudinally and laterally. The main longitudinal compartment has a granularity of $\Delta\eta\Delta\phi = 0.025 \times 0.025$. ATLAS introduced a novel absorber-electrode configuration, known as the accordion geometry, in which the particles traverse the chambers at angles around 45°. This avoids azimuthal cracks. The resolution is parametrized as $\frac{\sigma(E)}{E} = \frac{0.10}{\sqrt{(E)}} \oplus \frac{0.3}{E} \oplus 0.007$ (E in GeV). An excellent response uniformity, better than 0.7% has been demonstrated in test beams. To limit the amount of dead material in front of the em. calorimeter, the 2T solenoid and the LAr share the same cryostat.

The Barrel LAr calorimeter is assembled and will be soon installed in the experimental cavern.

4.4 Hadronic Calorimeters

In CMS, the Barrel and Endcap hadronic calorimeters (up to $|\eta| = 3$), located inside the magnetic coil, are brass-scintillator tile sampling calorimeters readout out by wavelength shifting fibres. The tiles are perpendicular to the particles. The measured resolution is $\frac{\sigma(E)}{E} = \frac{1.3}{\sqrt{(E)}} \oplus 0.065$ (E in GeV). The very forward calorimeter $3 < |\eta| < 5$ consists of steel plates with grooves in which quartz fibres are inserted and measures the Cerenkov light emitted by relativistic shower particles.

The ATLAS Barrel hadronic calorimeter is an iron-scintillator tile sampling calorimeter readout out by wavelength shifting fibres. The tiles are placed radially. The measured resolution can be parametrised as $\frac{0.7}{\sqrt{(E)}} \oplus 0.033 \oplus \frac{1.8}{E}$ (E in GeV). The Endcaps and Forward calorimeters use the liquid Argon

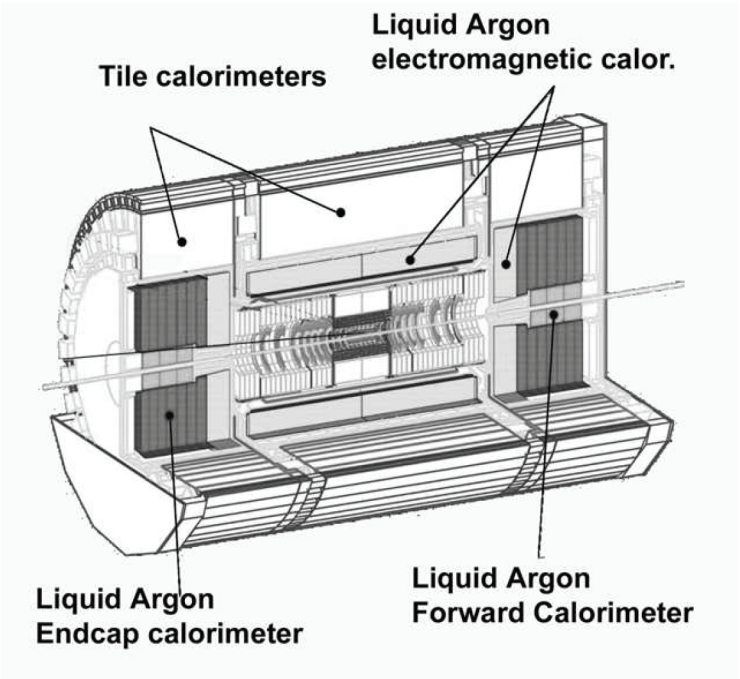

Figure 5: *Calorimetry in ATLAS.*

technology.

Both CMS and ATLAS Hadronic calorimeters are essentially ready.

It should be noted that the jet energy resolution is dominated by the jet reconstruction algorithm and not by the intrinsic performance of the hadronic calorimeter. A significant improvement in resolution is obtained by replacing, for charged tracks, the energy measured in the calorimeter by the momentum measured in the tracker and by adding charged tracks that bend out of the reconstruction cone, as measured in the tracker.

4.5 The muon detectors

Two kinds of muon detectors are used at LHC, serving complementary roles. These are gaseous drift chambers (DT), that provide accurate position measurement for momentum determination, and trigger chambers, such as resistive plate chambers (RPC), that have a short response time (< 25 ns) for precise

bunch crossing identification but a less accurate position measurement. In the endcap region, drift chambers are replaced by faster chambers such as cathode strip chambers (CSC). A sketch of the CMS muon system is shown in Fig. 6. To cope with the neutron induced background and provide a local angular measurement, each of the muon stations comprises several layers of detectors.

The main challenge is the construction, assembly and installation of a very large detection area. For example, the ATLAS muon chambers total a surface area of over 12000 m^2.

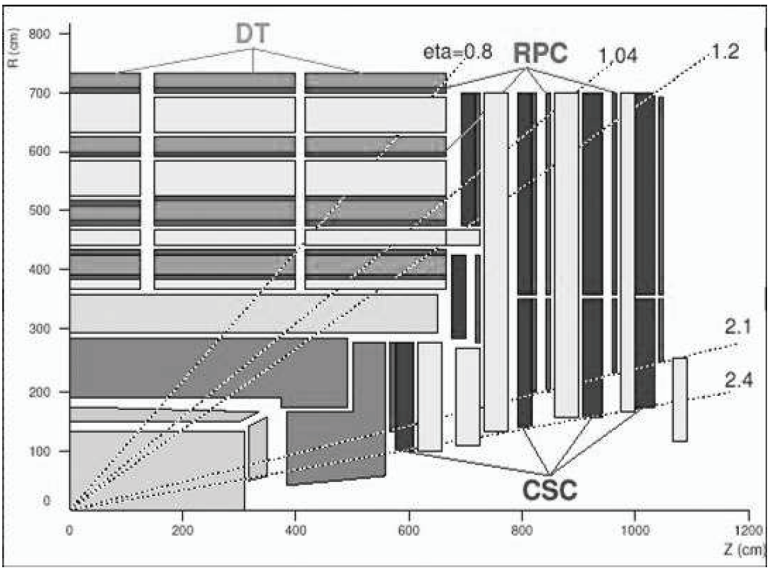

Figure 6: *The CMS Muon system.*

5 Trigger and Data Acquisition

The data acquisition and synchronization of $O(10^7)$ channels is a huge task, requiring large pipelines, very fast control and switching networks and large processing farms containing several thousands PCs. Furthermore, the initial interaction rate of 40 MHz has to be reduced to $\approx$ 100 Hz, corresponding to the storage capacity, while keeping the interesting physics events with high efficiency. A Level-1 trigger, using specialized boards with fast digital electronics

(FPGAs), reduces the initial rate to 100 KHz. The remaining factor 1000 is obtained by reconstructing the events in real time using commercial processors.

6 Conclusion

The construction of the LHC detectors required to meet a set of unprecedented challenges, due to the high rate of interactions, the hostility of the environment, the need for very high resolutions, acceptances and selectivity. More than 15 years were necessary between the initial ideas and the construction of the actual detectors, and many todays achievements seemed pure dreams at the start of this long enterprise. Most of the detectors are now in the phase of installation and commissioning and will probe very effectively the Physics that LHC will deliver starting 2007.

7 Acknowledgements

The author would like to thank Prof. J. Virdee for his help in preparing this presentation and the proceedings.

References

1. http://atlas.web.cern.ch/Atlas/internal/tdr.html
2. http://cmsdoc.cern.ch/docLHCC.shtml

Frascati Physics Series Vol. XL (2006), pp. 71–76
Frontier Science 2005, New Frontiers in Subnuclear Physics
Milano, 12-16 September, 2005

THE ATLAS TRACKER

Marc Weber
CCLRC, Rutherford Appleton Laboratory, Chilton, Didcot, UK

Abstract

The ATLAS tracker is a large-volume detector designed to measure charged particles produced in proton-proton collisions at the Large Hadron Collider (LHC) at CERN. I will discuss the tracking requirements at the LHC, introduce the design concepts chosen for the ATLAS tracker, and emphasize technical highlights. I will also summarize the ATLAS tracker project status.

1 Introduction

The ATLAS detector is designed to detect particles originating from proton-proton collisions in the Large Hadron Collider (LHC) at CERN in Geneva, Switzerland. The LHC will start operation in Summer 2007 and is expected to remain the highest-energy collider for at least two decades. The ATLAS detector is composed of many subdetectors, each providing particle identification

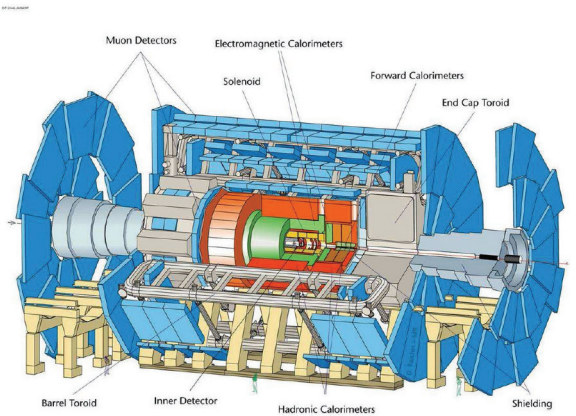

Figure 1: *Overall layout of the ATLAS detector.*

information and measuring particle position, energy or momentum accurately. Due to the high LHC beam energy of 7 TeV, the high collision rate of 40 MHz and the high lumnosity of 10^{34} $\mathrm{cm}^{-2}\mathrm{s}^{-1}$, the ATLAS detector must be large, massive, and granular. ATLAS is 46 m long, has a diameter of 22 m and weighs 7000 t. It consists of nearly 100 million electronic channels. A picture of the ATLAS detector is given in Figure 1.

The physics potential of the LHC experiments is huge and suggests that significant discoveries and advances in our understanding of particle physics could be achieved. The main scientific motivation for ATLAS and its competitor, the CMS experiment, is to investigate the mechanism of electroweak symmetry breaking and the origin of particle masses. This implies the search for the Standard Model Higgs boson and the measurement of vector boson scattering cross-sections. ATLAS is sensitive to many other signatures and hopes to discover physics beyond the Standard Model e.g. supersymmetry, compositeness of the fundamental fermions, unknown (hidden) space dimensions, and additional heavy vector bosons (Z', W'). In addition, ATLAS will be a top quark factory measuring the properties of the top quark with high precision. ATLAS will also provide a flood of more mundane but important measurements in QCD, b-physics, electroweak physics and more.

2 Detailed description of the ATLAS tracker

Precision reconstruction of the tracks of charged particles is crucial at the LHC. Measurement of the primary collision vertex is required to help distinguish the 25 or so interactions that occur simultaneously at every proton bunch-crossing. The identification of displaced vertices is crucial in tagging b-hadrons and thus selecting event samples enriched with Higgs boson or top quark candidates. Precise measurement of particle momenta is crucial to reconstruct the masses of unstable particles with good resolution.

Tracking at the LHC is particularly challenging because many particles are produced (1000 particles/bunch-crossing) in each collision at very short intervals (25 ns). This requires a detector with many channels to minimize occupancy and fast and power-hungry electronics. The large number of particles leads to radiation levels of 10 to 50 MRad in the tracking volume, corresponding to particle fluences of 10^{13} to 10^{15} 1-MeV neutron equivalent particles/cm^2 during the lifetime of the detectors. To-date, the technologies of choice in this environment are silicon microstrip or pixel detectors.

The ATLAS tracker consists of three subdetectors: a silicon pixel, a silicon microstrip, and a transition radiation gas detector. The subdetectors are arranged as several concentric barrel layers in the central region, while the endcap detectors consist of several disks or wheels. The combined tracker is a 7 m long cylinder with a diameter of 2.2 m. The detector is immersed in solenoidal magnetic field of 2 T.

2.1 The ATLAS pixel detector

The silicon pixel detectors are placed close to the beam line and measure event vertices with high spatial resolution ($\approx$ 10 μm). The pixel detector has 80 million electronic channels. The sensor area is 1.8 m^2 and is fully covered by the readout electronics. The power consumption of the detector is 7 kW.

The barrel part of the detector is organized in three layers of bi-staves placed at 5, 9 and 12 cm radius. Each stave is an 80 cm long compact package of 13 pixel modules. A picture of the bi-stave is shown in Figure 2. The forward and the backward region are covered by 3 disks placed at either end of the barrel. The material represented by the pixel detector, including support structure and services, is 10% of a radiation length at normal incidence and

Figure 2: *Bi-stave of the ATLAS pixel detector.*

substantially more at shallow angles.

The pixel detector is a most challenging and pioneering project in many respects and receives the largest radiation dose of all detectors. The pixel sensors are oxygenated n+ doped silicon on n bulk. They are capable of operating at up to 700 V bias voltage and provide a minimum signal of 10,000 electrons even after exposure to a fluence of 10^{15} particles / cm^2. Other highlights of this detector are the design of the readout chip; the packaging of the sensors, hybrids, chips; the composite support structure; and the aggressive bump-bonding techniques with only 50 μm pitch.

2.2 The ATLAS Semiconductor Tracker

The costs and the large fraction of passive material of the pixel detector call for a different technology at larger radii. Here silicon microstrips rather than pixels are chosen. The ATLAS Semiconductor Tracker (SCT) is again organized as a barrel (see Figure 3) with four layers at 30, 37, 45 and 52 cm radius and two endcaps with 9 disks at each end. The silicon area is 60 m^2 and the detector has 6 million channels. The electrical power of the detector is dominated by the front-end electronics which consume 50 kW.

The radiation environment and complexity of the electronics of the SCT are somewhat less challenging compared with the pixel detector. However, the detector area is much larger than any previous silicon detector and required a

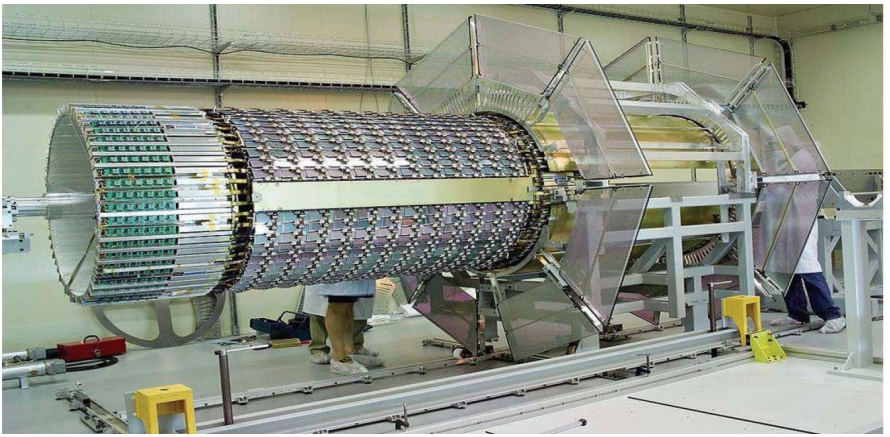

Figure 3: *The ATLAS SCT detector during insertion of Barrel 6, the largest barrel, into the Thermal Enclosure.*

word-wide mass production of four thousand detector modules. The mechanical tolerances of key module dimensions are better than 5 μm. Other challenges and highlights of the SCT project include the design and production of large precision carbon fiber support structures; the precision mounting of modules to these structures using a robot; and the engineering of a complex mechanical, thermal and electrical system.

2.3 The ATLAS Transition Radiation Tracker

The volume between a radius of 55 and 105 cm is covered by yet another tracking detector: the Transition Radiation Tracker (TRT), a straw tube detector. The TRT has 350 K electronic channels. Its building blocks are 4 mm thick straw tubes, filled with a $Xe(70\%)/CO_2(27\%)/O_2(3\%)$ gas mixture. The average number of TRT hits per track is 36. The TRT is much more affordable than a silicon detector of the same size would have been and the combination of many space points of limited resolution is equivalent to a single high-resolution hit. The TRT signal can arise from charged particle ionization as well as from the absorption of transition radiation (TR) photons, which provides electron identification capability. The low ionization signal and the high TR photon signal are detected using two different (adjustable) discriminator thresholds per straw tube.

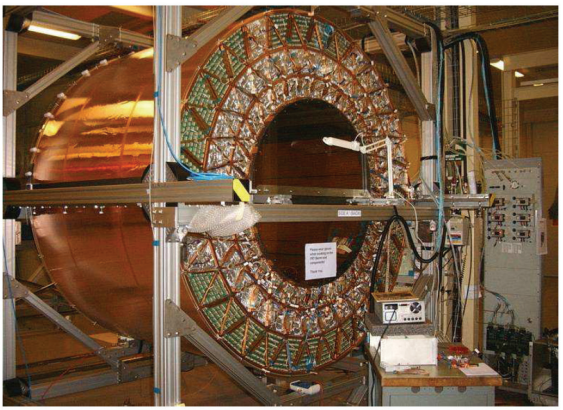

Figure 4: *The ATLAS TRT barrel detector.*

The main challenges of the TRT project are the size of the detector, the harsh radiation environment and high collision rates at LHC. The mechanical precision of the detector is impressive with wires being aligned within 20 μm. A picture of the TRT barrel is shown in Figure 4.

3 Status of the ATLAS tracker

After more than a decade of R&D, construction and assembly, the ATLAS tracker project progresses well and its status is most encouraging. The SCT barrel detector is at CERN and is almost complete. Currently 99.7% of its channels are operational. The assembly of the SCT endcap detectors is in its final stage and the first (of the two) endcap detectors will be shipped to CERN in February 2006. The TRT barrel is at CERN and is essentially completed. A fraction of the TRT has been taking cosmic data since July 2005. Most of the pixel modules are built.

While the tracker schedule remains tight and a number of problems are still being solved, we expect the ATLAS tracker to be ready for the very first LHC beam collisions in summer 2007.

4 Acknowledgments

I would like to thank the organizers for a wonderful conference in a beautiful city. I very much enjoyed the unorthodox and broad range of topics and was impressed by high standard and clarity of the talks. Thank you!

Frascati Physics Series Vol. XL (2006), pp. 77–86
Frontier Science 2005, New Frontiers in Subnuclear Physics
Milano, 12-16 September, 2005

THE ELECTROMAGNETIC CALORIMETER OF THE CMS EXPERIMENT

M. Diemoz
INFN Sezione di Roma, P.le A. Moro 2, 00185 Roma, Italy

Abstract

The Electromagnetic Calorimeter of the CMS experiment is made of about 75000 Lead Tungstate scintillating crystals. This project aims to achieve an extreme precision in photons and electrons energy measurement. General motivations, main technical challenges, performances achieved and the actual status of the project will be discussed in the following.

1 Introduction

The Large Hadron Collider will allow the study of pp interactions at a center of mass energy of 14 TeV. The main physics goals of the CMS experiment [1)] are the discovery of the Higgs boson and the search for new physics phenomena, in particular the appearance of particles predicted by Supersymmetric theories. The maximum design luminosity foreseen at LHC is 10^{34} cm^{-2} s^{-1} and the

bunch crossing rate will be 40 MHz. With the total cross-section $\sigma_{pp} = 80$ mb on average 20 events will be produced in one crossing corresponding to about 1000 tracks. The radiation environment is expected to be severe, in ten years of running (meaning a total integrated luminosity of 5x10^5 pb^{-1}) detector parts will be exposed to a neutron fluence as high as 10^{17} n/cm^2 and γ doses of 10^6 Gy. The typical signal to background ratio for intresting physics events is O(10^{-10}). These extreme conditions imposed a long R&D phase to obtain high granularity, fast, radiation resistant and selective detectors.

The electromagnetic calorimeter of the CMS experiment [2] is composed of 75848 Lead Tungstate ($PbWO_4$, about 90 t) crystals organized in a barrel (61200 crystals) covering the central rapidity region $|\eta| \leq 1.48$ and two end-caps which extend the coverage up to $|\eta|=3$. A pre-shower detector placed in front of the end-caps improves the γ - π^0 separation in this region. To obtain the most hermetic coverage the barrel has a nearly pointing geometry both in ϕ and η (crystals have a 3° tilt away from the interaction point in both directions). The scale of this detector is one order of magnitude higher than any crystal calorimeter built in the past, e.g. L3 calorimeter (about 10000 BGO crystals) operated at LEP [3] and the complexity as well.

2 The Challenges

Crystal calorimeters have an excellent energy resolution, the best attainable in electromagnetic calorimetry. The Higgs boson hunt in the "low mass" region is the basic ground for the CMS choice to build a crystal calorimeter. All the precision tests of the Standard Model performed by LEP experiments indicate a low mass Higgs [4]. In the mass interval 100 - 150 GeV the Higgs boson can be favorably detected by its decay in two photons. The H$\rightarrow \gamma\gamma$ reaction is not the most abundant but the cleanest one for detection in spite of the large irreducible background. The natural width of a Higgs in this mass region is of the order of few MeV making the resolution on the invariant mass of the two photons completely determined by the energy and angular resolution of the calorimeter. Thus the discovery potential is set by the experimental resolution and H$\rightarrow \gamma\gamma$ is a benchmark reaction for this instrument.

The energy resolution of a calorimeter can be parameterized by:

$$\frac{\sigma(E)}{E} = \frac{a}{\sqrt{(E)}} \oplus \frac{b}{E} \oplus c \qquad (1)$$

where a is the stochastic term related to any kind of Poisson-like fluctuation, b is the electronic noise term and c the so-called constant term. The target values for the coefficients in eq.(1) are a = 0.027 $\text{GeV}^{1/2}$, b $\leq$0.2 GeV and c $\sim$ 0.005 with an angular resolution $\sigma(\theta) \sim \frac{50mrad}{\sqrt{E(GeV)}}$. With these values a Higgs boson with a mass of 120 GeV could be detected by the CMS experiment with significance S = 5 collecting 30 fb^{-1} at luminosity 10^{33} $\text{cm}^{-2}\text{s}^{-1}$.

The precision experimentally attainable depends on a long list of instrumental effects which should be taken into account and kept under control. A crystal calorimeter is a very precise instrument that requires a tremendous effort to be finalized.

2.1 Lead Tungstate (PWO)

Lead tungstate ($PbWO_4$) is a very dense ($\rho = 8.28\ \text{g/cm}^3$) scintillating material. The most appealing properties of PWO crystals are the small radiation length (X_0 = 0.89 cm) and the small Moliere radius (R_M = 2.2 cm) which allow the construction of a compact and granular calorimeter, the fast scintillation light decay time (80% of light is emitted within 25 ns) and the basic radiation resistance. Nevertheless this material presents a few drawbacks. The low level of the light yield (100 photons/MeV, $\sim$ 0.2% with respect to NaI:Tl) requires that the light be read-out with a photo-detector able to amplify the signal, the high refractive index (2.29 at peak emission wavelength λ = 420 nm) makes the extraction of light from the crystal very difficult and finally the strong dependence of the light yield on temperature (-2%/°C around 18°C) requires a strict control and a system to avoid temperature variations exceeding 0.1°C.

A huge effort was done during R&D to improve the light yield of these crystals without spoiling their fast response and to guarantee their radiation hardness at a level sufficient to preserve the requested energy resolution. The radiation hardness of PWO and its optimization [5)] was one of the major problems to be overcome to allow the use of these crystals at LHC. At a radius of 1.29 m, corresponding to the front of the calorimeter, a γ dose rate of 0.15 Gy/h is expected at $\eta = 0$, while in the end-caps the dose rate can be as high as 15 Gy/h. PWO crystals are damaged by electromagnetic radiation through the creation of color centers that reduce their transparency. The scintillation mechanism remains untouched. The amount of the damage depends on the dose rate and reaches a stable level after a small administered dose. The observed

loss of light measured on production crystals irradiated with γ at 0.15 Gy/h is quite closely distributed around 3% for all crystals. The maximum accepted loss is set to 6%. This loss is tolerable and can be followed with a monitor system by injecting light through the crystals. Once irradiation ends, a partial recovery of crystal transparency happens in few hours.

After a pre-production of 6000 barrel crystals (whose dimensions depend on η but are approximately of 2 cm x 2 cm x 23 cm) to optimize growing techniques and quality, the mass production of high and uniform quality started in year 2001 in Bogoroditsk plant (Russia).

A dedicated R&D was needed to obtain end-caps crystals due to the larger (with respect to barrel) transversal dimensions: $\sim$ 3 cm x 3 cm. Few hundreds of these crystals have been produced to tune quality and optimize assembly procedures.

To maintain some flexibility in the production, after a process of validation of the quality, a small fraction of barrel and one half of end-cap crystals has been assigned to Shanghai Institute of Ceramic (SICCAS, China).

More than 75% of barrel crystals have been produced and tested.

2.2 Photo-detectors and read-out electronics

Avalanche photo diodes (APD) were developed for the barrel part of the calorimeter [6]. These devices are insensitive to the 4 T magnetic field of the experiment. Their quantum efficiency around the wavelength of the PWO emission peak is about 75%. The amplification is produced in a small region ($d_{eff} \sim 6$ μm) of very high electric field obtained with heavy doped silicon layers. To be operated in CMS, APD internal gain is set to M = 50. Two APDs of 25 mm^2 area are coupled to each crystal. In this configuration about 4000 photo electrons are produced per GeV of deposited energy. APD gives contributions to all terms in the energy resolution (1). In particular the gain stability is directly related to the constant term c. The variation of gain with bias voltage 3.1%/V and temperature -2.4%/°C made mandatory the development of a very stable bias system and to maintain temperature changes of the system below 0.1 °C. APDs have been developed and optimized with an extensive R&D program, the production in Hamamatsu Photonics (Japan) ended in 2004.

In the end-caps region radiation levels are too high to use APDs, the

longitudinal magnetic field allows there the use of vacuum photo triodes (VPT) [7]. These are single stage photo-multiplier tubes with a fine metal grid anode. Their active area is 280 mm^2, quantum efficiency is about 20% at 420 nm and a gain of 8 - 10 is expected in the 4 T magnetic field. The irradiation produces a loss of optical transmission of the UV glass window that is foreseen to be limited to less than 10% after ten year of LHC running.

The photo-detectors are followed by an on-detector read out electronics. The main properties of this system are the wide dynamic range (50 MeV to 2 TeV), the speed, the trigger capability, and the radiation hardness. The read-out chain is organized in a modular structure made of a matrix of 5 $\times$ 5 channels (trigger tower). Each trigger tower is composed of 1 motherboard, 5 Very Front End (VFE) cards, 1 Low Voltage Regulator (LVR) card and 1 Front End (FE) card. The motherboard distributes the high voltage to the APDs/VPTs and connects them to the 5 VFE cards, which preamplify, shape and digitize the signals with 3 different gains (1, 6, 12) at 40 MHz. The automatic gain switching, together with a 12-bit ADC leads to an effective dynamic range of 15-16 bits. The FE card estimates the tower energy and sends it to CMS Level-1 trigger, while storing the data from the 25 channels in a data buffer during the latency time (3 μs). The optical link system connects at 800 Mbit/s the Gigabit Optical Hybrid (GOH) chips on the FE card to the off-detectors electronics 100 m downstream. On reception of a Level-1 trigger, based on the energy of the trigger tower, the data from the 25 channels are transferred serially to the off-detector electronics. The whole trigger process takes place within 3 μs.

2.3 Regional Centers for assembly and test

The construction of the calorimeter is a distributed process. Parts as crystals, capsules, mechanical elements for the support structure etc. are produced under the responsibility of different Institutions taking part to the project and sent afterwards (barrel parts) in two Regional Centers located in CERN and Rome. The calorimeter has a modular structure. The basic sub-unit of the barrel, composed by a crystal and a capsule (hosting two APDs read in parallel) glued together, is inserted in a glass fiber alveolar structure. Ten sub-units fit in this structure that is closed by an aluminum element and constitute a "sub-module". Sub-modules are of 17 different types depending on η position. A

"module" is made by 40 or 50 sub-modules mounted on a 3 cm thick aluminum grid. Modules are of 4 η types. A "super-module" is a set of 4 modules and the barrel consists of two identical halves made by 18 super-modules. End-caps will have a simpler structure, 138 "super-crystals" made of 25 identical crystals are a so-called "dee" and two of them make an end-cap. Endcap crystals production will follow the barrel one and their assembly and test will happen at CERN. All the elements of the calorimeters are assembled and checked step by step, following a well defined quality control protocol to guarantee the perfect functionality of parts resulting from mounting operations. In particular all the crystals are subject to the systematic test of their properties. Both Centers are equipped with similar automatic machines to insure crystal quality [8]. Cooling system and read-out electronics are installed at CERN following an analogously strict quality insurance scheme. The severe control of quality at each step of the construction will insure a fully operational calorimeter at best of its potentiality. The presence of dead or malfunctioning channels in the first 9 super modules fully assembled is less than permill.

3 Key points in energy resolution

At high energy the most dangerous contribution to the energy resolution comes from the constant term c. Beside the uniformity of crystal's light collection which is guaranteed at crystal production level by an appropriate treatment of surfaces [9], key issues to keep the constant term c $\sim$ 0.5% are:

- system stability
- inter-calibration by monitor and physics signals at 0.5% including the effect of radiation damage

3.1 Temperature and APD gain stability

Temperature knowledge and stability is particularly important in the CMS electromagnetic calorimeter system. The temperature dependence of the calorimeter response of -4 %/°C (due to crystals and APDs) imply, in order to achieve the design resolution of 0.5 %, to maintain crystal's temperature stable at 0.05°C. The cooling system designed to this end [10] couples thermally the on-detector electronics cards (VFE), through gap pad and gap filler, to aluminum bars embedding water pipes in order to remove the power dissipated

by the electronics ($\simeq$ 2.5 W/channel). Laboratory tests validated the cooling system by measuring the temperature on the crystals with the electronics switched off and switched on. The maximum measured change in temperature was 0.1°C, with a mean change of 0.056°C.

The High Voltage system to bias APDs was designed to keep their gain stable to 10^{-4} ($\pm$30 mV / 400 V) [11] over a period of 3 month. During the acceptance and commissioning of the system, 1224 channels were tested measuring their voltage variation ΔV over a period of one month; 66 mV has been the maximum ΔV measured with the bulk of the distribution around 22 mV.

3.2 Calibration and monitoring crystals transparency loss

The ECAL calibration prior to LHC start-up is crucial both for the detector operation and for the early discovery potential for new physics. The calorimeter channels are mis-calibrated at the level of 10%, due to the intrinsic differences among individual PWO crystals (light yield), quantum efficiency of the photo-detectors and response of the read-out electronics. Before the start-up, three methods will give an inter-calibration of the channels with different precisions. A preliminary inter-calibration of all the crystals is obtained from the crystals Light Yield and APDs laboratory measurements. The comparison of this inter-calibration with the one (very precise) obtained using electron beams shows that the precision achievable with this method is of about 4%. Operating the APDs at gain 200, cosmics rays traversing the crystal along its longitudinal axis collected in about ten days can be used to intercalibrate crystals to about 2-3% [12]. Finally some modules will be calibrated with high energy electron beams to reach a calibration better than 0.5%. This data taking will be mandatory in order to understand: geometrical effects (energy deposition depends on η), effects of gaps between crystals and modules, MC simulation in all its aspects and finally in situ calibration having few regions precisely known.

In-situ ECAL will be calibrated with physics events and a general description of the foreseen strategy can be found in reference [13]. At the beginning of the detector operation a fast inter-calibration method can be used, based on the assumption that in average in minumum bias events the same energy is deposited over a ring of crystals in Φ. A Monte Carlo simulation has shown that the limit of this method is the non perfect Φ symmetry of the

detector and that a calibration at the level of about 1-2% can be obtained in the barrel and between 1-3% in the endcaps [14]. The Φ rings can be rapidly inter-calibrated using $Z \rightarrow e^+e^-$ events reconstructing the Z invariant mass. The $Z \rightarrow e^+e^-$ rate is about 1 Hz at low luminosity. The collection of 2fb^{-1} will be enough to obtain an intercalibration at 0.6% [15]. Once the tracker will be fully functional the process $W \rightarrow e\nu_e$ can be used for single crystal calibration. This method minimizes the difference between the measured momentum of the electron track and the energy associated to it in the ECAL. The calibration precision achievable depends on η and for an integrated luminosity of 5 fb^{-1} it may reach 0.5-1.0% in the barrel, the method limit being below 0.5% with higher statistics [16]. The major difficulty in using electrons for ECAL calibration is the presence of an important amount of material due to the "massive" tracker choice made by CMS. Studies are going on looking at π^0 and η^0.

In between calibrations with physics events the evolution of the system due to the loss of transparency induced by radiation damage will be followed with high accuracy by a light injection system. This monitoring system consists of two laser sources, which distribute four wavelengths (440 nm, 495 nm, 700 nm and 800 nm) to each crystal, during the 3 μs long abort gap of LHC, which will be present every 90 μs. The 440 nm light is used to monitor crystals transparency variations, while the 800 nm light will help in monitoring the stability of the electronics response (color centers present in the crystals weakly absorb in this wavelength range). The stability of the laser system has been measured to be better than 0.1 % by means of reference PN diodes. A detailed analysis of the crystal irradiations on beam demonstrated the validity of the relation $S/S_0 = (R/R_0)^\alpha$, where S and R are the signals obtained with the electron beam and with the laser light during irradiation compared to the starting values S_0 and R_0. The crystals (coming from the same producer) are expected to behave in the same way and the fitted exponents of this power law for the different crystals were found to have a spread of 6.3 %, around an average value of $\alpha = 1.55$. By correcting all the crystals for their loss of transparency with the same value of α the follow-up of the calibration coefficients is performed to an accuracy of 0.3 %.

4 Achieved performances

Tests on barrel modules were carried out in 2002 and 2003 [17]. In 2004 a complete supermodule (1700 crystals), built according to the final production specifications, was tested with an electron beam at CERN. This data taking allowed an accurate system test of ECAL and validated the testbeam calibration procedure.

The whole procedure for the energy reconstruction has been investigated. In each crystal the amplitude is reconstructed as a weighted sum of the 10 digitised signal samples, including three samples before the signal, which are used as an estimation of the baseline. By applying the same procedure to data taken with a random trigger, the noise in the single channel has been measured to be about 40 MeV, as expected. In order to study the energy resolution of the calorimeter, electrons in the range between 20 and 250 GeV were collected. The energy resolution measured on 18 towers of 3x3 crystals is in perfect agreement with what expected by design and crystals behave similar way. The average resolution obtained on these crystals is:

$$\frac{\sigma(E)}{E} = \frac{2.9\%}{\sqrt{E}(GeV)} \oplus \frac{0.125}{E} \oplus 0.30\% \qquad (2)$$

thus confirming the high performance achivable with this system.

5 Conclusions

The electromagnetic calorimeter of CMS is a challenging project. An intense R&D effort was performed over many years. The calorimeter is actually in the construction phase and the performances of the final system, as measured on test beam, fully satisfy the requirements to made precision physics measurements as needed to detect the rare decay H$\rightarrow \gamma\gamma$.

References

1. CMS Collaboration, The CMS Technical Proposal, CERN/LHCC **94-38**, 1994.

2. CMS Collaboration, "The CMS Electromagnetic Calorimeter Technical Design Report", CERN/LHCC **97-33**, 1997.

3. B. Adeva *et al*, Nucl. Instr. & Methods **A281**, 80 (1990).

4. R.Barate *et al* (The four LEP Collaborations), Phys. Lett. **B565**, 61 (2003).

5. E. Auffray *et al*, Nucl. Instr. & Methods **A402**, 80 (1998).

6. Z. Antunovich *et al*, Nucl. Instr. & Methods **A573**, 379 (2005).

7. K.W. Bell *et al*, Nucl. Instr. & Methods **A469**, 29 (2001).

8. S. Baccaro *et al*, Nucl. Instr. & Methods **A459**, 278 (2001); E. Auffray *et al*, Nucl. Instr. & Methods **A456**, 325 (2001); E. Auffray *et al*, Nucl. Instr. & Methods **A523**, 355 (2004).

9. S. Paoletti, Light Collection in $PbWO_4$ Crystals in: Proc. of the Int. Workshop on Tungstate Crystals, Roma, Oct. 1998.

10. P. Govoni, Performance of the cooling system of ECAL CMS, Proc. of the 8^{th} Conference on Astrop., Part., Space Phys., Detectors and Medical Phys. Appl., Como, Oct. 2003.

11. A. Bartoloni, The Power Supply System for the CMS-ECAL APD in: Proc. 7^{th} Workshop on Electronics for LHC Exp., Stockholm, Sweden, Sept. 2001.

12. M. Bonesini *et al*, CMS NOTE 2005/023

13. R. Paramatti, Calibration of the CMS Electromagnetic Calorimeter, Nucl. Phys. B Proc. Suppl. **125**, 107 (2003).

14. D. Futyan, CMS Note 2004/007.

15. P. Meridiani and R. Paramatti, CMS NOTE 2006/039

16. L. Agostino *et al*, CMS NOTE 2006/039

17. P. Adzic *et al*, Eur. Phys. J **C44**, 1 (2006).

CMS Documents are available at `http://cms.cern.ch/iCMS`.

Frascati Physics Series Vol. XL (2006), pp. 87–94
Frontier Science 2005, New Frontiers in Subnuclear Physics
Milano, 12-16 September, 2005

RING IMAGING CHERENKOV DETECTORS AND THEIR APPLICATION IN LHCb

O. Ullaland
CERN, CH 1211 Genève 23, Switzerland
for the LHCb RICH Collaboration

Abstract

Ring Imaging Cherenkov detectors play a central role in particle identification throughout experimental particle physics. We will in this article, by using the LHCb experiment as an example, discuss some of the requirements of the detector and how to realize them. The main emphasis will be on the interplay between complementary radiator materials, photon detectors and optical systems.

1 Introduction

The LHCb experiment [1)] has been conceived to study with high precision the CP violation and other rare phenomena in B meson decays. This will provide a detailed understanding of quark flavour physics in the framework of the Standard Model and may reveal a sign of the physics beyond. In order to achieve these goals, the LHCb detector must have a $\pi-$K separation capability from a few to $\sim 100\,\mathrm{GeV}/c$, in addition to high track reconstruction efficiency, excellent proper time resolution and high trigger efficiency. An example of the importance of a particle identification system is for the measurement of the CP asymmetry of ${B_d}^0 \to \pi^+\pi^-$ decay. This requires the rejection of two-body backgrounds with the same topology: ${B_d}^0 \to K^+\pi^-$, ${B_s}^0 \to K^-\pi^+$ and ${B_s}^0 \to K^+K^-$. Due to this large background, the signal channel is dwarfed without the particle identification provided by the Ring Imaging Cherenkov, RICH, detectors [2)].

The layout of the LHCb experiment is shown in Fig. 1. It is a forward single-dipole spectrometer with the LHC storage ring beam pipe passing through the apparatus. The spectrometer configuration is justified by the fact that the parton-parton interactions for production of relatively low-mass $b\bar{b}$-quarks at collider energies are inherently asymmetric in momentum and therefore leads to a rather striking forward-backward peaking and a strong directional correlation between B and $\bar{B}$ production. The acceptance of the spectrometer is from 25 to 250 mrad in

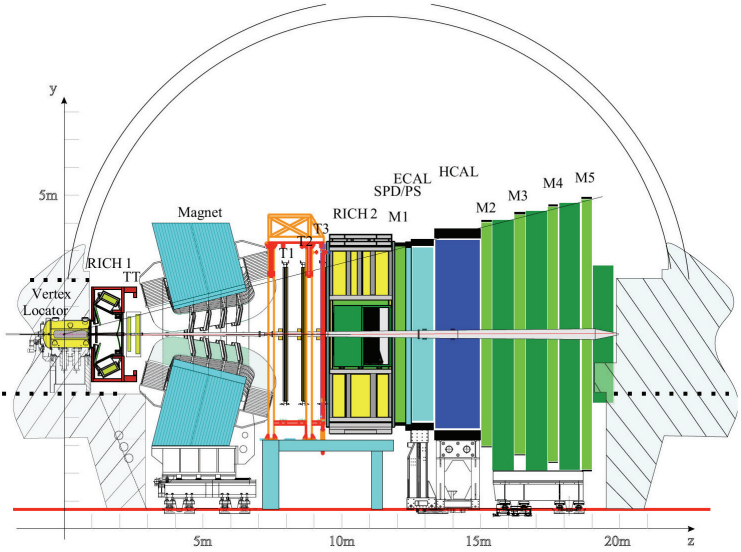

Figure 1: *Side view of the LHCb experiment.*

the vertical (non-bending) plane and up to 300 mrad in the horizontal (bending) plane. Due to the strong correlation between the polar angle Θ and the momentum of the decay products in B-decay, the LHCb experiment has two RICH detectors. The upstream detector, RICH 1, covers the full solid angle of the experiment and is optimised for lower momentum particles. The downstream detector, RICH 2, is optimised for higher momentum particles, but with a limited polar angle coverage. A sketch of the two RICH detectors is given in Fig. 2.

2 Cherenkov Radiators

The aim of the LHCb RICH detectors is to provide positive kaon identification over a wide momentum range. The choice of radiators is therefore governed by the difference in photon emission angle between kaon and pion, $\Theta_{\pi K} = \Theta_\pi - \Theta_K$, and kaon

and proton, $\Theta_{\mathrm{Kp}} = \Theta_{\mathrm{K}} - \Theta_{\mathrm{p}}$, for a given momentum and a given angular resolution. By choosing the lower kaon threshold momentum at 2 GeV/c, a refractive index of 1.03 is required. Appropriate refractive indices of radiators for higher momentum particles are chosen by considering saturation and threshold effects in $\Theta_{\pi\mathrm{K}}$ and Θ_{Kp} in order to cover the full momentum range up to $\sim$ 100 GeV/c.

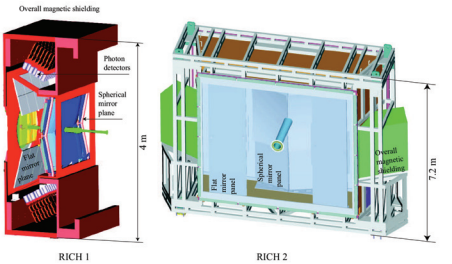

Figure 2: *Sketch of the RICH detectors.*

2.1 Silica Aerogel

Silica aerogel for use in high energy physics experiments was first established in 1970 [3]. Aerogel is a material of high porosity with a microstructure smaller than the wavelength of visible light. Its index of refraction, n, is therefore lower than the one of solid silica. The refractive index can to first order be approximated by $n-1 \sim 0.21 \cdot \rho$, where ρ is the density of the gel in units of g/cm^3. The transparency, T, is normally parameterised as:

$$T = A \cdot e^{-Ct/\lambda^4}$$

where t is the thickness of the aerogel in cm, λ is the photon wavelength in μm, C is the clarity coefficient in units of μm^4/cm and A is the transparency for $\lambda \to \infty$. The coefficient A describes faults in the gel, like cracks and surface deformations, whereas C gives a measure of the bulk performance. The λ^4-term shows that the transparency is governed by Rayleigh scattering. The transparency is thereby biased towards long wavelengths. This requires $C \leq 0.0071$ μm^4/cm in order to have $T \geq 0.25$ at 400 nm for a 5 cm thick aerogel sample.

Extensive research and development has been performed on silica aerogel throughout the last decennia. This work has been concentrated both on hydrophobic [4] and on hydrophilic [5] aerogel. Aerogel with excellent clarity in the range of 0.005 to 0.006 μm^4/cm is now readily available for a variety of different refractive indices ranging from 1.01 to 1.05.

2.1.1 The LHCb Aerogel

Large hydrophobic silica aerogel [1] tiles, $20.0 \times 20.0 \times 5.1$ cm^3, have been tested for use in the LHCb experiment [6]. The refractive index is 1.030 at 400 nm and the clarity is 0.0060 μm^4/cm. The gel is stable towards irradiation and shows no, or insignificant, change in transparency when tested after an accumulated fluence of up to $5.5 \cdot 10^{13}$ /cm^2 of neutrons or protons or a γ dose of $\sim 2.5 \cdot 10^5$ Gy. This aerogel is clearly sensitive to water vapour, but the initial transparency can be restored after a bake-out of the tile. The refractive index of these tiles is also fairly uniform across the gel. The spread is measured [2] to be $\sigma_{n-1}/(n-1) \sim 0.013$. The refractive index is well described by:

$$n - 1 = \frac{1.29 \cdot 10^{-4}}{88^{-2} - \lambda^{-2}} \cdot (n-1)_{\lambda \to \infty}$$

for the photon wavelength, λ, in nm.

[1] Produced by Boreskov Institute of Catalysis, Pr. Lavrentieva 5, RU-630090 Novosibirsk

2.2 The LHCb Gas Radiators

Two gas radiators with well matched refractive indices to the one of the silica aerogel have been chosen. C_4F_{10} is the complementary gas radiator to the aerogel in the lower momentum RICH 1 detector and CF_4 is the radiator in the higher momentum RICH 2. These fluorocarbons have low chromatic dispersion. The refractive index is given at 0 °C and 101325 Pa as

$$CF_4: \quad (n-1)10^6 = \frac{0.12489}{61.8^{-2} - \lambda^{-2}} \qquad C_4F_{10}: \quad (n-1)10^6 = \frac{0.25324}{73.7^{-2} - \lambda^{-2}}$$

for the photon wavelength, λ, in nm.

The photon detector, described in Section 3, has a quantum efficiency cut-off at about 190 nm. An admixture contaminant of air will therefore not influence the transparency of these radiators [7]. This greatly facilitates the operation and handling of these gas radiators which are run at atmospheric temperature and pressure.

3 Photon Detector

The use of aerogel and the chromatic error induced by the C_4F_{10} defines the wavelength range of the quantum efficiency, QE, of the photon detector. Setting the lower QE cut-off at around 190 nm, the contribution from the chromatic error in C_4F_{10} to the Cherenkov angle resolution is ~ 0.8 mrad. This error effectively sets the required pixel size of the photon detector equal to 2.5×2.5 mm^2.

3.1 Hybrid Photon Detector

The Hybrid Photon Detector, HPD [8], has been chosen as the photon detector for the RICH detectors of LHCb. The HPD is based on the design of an electrostatic cross-focusing vacuum tube with a quartz entrance window. The demagnification is ~ 5. The schematic view of the HPD is shown in Fig. 3a. Photons are absorbed in an S20 (multi-alkali) photocathode, with a typical QE shown in Fig. 3b. The generated photoelectrons are accelerated onto a silicon detector and create electron-hole pairs. The acceleration field results in a gain of ~ 5000 with -20 kV applied to the photocathode. The silicon pixel anode is bump-bonded to the readout chip, read out at 40 MHz. The total area covered by the HPDs in both RICH detectors is ~ 2.6 m^2, with a geometrical efficiency of ~ 65 %.

[2]Measured on a pre-production tile of $10 \times 10 \times 4.2$ cm^3.

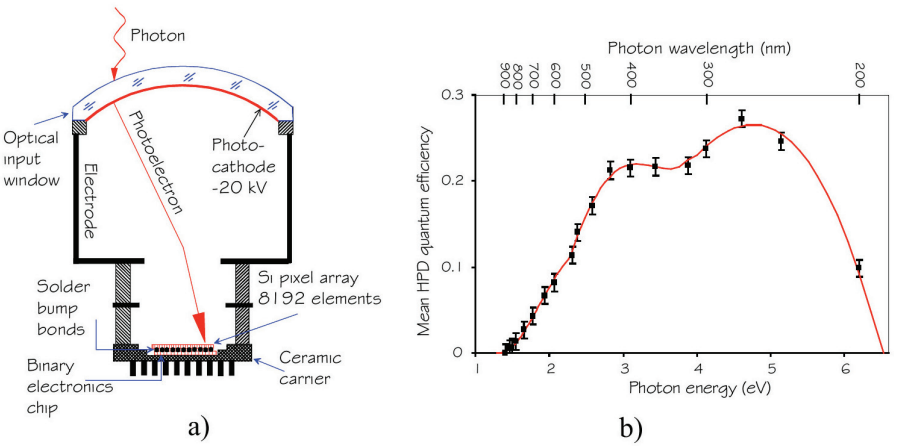

Figure 3: *a) A sketch of an HPD and b) the quantum efficiency as function of photon energy.*

3.2 B Field Influence

Both RICH detectors are located close to the LHCb dipole magnet and the photon detectors will therefore have to operate in this fringe field. The HPD electron optics is sensitive to magnetic flux densities. The Lorentz force due to a field parallel, $B_{\parallel}$, to the electrostatic axis of the tube changes the electron trajectories, causing them to rotate around the tube axis. This effect is visible as a significant distortion and magnification of the anode image. A transverse magnetic flux density, $B_{\perp}$, with

respect to the electrostatic axis of the tube, causes a lateral shift of the electronic image.

Large magnetic shieldings are installed around the photon detectors, shown in Fig. 2, together with local secondary magnetic shields of a high permeability alloy [3] which surround each HPD. The maximum residual field at the photocathode is calculated and measured to be $\sim$ 1 mT [9], however this could still result in some distortion of the image. The effect has been extensively studied [10]. A simple distortion correction algorithm was developed for axial fields and was used successfully for testing the photon position reconstruction and for the estimation of the axial magnetic flux density component. The measurements indicated negligible distortions caused by transverse fields. Calibration and distortion monitoring systems will be installed to follow any evolution of the magnetic behaviour.

4 The Optical System

The Cherenkov photons are generally mapped onto the photon detectors either by the proximity focusing technique or by mirrors with quadric surfaces. Proximity focussing can not be applied in the LHCb RICH detectors. The optical systems in RICH 1 and 2 are shown in Fig. 2. Spherical surfaces focus the Cherenkov photons onto the photon detectors. In order to have the detection planes well outside the acceptance of the spectrometer, a second plane of flat mirrors is interposed between the spherical mirrors and the photon detectors. Since for logistical reasons the mirrors and the support systems must be placed in the acceptance of the spectrometer, the added radiation and interaction lengths must be reduced as far as possible. The optical system must also be perfectly aligned in order to guarantee a precise reconstruction of the Cherenkov angle. The mirror support system must therefore allow a precise initial alignment and long-term stability. The system must also be compatible with the fluorocarbons CF_4 and C_4F_{10}.

[3] Mumétal: Magnetic Shielding Alloy (Ni77/Fe14/Cu 5/Mo 4)

In order to entirely fulfil all of the requirements above, two different solutions have been adapted. The spherical mirrors in RICH 1 are made from a self-supporting 4 mm beryllium substrate with a thin coating, $\sim$ 500 μm, of glass [4] as the support for the reflective surface. These mirrors do not have any part of their alignment system inside the acceptance. The added radiation length from the mirrors is 1.3 % of X_0. RICH 2 is the detector immediately upstream of the first muon chamber and the calorimeter system. A somewhat higher material budget for this optical system can therefore be tolerated. The mirrors are made from 6 mm thin glass substrates [5]. The support and alignment system is made from polycarbonate, which is attached

The support and alignment system is made from polycarbonate, which is attached to flat panel aluminium honeycomb structures. This makes up a sturdy, yet light, arrangement.

The reflective surface of the mirrors is made up from a layered stack. The thicknesses of the dielectric layers are optimised with respect to the angle of incidence of the light and the energy distribution of the detected photons [11]. The RICH 2 mirrors have typically incidence angles of 21° for the spherical mirrors, and 48° for the flat mirrors, and the best result is obtained with Cr(20 nm), Al(85 nm), SiO_2(28 nm), and HfO_2(38 nm). At 275 nm, the wavelength for which the coating is optimized, a reflectivity of about 96 % is reached.

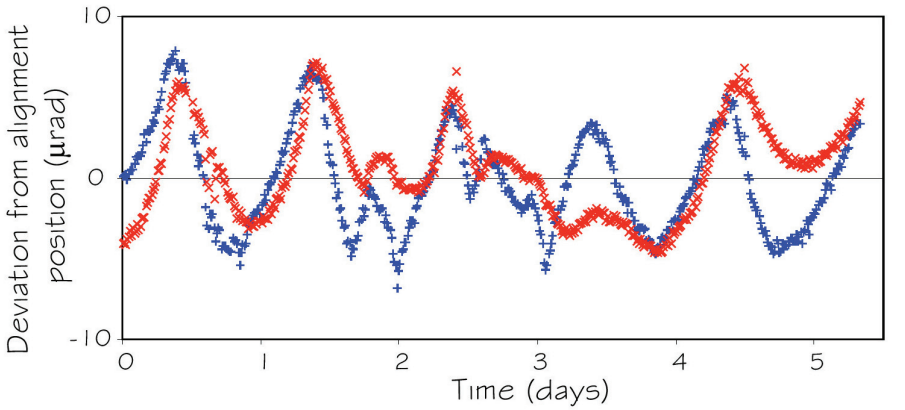

Figure 4: *Horizontal (+) and vertical (×) deviation from final alignment position as a function of time for the spherical mirrors of RICH 2.*

[4]Institute of Beryllium, JSCo "Kompozit", Moscow, Russian Federation
Vavilov State Optical Institute, St. Petersburg, Russian Federation

[5]Borosilicate Glass (Simax) by COMPAS, CZ-51101 Turnov

RICH 1 is currently under construction whereas RICH 2 has been fully furbished, apart from the photon detectors, and installed in the experiment. The alignment of the optical system for RICH 2 was achieved in three stages [12]. First all the spherical mirror elements on each of the two sides where aligned to their centre of curvature. Then a few flat mirrors, paired with their respective spherical elements, were aligned to their theoretical centres. Finally the rest of the flat mirrors were aligned with respect to these. Fig. 4 shows the stability and the precision of this alignment procedure. The estimated contribution from the alignment and stability of the optical system to the overall uncertainty of the single photon resolution, is in the order of ≤ 30 μrad.

5 Expected Performance

The R&D phase for the Ring Imaging Cherenkov detectors for the LHCb experiment has been successfully accomplished and their implementation into the experiment is well underway. Test beam data have validated the laboratory measurements and simulation studies. The expected efficiency for $\pi \rightarrow$ e, μ or π (light) and K $\rightarrow$ K or p (heavy) is well over 90 % for most of the momentum range up to 100 GeV/c. The misidentification, $\pi \rightarrow$ heavy or K $\rightarrow$ light, is well below 10 % for the same momentum range. Particle identification in LHCb will be available at the start-up of the LHC.

Acknowledgement

We gratefully acknowledge the invaluable support and help from all our collaborators and funding authorities of the experiment throughout the realisation of these RICH detectors. I am indebted to the organising committee for inviting me to give this overview talk.

References

1. LHCb Collaboration, LHCb Technical Design Report, Reoptimized Detector Design and Performance, CERN/LHCC 2003-030, LHCb TDR 9, 9 September 2003.

2. LHCb Collaboration, LHCb RICH Technical Design Report, CERN/LHCC 2000-0037, LHCb TDR 3, 7 September 2000.

3. A. Linney and B. Peters, The Powder Counter, a new Detector of High Energy Particles, Nucl. Instr. and Meth. **100**(1972)545
   M. Cantin *et al.*, Silica Aerogel used as a Cherenkov Radiator, Nucl. Instr. and Meth. **118**(1974)177.

4. A.Yu. Barnyakov *et al.*, Development of aerogel Cherenkov detectors at Novosibirsk, Nucl. Instr. and Meth. **553**(2005)70-75
   T. Bellunato *et al.*, Performance of aerogel as Cherenkov radiator, Nucl. Instr. and Meth. **519**(2004)493-507.
5. I. Adachi *et al.*, Study of highly transparent silica aerogel as a RICH radiator, Nucl. Instr. and Meth. **553**(2005)146-151
   S. Korpar *et al.*, RICH with multiple aerogel layers of different refractive index, Nucl. Instr. and Meth. **553**(2005)64-69.

6. C. Matteuzzi, A RICH with aerogel for a hadron collider, Nucl. Instr. and Meth. **553**(2005)356-363.

7. O. Ullaland, Fluid systems for RICH detectors, Nucl. Instr. and Meth. **553**(2005)107-113
E. Albrecht *et al.*, VUV absorbing vapours in n-perfluorocarbons, Nucl. Instr. and Meth. **510**(2003)262-272.

8. N. Kanaya *et al.*, Performance study of hybrid photon detectors for the LHCb RICH, Nucl. Instr. and Meth. **553**(2005)41-45.
M. Campbell *et al.*, Performance of hybrid photon detector prototypes with encapsulated silicon pixel detector and readout for the RICH counters of LHCb, Nucl. Instr. and Meth. **504**(2003)286-289.

9. M. Patel *et al.*, Magnetic shielding studies of the LHCb RICH photon detectors, Nucl. Instr. and Meth. **553**(2005)114-119.

10. G. Aglieri Rinella *et al.*, Characterisation and compensation of magnetic distortions for the pixel Hybrid Photon Detectors of the LHCb RICH, Nucl. Instr. and Meth. **553**(2005)120-124.

11. A. Braem *et al.*, Metal multi-dielectric mirror coatings for Cherenkov detectors, Nucl. Instr. and Meth. **553**(2005)1182-186.

12. C. D'Ambrosio, The RICH 2 Detector of the LHCb Experiment, Submitted to IEEE NSS 2005.

Frascati Physics Series Vol. XL (2006), pp. 95
Frontier Science 2005, New Frontiers in Subnuclear Physics
Milano, 12-16 September, 2005

THE MUON SYSTEM OF LHCb

A. Satta
University of Rome Tor-Vergata and INFN, Rome, Italy

Written contribution not received

Frascati Physics Series Vol. XL (2006), pp. 97
FRONTIER SCIENCE 2005, NEW FRONTIERS IN SUBNUCLEAR PHYSICS
Milano, 12-16 September, 2005

THE TRIPLE-GEM DETECTOR OF THE MUON SYSTEM OF LHCb

W. Bonivento
INFN-Cagliari, Italy

Written contribution not received

Frascati Physics Series Vol. XL (2006), pp. 99–102
Frontier Science 2005, New Frontiers in Subnuclear Physics
Milano, 12-16 September, 2005

TEST OF THE CMS BARREL MUON DRIFT CHAMBERS WITH COSMIC RAYS

Vincenzo Monaco
Università di Torino and INFN Sezione di Torino

Abstract

The muon detection system of the CMS experiment relies in the barrel part on 250 Drift Tube chambers, distributed in 4 concentric shells and 5 wheels. Accurate quality control procedures are required during the chamber construction to check the behaviour of each drift cell and the accuracy of the wire positions. In particular, cosmic ray tracks are used to certify the global performance of the chambers and of the associated electronics.

The typical results of the measurements performed with cosmic rays on the CMS Drift Tube chambers are briefly described and compared with results obtained from tests with muon beams.

1 Description of the CMS Drift Tube chambers

The Drift Tube chambers [1)] of the CMS experiment have dimensions ranging from 2.0×2.5 m^2 to 4.0×2.5 m^2. Each chamber is made of 3 or 2 independent

units, called SuperLayers (SL), glued together and with a honeycomb panel. Each SL consists of four layers of drift cells, with the even layers staggered by half a cell with respect to the odd layers. The individual cell (shown in Fig.1) has a transversal cross section of 13×42 mm^2 and is composed of a central anode wire, two cathodes deposited on C-shaped lateral profiles, and two field-shaping aluminium strips above and below the wire. The cell is filled with a gas mixture of Ar/CO_2 (85%/15%) slightly above the atmospheric pressure.

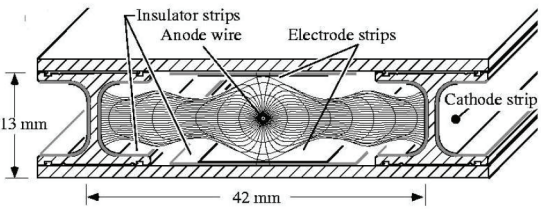

Figure 1: *Transverse view of the drift cell with drift lines and isochrones.*

The chamber performance has been extensively studied in test beams [2, 3, 4]: the single cell resolution for perpendicular tracks is below 200 μm, the cell efficiency is above 99 % in the active volume, and deviations from the space-time linearity are below 100 μm over most of the drift length.

2 Quality control tests

Different quality control tests are performed during and after the assembly of each chamber, according to procedures agreed between the assembly sites (Aachen, Legnaro, Madrid, Torino). During the construction of each SL, the wire positions are measured by a CCD camera. Each completed SL, equipped with the final front-end electronics and internal Low and High voltage boards, is tested for high voltage behaviour and for gas tightness; a comparator is used to measure the planarity of the SLs and of the chambers.

A powerful method used to study the performance of individual chambers is the reconstruction of cosmic ray tracks. In each assembly site cosmic rays are triggered by an external scintillator system and the drift times are measured with commercial TDCs. Several measurements are performed and used to identify potential problems; the analysis procedures and the typical results are described in the following section.

3 Measurements with cosmic rays

After a training period with the chamber under high gas flux and at nominal high voltage values ($V_{cathode}$=-1200 V, V_{anode}=+3600 V and V_{strip}=+1800 V), the hit rate of each cell is measured. The typical hit rate is about 40 Hz per cell, while higher noise levels could be related to bad high voltage internal connections or to other problems in the internal electronics.

When the hit rate reaches an acceptable level, data are collected in the cosmic ray test facility and the drift time distribution is measured in each cell. Sometime one or more cathodes or shaping strips are disconnected from the high voltage internal distribution chain: the drift time distribution of these cells is distorted, while cells with not connected wires give no signal. These problems are identified and the corresponding cells repaired before shipping the chamber to CERN or installing it in the iron yoke.

An important parameter defining the cell behaviour is the drift velocity, measured with the "meantime" method. The meantimes are linear combinations of the drift times t_j of cells in three successive layers:

$$MT_j = \frac{t_j + t_{j+2}}{2} + t_{j+1} \tag{1}$$

Under the assumption of a linear space-time relationship, the two meantimes (MT_1 and MT_2) have a peak value corresponding to the maximum drift time (related to the drift velocity) and independent of the angle and position of the track; the width of the MT distributions is related to the time resolution of the chamber. A Gaussian fit of the MT distributions provides both the drift velocity $\mathrm{v_{drift}}$ of the cell and a measurement of the space resolution σ_{x}. The typical results obtained from data collected with cosmic rays in the production sites are $\mathrm{v_{drift}} \simeq 55$ μm/ns and $\sigma_{\mathrm{x}} \simeq 300$ μm; the measurement of the space resolution is compatible with the width of the residual distribution of fitted tracks.

The space resolution measured with cosmic rays is higher than the resolution measured in test beams with tracks orthogonal to the chambers (~ 200 μm): the reasons are the spread of the cosmic angular distribution (the cell resolution gets worse for non perpendicular tracks), the multiple scattering of low energy muons, and the limited timing resolution of the large scintillator systems.

A precise alignment of the layers inside the SL and of the relative positions of the SLs is required for the trigger system to work correctly. The internal alignment parameters of the chambers can be measured with cosmic rays, by minimizing the mean values of the residuals of fitted tracks with an iterative procedure, or by comparing the MT distributions separately for tracks crossing a cell on the left or on the right of the wire. The relative layer positions inside a SL extracted from the data are compatible with the measurements obtained with the CCD camera. A maximum deviation from the nominal layer positions of 100 μm is measured in all the assembly sites, and the RMS of the wire positions inside a layer is below 50 μm. The relative position of the SLs inside a chamber can be measured with cosmic rays by comparing the segments fitted in the SLs and checked to be compatible with the required accuracy of 1 mm.

Other studies can be performed with reconstructed tracks: the cell efficiency, or the study of the deviations of the space-time relationship from the linearity, are all sensitive to problems in the cell performance.

4 Conclusions

The studies described and other measurements related to the behaviour of the trigger electronics are performed at the assembly sites and at CERN, before and after the installation of the chambers in the CMS iron yoke, allowing to commission and calibrate the detector and to test the external electronics. In 2006 a combined acquisition test with cosmics, involving most of the CMS subdetectors, is foreseen in order to validate the CMS DAQ and trigger system and for alignment studies.

References

1. CMS Collaboration, The Muon Project. Technical Design Report, CERN/LHCC/97-32 (1997).
2. M.Aguilar-Benitez *et al.*, Nucl.Instr.Meth. A **480**, 658 (2002).
3. C.Albajar *et al.*, Nucl.Instr.Meth A **525**, 465 (2004).
4. P.Arce *et al.*, Nucl.Instr.Meth. A **534**, 441 (2004).

SESSION III – FLAVOUR PHYSICS AND CP VIOLATION

A. Stocchi	CKM overview
F. Ferroni	CP violation in B-physics
G. Isidori	New Physics in the Heavy Flavour Sector
I. Mikulec	Kaon physics: present and future
G. Mohanty	New hadron spectroscopy with Babar
J. Bauer	Rare Decays and Search for New Physics with Babar
C. Bloise	$\|V_{us}\|$ extraction from KLOE measurements

Frascati Physics Series Vol. XL (2006), pp. 105–112
Frontier Science 2005, New Frontiers in Subnuclear Physics
Milano, 12-16 September, 2005

CKM OVERVIEW*

UTfit Collaboration
M. Bona
Università di Torino and INFN, Italy
M. Ciuchini, V. Lubicz
Università di Roma Tre and INFN, Italy
E. Franco, G. Martinelli, L. Silvestrini
Dip. di Fisica, Università di Roma and INFN, Italy
F. Parodi, C. Schiavi
Università di Genova and INFN, Italy
M. Pierini
Department of Physics, University of Wisconsin, Madison, WI, USA
P. Roudeau, A. Stocchi
LAL, IN2P3-CNRS et Université de Paris-Sud, BP 34, Orsay
V. Vagnoni
INFN, Sez. di Bologna, Italy

Abstract

We review the status of the Unitarity Triangle in the Standard Model and beyond.

1 Introduction

Within the Standard Model (SM), all flavour and CP violating quark weak interactions are governed by the CKM matrix, which can be parameterized in terms of three angles and one phase, or, more conveniently, in terms of the parameters λ, A, $\bar{\rho}$ and $\bar{\eta}$. This implies very strong correlations among flavour and CP violating observables within the SM. The Unitarity Triangle (UT) is a very useful tool to analyze these correlations. With the recent data on B

*Talk given by A. Stocchi

to test the CKM mechanism within the SM and to derive constraints on New Physics (NP). In this talk, we will quickly review these two aspects. More details on the procedure and on the results can be found in ref. [1, 2] (results by other groups can be found in ref. [3]).

2 The SM UT analysis

The values and errors of the relevant quantities used in the standard analysis of the CKM parameters are summarized in Table 2. Additional inputs corresponding to the measurements of the angles γ and α can be found in ref. [4], while ref. [1] describes the procedure followed to extract these constraints from experimental data.

Parameter	Value	Gaussian	Uniform
λ	0.2258	0.0014	-
$\|V_{cb}\|$(excl.)	$41.4 \cdot 10^{-3}$	$2.1 \cdot 10^{-3}$	-
$\|V_{cb}\|$(incl.)	$41.6 \cdot 10^{-3}$	$0.7 \cdot 10^{-3}$	$0.6 \cdot 10^{-3}$
$\|V_{ub}\|$(excl.)	$38.0 \cdot 10^{-4}$	$2.7 \cdot 10^{-4}$	$4.7 \cdot 10^{-4}$
$\|V_{ub}\|$(incl.)	$43.9 \cdot 10^{-4}$	$2.0 \cdot 10^{-4}$	$2.7 \cdot 10^{-4}$
Δm_d	0.502 ps^{-1}	0.006 ps^{-1}	-
Δm_s	> 14.5 ps^{-1} @ 95% C.L.		
$f_{B_s}\sqrt{\hat{B}_{B_s}}$	276 MeV	38 MeV	-
ξ	1.24	0.04	0.06
$\hat{B}_K$	0.79	0.04	0.09
ε_K	$2.28 \cdot 10^{-3}$	$1.3 \cdot 10^{-5}$	-
f_K	159 MeV	fixed	
$\sin 2\beta$	0.687	0.032	-
$\overline{m}_t$	165.0 GeV	3.9 GeV	-
$\overline{m}_b$	4.21 GeV	0.08 GeV	-
$\overline{m}_c$	1.3 GeV	0.1 GeV	-
$\alpha_s(M_Z)$	0.119	0.003	-

Table 1: Values of the relevant quantities used in the UT fit.

The main novelty in the last two years in the UT analysis is the measurement of the angles of the UT at the B factories. While $\sin 2\beta$ is by now part of the "classic" fit, it is only recently that the measurements of the CP asymmetry in $B \to J/\psi K^*$ (of $B \to D^0 h^0$ decays) have provided a determination of

$\cos 2\beta$ (β). These determinations and the corresponding constraints on the $\bar{\rho}$ – $\bar{\eta}$ plane are shown in Fig. 1. It is evident how these additional measurements can suppress one of the two bands determined by $\sin 2\beta$.

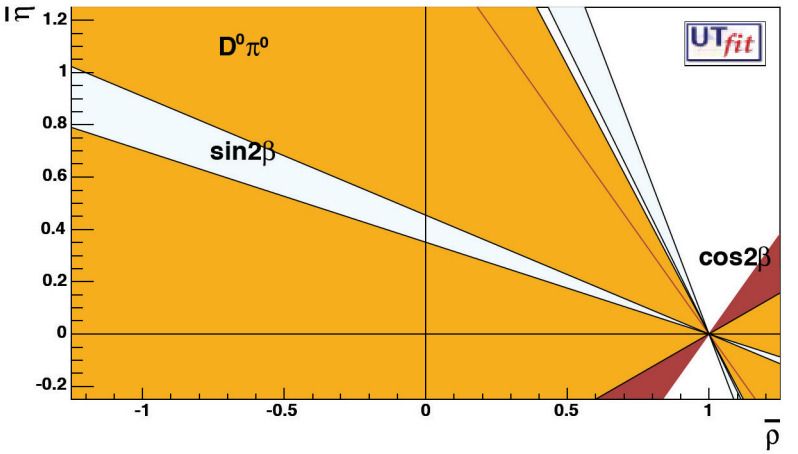

Figure 1: The regions in the $\bar{\rho}$ – $\bar{\eta}$ plane determined at 2σ probability by the measurements of $\cos 2\beta$ and β. For reference, the region selected by $\sin 2\beta$ is also reported.

The angle γ can be determined studying the interference of $b \to u$ and $b \to c$ transitions in $B \to D^{(*)}K^{(*)}$ decays, using the GLW, ADS or Dalitz methods. The resulting p.d.f. for γ is reported in Fig. 2.

Studying $B^0 \to D^{(*)}\pi(\rho)$ decays, it is possible to extract $\sin(2\beta+\gamma)$ from the time-dependent CP asymmetries. However, present data are insufficient to allow this determination, so that additional input is needed. This can come from SU(3)-related $B \to D_s$ channels, if one neglects annihilation contributions. The total theoretical error in this procedure can be estimated around 100%. Including this error, we obtain the constraint on $\sin(2\beta+\gamma)$ shown in Fig. 3, together with the impact on the $\bar{\rho}$ – $\bar{\eta}$ plane.

The angle α can be extracted from the time-dependent CP asymmetry in $B \to \pi\pi$, $\rho\pi$, $\rho\rho$ decays, with the uncertainty related to penguin pollution. Given the presently unclear experimental situation and the large penguin pollution, we do not consider here $B \to \pi\pi$ decays. The determination of α from the other modes using the BaBar data and the corresponding constraint on the $\bar{\rho}$ – $\bar{\eta}$ plane are reported in Fig. 4.

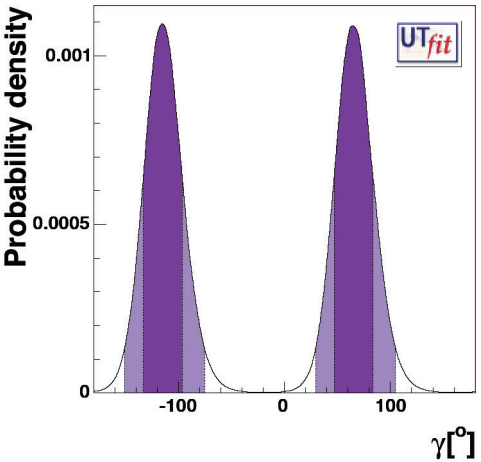

Figure 2: P.d.f. for γ using all available information.

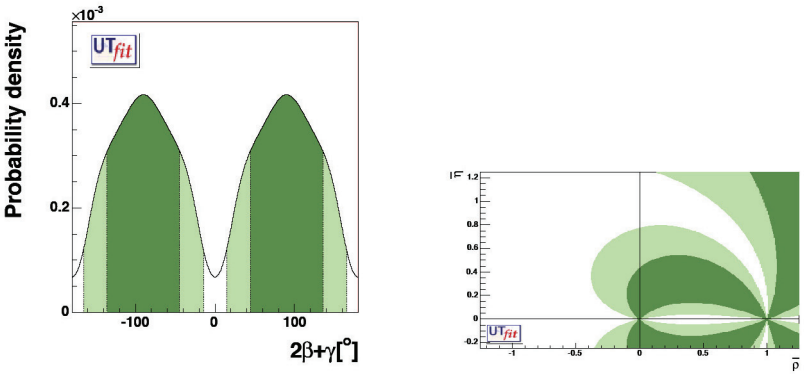

Figure 3: P.d.f. for $2\beta + \gamma$ and its impact on the $\bar{\rho} - \bar{\eta}$ plane.

Using the angle measurements described above, it is possible to obtain a determination of the UT with an accuracy comparable to the determination obtained using all the other measurements (see Fig. 5). The UT fit is therefore now strongly overconstrained, and it tests in a highly nontrivial way the CKM

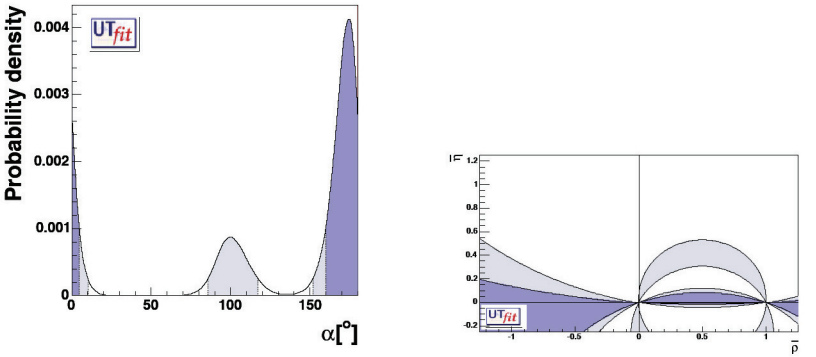

Figure 4: P.d.f. for α and its impact on the $\bar{\rho} - \bar{\eta}$ plane.

picture of flavour and CP violation.

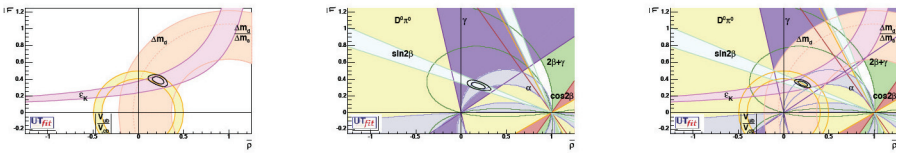

Figure 5: Determinations of the UT without using angle measurements (left), using only angles (middle) and using all information (right).

Combining all available information, we obtain the "state of the art" determination in Fig. 5, and the results for UT parameters reported in Table 2. Comparing the results of the fit with the input values, there is a small ($< 2\sigma$) discrepancy in the values of $\sin 2\beta$ and $|V_{ub}|$ from inclusive decays.

3 Constraints on NP from the UT

We remarked in the previous section that the UT fit is now strongly over-constrained. It is therefore possible to add NP contributions to all quantities entering the UT analysis and to perform a combined fit of NP contributions and SM parameters. In general, NP models introduce a large number of new parameters: flavour changing couplings, short distance coefficients and matrix

Table 2: Values and probability ranges for the UT parameters obtained from the UT fit using all constraints.

	68%	95%
$\bar{\rho}$	0.208 ± 0.036	$[0.135, 0.277]$
$\bar{\eta}$	0.347 ± 0.021	$[0.306, 0.388]$
$\alpha[^\circ]$	97.1 ± 5.6	$[86.0, 107.7]$
$\beta[^\circ]$	23.8 ± 1.4	$[21.3, 26.2]$
$\gamma[^\circ]$	58.9 ± 5.4	$[48.7, 69.9]$
$\sin 2\beta$	0.736 ± 0.023	$[0.690, 0.781]$
$\lvert V_{ub}\rvert$ $[10^{-4}]$	38.5 ± 1.4	$[35.7, 41.4]$

elements of new local operators. The specific list and the actual values of these parameters can only be determined within a given model. Nevertheless, each of the meson-antimeson mixing processeses is described by a single amplitude and can be parameterized, without loss of generality, in terms of two parameters, which quantify the difference between the full amplitude snd the SM one. Thus, for instance, in the case of $B_q^0 - \bar{B}_q^0$ mixing we define

$$C_{B_q}\, e^{2i\phi_{B_q}} = \frac{\langle B_q^0 | H_{\rm eff}^{\rm full} | \bar{B}_q^0 \rangle}{\langle B_q^0 | H_{\rm eff}^{\rm SM} | \bar{B}_q^0 \rangle}\,, \ (q = d, s) \tag{1}$$

where $H_{\rm eff}^{\rm SM}$ includes only the SM box diagrams, while $H_{\rm eff}^{\rm full}$ includes also the NP contributions. As far as the $K^0 - \bar{K}^0$ mixing is concerned, we find it convenient to introduce a single parameter C_{ϵ_K} which relates the imaginary part of the amplitude to the SM one. Therefore, all NP effects in $\Delta F = 2$ transitions are parameterized in terms of three real quantities, C_{B_d}, ϕ_{B_d} and C_{ϵ_K}. NP in the B_s sector is not considered, due to the lack of experimental information, since both Δm_s and $A_{\rm CP}(B_s \to J/\psi\phi)$ are not yet measured.

NP effects in $\Delta B = 1$ transitions can also affect some of the measurements entering the UT analysis, in particular the measurements of α and of the semileptonic asymmetry $A_{\rm SL}$ [2]. However, under the hypothesis that NP contributions are mainly $\Delta I = 1/2$, their effect can be taken into account in the fit of the $B \to \pi\pi, \rho\pi, \rho\rho$ decay amplitudes. Concerning $A_{\rm SL}$, penguins only enter at the Next-to-Leading order and therefore NP in $\Delta B = 1$ transitions produces subdominant effects with respect to the leading $\Delta B = 2$ contribution.

The results obtained in a global fit for C_{B_d}, C_{ϵ_K}, C_{B_d} vs. ϕ_{B_d}, and γ vs. ϕ_{B_d} are shown in Fig. 6, together with the corresponding regions in the $\bar{\rho}$–$\bar{\eta}$

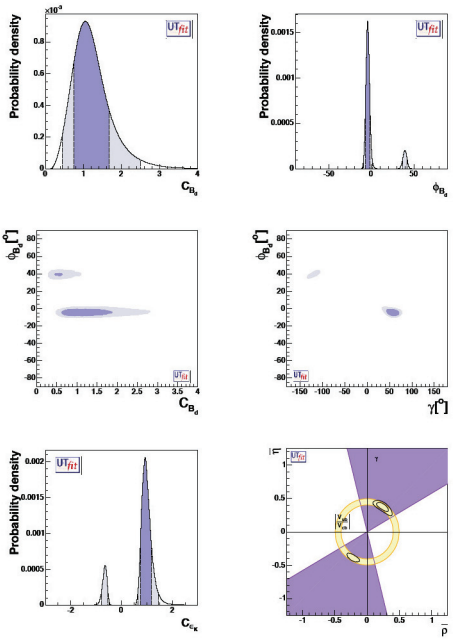

Figure 6: From top to bottom and from left to right, p.d.f.'s for C_{B_d}, ϕ_{B_d}, ϕ_{B_d} *vs.* C_{B_d}, ϕ_{B_d} *vs.* γ, C_{ϵ_K} and the selected region on the $\bar{\rho}-\bar{\eta}$ plane obtained from the NP analysis. In the last plot, selected regions corresponding to 68% and 95% probability are shown, together with 95% probability regions for γ (from DK final states) and $|V_{ub}/V_{cb}|$. Dark (light) areas correspond to the 68% (95%) probability region.

plane [2)]. The constraints on C_{B_d} and ϕ_{B_d} can be translated into bounds on the amplitude and phase of the NP contribution, writing

$$C_{B_d} e^{2i\phi_{B_d}} = \frac{A_{\rm SM} e^{2i\beta} + A_{\rm NP} e^{2i(\beta+\phi_{\rm NP})}}{A_{\rm SM} e^{2i\beta}}\,, \tag{2}$$

The result is reported in Fig. 7. We see that the NP contribution can be substantial if its phase is close to the SM phase, while for arbitrary phases its magnitude has to be much smaller than the SM one. Notice that, with the latest data, the SM ($\phi_{B_d} = 0$) is disfavoured at 68% probability due to the disagreement in the SM fit discussed in the previous section. This requires $A_{\rm NP} \neq 0$ and $\phi_{\rm NP} \neq 0$. For the same reason, $\phi_{\rm NP} > 90°$ at 68% probability and the plot is not symmetric around $\phi_{\rm NP} = 90°$.

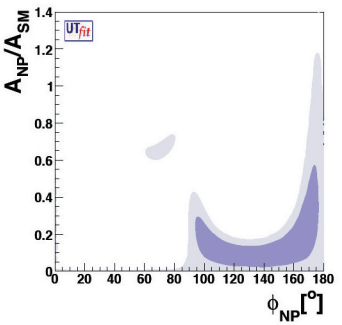

Figure 7: P.d.f. in the $(A_{\rm NP}/A_{\rm SM})$ vs. $\phi_{\rm NP}$ plane for NP in the $|\Delta B| = 2$ sector (see Eq. (2)).

Assuming that the small but non-vanishing value for ϕ_{B_d} we obtained is just due to a statistical fluctuation, the result of our analysis points either towards models with no new source of flavour and CP violation beyond the ones present in the SM (Minimal Flavour Violation, MFV [5]), or towards models in which new sources of flavour and CP violation are only present in $b \to s$ transitions. The UT determination and rare decays in MFV models have been recently discussed in refs. [2, 6].

References

1. M. Bona *et al.* [UTfit Collaboration], JHEP **0507** (2005) 028; `www.utfit.org`.

2. M. Bona *et al.* [UTfit Collaboration], arXiv:hep-ph/0509219.

3. J. Charles *et al.* [CKMfitter Group], Eur. Phys. J. C **41** (2005) 1; Z. Ligeti, arXiv:hep-ph/0408267; F. J. Botella *et al.*, Nucl. Phys. B **725** (2005) 155; K. Agashe *et al.*, arXiv:hep-ph/0509117.

4. The Heavy Flavour Averaging Group, summer 2005 averages.

5. E. Gabrielli and G. F. Giudice, Nucl. Phys. B **433** (1995) 3 [Erratum-ibid. B **507** (1997) 549]; G. D'Ambrosio *et al.*, Nucl. Phys. B **645** (2002) 155; A. J. Buras *et al.*, Phys. Lett. B **500** (2001) 161.

6. C. Bobeth *et al.*, Nucl. Phys. B **726** (2005) 252.

Frascati Physics Series Vol. XL (2006), pp. 113–122
Frontier Science 2005, New Frontiers in Subnuclear Physics
Milano, 12-16 September, 2005

CP VIOLATION IN B-PHYSICS

Fernando Ferroni
Università di Roma La Sapienza & INFN Roma,

Abstract

The two competing B-factories (KEKB and PEPII) are performing spectacularly well and the experiments they host (Belle and BaBar) have harvested an impressive amount of data. CP violation in B-physics has been established and it has become a precision measurement.

1 Introduction

The mystery of our existence is based on the premise that although our theory of fundamental sub-atomic particle interactions (the Standard Model) places matter and anti-matter at nearly equal footing, our Universe appears to be composed of matter only. Indeed the Standard Model accounts for small differences in the interactions of matter and anti-matter through a phenomena known as CP violation. This difference however falls short, by orders of magnitude,

in accounting for the observed matter asymmetry in the Universe. Therefore investigations of the matter/anti-matter asymmetries it is of vital importance for the possible understanding of what could exist beyond the Standard Model. Two powerful particle accelerators, KEKB [1)] and PEPII [2)] were built to study CP violation in the B meson decays. B-physics has some distinct advantage over K-physics for studying CP violation. Indeed the asymmetries expected in some decay channel of the B-mesons can be very large. The amount of CP violation in the theoretical framework of the Standard Model is fixed by the area of the unitary triangle ($O(10^{-6})$) and therefore, with the caveat of choosing rather rare decays, the ratio of the difference of the decay width with their sum can easily be of ($O(1)$). Better that any word the following figure (Fig. 1), showing the direct CP asimmetry observed in the decay of $B^0 \to K^+\pi^-$ makes the case.

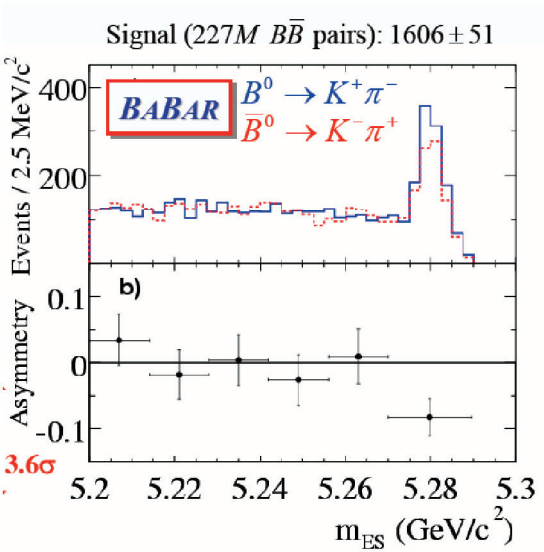

Figure 1: *Difference (above) and asymmetry (below) in the decay of B^0 and its antiparticle in $K\pi$.*

The requirement of studying rare decays calls for accelerators producing a lot of B-mesons. The ideal environment is found at an e^+e^- collider running at the center of mass energy of the Y(4S) resonance with a luminosity much in excess of 10^{33} cm^{-2} s^{-1}. One peculiarity of the game is that the CP asymmetry

cannot be integrated over the decay time due to the coherent nature of the Y(4S) state. This means in practice that one shall measure the time dependence of the decay asymmetry or in more experimental language the knowledge of the position of the decay vertices of the two B-meson is needed. The two vertices are in average separated by one lifetime and if the collision were to happen in a conventional collider the value would be of some tens of micron, too little to be measured precisely enough. The solution is in building an energy asymmetric collider [3] where one can create a boost ($O(0.5)$) that brings the separation to some hundreds of micron, a measure easily accessible to silicon vertex detectors performances.

2 CP Violation in Standard Model

In the three generation Standard Model the coupling between the quarks is described by the CKM matrix [4]. The unitarity of the CKM matrix implies definite relations between its elements. Three of these relations requires the sum of three complex quantities to vanish so that they can be geometrically represented in the complex plane as a triangle. The most exciting physics lies in the third of them, the so-called B_d-physics triangle (Fig. 2).

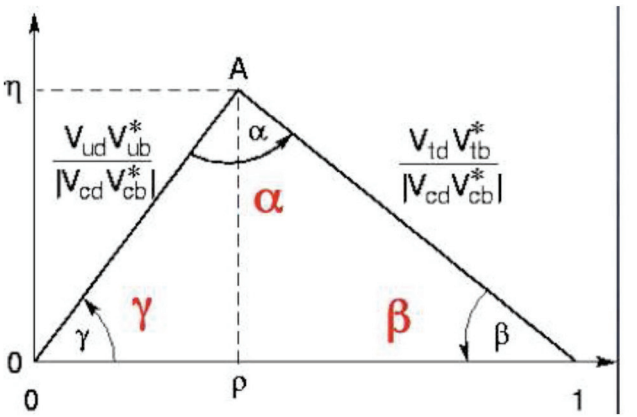

Figure 2: *The unitary triangle for the B_d physics.*

The name of the game is to measure all the three angles β, α, γ also known as ϕ_1, ϕ_2, ϕ_3 and show that their sum makes up to π. The challenge is in finding the processes that are interpretable in terms of theory prediction. The possi-

ble manifestations of CP violation can be classified in a model-independent way: CP violation in decay, which occurs in both charged and neutral decays, when the amplitude for a decay and its CP conjugate process have different magnitudes; CP violation in mixing, which occurs when the two neutral mass eigenstates cannot be chosen to be CP eigenstates; CP violation in the interference between decays with and without mixing, which occurs in decays into final states that are common to B^0 and $\overline{B}^0$. It often occurs in combination with the other two types but, important for B-factories physics, there are cases when, to an excellent approximation, it is the only effect. The best opportunities are found in the processes of the third type. The reference mode for measuring CP violation in B-physics has been identified since long time It is properly called the golden channel [5] . It is the decay $B^0 \to J/\Psi K^0$. The reason is that in this decay the mixing, mediated by V_{td} , carries the phase β while the decay mediated by V_{cb} is real, ending up in an effect proportional to $sin2\beta$. The non-tree amplitudes are tiny and however they carry the same weak phase. This channel is not only theoretically golden but also experimentally accessible in a rather easy way.

3 Colliders, experiments and technique of the measurement

The machines that have been built to accept the challenge posed by this fundamental measurement are KEKB in Tsukuba (Japan) and PEPII at SLAC (USA). Their asymmetric energy configuration matches the request and their performance in term of luminosity has been just extraordinary. KEKB has reached in terms of instantaneous luminosity the value of 1.5×10^{34} cm^{-2} s^{-1} and has delivered to its experiment 450 fb^{-1} of integrated luminosity corresponding to roughly a billion B decays (250 fb^{-1} for PEPII). BaBar [6] and Belle [7] are two classic style e^+e^- detectors. Their structure is pretty similar. From inside out they exhibit a Silicon Vertex Detector followed by a low mass Drift Chamber for tracking charged particles, a Cerenkov system for telling kaons from pions, and a CsI crystal electro-magnetic calorimeter. These detectors are immersed in a solenoidal field (1.5 T) provided by a superconducting magnet. Beyond the solenoid and interspersed in the iron of the return yoke resistive proportional chambers help in discriminating muons from hadrons and provide a determination of the impact point of neutral hadrons. A measurement of ACP requires the reconstruction of a BCP decay like $B^0 \to J/\Psi K^0$;

the determination of the experimental $\Delta t(z)$ resolution. Typical Δz resolution from data is 180 μm dominated by the tag B; the assignment of the B flavor to the CP decay and the fraction of events in which the tag assignment is incorrect. The effective efficiency of the tagging algorithm is of the order of 30%.

4 The physics programme and results

The physics programme as evolved with the experience of the couple of years of run and the billion of B-decays analyzed can be summarized as follows:

- precision measurement of the angle β in the charmonium modes
- alternative measurement of the same angle in the $b \to ss\overline{s}$ decays where the tree diagram is more or less absent, the amplitude is dominated by penguin diagrams that carry the phase β and where the possible presence of loops of new virtual particles (i.e. SUSY) would change the weak phase revealing evidence of New Physics beyond the Standard Model
- measurement of the angle α in the charmless two body decays
- measurement of the angle γ in a variety of modes, the most promising of all relying in a Dalitz analysis of the $B^+ \to D^0 K^+ (D^0 \to K_S \pi^+ \pi^-)$ decay

4.1 sin2β in charmonium modes

The measurement has become very precise, the world average is at the time of this workshop: $sin2\beta_{exp} = 0.685 \pm 0.032$ (5%). The prediction from the analysis of the unitary triangle is: $sin2\beta_{pre} = 0.734 \pm 0.024$. Excellent agreement that confirms the invincibility of the Standard Model.

4.2 sin2β in penguin modes

The prototype of this kind of modes is $B \to \Phi K^0$. It is a penguin diagram with the dominant contribution coming from the top loop. The dominant phase of the decay is V_{ts} (real) so that the expected CP violation phase is the one from the mixing leading to β. It is clear though that in case SUSY particles would mind to circulate in the loop they could bring a different phase. So

the comparison between the value of $sin2\beta$ measured in this mode with the one obtained in charmonium modes could show the presence of new particles not yet discovered. There are many modes that can be used for this test with some caveat. They are not all theoretically clean at the same level. It is rather arbitrary therefore to take their average for eventually enhancing the significance of an effect. It is however suggestive that the ones so far measured, systematically indicate a value of $sin2\beta$ somewhat lower than expected. The following figure (Fig. 3) shows the compilation [8] of the results for several modes Not much can be said at this moment except that a significant increase of statistics would be desirable.

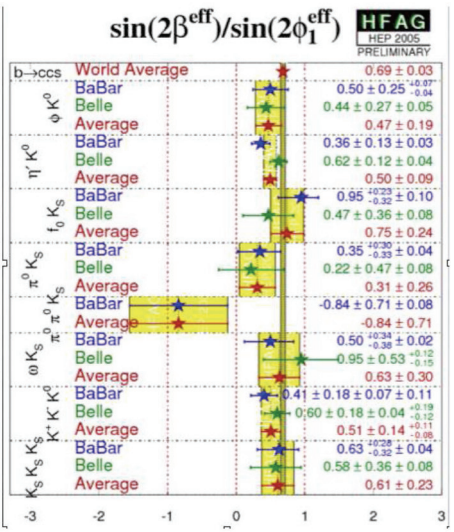

Figure 3: *$sin2\beta$ as determined in various $b \to s\bar{s}$ penguin dominated channels with respect to to the value obtained in charmonium modes.*

4.3 sin2α in charmless two-body decays

The decay of B-mesons in charmless two body decays is the key for the measurement of the angle α. Indeed the mixing provide the phase β and the V_{ub} transition add the phase γ bringing to $\alpha = \pi - (\beta + \gamma)$. This would be absolutely true only if the decay were dominated by the tree diagram. Unfortunately at

least in the simpler of all the charmless two body decays ($B \to \pi\pi$) it is observed an important, if not dominant, contribution of a penguin decay that brings a different weak phase. The solution in case of large statistics is known. It consists in a isospin analysis [9] making use of all the three $B \to \pi\pi$ decay amplitudes. This analysis however requires one of the following conditions to be verified to be carried out safely : the three sides are of the same order of magnitude and the statistics is large; the 00 amplitude is very small so that the triangle effectively collapses. In the case of $B \to \pi\pi$ neither of the conditions is verified since statistics is limited and the 00 amplitude is sizeable. The way out is found in the $B \to \rho\rho$ decay. Here the 00 amplitude, for which only un upper limit has been determined, results to be at least 30 times smaller than the $+-$ one. The triangle is therefore very squashed and the difference between the value of $sin2\alpha$ determined (effective) and the true one is small. The combined value [9] obtained by BaBar and Belle is $\alpha = (99^{+12}_{-9})^\circ$ where the last error also reflects the conservative estimate of the yet unknown contribution of the penguin amplitude. It is even more precise than the value obtained by the global fit to unitary triangle. The most precise result is due to $B \to \rho\rho$. However the $B \to \rho\pi$ channel is crucial in resolving the ambiguity. Very modest indeed is the contribution of $B \to \pi\pi$.

4.4 γ in $B^+ \to D^0 K^+$

The difficulty in measuring this angle at the B-factories comes from the problem that when using the B^0 decays you cannot get rid of the mixing phase β. Indeed this means that one shall move to the charged B decays occurring via the $b \to u$ transitions whose phase is indeed γ. Here however, at first glance the necessary interference between two diagrams leading to the same final state cannot take place. There are several possibilities that have been pointed out for circumventing this problem. Here we discuss the results obtained by exploiting the most promising [10] of all methods discovered so far. The basic idea is of making use of the interference between the two diagrams (one Cabibbo favoured and the other Cabibbo suppressed) that leads to the same final state $B^+ \to (K_S\pi^+\pi^-)K^+$. In the more than reasonable assumption that the $D^0 \to K_S\pi^+\pi^-$is dominated by quasi-two body amplitudes a simultaneous fit to $D^0 \to K_S\pi^+\pi^-$ Dalitz plots of B^+ and B^- data yields three parameters (r, γ, δ), respectively the amount of Cabibbo suppression, the

angle γ of the unitary triangle and the strong phase. The results [11] obtained by the two experiments for a few different modes are shown below:

	Modes	r	δ (°)	ϕ_3 (°)
BaBar	DK	$0.118 \pm 0.079 \pm 0.034^{+0.036}_{-0.034}$	$104 \pm 45^{+17\ +16}_{-21\ -24}$	
	D^*K	$0.169 \pm 0.096^{+0.030\ +0.029}_{-0.028\ -0.026}$	$296 \pm 41^{+14}_{-12} \pm 15$	
	combined			$70 \pm 31^{+12\ +14}_{-10\ -11}$
Belle	DK	$0.21 \pm 0.08 \pm 0.03 \pm 0.04$	$157 \pm 19 \pm 11 \pm 21$	
	D^*K	$0.12^{+0.16}_{-0.11} \pm 0.02 \pm 0.04$	$321 \pm 57 \pm 11 \pm 21$	
	combined			$68^{+14}_{-15} \pm 13 \pm 11$
	DK^*	$0.25^{+0.17}_{-0.18} \pm 0.09 \pm 0.04 \pm 0.08$	$358 \pm 35 \pm 8 \pm 21 \pm 49$	$112 \pm 35 \pm 9 \pm 11 \pm 8$

Figure 4: r, γ, δ

4.5 Status of the unitary triangle

The fit technology to the unitary triangle is a consolidated art by now. Two different approaches [9, 12] exist. They differ in the statistical methodology (frequentist vs. Bayesian) and in the choice of some either experimental or theoretical (lattice computation) result. The final value of the coordinates of the triangle apex (i.e. the amount of CP violation in the Standard Model) are however very close by. The complete analysis yield the impressive graphical result shown in Fig. 5. The value of the apex coordinates $\overline{\rho}, \overline{\eta}$) are:

$\overline{\rho} = 0.216 \pm 0.036\ \overline{\eta} = 0.342 \pm 0.022$.

CP-violation in B-physics exists and it is compatible with the Standard Model interpretation.

5 Conclusions

The primary goal of the B-factories has been achieved. The violation of the CP symmetry has been observed in the B system. The measurement of the angle β of the unitary triangle has reached a precision level. This allows to say that the CP violation observed both in K-physics and B-physics belongs to the all mighty Standard Model of the Electroweak Interactions. The long march to the measurement of the other two angles has started. The most promising methodologies have been already identified, statistics is the sole issue. The hunt to α) has already yielded a significant result. The angle γ that was not even considered in the initial program of the experiments has also been measured although not so precisely. The final hope is still to find a deviation between the

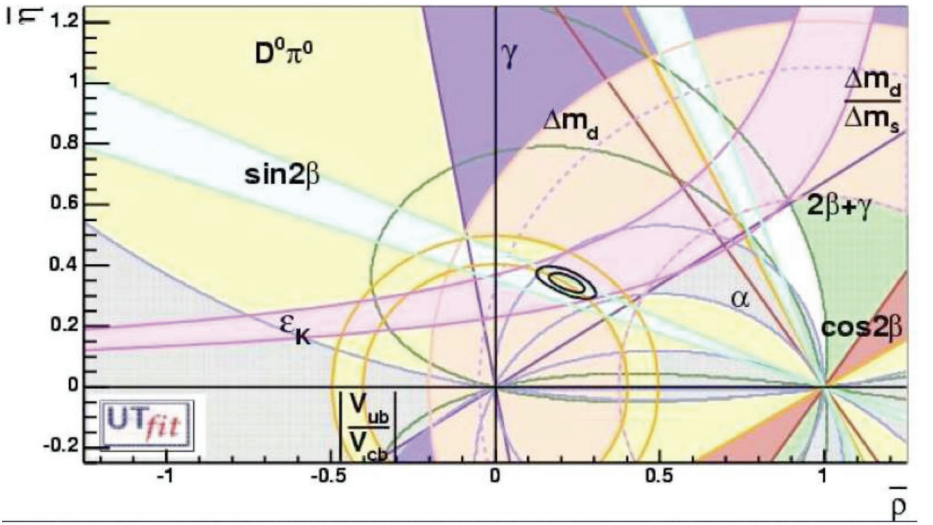

Figure 5: *Constraint on the apex of the unitary triangle as obtained by fitting all the experimental available results as well as the lattice simulations.*

observed and predicted quantities that points to some exciting New Physics beyond the Standard Model. This might be achievable during the life span of the existing B-factories that will eventually integrate of the order of 1-2 ab^{-1} each till the completion of their cycle foreseen for the end of the decade. The relay will then be hopefully taken both by a Super B-factory with a luminosity improved by a factor 20-50 with respect to now and an hadronic experiment (LHCb) that will disclose the doors of the Bs physics.

References

1. S. Kurokawa and E. Kikutani, Nucl. Instr. and Meth., **A499**, 1 (2003)
2. PEPII- An asymmetric B Factory, Conceptual Design Report, SLAC-418, LBL-5379, 1993.
3. A. Garren *et al*, IEEE Part. Accel. 1847 (1989).
4. N. Cabibbo, Phys. Rev. Letters., **10**, 531 (1966);
   M.Kobayashi and T. Maskawa, Progr. Theo. Physics, **49**, 652 (1973) .

5. A.B. Carter and A.I. Sanda, Phys. Rev. , **D23**, 1567 (1981); I.I. Bigi and A.I. Sanda, Nucl. Phys., **B193**, 85 (1981) .

6. B. Aubert *et al*, Nucl. Instr. and Meth., **A479**, 1 (2002)

7. A. Abashian *et al*, Nucl. Instr. and Meth., **A479**, 117 (2002)

8. http://www.slac.stanford.edu/xorg/hfag/

9. http://ckmfitter.in2p3.fr/

10. A. Giri *et al*, Phys. Rev. **D68**, 054018 (2003).

11. http://belle.kek.jp/belle/talks/LP05/Abe.pdf

12. http://utfit.roma1.infn.it/

Frascati Physics Series Vol. XL (2006), pp. 123
Frontier Science 2005, New Frontiers in Subnuclear Physics
Milano, 12-16 September, 2005

NEW PHYSICS IN THE HEAVY FLAVOUR SECTOR

G. Isidori
INFN-LNF, Frascati, Italy

Written contribution not received

Frascati Physics Series Vol. XL (2006), pp. 125–136
Frontier Science 2005, New Frontiers in Subnuclear Physics
Milano, 12-16 September, 2005

KAON PHYSICS: PRESENT AND FUTURE

Ivan Mikulec
Österreichische Akademie de Wissenschaften,
Institut für Hochenergiephysik, Nikolsdorfergasse 18, A-1050 Wien, Austria

Abstract

The most recent progress and future prospects in kaon physics are reviewed.

1 Introduction

The observation and understanding of kaon decays has been crucial for the progress in the theory of particle physics, especially for the Standard Model (SM). The first observation of the decay $K_L \to \pi^+\pi^-$ by Christenson, Cronin, Fitch and Turlay 41 years ago [1] has shown for the first time that the CP symmetry is violated in nature and guided Kobayashi and Maskawa, a decade later, to introduce a third quark family into their quark mixing scheme [2]. Low decay rates observed in the decay $K_L \to \mu^+\mu^-$, lead to the discovery of the GIM mechanism [3] and to the prediction of the charm quark. A few years ago, the direct violation of the CP symmetry in the decay amplitude, predicted by the Standard Model and first observed by NA31 with 3σ evidence [4], has been

firmly established by NA48 [5, 6] and KTeV [7]. At present, the field of kaon physics still provides exciting results.

2 V_{us} and related topics

The 2002 edition of PDG has revealed a slight deviation from the unitarity in the first row of the CKM matrix [8]. The expression $|V_{us}|^2 + |V_{ud}|^2 + |V_{ub}|^2$, where the V_{ub} is negligible, deviated from unity by 2.2 standard deviations. Both V_{us} and V_{ud} contribute with similar uncertainties.

This apparent discrepancy triggered an avalanche of experimental and theoretical results, especially concerning V_{us}. The most precise way of extracting the coupling V_{us} is by measuring the decay rate of the semileptonic kaon decay decay $K \to \pi l \nu$ (K_{l3}) and using the relation:

$$\Gamma(K_{l3}) \sim |V_{us}|^2 f_+^2(0) I_K^l (1 + \delta_{rad}^l) \tag{1}$$

where $f_+(0)$ is the form factor normalisation, I_K^l is the phase space integral and δ_{rad}^l represents the radiative corrections. More explicit formulae can be found elsewhere [8, 9, 10]. $\Gamma(K_{l3})$ and I_K^l are measured experimentally, while $f_+(0)$ and δ_{rad}^l are calculated by theorists. New developments in all four components have been made recently.

The experiment KTeV at Fermilab has published recently a set of measurements of all the main K_L decay modes [11]. The ratios are chosen such that a large part of the systematic effects, like e.g. trigger or detector efficiencies, cancel. Using the five ratios all main six K_L branching ratios can be extracted. All ratios involving the $K_L \to \pi e \nu$ (K_{e3}) decay disagree by several standard deviations from the 2004 world averages [12]. These results have been confirmed by new measurements from NA48 at CERN [13] and KLOE at Frascati [14]. Another contribution from the KLOE experiment to the extraction of the $|V_{us}|$ from K_L decays was an improved measurement of the K_L lifetime. Combining their results from two different methods, a direct measurement from the exponential decay distribution [15] and an indirect measurement by summing main branching fractions [14], one obtains $\tau_{KS} = (50.84 \pm 0.23) ns$. Working at the ϕ-factory DAPHNE, KLOE exploits the unique possibility to access K_S decay modes which, in fixed target experiments, would be flooded by K_L background, by tagging the opposite K_L in $\phi \to K_S K_L$ decays. KLOE's competitive measurement of $|V_{us}|$ from the $K_S \to \pi e \nu$ branching fraction [16]

is in a good agreement with K_L results. New measurements of semileptonic decays of charged kaons reported by ISTRA+ at Protvino [17] and NA48/2 [18] confirmed an earlier result by E865 at BNL [19] which was also in disagreement with PDG. The measurements of form-factor shapes, needed to extract the phase space integral in Equation 1, by these experiments agree in general with each other in the linear term while quadratic fits are less consistent.

Using all recent results a new experimental value of $|V_{us}|f_+(0) = 2.2173 \pm 0.0008$ can be extracted. This value is in agreement with unitarity if one is considering the original calculation of $f_+(0)$ by Leutwyler and Roos based on Chiral Perturbation Theory [20] or newer quenched lattice calculations [21]. On the other hand, estimates of higher order terms in Chiral Perturbation Theory [9, 22] lead to a less consistent unitarity test. New unquenched lattice calculation are expected to improve theoretical precision and clarify the situation.

3 CP violation

The decay $K_S \to \pi^0\pi^0\pi^0$ is purely CP-violating and is, up to now, unobserved. The CP-violation parameter $\eta_{000} \equiv A(K_S \to \pi^0\pi^0\pi^0)/A(K_L \to \pi^0\pi^0\pi^0)$ is proportional to the expression $\varepsilon + iImA_1/ReA_1$, where ε is the parameter of indirect CP violation in the kaon system and A_1 is the isospin $I = 1$ decay amplitude. The imaginary part of η_{000} is in principle sensitive to direct CP violation [12].

In a recently published paper, NA48 searches for the decay $K_S \to \pi^0\pi^0\pi^0$ by exploring the interference between K_S and K_L and fitting the decay distribution of the data taken during the special near-target run in the year 2000. The result [23] $Re\eta_{000} = -0.002 \pm 0.019, Im\eta_{000} = -0.003 \pm 0.021$ represents an order of magnitude improvement with respect to previous results. This can be translated to $BR(K_S \to \pi^0\pi^0\pi^0) < 7.4 \times 10^{-7}$ (at 90% CL) which is more than an order of magnitude better than the previously published limit but it is still two orders of magnitude above the SM expectation. Using the Bell-Steinberger [24] relation and other measured kaon CP-violating decay amplitudes one can extract a limit on the mass difference $m_{K^0} - m_{\overline{K^0}} < 4.7 \times 10^{-19}$ GeV/c^2 (at 90% CL) which is a precise test of the CPT symmetry.

Similar results have been recently published by the KLOE collaboration on a direct search for the $K_S \to \pi^0\pi^0\pi^0$ decay. Their observation of 2 events

with 3.0±0.8 events of expected background pushes further the limit $BR(K_S \to \pi^0\pi^0\pi^0) < 2.1 \times 10^{-7}$ at 90% CL or $|\eta_{000}| < 0.018$ [25]. New data from KLOE promise to improve these limits by another order of magnitude in the future.

Using their newly measured branching fractions of all main K_L decays, KTeV collaboration obtained also a more precise measurement of the CP-violating parameter $|\eta_{+-}|$. In reference [11] KTeV obtains $|\eta_{+-}| = (2.228 \pm 0.005_{KTeV} \pm 0.009_{\tau_{KL}}) \times 10^{-3}$. Using the new measurement of τ_{KL} by KLOE [15] one obtains $|\eta_{+-}| = (2.239 \pm 0.009) \times 10^{-3}$. Both results differ significantly from the 2004 world average [12].

New searches for direct CP-violation are under way in the decays of charged kaons. The second extension of the NA48 experiment, NA48/2 [26], uses simultaneous K^+ and K^- beams to measure the asymmetry in the Dalitz plot slope parameter g

$$A_g \equiv \frac{g(K^+ \to \pi\pi\pi) - g(K^- \to \pi\pi\pi)}{g(K^+ \to \pi\pi\pi) + g(K^- \to \pi\pi\pi)} \tag{2}$$

More than 3 billion $K^\pm \to \pi^\pm\pi^+\pi^-$ and more than hundred million of $K^\pm \to \pi^\pm\pi^0\pi^0$ have been collected in years 2003 and 2004. This will allow NA48/2 to measure A_g to a level below 2×10^{-4}, which is an order of magnitude better than previous experiments [27]. The theoretical predictions within SM vary between -5×10^{-5} and 5×10^{-5} [28], while enhancements to the level of 10^{-4} are predicted by models beyond SM [29]. The first preliminary results based on 2003 data have been presented by NA48/2 this year. In the $K^\pm \to \pi^\pm\pi^+\pi^-$ decay mode $A_g = (0.5 \pm 3.8) \times 10^{-4}$ [30] and in the $K^\pm \to \pi^\pm\pi^0\pi^0$ mode $A_g^0 = (1.7 \pm 2.4) \times 10^{-4}$ [31].

4 Tests of low energy QCD

Large sample of $K^\pm \to \pi^\pm\pi^0\pi^0$ decays collected by the NA48/2 experiment in the search for direct CP violation in charged kaon decays revealed a previously unobserved anomaly in the invariant $\pi^0\pi^0$ mass distribution (Figure 1). It has been shown by Cabibbo [32] that this effect is mainly due to charge exchange scattering process $\pi^+\pi^- \to \pi^0\pi^0$ and can be used for a precise determination of $a_0 - a_2$. This difference between the $\pi\pi$ scattering lengths of the isospin $I = 0$ and $I = 2$ states is one of the most precisely predicted quantities by Chiral Perturbation Theory: $(a_0 - a_2) = 0.265 \pm 0.004$ [33].

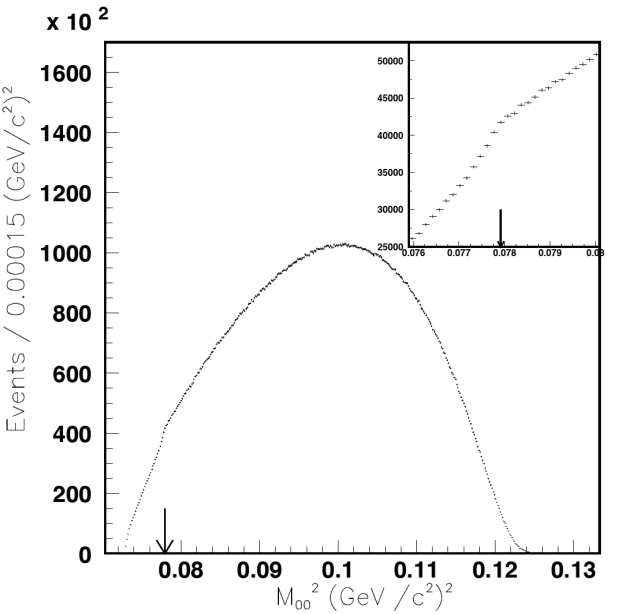

Figure 1: *Distribution of the* $\pi^0\pi^0$ *invariant mass squared from* $23 \times 10^6 K^{\pm} \to \pi^{\pm}\pi^0\pi^0$ *decays by NA48/2 with the enlarged region around the* $(2m_{\pi^+})^2$.

A fit to an improved rescattering model [34] which includes second order loops, corrected for isospin symmetry breaking, recently published by NA48/2, gives $(a_0 - a_2) = 0.264 \pm 0.006_{stat} \pm 0.004_{syst} \pm 0.013_{ext}$ [35]. This result, based only on a part of the total NA48/2 statistics, agrees well with theoretical prediction and shows the potential of this new method to test the Chiral Perturbation Theory. An improvement in the external uncertainty can be achieved by extending the underlying rescattering model to higher order loops.

5 Very rare decays

In the quest for New Physics (NP), the searches for SM-forbidden kaon decays, in particular those which violate the lepton flavor, are ceding territory to measurements in the quark flavor sector. GIM-suppressed one-loop FCNC (Flavor-Changing Neutral Current) processes are very sensitive to additional

flavor structure with up to an order of magnitude enhancements with respect to SM decay rates predicted by various NP models [36, 37, 38].

There are two classes of these decays (Fig. 2):

- Pure FCNC decays: $K_L \to \pi^0\nu\overline{\nu}$ and $K^+ \to \pi^+\nu\overline{\nu}$. These decays are fully dominated by short-distance dynamics which can be calculated perturbatively. The hadronic matrix element can be obtained from the well measured $K^+ \to \pi^0 e^+\nu$ decay. This leads to an extremely precise (to few %) relation between decay rates and the combination of CKM matrix elements $\lambda_t = V_{ts}^* V_{td}$. This level of theoretical cleanness in the constraints to the CKM unitarity triangle is only matched by the CP asymmetry in $B \to J/\psi K_S$. Unfortunately, from the experimental point of view these decays are very challenging.

- Decays with both short-distance and long-distance contribution: $K_L \to \pi^0 l^+ l^-$ $(l = e, \mu)$ and $K_{L,S} \to \mu^+\mu^-$. Here, the long-distance amplitudes must be determined to a sufficient precision in order to access the short-distance physics. The determination of the long-distance contributions is done in the framework of Chiral Perturbation Theory (χPT). In a combined theoretical [39, 40] and experimental [41] effort, accomplished in the last year by NA48/1 measurements of $K_S \to \pi^0 l^+ l^-$ decays [42], it has been shown that in the $K_L \to \pi^0 l^+ l^-$ decay the long-distance component does not saturate the decay rate and the short-distance contribution can be experimentally accessible.

The experiment E787 at BNL searched for the decay $K^+ \to \pi^+\nu\overline{\nu}$ between years 1995 and 1999 and found 2 events with only 0.14 ± 0.05 events background expectation [43]. The successor of the E787 experiment, E949, was able to obtain in 2002 about 20% of the total allocated time before it was turned off. The result is another observed event with 0.30 ± 0.03 events of expected background [44]. The combined experimental branching ratio is $BR(K^+ \to \pi^+\nu\overline{\nu}) = (14.7^{+13.0}_{-8.9}) \times 10^{-11}$. This result is compatible with the SM prediction $(7.8 \pm 1.2) \times 10^{-11}$ [45]. However, the fact that the central value is about factor two above the expectation and the uncertainties are large, leaves an exciting window for New Physics [46].

The decay amplitude of $K_L \to \pi^0\nu\overline{\nu}$ is entirely due to direct CP violation [47] and determines the height of the CKM unitarity triangle. SM calcula-

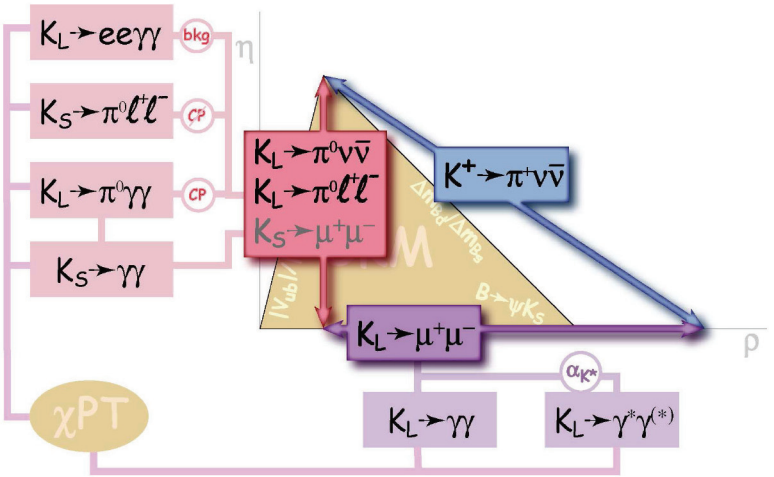

Figure 2: *Rare kaon FCNC reactions can fully determine the CKM unitarity triangle. Long-distance contributions to some of these processes are calculated in the framework of χPT with the help of other, related kaon rare decays.*

tions give $BR(K_L \to \pi^0\nu\overline{\nu}) = (3.0\pm0.6)\times10^{-11}$ [37, 46]. First dedicated experiment E391a at KEK, using pencil neutral beam, started to take data in 2004. These first data yielded a preliminary result $BR(K_L \to \pi^0\nu\overline{\nu}) < 2.86 \times 10^{-7}$ (at 90% CL) [48] which is already better than previous KTeV limit [49]. This experiment expects to reach single event sensitivity of about 10^{-9} which is close to the Grossman-Nir bound [50] relating $K_L \to \pi^0\nu\overline{\nu}$ and $K^+ \to \pi^+\nu\overline{\nu}$ decay widths and to some of the NP predictions [36, 37, 38].

6 Future projects

A new experiment OKA is under construction at Protvino IHEP as a continuation of the ISTRA+ collaboration. The main feature of this project is the use of RF-separated charged kaon beam at the IHEP U-70 accelerator. The commissioning of the RF-separated beam is scheduled for the December 2005. The main physics goals of this project are the search for direct CP violation

in $K^{\pm} \to \pi\pi\pi$ decays to sensitivity $A_g \sim 10^{-4}$, similar to NA48/2, search for T violation in radiative semileptonic decays and search for New Physics in leptonic and semileptonic charged kaon decays [51].

In Japan, the J-PARK facility will provide high intensity (3×10^{14} ppp) protons at 30-50 GeV. Several Letters of Intent for K projects have been submitted. The most important recommended project is proposing a search for the $K_L \to \pi^0\nu\overline{\nu}$ decay using modified E391a detector for the Phase I which should start around year 2008. The goal is to collect about 20 SM events in 3 years of running. For the Phase II a new detector is planned, based on experience from Phase I [52]. Among other recommended projects are search for $K^+ \to \pi^+\nu\overline{\nu}$ with stopped charged kaon beam and search for T violation in the transverse muon polarisation in decays $K^+ \to \pi^0\mu\nu$ and $K^+ \to \mu\nu\gamma$ [53].

At CERN, a new collaboration forming from the core of NA48 is preparing a new project P-326 at SPS. The goal is to collect about 80 SM $K^+ \to \pi^+\nu\overline{\nu}$ events in two years of running using unseparated 75 GeV K^+ beam from 400 GeV SPS protons with intensity of 3×10^{12} ppp. In contrary to the J-PARK project, in P-326 the kaons will decay in flight. Large variety of modern detector technologies are used to ensure high efficiency of photon-vetoing and redundancy in particle ID as well as momentum measurement at both beam and decay sides. The Proposal [54] for this project is in the process of approval. Data taking is planned to start in 2009.

Despite of the fact that all kaon projects in US (E949, CKM, KOPIO) have been discontinued, kaon physics is being pursued in Europe and Japan. Kaon decays, and notably the very rare K decays mediated by FCNC, offer a window to New Physics which is complementary to physics at large colliders and B factories. A continuing support from the theorists is essential to keep kaon physics attractive.

References

1. J.H. Christenson *et al.*, Phys. Rev. Lett. **13** 138 (1964).
2. M. Kobayashi and K. Maskawa, Prog. Theor. Phys **49** 652 (1973).
3. S.L. Glashow, J. Iliopoulos and L. Maiani, Phys. Rev. D **2** 1285 (1970).
4. G. Barr *et al.* (NA31), Phys. Lett. B **317** 233 (1993).
5. A. Lai *et al.* (NA48), Eur. Phys. J. C **22** 231 (2001).
6. J.R. Batley *et al.* (NA48), Phys. Lett. B **544** 97 (2002).
7. A. Alavi-Harati *et al.* (KTeV), Phys. Rev. D **67** 012005 (2003).
8. K. Hagiwara *et al.* (PDG), Phys. Rev. D **66** 010001 (2002).
9. V. Cirigliano, H. Neufeld and H. Pichl, hep-ph/0401173.
10. T.C. Andre, hep-ph/0406006.
11. T. Alexopoulos *et al.* (KTeV), Phys. Rev. D **70** 092006 (2004),
    T. Alexopoulos *et al.* (KTeV), Phys. Rev. D **70** 092007 (2004).
12. S. Eidelman *et al.* (PDG), Phys. Lett. B **592** 1 (2004).
13. A. Lai *et al.* (NA48), Phys. Lett. B **602** 41 (2004),
    A. Lai *et al.* (NA48), Phys. Lett. B **604** 1 (2004).
14. F. Ambrosino *et al.* (KLOE), hep-ex/0508027.
15. F. Ambrosino *et al.* (KLOE),Phys. Lett. B **626** 15 (2005).
16. B. Sciascia (KLOE), Talk given at EPS International Europhysics Conference on High Energy Physics HEP2005, Lisboa (July 2005), hep-ex/0510028.
17. V. Obraztsov (ISTRA+), Talk given at KAON2005, Evanston (June 2005).
18. A. Dabrowski (NA48/2), Talk given at KAON2005, Evanston (June 2005).
19. A. Sher *et al.* (E865), Phys. Rev. Lett. **91** 261802 (2003).

20. H. Leutwyler and M. Roos, Z. Phys. C **25** 91 (1984).

21. D. Bećirević *et al.*, hep-ph/0403217.

22. J. Bijnens and P. Talavera, Nucl. Phys. B **669** 341 (2003),
M. Jamin, J.A. Oller and A. Pich, hep-ph/0401080.

23. A. Lai *et al.* (NA48), Phys. Lett. B **610** 165 (2005).

24. J.S. Bell and J. Steinberger, Proc. of Oxford Int. Conf. on Elementary Part. (1965) 195.

25. F. Ambrosino *et al.* (KLOE),Phys. Lett. B **619** 61 (2005).

26. R. Batley *et al.* (NA48), CERN/SPSC/2000-003, CERN/SPSC/2003-033.

27. W.T. Ford *et al.*, Phys. Rev. Lett. **25** 1370 (1970).
W.S. Choong (HyperCP), PhD Thesis, LBNL-47014, Berkeley 2000.
K.M. Smith *et al.*, Nucl. Phys. B **91** 45 (1975).
G.A. Akopdzhanov *et al.*, Eur. Phys. J. C **40** 343 (2005).

28. L. Maiani and N. Paver, The second DAΦNE Physics Handbook, INFN, LNF, Vol 1. (1995) 51,
E.P. Shabalin, hep-ph/0405229,
A.A. Belkov, A.V. Lanyov and G. Bohm, hep-ph/0311209,
I. Scimemi, E. Gamiz and J. Prades, hep-ph/0405204,
J. Prades, E. Gamiz and I. Scimemi, hep-ph/0509346.

29. G. D'Ambrosio, G. Isidori and G. Martinelli, Phys. Lett. B **480** 164 (2000).

30. I. Mikulec (NA48/2), hep-ex/0505081.

31. S. Balev (NA48/2), Particle Physics seminar at CERN, November 2005.

32. N. Cabibbo, Phys. Rev. Lett. **93** 121801 (2004).

33. G. Colangelo, J. Gasser and H. Leutwyler, Phys. Lett. B **488** 261 (2000),
G. Colangelo, J. Gasser and H. Leutwyler, Nucl. Phys. B **603** 125 (2001).

34. N. Cabibbo and G. Isidori, JHEP **503** 21 (2005).

35. J.R. Batley *et al.* (NA48/2), hep-ex/0511056.

36. G. Colangelo and G. Isidori, JHEP **09** 009 (1998),
Y. Nir and M.P. Worah, Phys. Lett. B **423** 319 (1998),
A.J. Buras, A. Romanino and L. Silvestrini, Nucl. Phys. B **520** 3 (1998),
A.J. Buras *et al.*, Nucl. Phys. B **566** 3 (2000),
G. D'Ambrosio and G. Isidori, Phys. Lett. B **530** 108 (2002),
A.J. Buras *et al.*, Nucl. Phys. B **660** 225 (2003),
Y. Grossman, G. Isidori and H. Murayama, Phys. Lett. B **588** 74 (2004),
C. Bobeth *et al.*, Nucl. Phys. B **726** 252 (2005).

37. A.J. Buras, F. Schwab and S. Uhlig, hep-ph/0405132,
D. Bryman *et al.*, hep-ph/0505171.

38. A.J. Buras *et al.*, hep-ph/0402112.

39. G. Buchalla, G. D'Ambrosio and G. Isidori, Nucl. Phys. B **672** 387 (2003).

40. G. Isidori, C. Smith and R. Unterdorfer, hep-ph/0404127.

41. A. Lai *et al.* (NA48), Phys. Lett. B **536** 229 (2002),
A. Alavi-Harati *et al.* (KTeV), Phys. Rev. Lett. **83** 917 (1999).

42. J.R. Batley *et al.* (NA48), Phys. Lett. B **576** 43 (2003),
J.R. Batley *et al.* (NA48), Phys. Lett. B **599** 197 (2004),
A. Ceccucci, Int. J. Mod. Phys.A **19** 889 (2004).

43. S. Adler *et al.* (E787), Phys. Rev. Lett. **88** 041803 (2002),
S. Adler *et al.* (E787), Phys. Rev. D **70** 037102 (2004).

44. V.V. Anisimovski *et al.* (E949), hep-ex/0403036.

45. A.J. Buras *et al.*, hep-ph/0508165.

46. G. Isidori, hep-ph/0307014.

47. L.S. Littenberg Phys. Rev. D **39** 3322 (1989).

48. K. Sakashita (E391a), Talk given at KAON2005, Evanston (June 2005).

49. A. Alavi-Harati *et al.* (KTeV), Phys. Rev. D **61** 072006 (2000).

50. Y. Grossman and Y. Nir, Phys. Lett. B **398** 163 (1997).

51. V. Obraztsov (OKA), Talk given at KAON2005, Evanston (June 2005).

52. T. Yamanaka (JPARK), Talk given at KAON2005, Evanston (June 2005).

53. J. Imazato (JPARK), Talk given at KAON2005, Evanston (June 2005).

54. G. Anelli *et al.* (P-326), CERN-SPSC-2005-013, CERN-SPSC-P-326.

Frascati Physics Series Vol. XL (2006), pp. 137–142
Frontier Science 2005, New Frontiers in Subnuclear Physics
Milano, 12-16 September, 2005

NEW HADRON SPECTROSCOPY WITH *BABAR*

Gagan B. Mohanty
Representing the *BABAR* Collaboration
Department of Physics, University of Warwick, Coventry, United Kingdom

Abstract

We review hadron spectroscopy at *BABAR* with emphasis on recent results from the studies of the $X(3872)$ state, inclusive charmonia on B recoil, double charmonium production, and the broad structure observed at around 4.26 GeV/c^2. These results are preliminary, unless otherwise specified.

1 Introduction

Hadron spectroscopy plays a crucial role in validating quantum chromodynamics (QCD) and the quark substructure of matter. In recent years this field of particle physics has received a renewed interest, thanks to the discovery of many new states at the B factories. Some of these states, such as $D_{sJ}(2317)^+$ and $D_{sJ}(2460)^+$, are by now well established and appear to be ordinary charm mesons. Others, such as $X(3872)$ and $Y(3940)$, could be new excited charmonium ($c\bar{c}$) states or new forms of matter, but require more measurements with better statistical precision for a definitive identification.

The *BABAR* experiment [1)] is located at the PEP-II asymmetric-energy e^+e^- storage rings, and takes data at or just below the $\Upsilon(4S)$ resonance. It was designed to study CP violation in the B system, however it has proved to have a significantly broader physics reach, especially in the spectroscopy sector. We report here recent results on new charmonium-like states studied using the *BABAR* data sample.

2 Studies of the $X(3872)$ State

The $X(3872)$ state was first observed in the decay $B^- \to X(3872)K^-, X \to J/\psi\pi^+\pi^{-1}$ by the Belle Collaboration [2)]. Later it was confirmed by the CDF [3)], D0 [4)] and *BABAR* [5)] Collaborations. The distribution of the $\pi^+\pi^-$ invariant mass in the decay $X(3872) \to J/\psi\pi^+\pi^-$ suggests that the decay may proceed through an intermediate ρ^0 resonance. If so, one can expect to find its charged isospin partner $X(3872)^-$. We have searched for this state in the decays $B^- \to J/\psi\pi^-\pi^0 K^0_S$ and $B^0 \to J/\psi\pi^-\pi^0 K^+$. However, no evidence for a charged $X(3872)$ has been found [6)] and we set the following upper limits at 90 % confidence level (CL): $\mathcal{B}(B^- \to X(3872)^- K^0_S, X^- \to J/\psi\pi^-\pi^0) < 11\times10^{-6}$ and $\mathcal{B}(B^0 \to X(3872)^- K^+, X^- \to J/\psi\pi^-\pi^0) < 5.4\times10^{-6}$. A search for $X(3872)$ in the initial state radiation (ISR) process $e^+e^- \to X(3872)\gamma_{ISR}$ via the decay to $J/\psi\pi^+\pi^-$ has yielded a null result [7)]. This strongly disfavors a $J^{PC} = 1^{--}$ assignment to X. The small width of the $X(3872)$, and its proximity to the $D^0\bar{D}^{0\star}$ threshold, suggest that it may not be a simple charmonium state. Alternative explanations have been proposed; for example, it could be a weakly bound $D\bar{D}^\star$ molecule-like state [8)] or a diquark-antidiquark state [9)]. To investigate these models, *BABAR* has updated its earlier study with increased statistics.

Using 232 million $B\bar{B}$ pairs recorded by *BABAR*, $X(3872)$ candidates are reconstructed in the decays $B^- \to J/\psi\pi^+\pi^-K^-$ and $B^0 \to J/\psi\pi^+\pi^-K^0_S$. Figure 1 shows the $J/\psi\pi^+\pi^-$ invariant mass distributions for these two B decay modes [10)] which are fitted to a nonrelativistic Breit-Wigner shape for the signal, and to a linear function for the nonresonant and combinatorial backgrounds. For the charged B mode, we obtain 61.2 ± 15.3 while for the B^0 mode only 8.3 ± 4.5 signal events. These yields are translated to the respective branching fractions by taking efficiency corrections into account: $\mathcal{B}^- \equiv \mathcal{B}(B^- \to X(3872)K^-, X \to J/\psi\pi^+\pi^-) = (10.1 \pm 2.5 \pm 1.0) \times 10^{-6}$ and $\mathcal{B}^0 \equiv \mathcal{B}(B^0 \to X(3872)K^0_S, X \to J/\psi\pi^+\pi^-) = (5.1 \pm 2.8 \pm 0.7) \times 10^{-6}$, where uncertainties are statistical and systematic, respectively. From these we derive

[1] Charge conjugate reactions are included implicitly throughout.

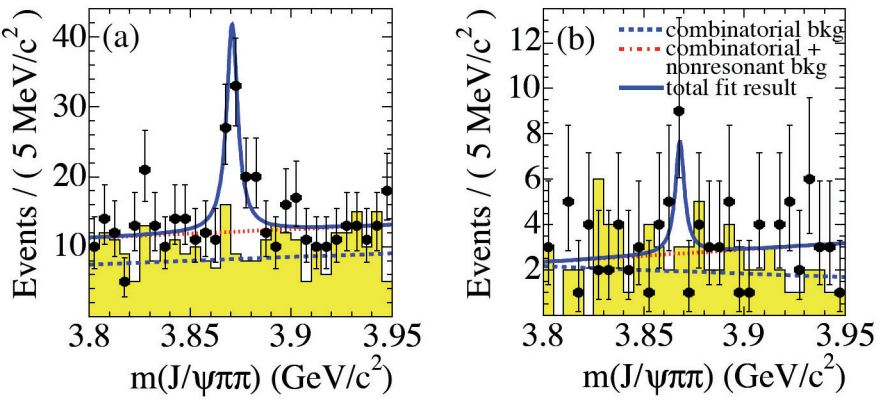

Figure 1: The $J/\psi\pi^+\pi^-$ invariant mass distribution in the signal region for (a) $B^- \to X(3872)K^-$ and (b) $B^0 \to X(3872)K^0_S$ decays.

a ratio of the branching fractions, $\mathcal{R} = \mathcal{B}^0/\mathcal{B}^- = 0.50 \pm 0.30 \pm 0.05$. We also measure the mass difference of the $X(3872)$ state from the charged and neutral B decay modes, Δm, to be $(2.7 \pm 1.3 \pm 0.2)\,\mathrm{MeV}/c^2$. The diquark-antidiquark model predicts $\mathcal{R} = 1$ and Δm to be $(7 \pm 2)\,\mathrm{MeV}/c^2$. The expected ratio of branching fractions is consistent with our measurement, $0.13 < \mathcal{R} < 1.10$ at 90 % CL, and the observed Δm is consistent with zero, and with the model prediction within two standard deviations (σ). This result seems to slightly disfavor the molecule model that predicts $\mathcal{R}$ to be at most 10 %. However, we need more data to discriminate convincingly between these models.

3 Inclusive Charmonia on B recoil

A novel recoil technique is devised to measure various charmonium states, $X_{c\bar{c}}$, in inclusive B decay via $B^- \to K^- X_{c\bar{c}}$. A two-body B^- decay corresponds to a unique K^- momentum in the B^- rest frame, so that if the K^- and the recoil B^+ are reconstructed, the $X_{c\bar{c}}$ is detected regardless of its decay products. Therefore, this method allows us to determine the absolute branching fractions (or set upper limits) for the production of any known or unknown charmonium resonances. The analysis is performed using 210 fb^{-1} of data where a charged B meson is fully reconstructed, so that the momentum of the recoiling B candidate can be calculated from the measured B and the beam parameters. The kaon energy ($E^\star_K$) in the second B rest frame is related to the mass (m_X) of the system recoiling against it by $m_X = \sqrt{m_B^2 + m_K^2 - 2E^\star_K m_B}$, where m_B is the

charged B meson mass. Therefore, the signature of any charmonium state will be in the kaon momentum spectrum at corresponding value. In addition to the clear J/ψ, η_c and χ_{c1} signals, we also have $3.2\,\sigma$, $1.8\,\sigma$ and $1.4\,\sigma$ indications for $\psi(2S)$, $\eta_c(2S)$ and $\psi(3770)$, respectively. No evidence for $X(3872)$ is found and we derive $\mathcal{B}(B^- \to X(3872)K^-) < 3.2 \times 10^{-4}$, which, in conjunction with the world-average value of the branching fraction product, allows us to set the lower limit $\mathcal{B}(X(3872) \to J/\psi\pi^+\pi^-) > 4.2\,\%$ at 90 % CL.

4 Double Charmonium Production

In *BABAR*, exclusive B decays are not the only source of charmonium states. We have also studied double charmonium production in the process $e^+e^- \to \gamma^\star \to J/\psi\, c\bar{c}$ using 124 fb^{-1} of data [11]. Only $c\bar{c}$ states with even C-parity are expected in this reaction, although if there is a contribution from $e^+e^- \to \gamma^\star\gamma^\star \to J/\psi\, c\bar{c}$, odd C-parity states could also be produced. In this study, we first reconstruct a J/ψ candidate via the e^+e^- or $\mu^+\mu^-$ decay mode and then calculate the mass of the system recoiling against it. Three even C-parity charmonium states, η_c, χ_{c0} and $\eta_c(2S)$, are observed, while there is no evidence for any odd C-parity state such as the J/ψ. The distribution is fit to obtain the yield for each state, from which the production cross section is calculated. Due to the requirement of at least five charged tracks in the event for background suppression purposes, we report the product of the production cross section and the branching fraction to states with more than two tracks. The results are $17.6 \pm 2.8^{+1.5}_{-2.1}$ fb, $10.3 \pm 2.5^{+1.4}_{-1.8}$ fb and $16.4 \pm 3.7^{+2.4}_{-3.0}$ fb for η_c, χ_{c0} and $\eta_c(2S)$, respectively. These values are an order of magnitude higher than those predicted by non-relativistic QCD [12]. However, recent works incorporating charm quark dynamics [13] seem to narrow down the discrepancy.

5 Observation of the $Y(4260)$

ISR events produced in the $\Upsilon(4S)$ energy region at the B factories serve to probe interesting physics occurring at lower center-of-mass energies. Motivated by this, *BABAR* has investigated the process $e^+e^- \to J/\psi\pi^+\pi^-\gamma_{ISR}$ across the charmonium mass range, using a data sample of 233 fb^{-1} integrated luminosity [14]. These events are characterized by two pions, two leptons (electron or muon) making a J/ψ candidate and a small recoil mass squared against the $J/\psi\pi^+\pi^-$ system. Figure 2 shows the $J/\psi\pi^+\pi^-$ invariant mass spectrum for the selected candidates. A clear enhancement near 4.26 GeV/c^2 is observed in addition to the expected $\psi(2S)$ peak. No other structure is evident in the spectrum, including the $X(3872)$. Using a maximum likelihood fit in

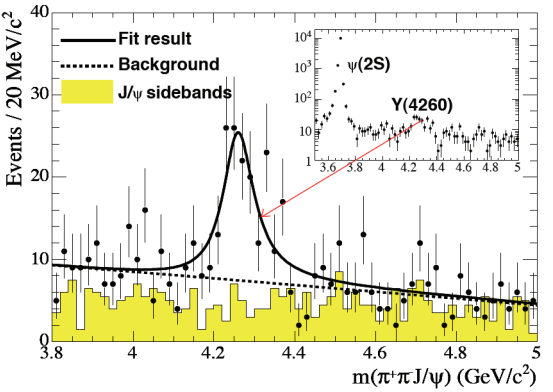

Figure 2: The $J/\psi\pi^+\pi^-$ invariant mass spectrum in the range 3.8–5.0 GeV/c^2 and (inset) over a wider range that includes the $\psi(2S)$ state.

which the signal is described by a single relativistic Breit-Wigner lineshape, we obtain a yield of 125 ± 23 events with a statistical significance of $8\,\sigma$ (the signal is referred to as the $Y(4260)$). The mass and width are found to be $(4259 \pm 8^{+2}_{-6})\,\mathrm{MeV}/c^2$ and $(88 \pm 23^{+6}_{-4})\,\mathrm{MeV}$, respectively. We also calculate a value of $\Gamma(Y(4260) \to e^+e^-) \cdot \mathcal{B}(Y \to J/\psi\pi^+\pi^-) = (5.5 \pm 1.0^{+0.8}_{-0.7})$ eV. Although these results are from a single resonance fit, we cannot exclude a multi-resonance hypothesis at the current level of statistics. More data are needed to reveal the exact nature of this state.

6 Conclusions

The last few years have been very exciting for hadron spectroscopy studies at the B factories. Specifically, *BABAR* is pioneering several sensitive searches for new charmonium states, some of which are summarized in this paper, including the measurement of the $X(3872)$ state in neutral and charged B decays and the first observation of a new broad resonance, the $Y(4260)$.

References

1. B. Aubert *et al.* [*BABAR* Collab.], Nucl. Instr. Meth. A **479**, 1 (2002).
2. S.-K. Choi *et al.* [Belle Collab.], Phys. Rev. Lett. **91**, 262001 (2003).
3. D. Acosta *et al.* [CDF Collab.], Phys. Rev. Lett. **93**, 072001 (2004).

4. V.M. Abazov *et al.* [D0 Collab.], Phys. Rev. Lett. **93**, 162002 (2004).
5. B. Aubert *et al.* [*BABAR* Collab.], Phys. Rev. D **71**, 071103 (2005).
6. B. Aubert *et al.* [*BABAR* Collab.], Phys. Rev. D **71**, 031501 (2005).
7. B. Aubert *et al.* [*BABAR* Collab.], Phys. Rev. D **71**, 052001 (2005).
8. F.E. Close and P.R. Page, Phys. Lett. B **578**, 119 (2004);
   E. Braaten and M. Kusunoki, Phys. Rev. D **71**, 074005 (2005).
9. L. Maiani *et al.* Phys. Rev. D **71**, 014028 (2005).
10. B. Aubert *et al.* [*BABAR* Collab.], hep-ex/0507090, in press.
11. B. Aubert *et al.* [*BABAR* Collab.], Phys. Rev. D **72**, 031101 (2005).
12. E. Braaten and J. Lee, Phys. Rev. D **67**, 054007 (2003);
    K.-Y. Liu *et al.*, Phys. Lett. B **557**, 45 (2003) and hep-ph/0408141.
13. A.E. Bondar and V.L. Chernyak, Phys. Lett. B **612**, 215 (2005);
    Y.-J. Zhang *et al.*, hep-ph/0506076.
14. B. Aubert *et al.* [*BABAR* Collab.], Phys. Rev. Lett. **95**, 142001 (2005).

Frascati Physics Series Vol. XL (2006), pp. 145–146
Frontier Science 2005, New Frontiers in Subnuclear Physics
Milano, 12-16 September, 2005

RARE DECAYS AND SEARCH FOR NEW PHYSICS WITH BABAR *BABAR*

Johannes M. Bauer
University of Mississippi, University, MS 38677, U.S.A.
for the *BABAR* Collaboration

Abstract

Rare B decays permit stringent tests of the Standard Model and allow searches for new physics. Several rare radiative-decay studies of the B meson from the *BABAR* collaboration are described. So far no sign for new physics was discovered.

1 Introduction

At the SLAC PEP-II B-Factory, the *BABAR* detector collected so far more than 250M $B\overline{B}$ pairs, created by e^+e^- collisions at the $\Upsilon(4S)$ resonance. This data set makes searches for rare decays feasible at branching fractions (BF) of 10^{-4} or less. This talk concentrates on radiative B decays. Additional results from *BABAR* were discussed elsewhere at this conference. [1)]

2 Fully- and Semi-inclusive $B \to X_s\gamma$, $B \to K^*(892)\gamma$ & $B \to K_2^*(1430)\gamma$

The lowest-order Feynman diagram of $b \to s\gamma$ is a one-loop electromagnetic penguin, in which non-Standard Model (non-SM) virtual particles (like the

Higgs) might influence the decay rate. Measuring the energy distribution of the b quark inside the B meson helps extract $|V_{ub}|$ from $B \to X_u l\nu$. The decay $b \to s\gamma$ was studied in inclusive and exclusive modes using ~ 89M $B\overline{B}$ pairs.

In the so-called "fully-inclusive" measurement only the photon of $B \to X_s\gamma$ needs to be detected, but large background has to be suppressed. In the "semi-inclusive" measurement, the $B \to X_s\gamma$ BF is determined from 38 exclusive states with about 45% of the total rate estimated to be missing.

The E_γ spectra from the two $B \to X_s\gamma$ analyses are shown in Fig.1. The $K^*\gamma$ peak, prominent at high E_γ for the semi-inclusive analysis, is not visible for the inclusive analysis due to resolution constraints. Fig.2 left plots the fully-inclusive partial BFs against the value of the lower cut in E_γ. The overall semi-inclusive BF, when extrapolated to $E_\gamma > 1.6\,\text{GeV}$, agrees with the SM prediction and with the results from other experiments (Fig.2 right). [2, 3]

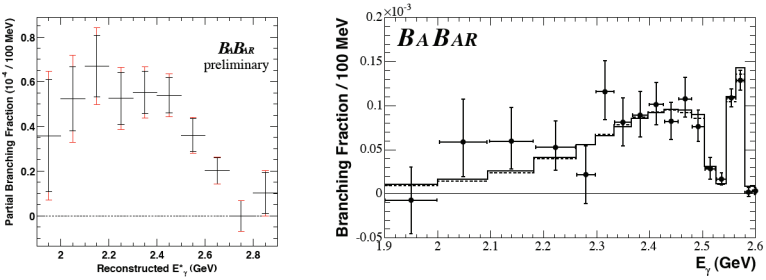

Figure 1: *Photon energy spectrum from fully- (left, in $\Upsilon(4S)$ frame) and semi-inclusive $B \to X_s\gamma$ analyses (right, in B frame, with theory spectra overlaid).*

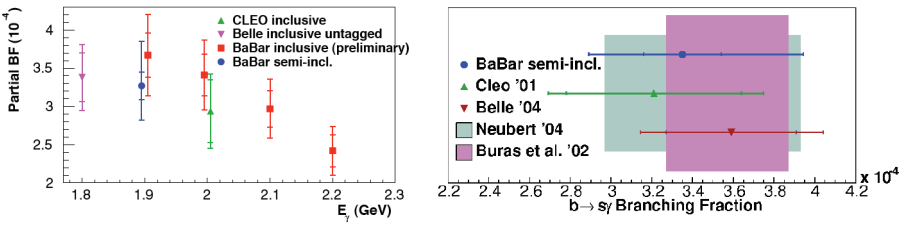

Figure 2: *Partial BFs versus lower cut in E_γ (left) and overall BF measurements (right) of $B \to X_s\gamma$ for $E_\gamma > 1.6\,\text{GeV}$.*

Non-perturbative hadronic effects complicate the theoretical calculations of exclusive decays like $B \to K^*(892)\gamma$ and $B \to K_2^*(1430)\gamma$, so that the measurements are currently more accurate than the predictions. A summary

of the results is shown in Fig.3. [4, 5]

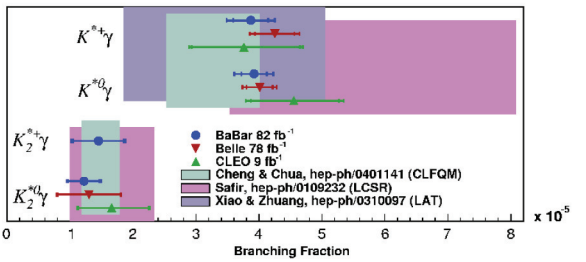

Figure 3: *Branching fractions of* $B \to K^*(892)\gamma$ *and* $B \to K_2^*(1430)\gamma$.

3 $B \to X_s ll$, $B \to K^{(*)} ll$ and $B \to (\rho, \omega)\gamma$

The decay $b \to sll$ has been measured semi-inclusively ($B \to X_s ll$) on 89M $B\overline{B}$ pairs, and exclusively ($B \to K^{(*)} ll$) on 229M $B\overline{B}$ pairs. The former measurement is again based on a sum of exclusive states, with about half of the total rate missing, and its BF [6] of $(5.6 \pm 1.5 \pm 0.6 \pm 1.1) \times 10^{-6}$ for $m_{ll} > 0.2\,\mathrm{GeV}/c^2$ agrees well with the SM prediction. The exclusive decay results are shown in Fig.4 left. [7]

The decay $b \to d\gamma$ has been studied in 221M $B\overline{B}$ pairs by searching for $B \to (\rho, \omega)\gamma$. These decays go primarily through penguin diagrams, but also through W-exchange or W-annihilation. The background originates mainly from $q\overline{q}$ (=$udsc$) events. The BF results are summarized in Fig.4 right. [8]

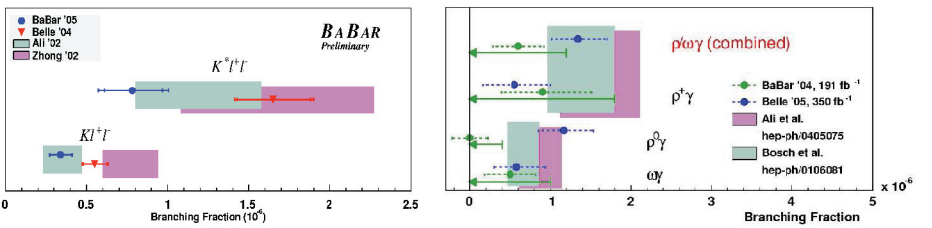

Figure 4: *BF measurements and SM predictions for* $K^{(*)} ll$ *(left) and* $B \to (\rho, \omega)\gamma$ *decays (right).*

4 $\overline{B}^0 \to D^{*0}\gamma$ and $B^0 \to \phi\gamma$

The $\overline{B}^0 \to D^{*0}\gamma$ decay with SM predictions around 10^{-6} is dominated by W-exchange. The final B candidates from 88M $B\overline{B}$ pairs are described by $m_{\rm ES} = \sqrt{E^{*2}_{\rm beam} - p^{*2}_B}$ and $\Delta E^* = E^*_B - E^*_{\rm beam}$, with $E^*_{\rm beam}$ being the center-of-mass (CM) beam energy, and E^*_B and p^{*2}_B the B candidate's CM energy and momentum. Background, mainly from $B\overline{B}$ decays, is estimated to be 9.4 ± 1.7 events in the $m_{\rm ES}$-ΔE signal box. Thirteen observed data events (Fig.5 left) lead to a BF upper limit of 2.5×10^{-5} at 90% confidence level (CL). [9]

The experimental signature of the $B^0 \to \phi\gamma$ decay is clean, but the SM prediction of the BF is very low with 3.6×10^{-12}. Candidates are selected from 124M $B\overline{B}$ pairs. In the signal region, a $q\overline{q}$ ($B\overline{B}$) background of 6.0 ± 1.0 (<0.1) events is expected. Eight events observed in data (Fig.5 right) result in a BF upper limit of 8.5×10^{-7} at 90% CL. [10]

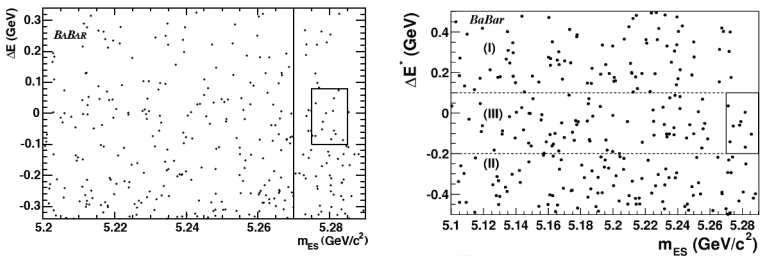

Figure 5: *$m_{\rm ES}$-ΔE plane of real data for $\overline{B}^0 \to D^{*0}\gamma$ (left) and $B^0 \to \phi\gamma$ (right). In both plots the signal box is indicated on the right side.*

The author thanks the *BABAR* collaboration, the SLAC accelerator group and all contributing computing organizations. He was supported by U.S. Department of Energy grant DE-FG05-91ER40622.

References

1. Presentations by Fernando Ferroni and Gagan Mohanty this conference.
2. *BABAR* Collaboration, B. Aubert *et al.*, hep-ex/0507001 (2005).
3. *BABAR* Collaboration, B. Aubert *et al.*, Phys. Rev. D **72**, 052004 (2005).
4. *BABAR* Collaboration, B. Aubert *et al.*, Phys. Rev. D **70**, 112006 (2004).
5. *BABAR* Collaboration, B. Aubert *et al.*, Phys. Rev. D **70**, 091105 (2004).
6. *BABAR* Collaboration, B. Aubert *et al.*, Phys. Rev. Lett. **93**, 081802 (2004).
7. *BABAR* Collaboration, B. Aubert *et al.*, hep-ex/0507005 (2004).
8. *BABAR* Collaboration, B. Aubert *et al.*, Phys. Rev. Lett. **94**, 011801 (2005).
9. *BABAR* Collaboration, B. Aubert *et al.*, Phys. Rev. D **72**, 051106 (2005).
10. *BABAR* Collaboration, B. Aubert *et al.*, Phys. Rev. D **72**, 091103 (2005).

Frascati Physics Series Vol. XL (2006), pp. 149–155
Frontier Science 2005, New Frontiers in Subnuclear Physics
Milano, 12-16 September, 2005

$|V_{us}|$ EXTRACTION FROM KLOE MEASUREMENTS

C. Bloise
Laboratori Nazionali di Frascati dell'INFN - Via Fermi, 40 - 00044 Frascati
on behalf of the KLOE Collaboration *

Abstract

Recent measurements of the KLOE experiment at the Frascati ϕ-factory, DAΦNE, relevant for the extraction of the V_{us} element of the CKM matrix, are summarized. $|V_{us}|$ values from semileptonic branching ratios, dominated by the accuracy in the calculation of $f_+(0)$, are fully consistent each other and in

* F. Ambrosino, A. Antonelli, M. Antonelli, C. Bacci, P. Beltrame, G. Bencivenni, S. Bertolucci, C. Bini, C. Bloise, V. Bocci, F. Bossi, D. Bowring, P. Branchini, R. Caloi, P. Campana, G. Capon, T. Capussela, F. Ceradini, S. Chi, G. Chiefari, P. Ciambrone, S. Conetti, E. De Lucia, P. De Simone, G. De Zorzi, S. Dell'Agnello, A. Denig, A. Di Domenico, C. Di Donato, S. Di Falco, B. Di Micco, A. Doria, M. Dreucci, G. Felici, A. Ferrari, M. L. Ferrer, G. Finocchiaro, C. Forti, P. Franzini, C. Gatti, P. Gauzzi, S. Giovannella, E. Gorini, E. Graziani, M. Incagli, W. Kluge, V. Kulikov, F. Lacava, G. Lanfranchi, J. Lee-Franzini, D. Leone, M. Martini, P. Massarotti, W. Mei, S. Meola, S. Miscetti, M. Moulson, S. Mueller, F. Murtas, M. Napolitano, F. Nguyen, M. Palutan, E. Pasqualucci, A. Passeri, V. Patera, F. Perfetto, L. Pontecorvo, M. Primavera, P. Santangelo, E. Santovetti, G. Saracino, B. Sciascia, A. Sciubba, F. Scuri, I. Sfiligoi, T. Spadaro, M. Testa, L. Tortora, P. Valente, B. Valeriani, G. Venanzoni, S. Veneziano, A. Ventura, R. Versaci, G. Xu.

agreement with both, the unitarity in the first row of the CKM matrix, and the value extracted from the BR($K^+ \to \mu^+\nu(\gamma)$) using lattice calculations for the meson-decay constant ratio f_K/f_π.

1 Introduction

The KLOE results relevant for the extraction of $|V_{us}|$ include the measurements of the absolute semileptonic branching ratios (BR), fully inclusive of the radiative decays, for both neutral, and charged kaons, the measurement of the lifetime and the slopes of the semileptonic form factors of the neutral kaons and the measurement of the BR($K^+ \to \mu^+\nu(\gamma)$).

During data taking in years 2001-2002, KLOE has collected an integrated luminosity of about 450 pb^{-1}. The presented results refer to the analyses of this sample.

The KLOE detector is composed of a large drift chamber and a hermetic electromagnetic calorimeter immersed in the 0.52 T field of a superconducting solenoid. The drift chamber (DC) [1], 2 m radius, 4.2 m length, provide a transverse momentum resolution, $\sigma(p)/p$ better than 0.4% for tracks at large zenith angles ($40° \leq \theta \leq 140°$). The lead-scintillating fiber calorimeter (ECAL) [2] has been designed to detect photons with energy as low as 20 MeV, and to accurately determine their energy and time of flight. Particularly relevant is the performance in term of time resolution, $\sigma_T = 57$ ps$/\sqrt{E(GeV)}$. The trigger [3] for Data Acquisition (DAQ) is provided by energy deposits in the calorimeter or by hit wires in the DC. Trigger logic is very efficient for ϕ-decays and residual dependences of the efficiency on event topologies can be directly measured comparing DC and calorimeter triggers, that rely on independent criteria. A cosmic-muon veto based on the energy deposits in the outermost calorimeter planes is also enforced by the acknowledge of a 3rd-level trigger, able to identify most of the ϕ decays among cosmic-muon candidates. Another possible source of event rejection in KLOE is the procedure (FILFO) to filter out mostly events triggered by machine background. For both, cosmic-ray veto, and FILFO, control samples which do not undergo the respective selection procedures are kept in order to study their effect on the measurements.

2 The measurements

One of the key-features of the measurements at the ϕ-factory is the opportunity to tag K_L, K_S, $K^\pm$ events independently from their decay channel. The reconstruction of $K_S \to \pi^+\pi^-$ guarantees, for example, that one K_L with 4-momentum $P_{K_L} = P_\phi$ - P_{K_S} has been produced. In the case of charged kaons, 2-body decays, i.e. $K^\pm \to \pi^0\pi^\pm$ and $K^\pm \to \mu^\pm\nu$, have been used to tag kaons of opposite charge. K_S are tagged by the detection of K_L interactions in the calorimeter, with typical arrival times and energy deposits, $E_d \geq$100 MeV. To minimize biases in the BR measurements due to the tagging criteria, particles giving the tag are required to satisfy also trigger conditions for DAQ. In this way, dependences coming, for example, from different energy deposits in the calorimeter of the decay products of the tagged kaon do not affect tagged samples since the trigger is independently ensured. Residual, small dependences of the tagging criteria from the decay mode of the tagged kaon are studied using Monte Carlo (MC) and data control samples. Absolute BR's are obtained normalizing signal countings to the events in the tagged samples.

$|V_{us}|$ is extracted from kaon semileptonic BR's by:

$$\frac{BR(K \to \pi l \nu(\gamma))}{\tau_K} = \frac{G_\mu^2 m_K^5}{768\pi^3} S_{EW} C_K^2 (1+\delta_l) |V_{us}|^2 f_+^2(0) I_K^l(\lambda'_{+,0}, \lambda''_{+,0}) \quad (1)$$

where S_{EW} is the short range radiative correction factor [4], δ_l is the long-range e.m. correction, $f_+(0)$ is the normalization of the vector form factor (FF), and I is the phase space integral dependent on the slope (and curvature) of the FF as a function of $t = (p_K\text{-}p_\pi)^2/m^2_\pi$. Semileptonic K_L BR's have been obtained by the concurrent measurement [5] of all the major decay modes, namely $\pi e\nu$, $\pi\mu\nu$, $\pi^+\pi^-\pi^0$ and $\pi^0\pi^0\pi^0$. In particular, the fraction of events decaying in the 3 modes containing charged particles have been determined by a fit to the distribution of the variable $\Delta_{\mu\pi}$ defined as the minimum of $|P_{miss}|$ - E_{miss} in the $\mu\pi$ and $\pi\mu$ hypotheses. The distribution presents well separated peaks for the three decay modes. The counting of the 3-π^0 decays has been obtained looking for events with at least three clusters showing the correct time-correlation for photons coming from a common vertex and not associated with any track in the DC. A careful study of the systematics associated with analysis cuts, background subtraction, and with the knowledge of kinematical

distributions has been performed and reported in [6]. Since the measurements refer to 99.64% of all the K_L decays, assuming for the rest the world average of 0.0036, the constraint $\sum BR(K_L) = 1$ has been used to extract the lifetime of the K_L. In fact, the acceptance for the decays depends on K_L lifetime. Final results for the semileptonic BR's, fully inclusive of the radiative decays are:

$$BR(K_L \to \pi e\nu(\gamma)) = 0.4007 \pm 0.0006 \pm 0.0014,$$
$$BR(K_L \to \pi\mu\nu(\gamma)) = 0.2698 \pm 0.0006 \pm 0.0014$$

The K_L lifetime is $\tau_L = (50.72 \pm 0.17 \pm 0.33)$ ns, in agreement with the direct measurement [7], $\tau_L = (50.92 \pm 0.17 \pm 0.25)$ ns, performed by a fit to the proper-time distribution within the fiducial volume of a sample of the order of 10^7 $K_L \to 3\ \pi^0$ decays. The average, $\tau_L = (50.84 \pm 0.23)$ ns, is used in the following.

Phase space integral in Eq.1 depends on the slopes of the semileptonic form factors as a function of $t = (p_K\text{-}p_\pi)^2/m^2{}_\pi$. At present, the preliminary value of $\lambda_+ = (28.6 \pm 0.5 \pm 0.8)\times 10^{-3}$ has been obtained starting from the sample of $K_L \to \pi e\nu$ decays selected for the BR measurement, and using the time-of-flight technique to separate residual contaminations, mostly from $K_L \to \pi\mu\nu$ decays. Linear, as well as quadratic fits have been applied obtaining in both cases good χ^2/DOF values, i.e. 330/363 and 325/362. The preliminary results are in agreement with recent measurements from ISTRA+ [8], KTeV [9] and NA48 experiments [10].

KLOE has been analyzing a unique sample of $K_S \to \pi e\nu$ decays. The $BR(K_S \to \pi e\nu) = (7.09 \pm 0.08 \pm 0.05)\times 10^{-4}$ comes from a multivariate fit tailored to fix the signal and the contributions from various topologies of the background, made of $K_S \to \pi\pi$ events. In this case, signal counting has been normalized to the $K_S \to \pi^+\pi^-$ decays in the same sample.

We have also obtained first evidence for $K_S \to \pi\mu\nu$; the measurement of the $BR(K_S \to \pi\mu\nu)$ is underway.

Semileptonic decays of charged kaons [11] have been selected from tagged samples requiring the reconstruction of the kaon decay vertex within the fiducial volume and the detection of the photon clusters in the calorimeter with the correct time-correlation for photons coming from the same vertex, i.e. the reconstructed vertex in the DC. For signal counting we have used the distribution

of the mass-squared of the lepton, m^2_l, obtained from time-of-flight measurements, i.e. from T_l - $L_l/\beta_l = T_\gamma$ - L_γ, able to discriminate the two lepton masses as well as the 2-body decays, mostly rejected with a direct cut on the maximum momentum of the charged particle from the kaon decay vertex. Tagged sample coming from the reconstruction of $K^\pm \to \pi^0\pi^\pm$ and from $K^\pm \to \mu^\pm\nu$ are separately analyzed. We have obtained the averages BR($K \to \pi^0 e\nu(\gamma)$) = (5.047±0.046±0.080)%, BR($K \to \pi^0\mu\nu(\gamma)$) = (3.310±0.040±0.070)%, where systematic errors are preliminary, with the contribution related to signal selection currently under study.

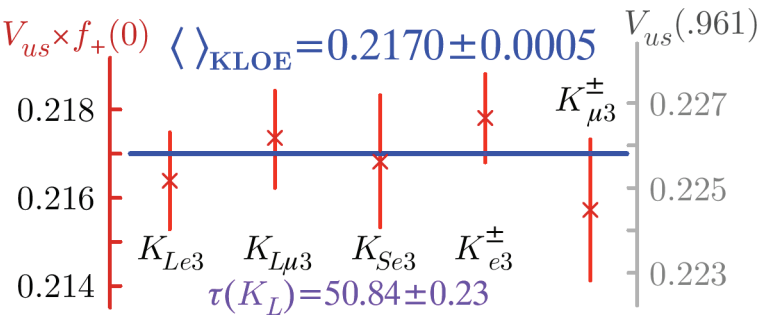

Figure 1: $|V_{us}|\times f_+(0)$ *from KLOE semileptonic BR's.*

The values of the product $|V_{us}|\times f_+(0)$ extracted from the KLOE measurements are summarized in fig.1.

The measurement of the BR($K^+ \to \mu^+\nu(\gamma)$) [12], has been performed on the tagged samples obtained from the reconstruction of $K^- \to \mu^-\nu$. The choice of the tagged sample allows the minimization of the effects coming from both the kaon nuclear interactions and the dependency of the tagging criteria from the decay mode of the tagged kaon (tag-bias). Signal counting has been performed by a fit to the distribution of the charged-particle momentum in the rest frame of the kaon (p*). A background subtraction procedure has been applied to cut $\pi^0\pi^+$ events and semileptonic decays from the range of interest for signal counting, 225 MeV $\leq p^* \leq$ 400 MeV. The procedure is based

on the direct measurement from data control samples of the p* distribution of charged-kaon events with one π^0 in the final state. Final results, based on 865,283 $K^+ \to \mu^+\nu(\gamma)$ decays is BR($K^+ \to \mu^+\nu(\gamma)$)= 0.6366 ± 0.0009 ± 0.0015. $|V_{us}|$ is extracted by:

$$\frac{BR(K \to \mu\nu(\gamma))\tau_\pi}{BR(\pi \to \mu\nu(\gamma))\tau_K} = \frac{m_K(1-m_\mu^2/m_K^2)^2}{m_\pi(1-m_\mu^2/m_\pi^2)^2}\frac{|V_{us}|^2}{|V_{ud}|^2}\frac{f_K^2}{f_\pi^2}\frac{1+\alpha/\pi\cdot C_K}{1+\alpha/\pi\cdot C_\pi} \qquad (2)$$

where f_K/f_π is the ratio of the kaon and the pion decay constants and $C_{K,\pi}$ parametrize the radiative-inclusive electroweak corrections. Using f_K/f_π from ref. [13], we extract the ratio $|V_{us}|^2/|V_{ud}|^2 = 0.05211(16)(19)(117)$, whose precision is dominated by lattice-QCD calculations. The $|V_{us}|$ value, $|V_{us}| = 0.2225(25)$ obtained using the unitarity relation, i.e. $|V_{ud}|^2 = 1$ - $|V_{us}|^2$, is in agreement with the value $|V_{us}| = 0.2223(26)$, as extracted from $|V_{ud}|$ determinated by the measurements of super-allowed β decays [14].

3 Conclusions

From the measurements of the semileptonic BR's we have obtained five values for the product $|V_{us}| \times f_+(0)$ fully consistent each other. The average, $|V_{us}| \times f_+(0) = 0.2170 \pm 0.0005$, allows the extraction of $|V_{us}| = 0.2260 \pm 0.0022$, at the 1% level of accuracy, dominated by present knowledge of $f_+(0) = 0.961 \pm 0.008$ [15]. This $|V_{us}|$ value is also consistent with the unitarity in the first row of the CKM matrix, and with the value extracted from the BR($K^+ \to \mu^+\nu(\gamma)$), $|V_{us}| = 0.2223 \pm 0.0026$, where the error is dominated by the precision in lattice calculation of the the meson-decay constant ratio $f_K/f_\pi = 1.210 \pm 0.013$, reported in ref. [13]. An even better agreement is found from more recent, unpublished results for the f_K/f_π ratio [16].

More data have been collecting; we expect a total of 2.5 fb^{-1} by the end of 2005. New samples will allow other significant measurements, like the slopes of the semileptonic form factors in the decays $K_L \to \pi\mu\nu$, $K^\pm \to \pi l\nu$, and the BR($K_S \to \pi\mu\nu$), and will improve the present results, especially those concerning the rare K_S semileptonic decays.

References

1. M. Adinolfi *et al*, [KLOE Collaboration], Nucl. Instr. & Meth. **A 488**, 51 (2002).
2. M. Adinolfi *et al*, [KLOE Collaboration], Nucl. Instr. & Meth. **A 482**, 364 (2002).
3. M. Adinolfi *et al*, [KLOE Collaboration], Nucl. Instr. & Meth. **A 492**, 134 (2002).
4. A. Sirlin, Nucl. Phys. **B 196**, 83 (1982).
5. F. Ambrosino *et al*, [KLOE Collaboration], Phys. Lett **B**, in print, hep-ex/0508027.
6. M. Antonelli *et al*, http://www.lnf.infn.it/kloe/pub/knote/kn204.ps
7. F. Ambrosino *et al*, [KLOE Collaboration], Phys. Lett **B 626**, 15 (2005).
8. O.P. Yushchenko *et al*, Phys. Lett **B 589**, 111 (2004).
9. T. Alexopoulos *et al*, [KTeV Collaboration], Phys. Rev. Lett **93**, 181802 (2004).
10. A. Lai *et al*, [NA48 Collaboration], Phys. Lett **B 604**, 1 (2004)
11. B. Sciascia *et al*, [KLOE Collaboration], hep-ex/0510028.
12. F. Ambrosino *et al*, [KLOE Collaboration], Phys. Lett **B**, in print, hep-ex/0509045.
13. C. Aubin *et al*, [MILC Collaboration], Phys. Rev. **D 70**, 114501 (2004).
14. I.S. Towner and J.C. Hardy, J. Phys. **G 29**, 197 (2003) and references therein.
15. H. Leutwyler and M. Roos, Z.Phys. **C 25**, 91 (1984).
16. C. Bernard *et al*, [MILC Collaboration], hep-lat/0509137.

SESSION IV – NEUTRINO PHYSICS

S. Petcov	The status of the neutrino oscillations
A. Blondel	The future of the neutrino physics
F. Terranova	The CNGS physics program
V. Antonelli	Global determination of mixing parameters from solar and reactor neutrinos and future perspective
G. De Rosa	Measurement of charm production and decay by CHORUS
M.V. Kosov	CHIPS simulation of the Charged Currents neutrino interactions with nuclei in Geant4
E. Previtali	Double beta decay

Frascati Physics Series Vol. XL (2006), pp. 157
Frontier Science 2005, New Frontiers in Subnuclear Physics
Milano, 12-16 September, 2005

THE STATUS OF THE NEUTRINO OSCILLATIONS

S. Petcov
SISSA, Trieste, Italy

Written contribution not received

Frascati Physics Series Vol. XL (2006), pp. 159
Frontier Science 2005, New Frontiers in Subnuclear Physics
Milano, 12-16 September, 2005

THE FUTURE OF THE NEUTRINO PHYSICS

A. Blondel
University of Geneva, Switzerland

Written contribution not received

Frascati Physics Series Vol. XL (2006), pp. 161–166
Frontier Science 2005, New Frontiers in Subnuclear Physics
Milano, 12-16 September, 2005

THE CNGS PHYSICS PROGRAM

Francesco Terranova
Laboratori Nazionali di Frascati dell'INFN, Frascati (Rome), Italy

Abstract

The CERN to Gran Sasso neutrino beam (CNGS) is now approaching the commissioning phase. Start of operations is planned in spring 2006 and the first physics runs could be available by summer 2006. In this talk we revise the status of the CNGS project and the construction of the experiments (OPERA and ICARUS) that will exploit this unique facility.

1 Introduction

Since 1998, an impressive sequence of experimental results have put on a solid ground the 40-year old hypothesis that neutrinos change flavor [1)]. First of all, a clear evidence of disappearance of atmospheric neutrinos has been reported by the Super-Kamiokande experiment and is corroborated by Soudan2 and Macro data. Furthermore, Super-Kamiokande provided evidence in favor

of a sinusoidal pattern of disappearance as a function of L/E. The most likely explanation for these data is an almost pure $\nu_\mu \rightarrow \nu_\tau$ transition, connected with the m_2 and m_3 mass eigenstates. This result is supported by K2K, a long-baseline experiment reporting a deficit of artificial ν_μ produced at KEK and sent to Super-Kamiokande through a path-length of $\sim$ 250 km. Atmospheric neutrinos offer the unique possibility of measuring in a direct manner the appearance of new flavors, while this measurement is impossible with solar neutrinos. The Δm^2 driving solar oscillations is of the order of $\sim 8 \times 10^{-5}$ eV^2. Therefore, for any realistic baseline the energy of the neutrino is too small to overcome the kinematic threshold for μ or τ production. On the other hand, if the current interpretation of oscillation data is correct, the oscillations at the atmospheric scale can be revealed in appearance mode only through the detection of τ leptons, a very challenging task for any large mass detector. The CNGS [2] beam has been tuned for such an ambitious measurement, i.e. to provide the first direct evidence for appearance of new flavors (ν_τ) from a pure ν_μ beam. Moreover, two experiments are under construction at the Gran Sasso underground laboratories, aimed at the unique identification of the τ leptons resulting from ν_τ CC interactions.

2 The CNGS beam

Given the distance of 732 Km between the CERN accelerator complex and the existing underground laboratories at Gran Sasso, the CNGS ("CERN neutrinos to Gran Sasso") beam has been designed maximizing the number of ν_τ charged current interactions occurring at the detector location. Therefore, the beam energy is *not* at the peak of the oscillation probability ($E_\nu \simeq 1.5$ GeV, i.e. below the τ kinematic threshold) but at the optimal value of 17 GeV. At CNGS, neutrinos are produced through the decay of pions resulting from the interaction of 450 GeV protons with a graphite target. The protons are accelerated by the CERN SPS and extracted in two 10 μs spills separated in time by 50 ms. Civil engineering for CNGS ended up in 2004 and infrastructures have been completed in summer 2005. The installation of the beam elements is in progress. The target station has been assembled and tested in surface. The installation of the target and the magnetic lens in the underground area will start in January 2006 while the commissioning of the beam is planned in spring 2006.

3 The OPERA experiment

OPERA [3] (Oscillation Project with Emulsion-tRacking Apparatus) searches for ν_τ appearance by detecting the final state τ and identifying its decay kink topology. This method requires detectors with μm-scale granularity. The superior space resolution needed for tau detection conflicts with the large target mass necessary to collect enough neutrino interactions off the peak of the oscillation maximum. The solution exploited by the designer of OPERA is based on the so-called "ECC brick". The brick is an implementation of the ECC (Emulsion Cloud Chamber), validated for τ search by the DONUT experiment. It represents the basic unit of OPERA and consists of a sandwich of 56 lead plates (1 mm thick) alternated with 56 nuclear emulsion sheets.

The lead constitutes the target mass for neutrino interactions while nuclear emulsion sheets, with angular resolution of about 2 mrad and a space resolution of 0.5 μm, allow for the reconstruction of the vertex and τ decay kink. Moreover, this basic ECC unit provides the momenta of charged particles produced in the interactions exploiting multiple Coulomb scattering in the lead plates; it allows the identification of electrons and photons and the measurement of their energy by sampling electromagnetic showers with emulsions sheets; moreover, it provides pion to muon separation from dE/dx in the proximity of the track end of range.

Since the ECC is a completely passive device, the brick has to be integrated with electronic detectors. Scintillator plane hodoscopes are inserted in the target section in between the bricks in order to provide a trigger and localize in which brick the neutrino interacted. The latter are arranged into walls and 31 walls + scintillator planes constitute the actual ν target. A muon spectrometer installed at the end of the target is needed for identification and measurement of the charge and momentum of penetrating tracks. OPERA is made of two such targets ("supermodules"), each followed by a spectrometer, as shown in Fig.1. The brick selected as the one in which the neutrino interacted is hence extracted from the target and its emulsion sheets are scanned with automatic microscopes. The installation of the two magnetic spectrometers has been completed in spring 2005 and the installation of the hodoscopes and the support structure for the wall is in progress (see Fig.2). About 50% of the emulsions are already stored underground at LNGS and brick production will start in 2006.

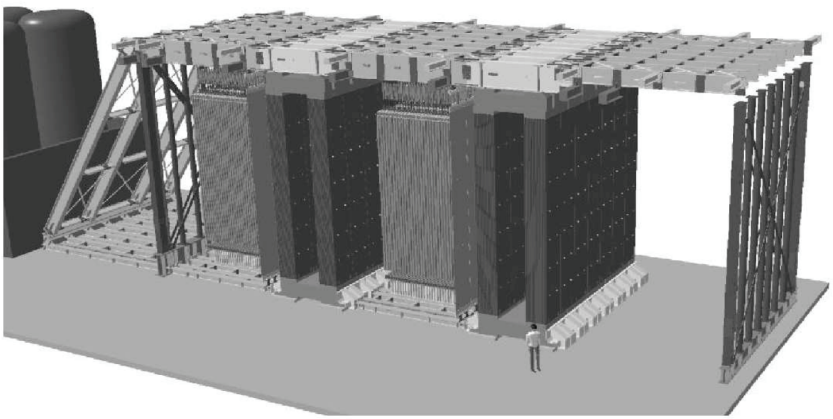

Figure 1: *Layout of the OPERA detector.*

Δm^2	1.9×10^{-3}	2.4×10^{3}	3.0×10^{3}	Bkgd.
Events	6.6 (10)	10.5 (15.8)	16.4 (24.6)	0.7 (1.1)

Table 1: A summary of expected events and background in five years of data taking for nominal and upgraded (in parenthesis) performance of the CNGS and various values of Δm^2 (units are eV^2).

The number of expected signal and background events is presented in Tab.1 for full mixing and various values of Δm^2. Five years of data-taking with the nominal beam (4.5×10^{19} protons on target per year) or with the beam upgrade ($\times 1.5$) are assumed. OPERA can also identify an excess of ν_e resulting from subdominant $\nu_\mu \rightarrow \nu_e$ transitions at the atmospheric scale [4] with a sensitivity comparable to the MINOS experiment (i.e. it can half the present Chooz [5] limit).

4 The ICARUS experiment

Another detector, developed by the ICARUS Collaboration [6], will exploit the CNGS beam. It consists of a large vessel of liquid Argon filled with three planes

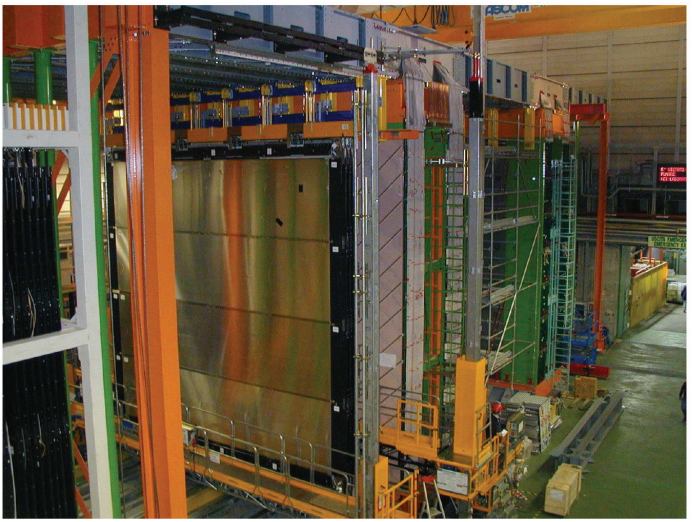

Figure 2: *Installation of OPERA (June 2005).*

of wires strung on different orientations. The device allows tracking, dE/dx measurements and a full-sampling electromagnetic and hadronic calorimetry. Furthermore, the imaging provides excellent electron and photon identification and electron/hadron separation. The energy resolution for electromagnetic showers is about $(3/\sqrt{E(\mathrm{GeV})} \oplus 1)\%$ and for contained hadronic showers $\sim 30/\sqrt{E(GeV)}\%$. ICARUS can gain evidence for ν_τ appearance through a kinematic analysis of neutrino interactions and, for a detector of ~ 3 kton mass, it has a sensitivity comparable with OPERA. At present, a 600 ton module has been successfully operated at surface and it has been installed underground in winter 2004. The construction of additional modules is under discussion and a significant increase of the mass could be achieved during the CNGS operation.

5 Conclusions

The CNGS physics program is aimed at performing a direct test of the oscillation hypothesis based on the explicit identification of the production of new flavors. Moreover this facility can investigate subdominant $\nu_\mu \rightarrow \nu_e$ transitions at the atmospheric scale with a sensitivity significantly better than the present Chooz limit. The construction of CNGS is nearly completed and com-

missioning will start in spring 2006. OPERA is in construction and the first supermodule (half of the total mass) will be operational during the first physics runs of CNGS. Completion of the full detector is expected by the end of 2006. By that time the commissioning underground of the ICARUS 600t module is expected.

References

1. For a review and reference to original literature see G. L. Fogli, E. Lisi, A. Marrone and A. Palazzo, arXiv:hep-ph/0506083, to appear in Progr. Part. Nucl. Phys.

2. G. Acquistapace et al., CERN 98-02, INFN/AE-98/05; CERN-SL/99-034(DI), INFN/AE-99/05 Addendum.

3. M. Guler et al. [OPERA Coll.], CERN-SPSC-2000-028.

4. M. Komatsu, P. Migliozzi and F. Terranova, J. Phys. G **29**, 443 (2003).

5. M. Apollonio et al. [CHOOZ Coll.], Eur. Phys. J. C **27**, 331 (2003).

6. F. Arneodo et al. [ICARUS Coll.], ICARUS-TM/2001-08 LNGS-EXP 13/89 add.2/01.

Frascati Physics Series Vol. XL (2006), pp. 167–172
Frontier Science 2005, New Frontiers in Subnuclear Physics
Milano, 12-16 September, 2005

GLOBAL DETERMINATION OF MIXING PARAMETERS FROM SOLAR AND REACTOR NEUTRINOS AND FUTURE PERSPECTIVES

V. Antonelli, M. Picariello
Dipartimento di Fisica, Università di Milano and INFN, Sezione di Milano
P. Aliani
Université Libre de Bruxelles, Bruxelles (Belgium)
M. Picariello
Dipartimento di Fisica, Università di Milano and INFN, Sezione di Milano
Dipartimento di Fisica, Università di Lecce and INFN, Sezione di Lecce
E. Torrente-Lujan
Universidad de Murcia (Spain) and CERN Theory Division

Abstract

We know by now that neutrinos are massive and oscillating particles and the long standing solar neutrino puzzle has been solved, confirming the Solar Standard Model validity. These results and their phenomenological interpretation are discussed, focusing the attention on the complete phenomenological analysis developed by the Milano group. A new era started, in which the main purpose is not anymore to prove the existence of neutrino oscillations, but to determine with the greatest possible accuracy the mixing parameters. The perspectives of the main running and future experiments are discussed. The new generation of experiments, planned to improve the knowledge of neutrino physics, will probably enable us also to test some Standard Model parameters at low energies.

1 Introduction

Solar and reactor neutrinos (ν) played a central role in ν physics, especially in the last years, when they gave very strong model independent evidences of the fact that ν are massive and oscillating particles. [1, 2, 3]. These results had a great impact on our knowledge of elementary particles and contributed to solve some long standing puzzles, but still important open questions are left. We don't know the real nature of ν (Dirac or Majorana fermion) and consequently the origin of its mass, nor we have a unique explanation of its lightness. The most important data we have at our disposal up to now come from oscillation experiments; they can tell us the values of the differences between the mass eigenvalue squares, but they are not sufficient to fix the absolute mass scale and not even to discriminate between different possible structures for the mass spectrum. Moreover, the level of accuracy at which we know the values of the mixing parameters in many cases is not yet fully satisfactory.

2 Brief history of Solar neutrino problem and of reactor neutrinos

The first indications in favour of the ν oscillation hypothesis came (since the '70s) from the radiochemical experiments on Solar neutrinos. Both Homestake and the experiments (SAGE and Gallex/GNO) using Gallium instead of Chlorine found a clear suppression, with respect to the Solar Standard Model (SSM) predictions, of the electron ν flux reaching the detector. The Gallium experiments included also all the low energy part of the spectrum. A strong confirmation of the existence of the Solar Neutrino Problem (SNP) was given in the last decade by the Japanese water Cerenkov experiments Kamiokande and SuperKamiokande (SK) [1], which studied the elastic $\nu_e - e^-$ scattering (sensitive only to ^8B and hep neutrinos). The milestone for Solar neutrino physics can be considered the SNO experiment [2], a D_20 Cerenkov detector that can study simultaneously different interactions channels. SNO measured the following 3 processes:(A) Charged Current (CC) (sensitive only to ν_e); (B) Neutral Current (NC) (equally sensitive to all active neutrino flavors); (C) Elastic Scattering (ES) (sensitive to all flavours ν but with different "weights"). Different sets of data were obtained in the various phases of working of SNO, since 2001 up to this year. The NC measurement offered the first direct measurement of the total solar ν flux, which was in very good agreement with the

SSM prediction. At the same time, only a small percentage (about 1/3) of this flux is still made up by ν_e, when they reach the detector. This is, up to now, the strongest evidence of oscillation in the leptonic sector. The reactor $\bar{\nu}$ experiments have the advantage of using well known energies and baselines. In a two flavour analysis the survival probability for ν ($\bar{\nu}$) of fixed flavour i depends on the factor $\sin^2(1.27\,\Delta m^2(eV^2)/(L(km)E(GeV))$. The previous reactor experiments had short and medium baselines and therefore couldn't access mass differences smaller than $10^{-3}eV^2$. They didn't find any indication of $\bar{\nu}_e$ disappearance and, hence, put some limitations on the mixing parameters (particularly θ_{13})). The KamLAND (KL) experiment [3] uses, instead, medium energy and baseline ($E \geq 1.8MeV$; baseline $\simeq 139 - 214$ Km) and it is able to test most of the Large Mixing Angle (LMA) region, that is the region of the mixing parameter space giving the SNP solution. The first KL results were published in December 2002. Updated data, with increased statistics were presented in summer 2004. In the most recent analysis signals of spectrum distortion (at low frequencies) have been found at 99.6% C.L. The "no oscillation models" are strongly disfavoured by these data. Combining KL with the solar ν data, one gets: $(\tan^2\theta, \Delta m^2) = (0.40^{+0.10}_{-0.07}, 7.9^{+0.6}_{-0.5} \times 10^{-5}eV^2)$. In the near future KL may improve the Δm^2 determination with a factor two, but the angle discrimination could at most be comparable with the solar one. In 2005 KL also detected for the first time geoneutrinos. In future KL plans to detect ^7Be solar ν detection, but further purification is needed in order to reach this goal.

3 Our analysis and future scenarios

In the last years our group performed a complete study of all the data available from the Solar ν experiments and from KamLAND, including also the limits coming from CHOOZ. We determined the oscillation mixing parameters with the best possible accuracy and investigated the potentialities of the already running and of forthcoming experiments. We can remember, among our main results [4, 5]: the mixing parameters determination in the pre and post-SNO framework; the predictions for Borexino potentialities an the study of KL potentialities before the advent of KL; the analysis of the data of different SNO and KL phases and of their impact. We assumed the ν oscillation hypothesis and included in our analysis the matter interaction effects for solar ν. We refer

the interested reader to [5] for the details of our analysis. Here we just remember that it is based on a series of codes we developed (to study ν propagation, transition probability and interaction with matter) and on a χ^2 analysis.
To appreciate the great impact of the recent experimental results, let's recall the results of the study we performed in 2001 (when only the data about CC were available by SNO and before the publication of the 2002 SK data). As discussed in the first paper, of [5] the best fit point was already in the LMA region, but also two other possible solutions survived at lower C.L: the LOW solution and the Small Mixing Angle. The 2002 data about SNO NC and SK essentially ruled out all the possible solutions apart from the LMA region (as one can see in fig.1). The values of the best fit point were ($\Delta m^2 = 5.44 \times 10^{-5} eV^2; tan^2\theta = 0.40$). KamLAND confirmed the validity of the LMA solution of the SNP. Combining the first KL data with the solar ν data the allowed region was further reduced and one could select two distinct sub-regions inside the LMA solution: the so called LMA I (corresponding to lower values of Δm^2) and LMAII (see fig.2).

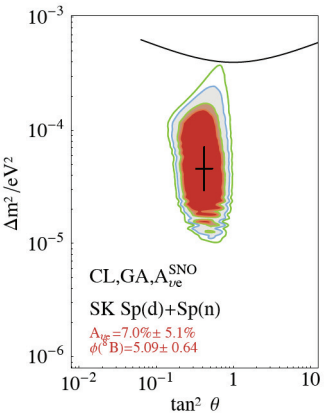

Figure 1: *Our global analysis of Solar ν after the first SNO-NC data*

In the last year new data have been produced by SK and mainly by SNO (salt phase with better efficiency for the NC detection) and KL. Including all these data in the analysis, the LMA-II solution is excluded at a confidence level $\geq 99\%$ and the maximal mixing is excluded at about $5\,\sigma$. Combining KL and the Solar ν data we got the new best fit point for $(tan^2\theta, \Delta m^2) =$

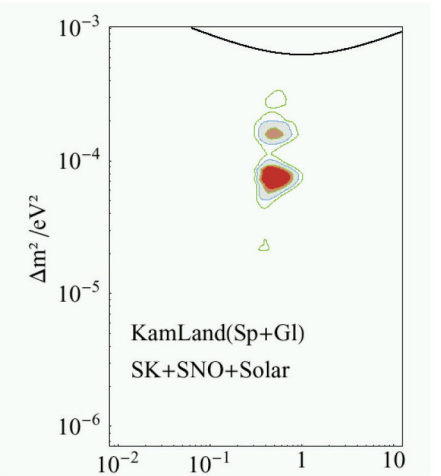

Figure 2: *Result of our global analysis after the first KL data*

$(0.45^{+0.09}_{-0.07}, 8.0^{+0.6}_{-0.4} \times 10^{-5} eV^2)$. In the near future the experiments on solar and reactor ν will continue to be the only way to determine Δm^2_{12} and θ_{12} and they will be essential also for other experiments (very long baselines, superbeams and ν factories) in which these parameters will rule the subleading oscillation effects. Three Solar ν experiments are still running: SAGE, SK and SNO. The SK detector should be fully reconstructed by 2006 and the threshold lowered down to $\simeq 4$ MeV. SNO, in its third phase of working will take advantage from the use of ^{3}He proportional counters to further improve the NC detection. The main issue of both SK and SNO will be the detailed study of ^{8}B and hep spectra, searching for signal of spectrum distortion (not found up to now) and studying the day-night asymmetries. Up to now only the high energy part of Solar ν spectrum (above 5 MeV) has been studied in a detailed way; the energy spectrum of more than 99% of Solar neutrinos have not been measured yet. In particular for the two main components (p-p and ^{7}Be neutrinos) we have only integral measurements of the flux, from the radiochemical experiments. It would be really important for future experiments to measure directly these components. There are a lot of proposal for new future Solar ν experiments and also to replace the heavy water in SNO with a liquid scintillator. Hence,

reactor and Solar experiments will continue to be very important also in the near future, even if they will not anymore play the unique central role of the last five years. We should be able to complement the Solar and reactor ν data with the ones coming from other already planned or proposed future experiments studying oscillations (long baseline accelerator experiments, superbeams and later on neutrino factories and/or β beams). An interesting by-product of these experiments will be the possibility of using high intensity neutrino beams to test some Standard Model parameters at energies much lower than the ones of LEP and future colliders [6].

4 Acknowledgements

We are grateful to R. Ferrari for the work done together and for many enlightening discussions. V.A. would like to thank the organizers for their kind invitation and for the pleasant and stimulating atmosphere of the Conference.

References

1. S. Fukuda *et al*, PLB **539** 179 (2002); J. Hosaka, hep-ex/0508053.
2. Q.R. Ahmad *et al*, PRL **89**, 011302 (2002); B. Aharmim *et al*, Phys. Rev. **72 C**, 055502 (2005).
3. K. Eguchi *et al*, PRL **90**, 021802(2003); T. Araki, PRL **94**, 081801 (2005).
4. P. Aliani, V. Antonelli, R. Ferrari, M. Picariello and E. Torrente-Lujan, Phys. Rev. **D 67**, 013006 (2003) and arXiv:hep-ph/0406182
5. P. Aliani, V. Antonelli, M. Picariello and E. Torrente-Lujan, NPB**634**, 393 (2002); N.J.Phys. **5**, 2 (2003); PRD **69**, 013005 (2004); hep-ph/0309156.
6. V. Antonelli, G. Battistoni and S. Forte, work in progress

Frascati Physics Series Vol. XL (2006), pp. 173–177
Frontier Science 2005, New Frontiers in Subnuclear Physics
Milano, 12-16 September, 2005

MEASUREMENT OF CHARM PRODUCTION AND DECAY BY CHORUS

G. De Rosa
University of Naples, Italy

Abstract

The CHORUS detector was exposed to the neutrino beam of the CERN SPS during the years 94-97. About 150,000 ν_μ events have been collected in the nuclear emulsion target and analyzed. With the present performance of the emulsion scanning systems, it has become possible to perform large area volume scanning around interaction vertex to detect decay topologies. This technique has been exploited to search for events where charmed particles are produced and very lose kinematical cut are applied. This translates into a very good sensitivity to low neutrino energy and so to the slow-rescaling threshold effects. More than 2000 events with a recognized charm decay have been collected. CHORUS results on charm production mechanism will be useful to improve MonteCarlo simulations and to get predictions on charm expected events in the present and future experiments.

1 The CHORUS experiment

CHORUS experiment was designed as hybrid, namely with electronic detectors to reconstruct the event kinematics and with nuclear emulsions used both as active target and as detector, allowing three-dimensional reconstruction of short-lived particles the charmed hadrons. For details on CHORUS detector we refer to Ref. [1].

The CHORUS detector was exposed to the wide band neutrino beam of the CERN SPS during the years 1994-1997, with an integrated flux of 5.06×10^{19} protons on target. The beam consists mainly of ν_μ of 27 GeV average energy with a 5% $\bar{\nu}_\mu$ component of 18 GeV average energy. From a sample of about 94,000 neutrino events in emulsion, 2013 events was confirmed as charm events by visual inspection in emulsion. In order to identify charm decays, a fiducial volume around the vertex position is analyzed and all track segments are recorded. We refer to this type of scanning, originally developed for the DONUT experiment [2], as NetScan data taking [3]. Events with all emulsion tracks not converging into a common vertex potentially contain a decay topology. For these events, a visual inspection of the nuclear emulsion allows to confirm the decay vertex and reject hadron interactions. A secondary vertex found in emulsion is tagged as a decay if no other activity (nuclear break-up or Auger electron) is observed at the decay point and if the number of charged tracks is consistent with charge conservation. Charm candidates are denoted as V2, V4 or V6 for neutral and C1, C3 and C5 for charged decays according to their multiplicity. The main background for D^0 detection comes from K_s^0 and Λ decays, whereas for charged charmed hadrons the main background are π, K and Σ decays in flight and the white interactions, namely hadron interactions without any visible nuclear break up. The sample of confirmed charm events is shown in Tab.1.

2 Charm Analysis

2.1 Measurements of D^0 production

From the sample of 2013 confirmed charm events, 1048 charged-current interactions with a D^0 in the final state were selected. The ratio of decay branching fractions of the D^0 into four charged particles to two charged particles was measured to be $B(D^0 \to V4)/B(D^0 \to V2) = 0.207 \pm 0.016 \pm 0.004$. The value

Table 1: *Confirmed charm sample in CHORUS.*

2ry vertex topology	Number of events
V2	819
V4	226
V6	3
C1	452
C3	491
C5	22

of the total D^0 production rate relative to the charged-current cross-section was found to be $\sigma(D^0)/\sigma(\mathrm{CC}) = (0.0269 \pm 0.0018 \pm 0.0013)$. From an observed number of three charged six-prong events the branching ratio into six charged particles was determined to be $(1.2^{+1.3}_{-0.9} \pm 0.2) \times 10^{-3}$. In addition, by using the well known $BR(D^0 \to V4) = (0.134 \pm 0.006)$ from the PDG [4] tables, a value of $(0.218 \pm 0.049 \pm 0.036)$ was found for the branching ratio of D^0 decaying into neutral particles. It is necessary for noting that it was previously assumed to be about 5%. Since this decay mode is not detectable in all the experiments which recognize the D^0 through its charged daughters, this new result affect a lot several previous measurements. Details on measurements of D^0 production in CHORUS can be found in Ref. [5].

2.1.1 *Measurement of D^{*+} production in charged-current neutrino interactions*

Using the decay mode $D^{*+} \to D^0\pi^+$ a production cross-section measurement of the D^{*+} in neutrino-nucleon charged-current interactions was performed. The low Q-value of the decay was used to isolate a sample of candidate events containing a positive hadron with a small p_T with respect to the D^0 direction. The D^{*+} production cross-section relative to the D^0 production cross-section, $\sigma(D^{*+})/\sigma(D^0)$, was estimated to be $0.38 \pm 0.09(\mathrm{stat}) \pm 0.05(\mathrm{syst})$. From this result, assuming that the D^{*+} and D^{*0} production rates are equal and recalling that the D^{*0} always decays into a D^0, the fraction of D^0's produced via the decay of a D^{*+} was deduced to be (0.63 ± 0.17). The D^{*+} production cross-section relative to the ν_μ charged-current interaction, $\sigma(D^{*+})/\sigma(CC)$, was estimated to be $1.02 \pm 0.25(\mathrm{stat}) \pm 0.15(\mathrm{syst})$. Details on D^{*+} production as measured in CHORUS can be found in Ref. [6].

2.1.2 Charm production in antineutrino charged-current interactions

Antineutrino induced charm production was never observed in emulsions. Thus no data is available for low neutrino energies, just where the antineutrino induced charm production differs from the neutrino case. In CHORUS, the analysis is based on a sample of 96,472 events with at least one reconstructed muon in the spectrometer [7)]. The number of $\bar{\nu}_\mu$CC interactions corrected for the contaminations and for the efficiencies is evaluated to be $4,975 \pm 194$. A selection criterion providing an improved charge determination over the whole antineutrino energy spectrum was applied on the events with an observed decay topology leaving 32 $\bar{\nu}_\mu$ candidates. A value of $\sigma(\bar{\nu}_\mu N \to \mu^+ \bar{c} X)/\sigma(\bar{\nu}_\mu N \to \mu^+ X) = (5.0^{+1.4}_{-1.0})\%$ is obtained for the charm production rate induced by $\bar{\nu}_\mu$ at an average antineutrino energy of 18 GeV.

2.2 The semi-muonic branching ratio

Based on the full charm data sample, the effective branching ratio of charmed particles into muons was determined [8)] to be $B_\mu = [7.3 \pm 0.8 \text{ (stat)} \pm 0.2 \text{ (syst)}] \times 10^{-2}$. Normalization of the muonic decays to charged-current interactions provides $\sigma_{\mu^-\mu^+}/\sigma_{\rm cc} = [3.16 \pm 0.34 \text{ (stat)} \pm 0.09 \text{ (syst)}] \times 10^{-3}$. Selecting only events with visible energy greater than 30 GeV gives a value of B_μ that is less affected by the charm production threshold and quasi-elastic Λ_c production. Combining this value with the current average of $B_\mu \times |V_{\rm cd}|^2$ at the leading order yields the value of $|V_{\rm cd}|_{\rm LO} = 0.236 \pm 0.016$.

2.3 Measurement of fragmentation properties of charmed particle production in charged-current neutrino interactions

Using a high-statistics inclusive D^0 sample obtained by selecting decay topologies in an emulsion target, a study of the fragmentation parameters was performed. In emulsion, the momentum of the parent D^0 can be inferred by exploiting the correlation between the momentum and the angular distribution of the decay products. These angles are measured very precisely allowing a measurement of the z variable. The mean value of z was measured to be $\langle z \rangle = 0.63 \pm 0.03 \pm 0.01$. From fits to the z distribution, values for the Peterson parameter $\epsilon_P = 0.108 \pm 0.017(\text{stat}) \pm 0.013(\text{syst})$ and the Collins-Spiller parameter $\epsilon_{CS} = 0.21^{+0.05}_{-0.04}(\text{stat}) \pm 0.04(\text{syst})$ are found. These results are in

agreement with other measurements. Details on measurement of fragmentation properties in CHORUS can be found in Ref. [9].

2.4 Associated charm production

The small cross section of neutrino interaction, together with the requirement for production of two charmed hadrons in the final state, makes the associated charm production very rare and, therefore, difficult to observe. In CHORUS, in a sample of in 95,540 CC events, 5 candidates for associated charm-production have been found. Similarly, 3 candidates have been found in a sample of 26,568 NC events. The data analysis is in progress.

References

1. E. Eskut, et al., CHORUS Collaboration, *Nuclear Instruments and Methods* **A401**, 7 (1997).
2. K. Kodama, et al., DONUT Collaboration, *Nuclear Instruments and Methods* **A493**, 45 (2002).
3. N. Nonaka. PhD thesis, Nagoya University, Japan, 2002.
4. Particle Data Group, K.Hagiwara *et al.*, Phys. Rev. D **66**, 010001 (2002).
5. Chorus Coll., Measurements of D^0 production and of decay branching fractions in neutrino nucleon scattering; Phys.Lett.B613:105-117,2005.
6. Chorus Coll., Measurements of D^*+ production in charged-current neutrino interactions; Phys.Lett.B614:155-164,2005.
7. Chorus Coll., Measurement of charm production in antineutrino charged-current interactions; Phys.Lett.B 604:11-21, 2004.
8. Chorus Coll., Measurement of topological muonic branching ratios of charmed hadrons produced in neutrino-induced charged-current interactions, Phys.Lett.B626:24-34,2005.
9. Chorus Coll., Measurement of fragmentation properties of charmed particle production in charged-current neutrino interactions; Phys.Lett.B 604:145-156,2004.

Frascati Physics Series Vol. XL (2006), pp. 179–184
Frontier Science 2005, New Frontiers in Subnuclear Physics
Milano, 12-16 September, 2005

CHIPS SIMULATION OF THE CHARGED CURRENTS NEUTRINO INTERACTIONS WITH NUCLEI IN GEANT4

M. V. Kosov
CERN, 1211 Geneva, Switzerland

Abstract

Structure functions of nucleons are approximated as a sum of multiperipheral and direct interaction terms. This approximation provides a good fit for electro- and muon-nuclear reactions at any Q^2 starting $Q^2 = 0$, so it fits the photo-nuclear total cross-sections. To fit the weak (ν, μ) reactions $f_2(x, Q^2) = F_2(x, Q^2)|_{e_V^2=1, e_S^2=1}$ structure functions are used (e_V^2 and e_S^2 are mean charges of valence and sea quarks). Being integrated the approximation fits the (ν, μ) total and quasi-elastic cross-sections for all energies of neutrinos.

Simulation of DIS reactions in the GEANT4 toolkit [1] includes reactions with high Q^2. The first approximation of the Q^2-dependent photonuclear cross-sections at high Q^2 was made in [2], where the modified photonuclear cross-sections of virtual photons [3] were used. Recently the structure functions of protons and deuterons have been approximated in CHIPS [4] as a sum

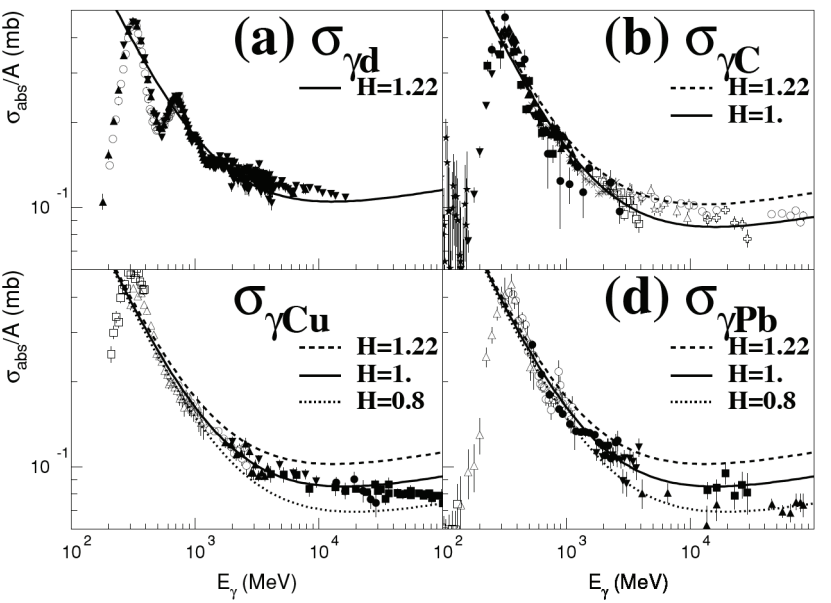

Figure 1: *Fit of γA cross-sections with different H values. Data are from* [2].

of nonperturbative multiperipheral and nonperturbative direct interactions of virtual photons with hadronic partons:

$$F_2(x,Q^2) = [A(Q^2)\cdot x^{-\Delta(Q^2)} + B(Q^2)\cdot x]\cdot(1-x)^{N(Q^2)-2}, \qquad (1)$$

where $A(Q^2) = \bar{e_S^2}\cdot D\cdot U$, $B(Q^2) = \bar{e_V^2}\cdot(1-D)\cdot V$, $\bar{e^2}_{V(p)} = \frac{1}{3}$, $\bar{e^2}_{V(d)} = \frac{5}{18}$, $\bar{e_S^2} = \frac{1}{3} - \frac{\frac{1}{3}-\frac{5}{18}}{1+m_\phi^2/Q^2} + \frac{\frac{1}{3}-\frac{5}{18}}{1+m_{J/\psi}^2/Q^2} - \frac{\frac{1}{3}-\frac{19}{63}}{1+m_\Upsilon^2/Q^2}$, $N = 3 + \frac{0.5}{\alpha_s(Q^2)}$, $\alpha_s(Q^2) = \frac{4\pi}{\beta_0 ln(1+\frac{Q^2}{\Lambda^2})}$, $\beta_0^{(n_f=3)} = 9$, $\Lambda = 200\ MeV$, $U = \frac{(3\ C(Q^2)+N-3)\cdot\Gamma(N-\Delta)}{N\cdot\Gamma(N-1)\cdot\Gamma(1-\Delta)}$, $V = 3(N-1)$, $D(Q^2) = H\cdot S(Q^2)\left(1 - \frac{1}{2}S(Q^2)\frac{\bar{e_V^2}}{\bar{e_S^2}}\right)$, $S = \left(1+\frac{m_\rho^2}{Q^2}\right)^{-\alpha_P(Q^2)}$, $\alpha_P = 1+\Delta(Q^2)$, $\Delta = \frac{1+r}{12.5+2r}$, $r = \left(\frac{Q^2}{1.66}\right)^{1/2}$, $C = \frac{1+f}{g\cdot(1+f/.24)}$, $f = \left(\frac{Q^2}{0.08}\right)^2$, $g = 1+\frac{Q^2}{21.6}$. The parton distributions are normalized to the unit total momentum fraction.

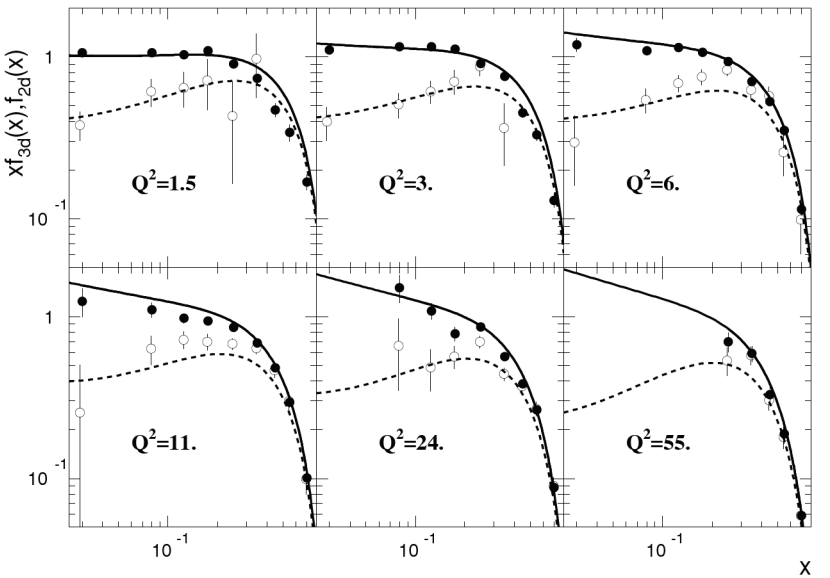

Figure 2: *Fit of $f_{2d}(x,Q^2)$ (filled circles, solid lines) and $f_{3d}(x,Q^2)$ (open circles, dashed lines) structure functions measured by WA25 experiment* [5].

The photonuclear cross-sections are calculated by the eikonal formula:

$$\sigma_{\gamma}^{tot} = \left[\frac{4\pi\alpha}{Q^2}F_2\left(\frac{Q^2}{2M\nu},Q^2\right)\right]_{Q^2=0}^{\nu=E}, \qquad (2)$$

An example of the approximation is shown in Fig. 1. One can see that the hadronic resonances are "melted" in nuclear matter and the multiperipheral part of the cross-section (high energy) is shadowed.

The differential cross-section of the (ν,μ) reaction was approximated as

$$\frac{yd^2\sigma^{\nu,\bar{\nu}}}{dydQ^2} = \frac{G_F^2\cdot M_W^4}{4\pi\cdot(Q^2+M_W^2)^2}\left[c_1(y)\cdot f_2(x,Q^2)\pm c_2(y)\cdot xf_3(x,Q^2)\right], \qquad (3)$$

where $c_1(y)=2-2y+\frac{y^2}{1+R}$, $R=\frac{\sigma_L}{\sigma_T}$, $c_2(y)=y(2-y)$. As $\bar{e_V^2}=\bar{e_S^2}=1$ in Eq.1, hence $f_2(x,Q^2) = \left[D\cdot U\cdot x^{-\Delta}+(1-D)\cdot V\cdot x\right]\cdot(1-x)^{N-2}$, $xf_3(x,Q^2) =$

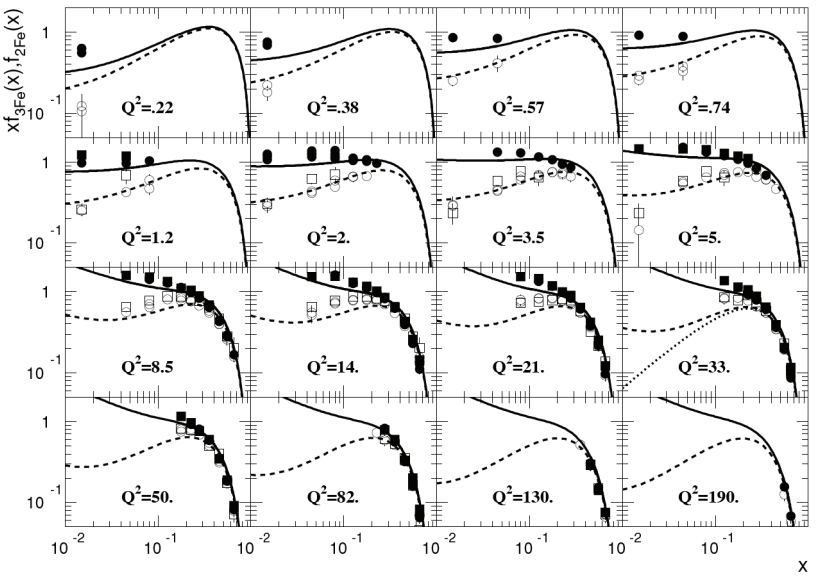

Figure 3: *Fit of $f_{2Fe}(x,Q^2)$ (filled markers, solid lines) and $f_{3Fe}(x,Q^2)$ (open markers, dashed lines) structure functions measured by CDHSW* [6] *(circles) and CCFR* [7] *(squares) experiments.*

$\left[D\cdot U_{f3}\cdot x^{-\Delta}+(1-D)\cdot V\cdot x\right]\cdot(1-x)^{N-2}$, with $D=H\cdot S(Q^2)\cdot\left(1-\frac{1}{2}S(Q^2)\right)$ and $U_{f3}=\frac{3\cdot C(Q^2)\cdot\Gamma(N-\Delta)}{N\cdot\Gamma(N-1)\Gamma(1-\Delta)}$. The approximation is compared with data in Fig.2 for deuterium [5] and in Fig.3 for iron [6, 7]. It must be emphasized that the CHIPS parton distributions are the same as for electromagnetic reactions.

For the (ν,μ) amplitudes one can not apply the optic theorem, so to calculate the total cross-sections, it is necessary to integrate the differential cross sections first over x and then over Q^2. For the (ν,μ) reactions the differential cross section can be integrated with good accuracy even for low energies because it does not have a $\frac{1}{Q^4}$ factor of the boson propagator. The quasi-elastic part of the total cross-section can be calculated as a $W<m_N+m_\pi$ part. The total (ν,μ) cross-sections are shown in Fig.4(a,b). The dashed curve corresponds to the GRV [8] approximation of parton distributions and the dash-dotted curves

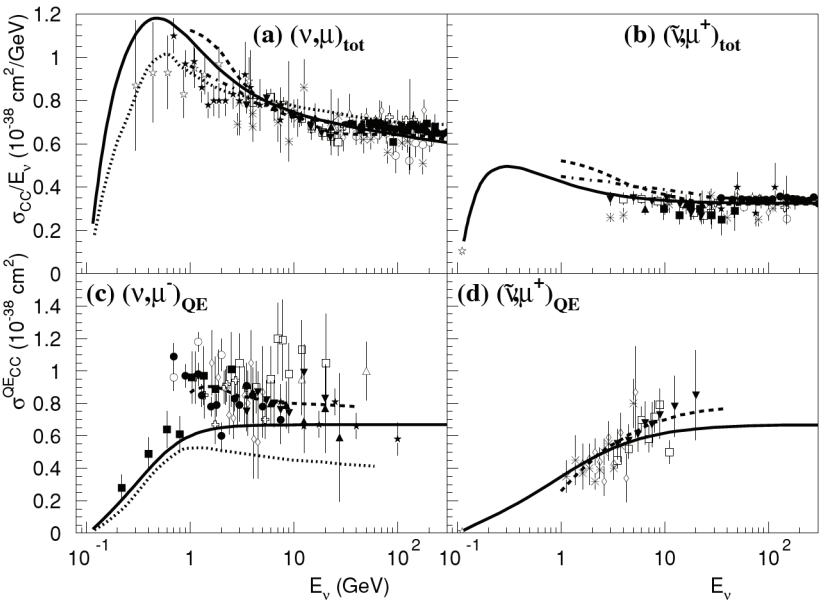

Figure 4: *Fit of total (a,b) and quasi-elastic (c,d) cross-sections of* (ν, μ) *reactions (Geant4 data base). The solid line is CHIPS approximation (for other lines see text).*

correspond to the KMRS [9] approximation. Both approximations do not fit low energies, because the perturbative calculations give parton distributions only for $Q^2 > 1\ GeV^2$. In [10] an attempt was made to freeze the DIS parton distributions at $Q^2 = 1$ and to use them at low Q^2. The $W < 1.4\ GeV$ part of DIS was replaced by the quasi-elastic and one pion production contributions, calculated on the basis of the low energy models. The results of [10] are shown by the dotted lines. The nonperturbative CHIPS approximation (the solid curves) fits both total and quasi-elastic cross-sections even at low energies.

The quasi-elastic (ν, μ) cross-sections are shown in Fig.4(c,d). The CHIPS approximation (solid line) is compared with calculations made in [10] (the dotted line) and the best fit of the $V - A$ theory made in [11] (the dashed lines). One can see that CHIPS gives reasonable approximation.

The Q^2 spectra for each energy are known as an intermediate result of the calculation of total or quasi-elastic cross-sections. For the quasi-elastic interactions ($W < m_N + m_\pi$) one can use $x = 1$ and simulate a binary reaction. In final state the recoiled nucleon has some probability to interact with the nucleus. If $W > m_N + m_\pi$ the Q^2 value is randomized and therefore the Q^2 dependent coefficients (the number of partons in nonperturbative phase space N, the Pomeron intercept α_P, the fraction of the direct interactions etc.) can be calculated. Then for the fixed energy and Q^2 the neutrino interaction with quark-partons (directly or through the Pomeron ladder) can be randomized and the secondary parton distribution can be calculated. In vacuum or in nuclear matter the secondary partons are creating quasmons [12, 13] which decay in secondary hadrons.

References

1. GEANT4 Collaboration,S.Agostinelli *et al*,Nucl.Inst.Meth.A**506**,250(2003).
2. M.V. Kossov, Eur. Phys. J. A **14**, 377 (2002).
3. F.W. Brasse *et al*, Nucl. Phys. B **110**, 413 (1976).
4. M.V. Kossov, Eur. Phys. J. A, **14**, 265 (2002).
5. D. Allasia *et al*, Z. Phys C **28**, 321 (1985).
6. P. Berg *et al*, Z. Phys C **49**, 187 (1991).
7. E. Oltman *et al*, Z. Phys C **53**, 51 (1992).
8. M. Glück *et al*, Z. Phys. C **48**, 471 (1990).
9. J. Kviecinski *et al*, Phys. Rev. D **42**, 3645 (1990).
10. P. Lipari *et al*, Phys. Rev. Let. **74**, 4384 (1995).
11. S.V. Belikov *et al*, Z. Phys. A **320**, 625 (1985).
12. P.V.Degtyarenko, M.V.Kossov, H.P.Wellisch, Eur. Phys. J. A **8**, 217 (2000).
13. P.V.Degtyarenko, M.V.Kossov, H.P.Wellisch, Eur. Phys. J. A **9**, 411 (2001).

Frascati Physics Series Vol. XL (2006), pp. 185–194
Frontier Science 2005, New Frontiers in Subnuclear Physics
Milano, 12-16 September, 2005

DOUBLE BETA DECAY

E. Previtali
INFN Sezione di Milano, Via Celoria 16, I-20133 Milano and
Universitá di Milano-Bicocca, Piazza della Scienza 3, I-20126 Milano

Abstract

The present status of experiments for neutrinoless double-beta decay searches ($\beta\beta(0\nu)$) is reviewed. With the present knowledge of neutrino masses and mixing parameters, after the results of neutrino oscillations experiments, there are indications that a $\beta\beta(0\nu)$ at a neutrino mass scale $m_\nu \approx$10-50 meV could be possible. These values represent a real challenge for the new proposed $\beta\beta(0\nu)$ projects, which are reviewed in this paper.

1 Introduction

The existence of neutrino oscillations demonstrates that neutrinos have finite masses and mixing. New oscillation experiments aiming at improving our present knowledge of neutrino masses and mixing parameters are currently

under preparation. However some relevant neutrino characteristics are inaccessible to them: oscillation experiments can only measure differences of the neutrino masses squared ($|\Delta m^2_{ij}|$) and, while Δm^2_{ij} sign could be in principle measured through oscillation matter effects, only experiments sensitive to a linear combination of neutrino masses have a reasonable capability to determine the absolute neutrino mass scale in a near future. It is the case for kinematic measurements of the β spectrum end-point, $\beta\beta(0\nu)$ and cosmological measurements which are respectively sensitive to

$$\langle m_\beta \rangle \equiv \sqrt{\sum_{k=1}^{3} |U^L_{ek}|^2 m_k^2} \tag{1}$$

$$\langle m_{\beta\beta} \rangle \equiv \sum_{k=1}^{3} |U^L_{ek}|^2 m_k e^{i\phi_k} \tag{2}$$

$$\langle m_{COSM} \rangle \equiv \sum_{k=1}^{3} m_k \tag{3}$$

where m_k are the neutrino mass eigenvalues and U^L_{ek} are elements of the first line of the neutrino mixing matrix. Two possible hierarchies are implied by current available data: the normal ($m_1 \approx m_2 << m_3$) and the inverted hierarchy ($m_3 << m_1 \approx m_2$) while nothing can be yet inferred about the lowest mass eigenvalue. A similar ignorance holds also for the neutrino nature (Dirac/Majorana). In the Standard Model (SM) of the electro-weak interactions neutrinos are Dirac particles by construction to conserve lepton number L. In the limit of vanishing masses however lepton number conservation can be equivalently stated in terms of neutrino helicity properties and Majorana or Dirac descriptions are equivalent. For finite neutrino masses the two descriptions are no more equivalent and can give rise to different physical scenarios for mass generation mechanisms [1)]: only Majorana massive neutrinos allow $\beta\beta(0\nu)$.

2 Double Beta Decay

Double Beta Decay ($\beta\beta$) is a rare nuclear decay in which one nucleus decay into an isobar with a simultaneous change of two neutrons into two protons. For some even-even nuclei this transition is possible thanks to the inhibition of

a single beta decay due to energy conservation. Nuclear transitions accompanied by positron emission or electron capture processes are also possible; they are however characterized by poorer experimental sensitivities and will not be discussed. Several $\beta\beta$ decay modes are possible: the 2ν mode

$$ {}^{A}_{Z}X \rightarrow {}^{A}_{Z+2}X + 2e^{-} + 2\overline{\nu} \tag{4} $$

it is allowed in the SM and it conserves the lepton number; the 0ν mode

$$ {}^{A}_{Z}X \rightarrow {}^{A}_{Z+2}X + 2e^{-} \tag{5} $$

which violates the lepton number by two units and it is considered as a powerful tool to test neutrino properties [2]; a third decay mode in which one or more light neutral bosons χ (Majorons) are also emitted

$$ {}^{A}_{Z}X \rightarrow {}^{A}_{Z+2}X + 2e^{-} + N\chi \tag{6} $$

it requires the existence of a Majoron, a massless Goldstone boson that arises upon a global breakdown of B–L symmetry, where B and L are the baryon and the lepton number respectively. In the following, we will focus our attention only to the $\beta\beta(0\nu)$ mode. In all envisaged modes, $\beta\beta(0\nu)$ is a very rare transition, hence characterized by very long lifetimes. $\beta\beta(0\nu)$ observation would necessarily imply that neutrinos are Majorana massive particles and it allows to fix the absolute neutrino mass scale. Experimental lower limits on the decay lifetimes can only translate into independent limits on each of the possible contributions to the decay amplitude. The $\beta\beta(0\nu)$ rate is usually expressed as

$$ [T^{0\nu}_{1/2}]^{-1} = G^{0\nu}|M^{0\nu}|^2|\langle m_\nu \rangle|^2 \tag{7} $$

where $G^{0\nu}$ is the phase space integral, $|M^{0\nu}|^2$ is the nuclear matrix element and $\langle m_\nu \rangle$ is the *effective neutrino* mass parameter (eq. 1) measured in $\beta\beta(0\nu)$. Predictions on $\langle m_\nu \rangle$ based on the recent neutrino oscillation results have been derived by various authors [3]: a $\beta\beta(0\nu)$ sensitivity in the range $\langle m_\nu \rangle$ ~10-50 meV could definitely rule out inverse and quasi-degenerate hierarchies.

As it is apparent from eq. (7) the derivation of $\langle m_\nu \rangle$ from the experimental results on $\beta\beta(0\nu)$ lifetime requires a precise knowledge of the transition Nuclear Matrix Elements (NME). Unfortunately a definite knowledge of NME values and uncertainties is still lacking in spite of the attention attracted by this

Table 1: Theoretically evaluated $\beta\beta(0\nu)$ half-lives (units of 10^{28} years for $\langle m_\nu \rangle = 10$ meV).

Isotope	[5)]	[6)]	[7)]	[8)]	[9)]	[10)]	[11)]	[4)]
^{48}Ca	3.18	8.83	-	-	-	-	2.5	-
^{76}Ge	1.7	17.7	14.0	2.33	0.26–0.58	3.2	3.6	5.7
^{82}Se	0.58	2.4	5.6	0.6	-	0.8	1.5	1.7
^{100}Mo	-	-	1.0	1.28	-	0.3	3.9	3.4
^{116}Cd	-	-	-	0.48	-	0.78	4.7	2.1
^{130}Te	0.15	5.8	0.7	0.5	0.077–1.1	0.9	0.85	2.2
^{136}Xe	-	12.1	3.3	2.2	-	5.3	1.8	4.6
^{150}Nd	-	-	-	0.025	-	0.05	-	0.23
^{160}Gd	-	-	-	0.85	-	-	-	-

research area. Many conflicting evaluations are available in literature and it is difficult to judge their correctness or accuracy. A popular attitude consists in considering the spread in the evaluations as an estimate of their uncertainties: this produces a spread of about one order of magnitude in the calculated half lifetimes (Tab. 1), which corresponds to a factor of ∼3 in $\langle m_\nu \rangle$.

3 Experimental approaches

Two main approaches have been followed so far to investigate $\beta\beta$: i) indirect or inclusive methods and ii) direct or counter methods. Inclusive methods are based on the measurement of anomalous concentrations of the daughter nuclei in properly selected samples, characterized by very long accumulation times. Counter methods are based instead on the direct observation of the two electrons emitted in the decay: different experimental parameters (energies, momenta, topology, etc.) can then be registered according to the capabilities of the employed detectors. Counter methods are further classified in *passive* (when electrons originate in an external sample) and *active* source experiments (when the source serves also as detector). The various $\beta\beta$ modes are characterized by different electron sum energies: a continuous distribution for $\beta\beta(2\nu)$ and $\beta\beta(0\nu, \chi)$, and a sharp line at the transition energy for $\beta\beta(0\nu)$. Direct counting experiments with good energy resolution are presently the most attractive approach for $\beta\beta(0\nu)$ searches. Experimental evidence for several $\beta\beta(2\nu)$ decays

as well as improved lower limits on the lifetimes of many $\beta\beta(0\nu)$ emitters (Tab. 2) have been provided using the measured two-electron sum energy spectra, the single electron energy distributions and the event topology.

Various different conventional counters have been used in $\beta\beta$ direct searches solid state devices (Germanium spectrometers and Silicon detector stacks), gas counters (time projection chambers, ionization and multiwire drift chambers) and scintillators (crystal scintillators and stacks of plastic scintillators). New techniques based on low temperature *true* calorimeters have been proposed and developed in order to improve the experimental sensitivity and enlarge the choice of suitable candidates for $\beta\beta$ searches. A common feature of all $\beta\beta$ experiments has been the fight against backgrounds caused mainly by environmental radioactivity, cosmic radiation and residual radioactive contaminations of the detector setup elements. The further suppression of such backgrounds will be the actual challenge for future projects whose main goal will be to maximize $\beta\beta(0\nu)$ rate while minimizing background contributions.

In order to compare the performance of different $\beta\beta$ experiments an experimental *sensitivity* or detector *factor of merit* is usually introduced. This is defined as the process half-life corresponding to the maximum signal n_B that could be hidden by the background fluctuations at a given statistical C.L. at 1σ level ($\mathrm{n}_B{=}\sqrt{BTM\Delta}$):

$$F_{0\nu} \quad = \quad \ln 2 \frac{x\ \eta\ \epsilon\ N_A}{A} \sqrt{\frac{M\ T}{B\ \Delta}}\ (68\% C.L.) \tag{8}$$

where B is the background level per unit mass and energy, M is the detector mass, T is the measure time, Δ is the FWHM energy resolution, $\mathrm{N}_{\beta\beta}$ is the number of $\beta\beta$ decaying nuclei under observation, η their isotopic abundance, N_A the Avogadro number, A the compound molecular mass, x the number of $\beta\beta$ atoms per molecule, and ϵ the detection efficiency. Despite its simplicity, equation (8) has the advantage of emphasizing the role of the essential experimental parameters: mass, measuring time, isotopic abundance, background level and detection efficiency. Only second generation experiments characterized by very large masses, good energy resolutions and extremely low background will have a chance to reach the $\langle m_\nu \rangle$ region below 50 meV.

large extension of the TeO_2 bolometric array concept pioneered by the Milano group at the Gran Sasso Laboratory since the eighties. CUORE would consist in a rather compact cylindrical structure of 988 cubic natural TeO_2 crystals of 5 cm side (750 g), arranged into 19 separated *towers* (13 *planes* of 4 crystals each) and operated at a temperature of 10 mK. The expected energy resolution is ∼5 keV FWHM at the $\beta\beta(0\nu)$ transition energy (2.528 MeV). A background level lower than 0.01 c/keV/kg/y is expected by extrapolating the CUORICINO background results and the dedicated CUORE R&D measurements to the CUORE setup. CUORE technical feasibility is demonstrated by the successful operation of CUORICINO which represents just a slightly modified version of one of its 19 towers. The high natural abundance of ^{130}Te results in a relatively low cost for a detector sensitive to the degenerate neutrino mass region (Tab. 3). Thanks to the bolometer's versatility, alternative options with respect to TeO_2 could be taken into consideration and moreover the cost of enriched ^{130}Te needed to extend the sensitivity, is lower than for other isotopes. CUORE has been approved by the Italian and LNGS Scientific committees and is under construction at LNGS. It is presently the only second generation experiment with a timely schedule for data taking in 2010.

EXO [28] (Enriched Xenon Observatory) is a challenging project based on a large mass (∼ 1–10 tons) of isotopically enriched (85% in ^{136}Xe) Xenon. An ingenuous tagging of the doubly charged Ba isotope produced in the decay ($^{136}Xe \rightarrow ^{136} Ba^{++} + 2e^-$) would allow an excellent background suppression. The technical feasibility of such an ambitious project aiming at a complete suppression of all the backgrounds requires a hard R&D phase. The unavoidable $\beta\beta(2\nu)$ contribution is however a serious concern due to the poor energy resolution of Xe detectors. To improve energy resolution, the energy deposited in the detector is measured by both charge and scintillation while only the ionization signal is used to localize the event vertex for background rejection. A smaller prototype experiment (EXO-200) with a Xe mass of 200 kg (80% ^{136}Xe), is presently under construction to be installed at WIPP and should be operational in 2008-2009. The prototype has no barium tagging and should reach an energy resolution of ∼1.6% at 2.5 MeV. The primary goal is to measure ^{136}Xe $\beta\beta(2\nu)$ and to study $\beta\beta(0\nu)$ with a sensitivity of $\sim 10^{25}$ y in two years of data taking. In parallel, different approaches for barium tagging to be incorporated in the final full-scale experiment are being investigated.

The proposed Super-NEMO experiment is based on a *passive source* approach. It is an extension of the NEMO3 concept scaled in order to accommodate ∼100 kg of ^{82}Se foils spread among 20 detector modules. The proposed geometry is planar. The energy resolution will be improved from 12% FWHM to 7% FWHM to improve the signal detection efficiency from 8% to 40% and reduce the $\beta\beta(2\nu)$ contribution. The detector modules will have an active water shield to further reduce any cosmic ray backgrounds. The proposed detector dimensions will require a larger hall than is currently available at Frejus, and can be installed in the new Canfranc underground lab. If funded, Super-NEMO is projected to start operations in 2011.

5 Conclusions

A renewed interest in $\beta\beta(0\nu)$ searches has been stimulated by recent neutrino oscillation results. $\beta\beta(0\nu)$ is recognized as a unique tool to measure neutrino properties (nature, mass scale, intrinsic phases) unavailable to the experiments on neutrino oscillations. Present $\langle m_\nu \rangle$ sensitivities are still outside the range required to test the inverted neutrino mass hierarchy. A phased $\beta\beta(0\nu)$ program based on a number of newly proposed experiments (possibly on different isotopes) is of primary importance. The success of such a program strongly depends on the true capability to reach the required background levels in the $\beta\beta(0\nu)$ region. An experimental confirmation of the background predictions of the various projects is therefore worthwhile and the construction of preliminary intermediate scale setups is recommended. Actually, for most of the proposed projects (CUORE, GERDA, MAJORANA, EXO and MOON) a smaller scale detector has already been funded. CUORE is the first full scale project funded and under construction.

References

1. B. Kayser *The Physics of Massive Neutrinos* (World Sci., Singapore, 1989).
2. W.H. Furry, *Phys. Rev.* **56**, 1184 (1939).
3. S. Pascoli, S.T. Petcov and T. Schwetz, hep-ph/0505226.
4. V.A. Rodin et al., *Phys. Rev.* C **68**, 044302 (2003) and nucl-th/0503063.
5. W.C. Haxton, G.J. Stephenson Jr., *Progr. Part. Nucl. Phys.* **12**, 409 (1984).

6. E. Caurier et al., *Nucl. Phys.* A **654**, 973 (1999).
7. J. Engel et al., *Phys. Rev.* C **37**, 731 (1988).
8. A. Staudt et al., *Europhys. Lett* **13**, 31 (1990).
9. A. Staudt et al., *Phys. Rev.* C **46**, 871 (1992).
10. A. Faessler and F. Simkovic, *J. Phys.* G **24**, 2139 (1998).
11. G. Pantis et al., *Phys. Rev.* C **53**, 695 (1996).
12. A.S. Barabash, *Czech. J. Phys.* **52**, 567 (2002).
13. You Ke et al., *Phys. Lett.* B **265**, 53 (1991).
14. H.V. Klapdor-Kleingrothaus et al., *Eur. Phys. J.* A **12**, 147 (2001).
15. C.E. Aalseth et al., *Phys. Rev.* C **59**, 2108 (1999).
16. Shitov et al., *Proc. of NANP05*, Dubna, Russia, June 20–25 2005.
17. R. Arnold et al., *Nucl. Phys.* A **658**, 299 (1999).
18. F.A. Danevich et al., *Phys. Rev.* C **62**, 044501 (2000).
19. T. Bernatowicz et al., *Phys. Rev.* C **47**, 806 (1993).
20. C. Arnaboldi et al., *Phys. Rev. Lett.* **95**, 142501 (2005).
21. J.M. Gavriljuk et al., *Phys. Rev.* C **61**, 035501 (2000).
22. R. Bernabei, *Phys. Lett.* B **546**, 23 (2002).
23. A. De Silva et al., *Phys. Rev.* C **56**, 2451 (1997).
24. H.V. Klapdor-Kleingrothaus, A. Dietz, H.V. Harney and I.V. Krivosheina, *Modern Physics Letters* A **16**, 2409 (2001) and hep-ph/0201231.
25. C. Aarnaboldi et al., hep-ex/0501010.
26. I. Abt et al., hep-ex/0404039.
27. C.E. Aalseth et al., hep-ex/0201021.
28. M. Danilov et al., *Phys. Lett.* B **480**, 12 (2000).
29. H. Ejiri et al., *Phys. Rev. Lett.* **85**, 2917 (2000).
30. H.V. Klapdor-Kleingrothaus HV, hep-ph/0103074.

SESSION V – FUTURE e+e- COLLIDERS

M. Piccolo	The International Linear Collider
C. Pagani	From TESLA to the International Linear Collider
H. Braun	CLIC R& D Status
S. Bertolucci	X-FEL

Frascati Physics Series Vol. XL (2006), pp. 197
Frontier Science 2005, New Frontiers in Subnuclear Physics
Milano, 12-16 September, 2005

THE INTERNATIONAL LINEAR COLLIDER

M. Piccolo
INFN-LNF, Frascati, Italy

Written contribution not received

Frascati Physics Series Vol. XL (2006), pp. 199–206
Frontier Science 2005, New Frontiers in Subnuclear Physics
Milano, 12-16 September, 2005

FROM TESLA TO THE INTERNATIONAL LINEAR COLLIDER

Carlo Pagani
Universitá degli Studi di Milano e INFN - Sezione di Milano, LASA

Abstract

I summarize here the hystorical path leading from the original Tigner idea of a linear collider to the current ILC proposal, which was made possible by successful experience of the TESLA Collaboration.

1 Introduction

Since the AdA proof of principle experiment in Frascati, colliding beams have been used to reach and advance the energy frontier in particle physics. With respect to the fixed target experiments, colliding two elementary particles with the same energy has the great advantage to allow in the center of mass (c.m.) all the energy transferred to them by the particle accelerator. Conversely, when a fixed target is used, relativity associates just one fraction of the beam energy to the moving center of mass.

The draw back of this concept is that the collision probability for the interacting particles is quite small because of the low beam density. Luminosity [cm^{-2} s^{-1}] is then the quality parameter that is required for a collider to produce a sufficient event rate of a given cross section. In principle higher

energy demands higher luminosity, but for the same beam quality luminosity is inversely proportional to the beam energy. In spite of the hardness of the game, for more than 2 decades, from ADONE (1969) to LEPII and TEVATRON, the discovery energy frontier had an exponential grow, following the so called "Livingston Plot".

From the accelerator side, the reference machine of all colliders has been a synchrotron based storage ring. Once accelerated to the nominal energy, the two beams are stored and used for collision for billions of times. In a synchrotron the maximum energy is proportional to both the ring radius and the average magnetic field. To follow the Livingston Plot superconducting magnet technology has been developed for the magnetic field improvement while machine size and cost are naturally associated with the radius increase. With increasing energies, the energy lost by synchrotron radiation has been the enemy for the elementary leptons. The factor 2000 in the relativistic γ together with the power of 4 dependence of the energy lost per turn, stopped any dream for lepton synchrotrons above the c.m. energy of ≈ 200 GeV, which was successfully reached by LEPII in its 27 km ring. Scaling LEPII to 1 TeV with a luminosity of $\approx 10^{34}$ [cm^{-2} s^{-1}] would require to conceive a circular machine close to 1000 km in length and consuming an amount of electrical power of the order of the whole US consumption. Conversely, the large hadron collider, LHC, in advanced construction at CERN utilizes the LEP tunnel and in a couple of years will collide two proton beams of 7 TeV each.

2 Origin and Challenges of a Linear Collider

In 1965, Maury Tigner proposed the idea of a linear collider to avoid the synchrotron radiation show stopper, but almost 40 years of research have been spent to demonstrate its practical feasibility. The two major problems of a linear collider are the luminosity and the efficiency to economically transfer the energy to the beams.

Luminosity is the measure of the number of particle collision per second. Simplifying the picture to the essential, luminosity is then directly proportional to the average beam current together with the particle transverse density obtainable at the collision point that is limited by the beam quality expressed by its phase space volume, the emittance. It turns out that for a given energy luminosity is determined by the maximum acceptable beam power and by the

minimum obtainable emittance. To give the impression of the meaning it is worthwhile to point out that in a storage ring collider as LHC the same particles are circulating 10^4 times in a second, contributing 10^4 time to the beam current, and, once accelerated, the survive for a few 10^4 seconds. Conversely in a linear collider each accelerated particle is given a single chance to collide before being dumped. As guiding numbers the power of each of the two LHC beams is close to 4 TW, while for a linear collider 10 MW is a reference value, that can be conceived only if the linac technology will prove able to transform plug power into beam power with unprecedented conversion efficiency.

Concerning the beam quality, in a storage ring collider it is determined by machine and beam dynamic issues and the machine design is done making a compromise between the relatively high density at the interaction points and the need of preserving a reasonable life time of the beam. Conversely, in a linac based collider the beam is spent after collision and minimum emittance is required to allow maximum density at the interaction point. In practice once a minimum normalized emittance beam has been generated, in a damping ring, the linac has to preserve this value all along the acceleration up to the interaction point. Moreover flat beams are required to minimize the beamstrahlung induced energy spread at the collision and, for two 10 MW beams at 250 GeV, 5 10^{14} fresh particles have to be generated and cooled every second, half electrons and half positrons.

In the Eighties, a number of ideas emerged, most of them proposing conceptual schemes focused on the reach of high energies with a relatively short linac length, neglecting the two major issues outlined above that are required to obtain consistent luminosity. The Interlaboratory Collaboration for R&D toward TeV-Scale Electron-Positron Linear Colliders at a meeting in London in June 1994 constituted an International panel, the ILC-TRC chaired by Greg Loew, that by the end of 1995 produced its first report which for the first time gathered in one document the current status of eight major e+e- linear collider designs in the world. The eight projects were analyzed and compared. In 2001, after the abandon of three of the original projects, ICFA requested that the ILC-TRC reconvene its activities to produce a second report that was delivered in February 2002. Among these 5 projects (JLC-C, JLC-X, NLC, TESLA and CLIC), JLC-X/NLC and TESLA have been considered close to the demonstration of their feasibility, with pros and cons in both sides [1)]. It was also

recognized that, in spite of the choice between the two alternative technologies, "warm" or "cold", a huge internationally organized effort was required to move to a real machine to be proposed for construction.

In 2002 ICFA created the International Linear Collider Steering Committee (ILCSC), chaired by Maury Tigner, to engage in outreach, explaining the intrinsic scientific and technological importance of the project, monitor the machine R&D activities and make recommendations on the coordination, identifying models of the organizational structure, based on international partnerships, adequate for constructing the LC facility.

The growing interest of the HEP community for the foreseen synergies between LHC and the lepton collider pushed the ILCSC to find a way to concentrate the worldwide effort on a single design, concluding the now expensive technology competition. By the end of 2003, twelve "Wise Persons" (Asia: G.S. Lee, A. Masaike, K. Oide H. Sugawara; Europe: J-E Augustin, G. Bellettini, G. Kalmus, V. Soergel; America: J. Bagger, B. Barish, P. Grannis, N. Holtkamp) were selected to form the International Technology Recommendation Panel (ITRP), the aim being to produce a globally accepted choice between the two remaining competitors: the "warm" JLC-X/NLC and the "cold" TESLA. The ITRP, chaired by Barry Barish, completed the recommendation process in eight months, through documentation, presentations, visits and discussions, and the three project leaders (Kaoru Yokoya for JLC-X, David Burke for NLC and Carlo Pagani for TESLA,) were invited to participate to all the process as the "technology experts".

The ITRP recommendation for the "cold" TESLA technology was unanimously endorsed by ICFA at the Beijing meeting in August 2004, starting the process towards the International Linear Collider, ILC.

3 TESLA: the ILC Technology precursor

The idea of investigating the use of superconducting accelerating structure as the basic technology for the future Linear Collider, called TESLA, was discussed for the first time in a small workshop held at Cornell in July 1990, organized by Ugo Amaldi and Hasan Padamsee. Two years later the TESLA Collaboration was set up at DESY for the development of a SRF-based TeV e+e- Linear Collider.

The baseline idea was simply that pushing to the limit the niobium SRF

technology, accelerating field up to 50 MV/m could be conceived, with efficiency from plug to beam power much higher than any other NC competitor . Due to the lower frequency and larger beam apertures a better beam quality preservation could be expected. The combination of these two effects would have produced a higher luminosity for a cold machine, if compared at the same plug power and beam quality.

Three were the major challenges of this scheme:

- Push the gradient to at least 25 MV/m, at high Q.
- Reduce by a factor of 20 the linac cost per MV.
- Develop the technology for pulsed operation.

Taking advantage of the experience of all the major laboratories investing in this technology, an optimum cavity design was developed and a large infrastructure was set up at DESY for the cavity processing and test. Stiffening rings were included in the cavity design to minimize the effect of Lorentz-force detuning in the high power pulsed regime. The major contributions came from CERN, Cornell, DESY and CEA-Saclay, but important inputs from TJNAF and KEK were essential. In parallel INFN, supported by the experience on long SC dipole construction of DESY and FNAL, lead the effort of developing with the Italian industry a new concept of an eight-cavity cryomodule with a low cost per meter and unprecedented cryogenic efficiency.

More than 100 cavities have been industrially produced, all processed and tested at DESY. Details on the fabrication and processing can be found in Ref. [2, 3]. A few key steps determined the success of the high gradient mission: 1) detection of niobium sheet defects and inclusions that pushed industry to invest in the production of a much better material for SRF application; 2) more stringent requirement in term of cleanness and quality control for the industrial fabrication; 3) more stringent specifications and controls for ultra high pure water, chemical compounds and close loop processing plant. Standard Buffered Chemical Polishing (BCP) was applied; 4) wide use of high pressure pure water rinsing (HPR), in clean room environment and with subsequent clean drying, to avoid particles residuals from chemistry; 5) 800 °C annealing for hydrogen desorption and 1400 °C treatment with Ti getters to improve thermal conductivity.

The further steps to approach the physical limits for niobium were mainly determined by the combined introduction of two new ideas originated by the ongoing R&D, mainly at KEK, TJNAF and CEA-Saclay: 1) electro-polishing (EP) instead of BPC to process the cavity active surface in order to smooth out asperities and improve the effect of HPR; 2) moderate temperature baking (100-140 °C) in ultra-high vacuum to re-distribute oxygen in the surface, to mitigate resistive effects. The first step raised the onset of field emission, while the second cured the Q drop. Applying these concepts cavity gradients of more than 35 MV/m have been obtained with very low values of the residual resistance (few nΩ) and high onset for the field emission [4].

In March 2001 the TESLA Technical Design Report [5] was published, for a Superconducting linear Collider with c.m. energy of 500 GeV, upgradable to 800 GeV. A full machine costing was included, based on specific industrial studies of all the major components, whose critical parts had been meanwhile developed and tested, in view of the required mass production.

4 ILC Status and Perspectives

The unanimous recommendation of the ITRP, endorsed by ICFA at the Beijing meeting, opened the way for the International Linear Collider. The main motivations of the "cold" decision are in the following as summarized in the ITRP Executive Summary document:

- *The large cavity aperture and long bunch interval reduce the complexity of operation, reduce the sensitivity to ground motion, permit inter-bunch feedback and may enable increased beam current.*
- *The main linac RF systems, the single largest technical cost elements, are of comparatively lower risk.*
- *The construction of the superconducting XFEL free electron laser will provide prototypes and test many aspects of the linac.*
- *The industrialization of most major components of the linac is underway.*
- *The use of superconducting cavities significantly reduces power consumption.*

The reaction of the Linear Collider community was impressively positive and the two major labs, KEK and SLAC, so far engaged in the development of the alternative "warm" technology switched immediately all the resources into the new global design. At the first ILC Workshop held at KEK in November 2004, three months after the decision, 220 accelerator physicists participated, setting up the embryo of the ILC global organization deemed to finally build the Linear Collider.

In Spring 2005 a group of 50 persons has been selected to form the Global Design Effort (GDE) team and Barry Barish, the former chairman of the ITRP, has bean appointed as Director. The Snowmass Workshop in August this year created the group structure and chose the base line parameters of the ILC to be designed and proposed, selecting the reference machine design, while letting open few alternatives that could produce positive impact in terms of either costs or performances. A similar group for detector development has been also created on a fully International basis. The option of having one or two interaction points is still pending and will depend on cost and funding issues.

The principal ILC parameters as agreed with the HEP community are summarized in the following numbers: c.m. energy of 500 GeV at a luminosity of 3 10^{34} [cm^{-2} s^{-1}]. The machine will be designed to be upgradable up to 1 TeV after a few years of operation, should physics results demand for this effort. The most important milestones of the GDE in the process of building the ILC are the following:

- by end 2005: Baseline Configuration Document (BCD)
- by end 2006: Reference Design Report (RDR), including cost and site studies
- by mid 2008: Technical Design Report

In parallel, after the publication of the RDR, the process of bids to host ILC and of money collection will start. This time scale is considered fully consistent with the effort still remaining to be done for the machine and detector design and is also compatible with a possible fine tuning that should be suggested by the LHC physics results. Construction should start sometime after 2010 and the possibility of contextual operation of the two large hadron and lepton colliders remains open.

5 Conclusions

The worldwide coordinated effort behind the TESLA project has been driving a new level of understanding of the SRF technology pushing its limits close to the physical ones. These results have been recognized by the HEP community and taken as the basis for the next global effort, the International Linear Collider.

Under the GDE, the path toward ILC is well defined and a growing interest is converging in this initiative increasing allowable resources and competencies. All the machine components and systems are at the limit of the present technology and accelerator physics achievements. They need a consistent design and engineering effort to reach the level required to perform their tasks in term of parameters and reliability. A new level of detailed understanding and quality control has to be transferred to industry for the large scale production. The LHC experience is the reference, but for the ILC more has to be done.

Most of the recent accelerator projects, under construction or being proposed, are extensively using SRF technology. Their realization is naturally synergic with the superconducting International Linear Collider and through it once more HEP has the chance to drive an important technological step.

References

1. International Linear Collider Technical Review Committee: Second Report 2003, Gregory Loew Editor, SLAC-R-606.
2. B. Aune et al. Phys. Rev. ST-AB, 3(9), 2000, 092001.
3. L. Lilje et al., Nucl. Inst. Meth., A 524 (1-3); 2004; p. 1.
4. C. Pagani, Proceedings of HEP 2005, Lisboa, Portugal, July 2005.
5. R. Brinkmann, et al. (editors), TESLA - Technical Design Report, Volume II. DESY, March 2001. ECFA 2001-209, TESLA Report 2001-23.

Frascati Physics Series Vol. XL (2006), pp. 207–212
Frontier Science 2005, New Frontiers in Subnuclear Physics
Milano, 12-16 September, 2005

CLIC
R & D Status

H.H. Braun, R. Corsini
CERN, CH 1211 Genève 23, Switzerland

Abstract

A high luminosity (10^{34} cm^{-2}s^{-1}) electron-positron Collider (CLIC) with a nominal centre-of-mass energy of 3 TeV has been under study for a number of years in the framework of an international collaboration of laboratories and institutes, with the aim to provide the HEP community with a new facility for the post-LHC era. After a brief description of a CLIC scheme to extend Linear Colliders into the Multi-TeV colliding beam energy range, the main challenges and the very promising results already achieved will be presented. The presentation will mainly focus on the new Test Facility (CTF3) presently under construction at CERN in order to address the main key issues and demonstrate the feasibility of the CLIC technology before 2010.

1 The CLIC challenges

The CLIC (Compact Linear Collider) design [1] is optimised for 3 TeV but can be built in stages, increasing its energy without major modifications. To limit its total length, CLIC uses normal conducting accelerating structures operating at a very high gradient (150 MV/m), and powered by high power (150 MW) 30 GHz RF pulses. Conventional RF sources do not cover this range and CLIC relies upon a two-beam-acceleration concept [2], in which a high current

electron beam (drive beam) runs parallel to the main beams and is decelerated to produce the RF power.

The generation of high-intensity drive beam pulses with the right time structure is one of the main challenges in CLIC. A long pulse is accelerated in a low frequency (937 MHz) normal-conducting linac, operated in the "full beam loading" condition, where the beam extracts efficiently (about 97 % RF-power-to-beam) the power from the accelerating structures. The electron bunches are then interleaved in stages by transverse RF deflectors in delay lines and rings to give the beam the desired bunch structure while increasing its intensity. The bunch spacing is reduced from 64 cm to 2 cm, and the beam current is increased from 5.7 A to 180 A.

It is generally accepted that CLIC is the only viable technology for multi-TeV colliders. However, several critical issues still need to be addressed. In the past years, the International Linear Collider Technical Review Committee [3] has listed a number of crucial items to prove CLIC feasibility (the so-called R1 items), and to arrive at a conceptual design (the R2 items). The experimental program of the new CLIC Test Facility (CTF3) deals with all the CLIC technology-related R1 and R2 issues, while issues common to all linear collider studies are investigated in the framework of the EuroTeV collaboration. The goal is to get an answer on the CLIC feasibility before 2010. By then the first LHC results should be available and the energy required for a future linear collider better known.

CTF3 [4] is presently being built and commissioned in stages at CERN, by an international collaboration including Ankara University, BINP, CIEMAT, DAPNIA-Saclay, INFN-Frascati, LAL-Orsay, LAPP-Annecy, North Western University of Illinois, RAL, SLAC, Uppsala University and Finnish industry, while other institutes have shown interest in joining the CTF3 collaboration. CTF3 uses the buildings of the former LEP pre-injector complex (LPI) and makes maximum use of existing hardware. The experimental program will cover the following points:

- Test of a prototype CLIC accelerating structure (including design features to damp higher order modes) at design gradient and pulse length (R1).
- Validation of the drive beam generation scheme with a fully-loaded linac (R1).

- Design and test of an adequately damped power-extraction structure, which can be switched on and off (R1).
- Validation of beam stability and losses in the drive beam decelerator, and design of a machine protection system (R2).
- Test of a relevant linac sub-unit with beam (R2).

2 Experimental results and planned tests

Many experimental results have been obtained in the past years, which have guided and confirmed the technical choices undertaken.

The feasibility of two-beam acceleration was already demonstrated in the CLIC Test Facility CTF2. There, an electron bunch was accelerated by 60 MeV using a string of 30 GHz structures powered by a drive beam. Such drive beam, produced directly from a photocathode gun, had however a total charge and pulse length much lower than the nominal CLIC values.

CTF2 has also been essential as a test bed for CLIC components. Its last two years of operation were indeed dedicated to testing of accelerating structures after damage to their copper irises was observed at high field. New structure designs, aimed at reducing the peak surface field for a given accelerating gradient, were explored. A big improvement in performance was obtained by employing irises made of arc-resistant materials like tungsten or molybdenum (see Figure 1).

Eventually, an accelerating gradient of 190 MV/m was reached using molybdenum irises [5]. The RF pulse length was however limited by the drive beam injector to 16 ns, well below the CLIC nominal value (70 ns). CTF3 is meant to extend these investigations to longer pulse lengths, up to and beyond the nominal value.

The technical feasibility of interleaving the drive beam bunches to increase current and bunch frequency was successfully demonstrated in 2001 and 2002 at low current (0.3 A), using the modified LPI complex, during the so-called preliminary phase of CTF3 [6]. Up to five bunch trains were interleaved over five turns in a combiner ring to reach 1.5 A, without measurable losses. One of the aims of the new CTF3 programme is to demonstrate this combination process with long, high current pulses.

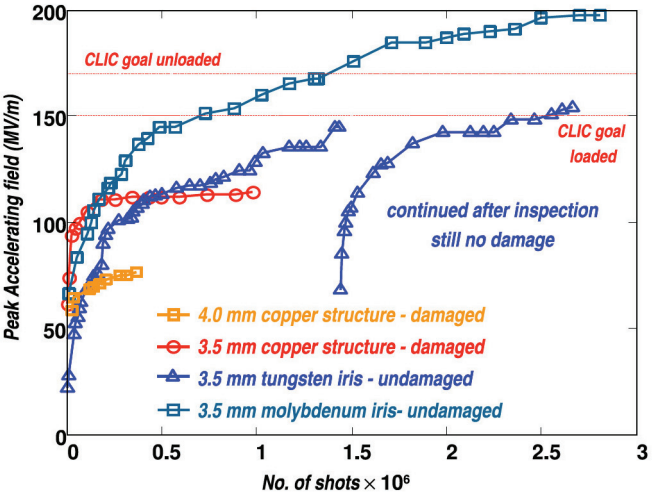

Figure 1: *RF conditioning history of several accelerating structures, with irises made of different materials and with different apertures, tested with beam in CTF2.*

3 Status of the test facility CTF3

The CTF3 complex is designed to work at a lower beam current and a lower energy than foreseen for the CLIC drive beam (3.5 A instead of 5.7 A and 150 MeV instead of 2.4 GeV) [4].

In its final configuration (see Figure 2) CTF3 will be composed of a 70 m long drive-beam linac followed by a 42 m delay loop and and a 84 m ring, where the bunch manipulations will be carried out. After combination the drive beam will have a current of 35 A, and will be transported to an experimental area to produce 30 GHz RF power in a high power test stand. In the same area a separate linac will provide a main beam for a representative CLIC two-beam module, and a test decelerator will be dedicated to drive beam stability studies.

The installation also includes a second high power test stand (halfway along the linac) working at a lower beam current, needed to continue RF component testing during installation and commissioning.

The project is proceeding as planned, alternating installation and commissioning periods. In 2003 and 2004, the injector, the linac with its 30 GHz

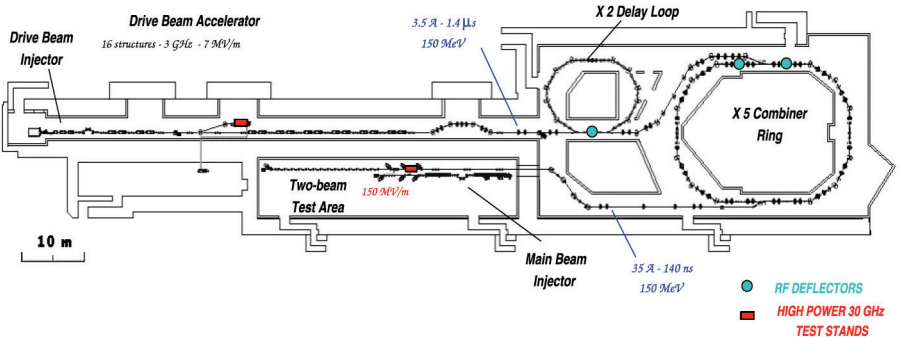

Figure 2: *CTF3 layout.*

power production line and an end-of-linac chicane and instrumentation section have been installed and commissioned. In 2005, the installation of the delay loop was completed. The combiner ring and the experimental area will be put in operation in 2006 and 2007. In the linac, the design beam current and pulse length were reached rapidly. The beam was remarkably stable and no sign of beam break-up was observed at high current, successfully demonstrating the operation under under full beam loading of the linac structures with their novel damping scheme [7]. The RF-to-beam efficiency was evaluated from input and output RF signals and confirmed by beam energy gain measurements. For a 4 A beam, an efficiency of 94 % was obtained, in agreement with simulations.

Several beam measurements were performed in the end-of-linac chicane, built by INFN/LNF, varying its optics to obtain different momentum compaction values, both positive and negative. A vertically deflecting RF structure was used together with an OTR screen to make bunch length measurements, which showed bunch compression to less than 0.5 mm rms for an initial bunch length of 2 mm. Comparison with the MAD model showed good agreement. Commissioning of the delay loop, also built by INFN/LNF, started recently, with the first beam circulating in November 2005.

CTF3 has started its role as a 30 GHz power production facility and the first accelerating structure tests started in 2005. These are ongoing, and at present RF pulses up to 90 MW were generated. Preliminary measurements shows that more than 60 MW are delivered to the molybdenum iris structure

under test, corresponding to a gradient in the first cell above 150 MV/m, with a pulse duration close to the nominal CLIC value of 70 ns.

References

1. CLIC Study Team, Ed. G. Guignard, *A 3 TeV e+e- linear collider based on CLIC technology*, CERN 2000-008, 2000.

2. H. Braun et al., Ed. R. Corsini, *The CLIC RF power source*, CERN 99-06, 1999.

3. Editor G. Loew, *International linear collider technical review committee second report*, SLAC-R-606.

4. G. Geschonke and A. Ghigo Eds, *CTF3 Design Report*, CERN/PS 2002-008 (RF).

5. W. Wuensch, C. Achard, S. Dbert, H. H. Braun, I. Syratchev, M. Taborelli, I. Wilson, *A Demonstration of High Gradient Acceleration*, CERN-AB-2003-048-RF, Proc. PAC 2003.

6. R. Corsini, A. Ferrari, L. Rinolfi, P. Royer, F. Tecker, *Experimental results on electron beam combination and bunch frequency multiplication*, Phys. Rev. ST Accel. Beams 7, 040101 (2004).

7. E. Jensen, *CTF3 Drive Beam Accelerating Structures*, Proc. LINAC 2002, 9-23 August 2002, Gyeongju (Kyongju), Korea, CERN/PS 2002-068 (RF) and CLIC Note 538.

Frascati Physics Series Vol. XL (2006), pp. 213
Frontier Science 2005, New Frontiers in Subnuclear Physics
Milano, 12-16 September, 2005

X - FEL

S. Bertolucci
INFN-LNF, Frascati, Italy

Written contribution not received

SESSION VI – SPECIAL TOPICS

L. Trentadue	Measuring α_{QED} in e^+e^-: an alternative approach
M. Picariello	The flavour physics in unified gauge theories
K. Kordas	Top mass measurement at CDF
I. Shipsey	Recent results in charm flavour physics
M. D'Alfonso	Long term tests of large CMS silicon detector structures
S. Mersi	Integration of the CMS silicon tracker
M. Chiorboli	The construction of the CMS silicon strip modules
G. Cerminara	Muon reconstruction software in CMS
R. Santoro	Test of prototypes and performance simulation of the ALICE silicon pixel detector
A. Heikkinen	Validation of GEANT4 Bertini cascade nuclide production
G. Santin	GEANT4 for the Medicine

SESSION VI – SPECIAL TOPICS

L. Trentadue	Measuring α_{QED} in e^+e^-: an alternative approach
M. Picariello	The flavour physics in unified gauge theories
K. Kordas	Top mass measurement at CDF
I. Shipsey	Recent results in charm flavour physics
M. D'Alfonso	Long term tests of large CMS silicon detector structures
S. Mersi	Integration of the CMS silicon tracker
M. Chiorboli	The construction of the CMS silicon strip modules
G. Cerminara	Muon reconstruction software in CMS
R. Santoro	Test of prototypes and performance simulation of the ALICE silicon pixel detector
A. Heikkinen	Validation of GEANT4 Bertini cascade nuclide production
G. Santin	GEANT4 for the Medicine

Frascati Physics Series Vol. XL (2006), pp. 217–222
Frontier Science 2005, New Frontiers in Subnuclear Physics
Milano, 12-16 September, 2005

MEASURING α_{QED} IN e^+e^-: AN ALTERNATIVE APPROACH

A.B. Arbuzov, D. Haidt, C. Matteuzzi, M. Paganoni
and
Luca Trentadue
Dipartimento di Fisica, Università di Parma
and
INFN, Gruppo Collegato di Parma, I-43100 Parma, Italy

Abstract

We propose a method to determine the running of α_{QED} from a measurement of the small angle Bhabha scattering. The method is suited to high statistics experiments at e^+e^-colliders equipped with luminometers in the appropriate angular region. The new simulation code SAMBHA predicting small angle Bhabha scattering is presented. We discuss a recent application using LEP data.

1 Introduction

The electroweak Standard Model $SU(2) \otimes U(1)$ contains as a constitutive part Quantum Electrodynamics (QED). The running of the electromagnetic coupling α is determined by the theory

$$\alpha(q^2) = \frac{\alpha(0)}{1 - \Delta\alpha(q^2)} \tag{1}$$

where $\alpha(0) = \alpha_0$ is the Sommerfeld fine structure constant, which has been measured to a precision of $3.7{\cdot}10^{-9}$ [1]. $\Delta\alpha(q^2)$ positive, arises from loop

contributions to the photon propagator. The numerical prediction of electroweak observables involves the knowledge of $\alpha(q^2)$, usually for $q^2 \neq 0$. For instance, the knowledge of $\alpha(m_Z^2)$ is relevant for the evaluation of quantities measured by the LEP experiments. This is achieved by evolving α from q^2=0 up to the Z mass scale $q^2 = m_Z^2$. The evolution expressed by the quantity $\Delta\alpha$ receives contributions from leptons, hadrons and the gauge bosons. The hadronic contribution to the vacuum polarisation, which cannot be calculated from first principles, is estimated with the help of a dispersion integral and evaluated [2] by using total cross-section measurements of $e^+e^- \rightarrow hadrons$ at low energies. Therefore, any evolved value $\alpha(q^2)$,particularly for $|q^2| > 4m_\pi^2$, is affected by uncertainties originating from hadronic contributions. The uncertainty on $\alpha(m_Z^2)^{-1}$ induced by these data is as small as $\pm$ 0.09 [2], nevertheless it turned out [3] that it limits the accurate prediction of electroweak quantities within the Standard Model, particularly for the prediction of the Higgs mass [4]. While waiting for improved measurements from BEPC, VEPP-4M and DAFNE as input to the dispersion integral, intense efforts are made to improve on estimating the hadronic shift $\Delta\alpha_{had}$, as for instance [5, 6, 7, 8], and to find alternative ways of measuring α itself. Attempts have been made to measure $\alpha(q^2)$ directly using e^+e^--data at various energies, such as measuring the ratio of $e^+e^-\gamma/e^+e^-$ [9] or more directly the angular distribution of Bhabha scattering [10]. We propose [11] to determine the running of α by using small angle Bhabha scattering. This process provides unique information on the QED coupling constant α at low *spacelike* momentum transfer $t = -|q^2|$, where $t = -\frac{1}{2}\ s\ (1 - \cos\theta)$ is related to the total invariant energy $\sqrt{s}$ and the scattering angle θ of the final state electron. The small angle region has the virtue of giving access to values of $\alpha(q^2)$ without being affected by weak contributions. The cross-section can be theoretically calculated with precision at the per mille level. A comparable experimental accuracy has been obtained at LEP [13]. It is dominated by the photonic t-channel exchange and the non-QED contributions have been computed [12] and are on the order of 10^{-4}. In particular contributions from boxes with two weak bosons are safely negligible. In general, the Bhabha-cross-section is computed from the entire set of gauge invariant amplitudes in the s- and t-channel. The s-channel contribution gives only a negligible contribution [11] . Recently, new important results, improving the accuracy of the Bhabha cross-sections have been obtained [14]. The

measurement of the angular distribution allows indeed to verify directly the running of the coupling $\alpha(t)$. Such a measurement constitutes a genuine test of QED alone. In fact, QED - as part of the electroweak theory - is valid as a consistent theory by itself, since for the applications considered here the conditions $|q^2| \ll m_W^2, m_Z^2$ are fulfilled. Furthermore, for the actual calculations $\theta \gg m_e/E_{beam}$ and $E_{beam} \gg m_e$ must be satisfied. Obviously, in order to manifest the running, the experimental precision must be adequate. This idea can be realized by high statistics experiments at e^+e^--colliders equipped with finely segmented luminometers, in particular by the LEP experiments given their large event samples, by SLC and future Linear Colliders. The relevant luminometers cover the t-range from a few GeV^2 to order 100 GeV^2. The t-dependence of the quantity $\Delta\alpha(t)$ at small values of t may be obtained using the program *alphaQED* by Jegerlehner [2]. At low energies is dominated by the contribution from the leptons, while with increasing energy also the contribution from loops due to hadrons becomes relevant. The region where hadronic corrections are critical is contained in the considered t-range.

2 The Method

The experimental determination of the angular distribution of the Bhabha cross-section requires the precise definition of a Bhabha event in the detector. The analysis follows closely the procedure adopted in the luminosity measurement which is described in detail, for instance in the Yellow Report (1996) [15], and elaborates on the additional aspect related to the measurement of a differential quantity. To this aim the luminosity detector must have a sufficiently large angular acceptance and adequate fine segmentation. The variable t is reconstructed on an event-by-event basis.

The method to measure the running of α exploits the fact that the cross-section for the process $e^+e^- \to e^+e^-$ can be conveniently decomposed into three factors :

$$\frac{d\sigma}{dt} = \frac{d\sigma^0}{dt} \left(\frac{\alpha(t)}{\alpha(0)} \right)^2 (1 + \Delta r(t)). \qquad (2)$$

All three factors are predicted to a precision of 0.1 % or better. The first factor on the right hand side refers to the Bhabha Born cross-section including soft and virtual photons [12] , which is precisely known, and accounts for the strongest dependence on t. The vacuum polarization effect in the leading pho-

ton t-channel exchange is incorporated in the running of α and gives rise to the squared factor in eq.2. The third factor $\Delta r(t)$ collects all the remaining real (in particular collinear) and virtual radiative effects not incorporated in the running of α [12, 16]. The experimental data, after the correction for detector effects, have to be compared with eq.2. This goal is achieved by using a newly developped program based on the already existing semianalytical code `NLLBHA` [12, 17] called `SAMBHA` [11]. The two-point functions $\Pi(t) = \Delta\alpha(t)$ and $\Pi(s) = \Delta\alpha(s)$ are responsible for the running of α in the space-like and time-like regions. In the language of Feynman diagrams the effect arises from fermion loop insertions into the virtual photon lines. In the real measure electrons, positrons and photons are observed as clusters. Their reconstruction is based on a specific algorithm. By applying the selection criteria [11] the event sample may be divided in clusters which are attibuted to various rings in the luminometer. This method has been recently applied to extract the running of α from LEP data [11, 18]. As shown in Ref. [11] the hadronic contribution to the vacuum polarization may be deduced by subtracting the leptonic contribution which is theoretically precisely known. The extraction of the hadronic contribution is only limited by the experimental precision. Anologous measurements, with a slightly different approach, have been recently carried by the L3 collaboration in order to extract the running of α [19].

We propose a novel approach to access directly the running of α in the t-channel. It consists in analysing small angle Bhabha scattering. Depending on the particular angular detector coverage and on the energy of the beams, it allows to cover a sizeable range of the t-variable. The information obtained in the t-channel can be compared with the existing results of the s-channel measurements. This represents a complementary approach which is direct, transparent and based only on QED interactions and furthermore is free from some of the drawbacks inherent in the s channel methods. The method outlined has been readily applied to the experiments at LEP [18]. More importantly It can also be exploited by other e^+e^- colliders as well as by existing lower energy machines and exceedingly precise measurements of the QED running coupling $\Delta\alpha(t)$ for small values of t may be possibly envisaged with dedicated luminometers.

Acknowledgement

I would like to thank Marco Paganoni and Tonino Pullia for organizing this Conference.

References

1. D.E. Groom et.al.: Eur. Phys. J. **C15** (2000) 1.
2. S. Eidelman and F. Jegerlehner: Z. Phys. **C67** (1995) 602.
3. K. Hagiwara, D. Haidt, S. Matsumoto and C.S. Kim : Z.Phys. **C64** (1994) 559; Z.Phys. **C68** (1995) 353;
   K. Hagiwara, D. Haidt and S. Matsumoto: Eur. Phys. J. **C2** (1998) 95.
4. The LEP Collaborations, CERN-PH-EP/2004-069; LEPEWWG/2004-01; hep-ex/0412015.
5. F. Jegerlehner: hep-ph/0308117.
6. M. Davier and A. Höcker : Phys. Lett. **B435** (1998) 427;
   M. Davier, S. Eidelman, A. Höcker, Z. Zhang, Eur. Phys. J. **C27**(2003) 497-521.
7. D.Karlen and H.Burkhardt, Eur. Phys. J. **C22** (2001) 39; hep-ex/0105065 (2001)
8. A.A. Pankov, N. Paver, Eur. Phys. J. **C29**(2003) 313-323.
9. TOPAZ Collaboration, I. Levine et al.: Phys. Rev. Lett. **78** (1997) 424
10. L3 Collaboration: M. Acciarri *et al*, Phys. Lett. **B476** (2000) 48.
11. A.B.Arbuzov, D.Haidt, C.Matteuzzi, M.Paganoni and L. Trentadue, European Physics Journal C35, 267 (2004) . hep-ph/0402211.
12. A.B. Arbuzov, V.S. Fadin, E.A. Kuraev, L.N. Lipatov, N.P. Merenkov and L. Trentadue, Nucl. Phys. **B485** (1997) 457.
13. A. Arbuzov *et al.*, Phys. Lett. **B383** (1996) 238; hep-ph/9605239.

14. A. Penin, hep-ph/0501120; hep-ph/0508127;
M. Czakon,J. Gluza,T. Riemann, Phys. Rev. D71, 073009 (2005).

15. LEP Working Group, Yellow Report CERN 96-01, Event Generators for Bhabha scattering, Convenors : S.Jadach and O.Nicrosini, p. 229.

16. E.A. Kuraev and V.S. Fadin, Sov. J. Nucl. Phys. **41** (1985) 466. O. Nicrosini and L. Trentadue, Phys.Lett. **B196** (1987) 551; Z. Phys. **C39** (1988) 479.

17. Yellow Report CERN 96-01 : *description of NLLBHA*.

18. G. Abbiendi et al., Eur. Phys. J. C45, 1 (2006); hep-ex/0505072.

19. P. Achard et al., Phys. Lett. B623, 26 (2005); hep-ex/0507078.

Frascati Physics Series Vol. XL (2006), pp. 223–226
Frontier Science 2005, New Frontiers in Subnuclear Physics
Milano, 12-16 September, 2005

THE FLAVOUR PHYSICS IN UNIFIED GAUGE THEORIES

Marco Picariello
Università degli studi di Lecce and INFN-Milano
Morisi Stefano
Università degli studi di Milano and INFN-Milano
Emilio Torrente-Lujan
Universidad de Murcia, GFT, Dept. de Fisica

Abstract

We investigate the phenomenological implication of the discrete symmetry $S_2 * P$ on flavor physics in $SO(10)$ unified theory. We construct a minimal renormalizable model which reproduces all the masses and mixing angles of both quarks and leptons. The underlining discrete symmetry gives a strong correlation between the down quark and charged lepton masses, and the lepton mixing angles. The small entries V_{ub}, V_{cb}, V_{td}, and V_{ts} in the CKM matrix are related to the small value of the ratio $\delta m^2_{sol}/\delta m^2_{atm}$.

1 Introduction

Recent neutrinos experimental data show that in first approximation, the lepton mixing MNS matrix is tri-bimaximal, i.e. the atmospheric mixing angle is maximal, $\theta_{13} \approx 0$ and the solar angle is $\theta_{12} \approx \arcsin(1/\sqrt{3})$. The tri-bimaximal matrix follows in a natural fashion in models invariant under discrete symmetry like S_3 which is the permutation symmetry of tree object [1)]. These motivations suggest us to consider discrete symmetries in extensions of the unified version of the SM. In literature both models based on extensions of the standard model

such us $SO(10)$ symmetry with or without continuous flavor symmetries, and models based on discrete symmetries are investigated [2, 3, 4]. Although some of them appear to be promising in understanding the flavor physics and unification we are still far from an unitarity vision of the flavor problem [5]. In this paper we study a model invariant under the $SO(10) \times S_2 \times \mathcal{P}$ group, where the $S_2 \times \mathcal{P}$ group is a discrete flavor symmetry. We analyse the phenomenological implications of such discrete symmetry on flavor physics and our aim is to construct a minimal renormalizable model which reproduces all the masses and mixing angles of both quarks and leptons. The $S_2 \times \mathcal{P}$ symmetry implies that the resulting mass matrices of the fermion are not general, but depending each one on 5 free parameters only. Together with the assumption that the two Higgs in **10** couple to fermions with a Yukawa matrix of rank one [4], we obtain that the left mixing matrices are all bimaximal with the remaining mixing angle small. This implies that the CKM is almost diagonal in the S_2 exact case. In our model the tri-bimaximal MNS mixing matrix is achieved by rotating the low energy neutrino mass matrix. In a very surprising way we obtain that the small entries V_{ub}, V_{cb}, V_{td}, and V_{ts} are related to the small value of the ratio $\delta m^2_{sol}/\delta m^2_{atm}$ (coming from both the $S_2 \times \mathcal{P}$ structure of our model and the small ratio of the quark masses with respect to m_t). On the other side when the S_2 symmetry is dynamically broken only the Cabibbo angle becomes relevant.

2 Our model

In $SO(10)$ all the fermion fields, with the inclusion of the right-handed neutrino, can be assigned to the **16** dimensional multiplet. We introduce a $\mathbf{16}^i$ multiplet for each flavor i. We split the fermions into the $\{1, 2\}$, which are taken doublet under S_2, and $\{3\}$, S_2 singlet. We add two Higgs scalars $\overline{\mathbf{126}}^\alpha$, and a **120**. We assume that the two fields $\overline{\mathbf{126}}^\alpha$ form a doublet under S_2, and we write the $SO(10) \times S_2$ renormalizable invariant Lagrangian

$$L^b_{yuk} = \mathbf{I}_{ij}\ \mathbf{16}^i\ \mathbf{16}^j\ \mathbf{10} + \mathbf{g}_{ija}\mathbf{16}^i\ \mathbf{16}^j\ \overline{\mathbf{126}}^\alpha + \mathbf{A}_{ij}\mathbf{16}^i\ \mathbf{16}^j\ \mathbf{120} + h.c.$$

The flavor indices $\{i, j\}$ run over $\{1, 2, 3\}$, and the α over $\{1, 2\}$. We introduce a parity operator $\mathcal{P}$ under which the fields transform as follow:

$$\mathcal{P}\mathbf{16}^\alpha = -\mathbf{16}^\alpha \quad \mathcal{P}\mathbf{16}^3 = \mathbf{16}^3 \quad \mathcal{P}\mathbf{126}^\alpha = \mathbf{126}^\alpha \quad \mathcal{P}\mathbf{120} = -\mathbf{120} \quad \mathcal{P}\mathbf{10} = \mathbf{10}$$

The symmetric tensor $\mathbf{g}_{ija}$, and the antisymmetric matrix $\mathbf{A}$ are the most general $S_2 \times \mathcal{P}$ invariant, The neutrino Majorana mass comes from the $(1, \overline{3}, 10)$ component of $\overline{\mathbf{126}}$ and the Dirac masses come from the (2,2,1) and (2,2,15) components respectively of the **10**, **120** and $\overline{\mathbf{126}}$. We are able now to write down the mass matrices of the quarks and leptons that follow from the model given by the Yukawa interactions (1)

$$M^u = k^u\ \mathbf{I} + \mathbf{\Delta^u} + (q^u_s + q^u_{adj})\mathbf{A}\,; \quad M^{\nu_R} = \mathbf{\Phi}\,; \quad M^d = k^d\ \mathbf{I} + \mathbf{\Delta^d} + (q^d_s + q^d_{adj})\mathbf{A}$$
$$M^l = k^d\ \mathbf{I} - 3\ \mathbf{\Delta^d} + (q^d_s - 3q^d_{adj})\mathbf{A}\,; \qquad M^\nu = k^u\ \mathbf{I} - 3\ \mathbf{\Delta^u} + (q^u_s - 3q^u_{adj})\mathbf{A}$$

where $k^{u,d}$ are the *vev*s of the two standard Higgs doublets of (2,2,1) in **10**, the $q^{u,d}$ are the *vev*s in **120** and the index s and adj stand for $SU_c(4)$ singlet and adjoint representation [3]. The matrices $\mathbf{\Delta}^{u,d}$, and $\mathbf{\Phi}$ are

$$\begin{pmatrix} \mathrm{b}\rho_1 + \mathrm{e}\rho_2 & \mathrm{d}(\rho_1 + \rho_2) & 0 \\ \mathrm{d}(\rho_1 + \rho_2) & \mathrm{e}\rho_1 + \mathrm{b}\rho_2 & 0 \\ 0 & 0 & \mathrm{f}(\rho_1 + \rho_2) \end{pmatrix} \tag{1}$$

with $\rho = \{\delta^u, \delta^d, \phi\}$ respectivally for $\{\mathbf{\Delta^u}, \mathbf{\Delta^d}, \mathbf{\Phi}\}$, and $\delta^{u,d}_\alpha$ are the *vev*s of the (2,2,15), and ϕ_α, are the *vev*s of $(1, \overline{3}, 10)$ component in the two $\overline{\mathbf{126}}^\alpha$s. In the case that $\delta^{u,d}_1 = \delta^{u,d}_2$, and $\phi_1 = \phi_2$ than we obtain that the S_2 discrete symmetry is unbroken. However this is not the choice taken by Nature. For example this case will give a wrong Cabibbo mixing angle. To obtain a good masses and mixing angles pattern we must require that S_2 is dynamically broken.

3 Results and conclusions

We analysed a model based on $SO(10)$ gauge symmetry times and $S_2 \times \mathcal{P}$ discrete flavor symmetry. By using the most general $S_2 \times \mathcal{P}$ invariant Lagrangian with one **10**, one **120**, and two **126** Higgs, we are able to reproduce all the quark and lepton masses and mixing angles. We are able to construct a model which predicts the usual unification relations between the down and the charged lepton masses. Our model agrees very well with the recent neutrinos experimental data, that in first approximation give the lepton mixing MNS matrix tri-bimaximal, which follows in natural fashion in our model. The $S_2 \times \mathcal{P}$ symmetry implies that the left mixing matrices are all bimaximal with the remaining mixing angle small. This implies that the CKM is almost diagonal in the S_2 exact case. By giving as input the three charged lepton masses

and the down quark mass, we obtain as output the right values for the strange and bottom masses. Moreover we predict that the atmospheric mixing angle is maximal, and $\theta_{13} = 0$ lepton mixing angle. By using the value of the top, charm and up quark masses we predict a small value for $\delta m^2_{sol}/\delta m^2_{atm}$ and for the entries V_{ub}, V_{cb}, V_{td}, and V_{ts}. Due to a property coming from the S_2 structure of our model, they are all related to the small value of the ratio of the other quark masses with respect to m_t. On the other side when the S_2 symmetry is dynamically broken the Cabibbo angle becomes relevant.

References

1. F. Caravaglios and S. Morisi, arXiv:hep-ph/0503234.

2. R. Barbieri et al.Nucl. Phys. B **493**, 3 (1997), Phys. Lett. B **401**, 47 (1997)

3. B. Dutta, Y. Mimura and R. N. Mohapatra, Phys. Lett. B **603**, 35 (2004) B. Bajc, G. Senjanovic and F. Vissani, arXiv:hep-ph/0110310.

4. G. Altarelli and F. Feruglio, arXiv:hep-ph/0504165. S. L. Chen, M. Frigerio and E. Ma, arXiv:hep-ph / 0504181, Phys. Rev. D **70**, 073008 (2004) [Erratum-ibid. D **70**, 079905 (2004)] K. Siyeon, Phys. Rev. D **71** (2005) 036005 W. Krolikowski, Acta Phys. Polon. B **36** (2005) 865

5. F. Caravaglios et al. Nucl. Phys. B **633**, 193 (2002) V. Antonelli, F. Caravaglios, R. Ferrari and M. Picariello, Phys. Lett. B **549**, 325 (2002)

6. H. Georgi and D. V. Nanopoulos, Nucl. Phys. B **159**, 16 (1979).

7. Q.R. Ahmad et al. Phys. Rev. Lett. **89** (2002) 011301; S.Fukuda et al. Phys. Lett. B **539**(2002) 179; J.W. Hampel et al. Phys. Lett. B **447** (1999)127; k.Eguchi et al. Phys. Rev. Lett. **90** (2003) 021802; Y.Fukuda et al. Phys. Rev. Lett. **85** (2000) 3999, Phys. Rev. Lett. **81** (1998) 1562; M. Apollonio et al. Eur. Phys. J. C **27** (2003) 331, Phys. Lett. B **466** (1999) 415;

8. S. Eidelman *et al.* [Particle Data Group], Phys. Lett. B **592**, 1 (2004).

Frascati Physics Series Vol. XL (2006), pp. 227–232
Frontier Science 2005, New Frontiers in Subnuclear Physics
Milano, 12-16 September, 2005

TOP MASS MEASUREMENT AT CDF

Kostas Kordas
LNF-INFN, Frascati (RM) 0044, Italy
(for the CDF Collaboration)

Abstract

We report on recent measurements of the top quark mass using $t\bar{t}$ candidate events selected in $\simeq 320$ pb^{-1} of data from the "Run II" operation period of the Tevatron $p\bar{p}$ collider. More emphasis is given on the best single measurement to date ($M_{top} = 173.5^{+3.9}_{-3.8}$ GeV/c^2), provided by CDF using the "lepton plus jets" channel, where one W decays to a lepton-neutrino pair and the other into quarks (top quarks decay to Wb almost 100% of the time).

1 Introduction

The top quark is the heaviest fundamental particle of the Standard Model (SM): about 35 times larger than the next heaviest quark (b) in the theory. A precise measurement of its' mass (M_{top}) is important for SM's prediction power, because top quark loops affect many Electro Weak (EW) observables. The top mass is also linked with the mass of the W and the Higgs bosons via radiative corrections; a fact exploited by EW fits which use measured observables to simultaneously constrain the three masses assuming the Standard Model [1]. Since the Higgs eludes experimental observation, a precise measurement of the top quark and the W masses serve as a constraint to the Higgs mass.

Top quarks were first observed by the CDF and DØ collaborations in 1995 [2], in events produced at $p\bar{p}$ collisions of $\sqrt{s} = 1.8$ TeV during the "Run I" operation of the Fermilab Tevatron collider. The two experiments combined top mass measurements to find $M_{top} = 178.0 \pm 4.3$ GeV/c^2 [3]. In the current mode of operations ("Run II") the Tevatron provides $p\bar{p}$ collisions of $\sqrt{s} = 1.96$ TeV. At the time of this conference, it has delivered 1.3 fb^{-1} of integrated luminosity, with about 1 fb^{-1} recorded by each experiment (almost ten times the Run I data sample). The Tevatron plans to deliver 4 to 8 fb^{-1} per experiment, which aim to measure the top mass with an accuracy of ~ 2 GeV/c^2 each.

We present here four recent M_{top} measurements at CDF, obtained with datasets of 320 to 360 pb^{-1}. More emphasis is given on a novel method to attack the dominant systematic uncertainty of the measurement [4].

2 Top mass reconstruction

2.1 Event selection

Top quarks are mostly pair produced at the Tevatron, via $q\bar{q}$ annihilation ($\sim$ 85%) or gluon-gluon fusion, and they decay $\sim 100\%$ of the time to Wb, with the b quark hadronizing into a jet (j) of particles. Subsequently, W's decay to quarks ($q_1\,\bar{q_2}$) or to a lepton-neutrino ($\ell\nu$) pair and their decay mode sets the characteristics of the $t\bar{t}$ event. The most precise measurements are obtained in i) the *lepton plus jets* channel ("$\ell + jets$"), where $t\bar{t} \to W^+\,b\,W^-\,\bar{b} \to b\,\bar{b}\,\ell\,\nu\,q_1\,\bar{q_2}$ (30% of $t\bar{t}$ decays, when $\ell \equiv e$ or μ), or ii) the *dilepton* channel, where $t\bar{t} \to W^+\,b\,W^-\,\bar{b} \to b\,\bar{b}\,\ell_1^{\pm}\,\ell_2^{\mp}\,\nu\,\bar{\nu}$ (5% of the time, when $\ell \equiv e$ or μ).

We select events containing a well identified and isolated electron or muon, large missing transverse energy from the neutrino(s) produced in the W decay(s), and jets with a multiplicity depending on the decay channel. All reconstructed objects are required to have high transverse energy (e.g., $E_T > 15$ GeV) [4]. In the dilepton channel, a second lepton is also requested; most commonly an e or μ candidate again, but sometimes we just ask for a well isolated and energetic track in order to recover some of the τ decays ("lepton plus track" selection) [5]. Dilepton and $\ell + jets$ samples are constructed to be mutually exclusive.

2.2 Measurement challenges

To reduce the combinatorial and physics background in the $\ell + jets$ channel, it is common to request at least one b-tagged jet, i.e., a jet identified as originating

from a b quark, typically via the presence of a secondary vertex. Thus, if at least one jet is b-tagged, the possible jet-parton assignments are reduced from 12 to 6, and to just two if both b jets are tagged (the two W daughter jets are interchangeable in the reconstruction).

The largest systematic uncertainty in the M_{top} measurement is due to the uncertainty on the Jet Energy Scale (JES, i.e., the jet-to-parton energy translation). The original parton energy is estimated by correcting the jet for instrumental, radiation and fragmentation effects, with a $\sim 3\%$ uncertainty for high energy jets [6]. The novel top mass measurement we report here, uses the hadronic W decays in the $t\bar{t}$ data sample itself to further constrain the JES.

Even though statistically limited, the dilepton channel has a higher signal to background ratio due to the second lepton. No b tagging is then required. The two highest energy jets are assumed to be b jets and we are left with just two possible jet-parton assignments. Nevertheless, the measured missing energy is due to two neutrinos and we are faced with an under-constrained problem. We thus iterate over more assumptions about the event topology compared to the over-constrained case of the lepton plus jets channel. This complication results in a larger statistical uncertainty in this channel, but the smaller number of jets yields a smaller JES contribution to the systematic uncertainty.

2.3 Measurement methods

In template methods, we impose kinematic constraints on the event according to the $t\bar{t}$ decay hypothesis and for each possible topological configuration we compute an event χ^2 which takes into account the detector resolution and the W and top decay widths. We get the most probable reconstructed top mass per event and we compare the distribution with similarly obtained "template" p.d.f's from simulated background and signal events with known M_{top}. A likelihood minimization yields the M_{top} which best describes the measured distribution as an admixture of $t\bar{t}$ and background events.

In matrix-element methods, for each $t\bar{t}$ candidate event we calculate a likelihood, as a function of M_{top}, which is the differential probability that the measured quantities (4-momenta of reconstructed objects) correspond to a $t\bar{t}$ signal event. The likelihood is the convolution of the leading-order (LO) $t\bar{t}$ matrix element and detector resolution functions, integrated over all possible configurations. Similarly, we can also compute a likelihood for each event being background (e.g., W plus jets in the $\ell+jets$ case, or Drell-Yan for dilepton) and sum the likelihoods according to the relative abundance of each contribution.

The product of the individual event likelihoods forms the joint likelihood of the data sample, which is fitted to yield the top mass measured from the sample.

3 Top mass measurements

3.1 The best single measurement

The most precise measurement is obtained with a 2-Dimensional template analysis of 318 pb^{-1} of $\ell + jets$ data [4]. This analysis uses the dijet mass from the in-situ $W \to jj$ decays to constrain the jet energy scale. Since the dijet mass is largely insensitive to the true top mass, we create separate templates of the reconstructed top and W masses in simulated events as a function of the true top mass and JES, respectively, and compare them with the data distributions.

In order to improve the statistical power of the method, four mutually exclusive subsamples are used, defined by the number of b-tagged jets and the jet E_T cuts. Sample "1-tag(T)" has one b-tag and $E_T > 15$ GeV for all jets, whereas "1-tag(L)" relaxes one jet's requirements to $8 < E_T < 15$ GeV. In each subsample we select the most "reasonable" $t\bar{t}$ candidates by applying a cut on the χ^2 mentioned in Section 2.3. Figure 1 shows the reconstructed top mass in the data, with the best fits from the simulated templates overlaid. Similar plots are obtained for the dijet mass. A two-dimensional likelihood fit yields both the measured top mass and the JES shift (in σ's) from the a-priori estimate via independent means [6]. We get $M_{top} = 173.5^{+3.7}_{-3.6}$ (stat.) GeV/c^2, were the uncertainty is statistical and incorporates the JES contribution ($\sim$ 2.5 GeV/c^2, to be compared to a 3.1 GeV/c^2 contribution in the 1-D template method, where the hadronic W decays are not used to constrain the JES). The systematic uncertainties not included in the JES are small (1.3 GeV/c^2), resulting in $M_{top} = 173.5^{+3.9}_{-3.8}$ GeV/c^2.

3.2 Other measurements

Matrix-element methods are used on both the $\ell + jets$ and the dilepton channels, and are proved to be very powerful statistically. We select events with exactly four or exactly two energetic jets for the $\ell + jets$ and the dilepton channels, respectively; this way, NLO effects are minimized when comparing the data with the LO matrix element for the $t\bar{t}$ production and decay. With 63 $\ell + jets$ events containing at least one b-tagged jet each, a matrix-element analysis measures $M_{top} = 173.2^{+2.6}_{-2.4}$ (stat.) ± 3.2 (syst.) $= 173.2^{+4.1}_{-4.0}$ GeV/c^2, where

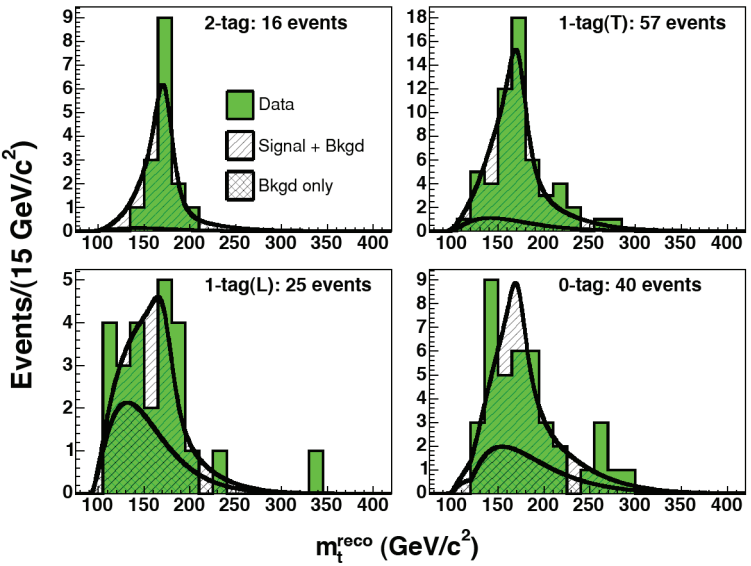

Figure 1: *Reconstructed top mass in the four data subsamples (solid), with the best fits from the simulated templates overlaid (hatched). The contribution of background events is also shown (double-hatched).*

the JES contributes a 3 GeV/c^2 systematic uncertainty [4]. In the dilepton channel, 33 events reconstructed in 340 pb−1 of data yield $M_{top} = 165.3 \pm 6.3$ (stat.) ± 3.6 (syst.) GeV/c^2 (with a 2.6 GeV/c^2 systematic uncertainty due to the JES) [7].

The most precise measurement with a template method in the dilepton channel comes from the Neutrino Weighting Algorithm; for each top mas hypothesis we integrate over all possible neutrino η's and calculate the probability that the measured missing energy is matched. The most probable top mass from each event serves as input to the template methodology (Section2.3). With 45 "lepton plus track" events reconstructed in 360 pb^{-1} of data, this method gives $M_{top} = 170.7^{+6.9}_{-6.5}$ (stat.) ± 4.6 (syst.) GeV/c^2, where the JES contributes a 3.4 GeV/c^2 systematic uncertainty [7]. Combining the dilepton measurements at CDF we get $M_{top} = 167.9 \pm 5\ 2$ (stat.) ± 3.7 (syst.) GeV/c^2 [7].

4 Summary and outlook

The top mass measurement is entering a precision phase. CDF has provided the single best measurement to date ($M_{top} = 173.5^{+3.9}_{-3.8}$ GeV/c^2) by using a 2-dimensional template method which constraints the jet energy scale by using the dijet mass from the in-situ hadronic W decays in lepton plus jets $t\bar{t}$ candidate events. The jet energy scale is the biggest contributor to the M_{top} systematic uncertainty: ~ 2.5 GeV/c^2 with the 320 pb^{-1} data sample of this measurement, but it's expected to contribute ~ 1.5 (1) GeV/c^2 when 2 (4) fb^{-1} are collected and analyzed.

By using exclusive datasets and combining the best measurement from each channel, a preliminary Tevatron average ($M_{top} = 172.7 \pm 2.9$ GeV/c^2) was obtained in the summer of 2005 [8]. This is already a 1.7% measurement.

References

1. LEP ElectroWeak Working Group, `http://lepewwg.web.cern.ch/LEPEWWG` CERN-PH-EP/2005-051 and hep-ex/0511027, to be published (2005).

2. F. Abe *et al.* (CDF Collaboration), Phys. Rev. Lett. **74**, 2626 (1995); S. Abachi *et al.* (DØ Collaboration), Phys. Rev. Lett. **74**, 2632 (1995).

3. CDF and DØ Collaborations, hep-ex/0404010 (2004).

4. A. Abulencia *et al.* (CDF Collaboration), FERMILAB-PUB-05-472-E, submitted to Phys. Rev. **D**, hep-ex/0510048 (2005); A. Abulencia *et al* (CDF Collaboration), FERMILAB-PUB-05-474-E, submitted to Phys. Rev. Lett., hep-ex/0510049 (2005).

5. D. Acosta *et al.* (CDF Collaboration), Phys. Rev. Lett. **93**, 142001 (2004).

6. A. Bhatti *et al.*, submitted to Nucl. Instr. Meth. A, hep-ex/0510047 (2005).

7. A. Abulencia *et al.* (CDF Collaboration), FERMILAB-PUB-05-551-E, submitted to Phys. Rev. Lett., hep-ex/0512070 (2005); A. Abulencia *et al* (CDF Collaboration), FERMILAB-PUB-06-019-E, submitted to Phys. Rev. **D** hep-ex/0602008 (2006).

8. CDF Collaboration, DØ Collaboration and the Tevatron Electroweak Working Group, FERMILAB-TM-2323-E, hep-ex/0507091 (2005).

Frascati Physics Series Vol. XL (2006), pp. 233
Frontier Science 2005, New Frontiers in Subnuclear Physics
Milano, 12-16 September, 2005

RECENT RESULTS IN CHARM FLAVOUR PHYSICS

I. Shipsey
Purdue University, US

Written contribution not received

Frascati Physics Series Vol. XL (2006), pp. 235
Frontier Science 2005, New Frontiers in Subnuclear Physics
Milano, 12-16 September, 2005

LONG TERM TESTS OF LARGE CMS SILICON DETECTOR STRUCTURES

M. D'Alfonso
INFN-Pisa, Italy

Written contribution not received

Frascati Physics Series Vol. XL (2006), pp. 237–242
Frontier Science 2005, New Frontiers in Subnuclear Physics
Milano, 12-16 September, 2005

INTEGRATION OF THE CMS SILICON TRACKER

Stefano Mersi on behalf of the CMS Collaboration
Istituto Nazionale di Fisica Nucleare,
Università degli Studi di Firenze
Via G. Sansone, 1, 50019 Sesto F.no (FI), Italy

Abstract

The CMS experiment at LHC features the largest Silicon Strip Tracker (SST) ever built. The aim of this article is to give a sketch on how single detectors are being assembled into more complex structures (sub detectors) in the SST, but it will not cover the assembly of sub detectors which will be performed at CERN. This overview also shows how different are the designs of sub detectors, and gives a glance of the tests being performed during the assembly.

1 Context

The Compact Muon Solenoid (CMS) experiment will observe pp collision at $\sqrt{s} = 14$ TeV with a luminosity of 10^{34} cm^{-2}s^{-1}. The bunch crossing frequency will be 40 MHz, with ~ 2000 charged tracks per event and a hadron flux up to 10^{14} cm^{-2}y^{-1} close to the interaction point.
The physics requirements, a momentum resolution of 1−2% P_T at ~ 100 GeV/c and an impact parameter resolution of $\sim 10 - 20$ μm, were obtained by designing a volume of 5.4 m in length and 2.4 m in diameter immersed in a 4 T axial magnetic field. The innermost region (r $\leq$ 15 cm) is occupied by a pixel

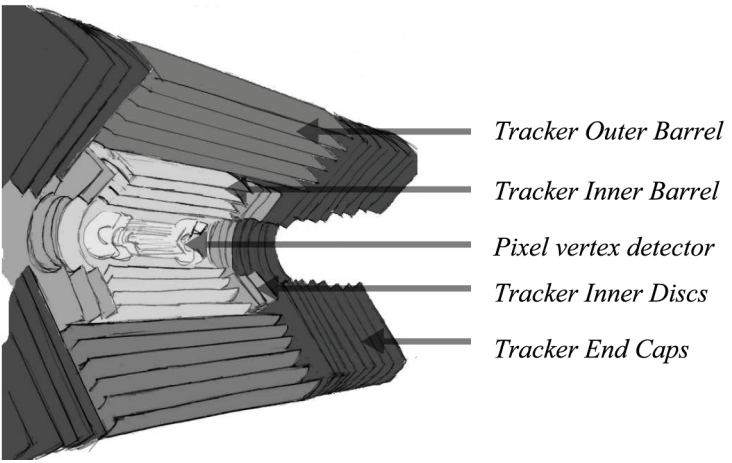

Figure 1: *A view of the SST and its sub-detectors.*

vertex detector, described elsewhere [1, 2, 3], while the remaining volume will be instrumented by using $\sim$ 15000 Silicon microstrip modules organized in 10 cylindrical layers and 12 discs, as sketched in Figure 1, corresponding to more than 200 m^2 of active surface. The Silicon Strip Tracker (SST) is divided in 4 separate regions (sub-detectors), each with a peculiar design approach. A detailed description of the SST and its expected performances can be found elsewhere [4, 5].

It is evident that a well defined production chain with accurate quality assurance was to be set in place, but also the integration procedures of the modules into sub-detectors is to be accurately monitored, as the SST shall endure 10 years of operation, with little or no chance for maintenance after LHC start-up.

2 SST integration

Despite several design differences, the whole SST shares the same DAQ structure: a group of detector modules is driven by a control unit (CCU, which provides clock, trigger, monitoring, ...), while a set of CCUs are linked in a token-ring configuration (control loop), which is controlled from outside the detector through optical fibres. Also the analogue signal from the modules is

routed optically, to be digitized far from the detector.

2.1 Tracker Inner Barrel

The Tracker Inner Barrel (TIB) is made of 4 separate layers, each layer is divided into 2 symmetrical barrels (TIB+, TIB-) each divided in 2 semi-cylinders (shell). Each shell has modules mounted both on the inside and the outside surface. In TIB the smallest functional unit is a shell, and this is realized with a carbon fibre support structure, with cooling pipes, which are in touch with modules and with the linear laser driver for the optical readout. Also control cables and boards are integrated on a shell as well as power cables and optical remote control devices.

As in other sub-detectors, every module has its own laser driver and set of fibres, which are the first to be set in place; control loop cables are then to be prepared and bent individually to fit in the structure. A carbon fibre 'skin' had to be implemented in order to hold the cables and control boards in place and to provide a shielding between control cables and modules.

In TIB modules are individually mounted on the structure and registered in the Tracker Construction Database. As removing a module from the final structure is a risky operation, for each one the control logic is tested with a software that also cross checks the components' identity with the database; this guarantees correct connections, module's functionality and reduces the probability of a further substitution.

Each time a group of 3 modules is mounted, the full readout is tested by measuring the noise and the calibration signal; this not only allows to check the modules and laser drivers functionality, but also to test against possible noise sources in the chosen configuration. A longer functional test follows the completion of a shell, with a full readout of all the mounted modules, both at room temperature and at a temperature of $-24°$ C. At last the redundancy in the connections on the control boards is tested. By now the first 4 shells were completed and tested (see fig. 2).

A cosmic muons test was also performed by setting up a duplicate system, and analysis confirms that a stable readout can be achieved with a good signal-to-noise ratio ($\simeq 24$).

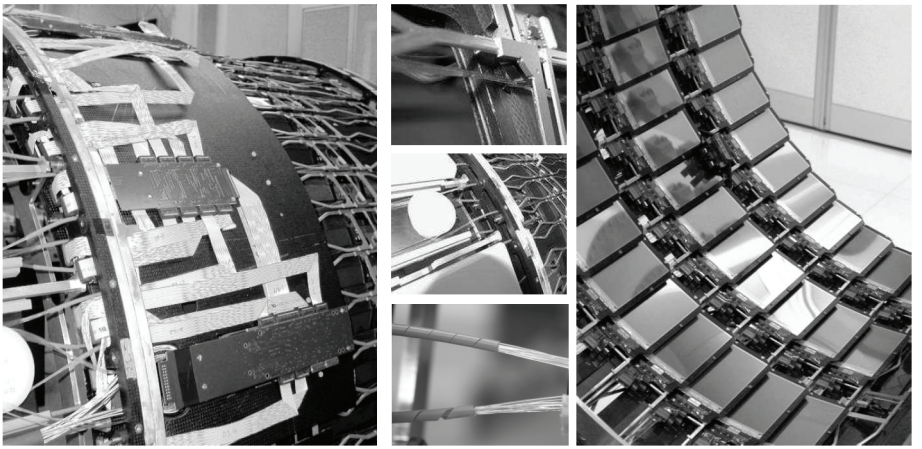

Figure 2: *Steps in the TIB integration: routing of optical fibres for analogue readout (center), control loop cables and boards set on the carbon fibre 'skin' (left), modules mounted on a shell (right).*

2.2 Tracker Inner Discs

Also in the Tracker Inner Discs (TID) modules are individually mounted onto disc support structures, which are the shell equivalents. TID has fewer modules with respect to TIB (816 vs. 2724), but they come in 7 different designs; thus the production of tooling and modules is more difficult, but integration will be quicker. Integration tooling has been qualified and the integration of the first disc is just started. TID shares with TIB all the integration quality assurance procedures.

2.3 Tracker Outer Barrel

The Tracker Outer Barrel (TOB) is a monolithic cylinder of about 2.2 m length and 2.3 m diameter. It mounts on its inner surface the rails that support the TIB and the TID and the modules are mounted on 688 sub assemblies (rods), arranged in 6 concentric layers inside a supporting mechanical structure (wheel), mostly made of carbon fibre. The wheel has been completed and measured: it has a precision better than 200 μm over its whole size.

A rod houses 6 or 12 modules, all the interconnection electronics and the readout optical hybrids; rods are inserted in the wheel from both ends, overlapping in the centre (z=0). All rod frames are produced and individually measured (typical precision of inserts supporting the modules ~ 30 μm). Assembling of electronics boards and optical hybrids and validation is at about 70% complete. First rods populated with modules have been inserted in the wheel.
Installation procedures and tools were finalized and the quality control of completed segments of the TOB fully defined and being commissioned. The integration procedure consists in the insertion of a rod in the wheel, and its registration in the Construction Database, the soldering and testing of the cooling pipes and the connection of proper cables. A long-term functional test ($\sim$ 6h) follows when a sector is finished.

2.4 Tracker End Cap

Tracker End Caps (TEC) has also a modular structure, with modules assembled onto petals and petals mounted onto two cylindrical structures, each containing 9 discs. The whole TEC has a total 288 petals with 6400 module. Both mechanical structures are ready, with optical ribbons for readout mounted, while cooling pipes and power cables have to be mounted. Petals for the first sector were built and are under test. Integration of first TEC will start in October 2005 and will proceed sector by sector. A cold test at CMS operating temperature is planned for the first sector and grounding and shielding scheme will be studied.
By now a trial assembly of two petals in the TEC with full readout was performed: the insertion procedure, cabling and handling of optical fibres were exercised, and experience with cosmic muon trigger was gained. In this test a stable readout was achieved and cosmic muons detected; preliminary results show signal and noise similar to previous test beam results.
Two additional test structures were produced to be partially filled with modules: 1 for the CMS Magnet Test and 1 for a SST DAQ test.

3 Conclusions

Integration and commissioning of the Silicon Strip Tracker presents difficulties both for the volume of work to be handled and because of its uniqueness. Thus

a step-by-step quality check is essential to spot any problem in time for implementing proper solutions. A parallel work now in progress is the commissioning of a tracker's segment duplicate (with a limited subset of detectors) to check how these sub detectors will work together inside a 4T magnetic field and test its tracking capability.

References

1. W. Erdmann, The CMS pixel detector. Nucl. Instr. and Meth. A **447**, 178 (2000).

2. S. Schnetzer, The CMS pixel detector, Nucl. Instr. and Meth. A **501**, 100 (2003).

3. L. Cremaldi, CMS pixel detector - Overview, Nucl. Instr. and Meth. A **511**, 64 (2003).

4. CMS Collaboration, The Tracker System Project Technical Design Report, **CERN-LHCC/98-6** (1998).

5. CMS Collaboration, Addendum to the CMS Tracker TDR, **CERN-LHCC/2000-16** (2000).

Frascati Physics Series Vol. XL (2006), pp. 243–246
Frontier Science 2005, New Frontiers in Subnuclear Physics
Milano, 12-16 September, 2005

THE CONSTRUCTION OF THE CMS TRACKER SILICON STRIP MODULES

Massimiliano Chiorboli
on behalf of the CMS Tracker Collaboration
Dipartimento di Fisica e Astronomia, Università di Catania
Via S. Sofia 64, 95123 Catania

Abstract

The procedures followed for the construction of the Silicon Strip Modules to be used in the CMS Tracker Detector are presented. The steps of the production chain are described, and the results are given.

1 The CMS Tracker

The Tracker of the Compact Muon Solenoid (CMS) detector is a cylindrical device of 5.4 m in length and 2.4 m in diameter. It is composed by a pixel detector system in the innermost region ($r < 15$ cm) and a silicon microstrip detector system in the remaining volume. The Silicon Strip Tracker (SST) [1)] is divided in four subdetectors as shown in fig.1 left. The pixel system will not be covered in this report.

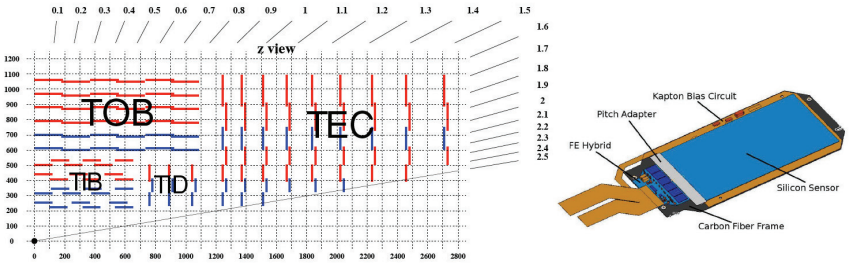

Figure 1: *Left: schematic of one quadrant of the SST. The thin lines represent single sided layers; the thick lines represent layers with stereo modules; Rigth: sketch of a TIB module with its components.*

The barrel modules and the disks modules have the readout strips laying along the z and radial direction, respectively, allowing the readout of the $r\phi$ coordinate. In order to have three-dimensional information, double-sided modules equip the first two layers of TIB and TOB, the two innermost rings of TID and the TEC rings with $r < 40$ cm and 60 cm $< r <$ 76 cm. They consist of back-to-back sandwiches of $r\phi$ modules and special *stereo* modules with the strips tilted by 100 mrad.

The basic element of the SST is the module. It consists of a carbon fiber support structure, one or two single-sided sensors (two daisy-chained sensors in TOB and TEC modules), with different geometries according to the subdevice they belong to, and a front-end hybrid, housing four or six chips for signal amplification and buffering (APV), and other chips for module monitoring and trigger control. Fig.1 right shows a sketch of a TIB module.

2 Module Construction Production Chain

The SST consists of 24'000 sensors arranged in almost 15'400 modules. More than 75'000 readout chips provide about 10 million readout channels. The enormous effort needed to construct such a complex device has to be faced with an industrial and distributed approach. The CMS Tracker collaboration developed a production chain distributing the work in several laboratories around the World, keeping the quality at an excellent level and the best possible uniformity among the various centres.

2.1 Module Assembly

An accuracy of the mechanical assembly within a few tens of microns, together with a high uniformity between multiple centres have been achieved with the usage of the semi-automatic Aerotech Gantry Machine [2]. Module components are placed on a plate providing motion in 3 linear and 1 rotational coordinates; a software-driven arm is equipped with a CCD camera and a syringe to dispense the glue. A pattern recognition software can locate some fiducial markers placed on the module components. The assembly quality is given in terms of the difference in the local x and y distances and the angle tilt θ between the sensors and the carbon frame. The RMS of the distribution of the assembled modules is less than 10 μm in Δx and Δy distances and nearly 6 mrad in $\Delta\vartheta$.

2.2 Module Bonding

Different models of automatic wire bonders, depending on the bonding centres, perform the bonding between the silicon strips and the APV readout channels and between the strips of two different sensors in a thick module. On a sample basis, pull tests are done to have a quality control of the bond strength. The force at which the bonds break is required to be larger than 5 grams. All centres demonstrated pull forces well beyond the required threshold, with a good uniformity between the different laboratories.

2.3 Quality Control Tests

After the bonding, modules are delivered to Quality Control laboratories.

The "module fast test" follows almost immediately the bonding to quickly identify and possibly correct module problems. It is performed using a compact stand-alone test system called ARC [3], which is capable to perform a full sensor I-V curve up to 450V; a pedestal, noise and pulseshape run in order to detect open, noisy or shorted neighbouring channels; a pinhole identification by means of light-induced sensor leakage current. A pinhole is a short or ohmic connection between the aluminium strip and its corresponding p^+ implant, and is a potentially dangerous defect, since it can prevent the whole chip from being properly read out. Fig.2 left shows the I-V of a module. Fig.2 right shows the noise pattern for a module with eleven defects. About 2% of modules are rejected at this stage.

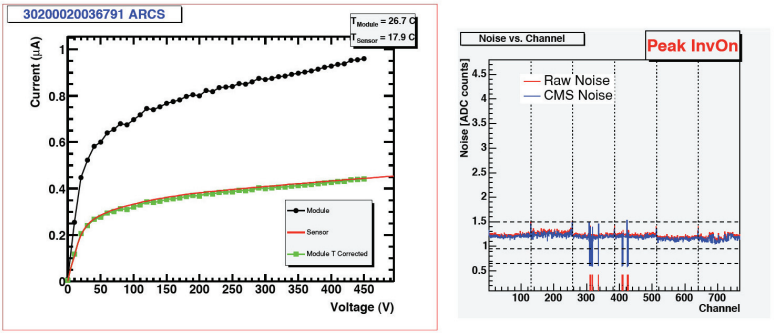

Figure 2: Left: I-V characteristics of a TIB module. Right: Noise pattern for

Modules qualified by the fast test are further processed through a long term test procedure. In each test, up to ten modules are put in a climatic chamber which performs thermal cycles between -20 ^oC and +20^oC for a total period of 48 hours During the whole cycle they are fully monitored with a DAQ similar to the one that will be used for data taking during LHC running. Less than 1% of modules are rejected because of defects appearing during the thermal cycle stress.

3 Conclusions

The industrial, distributed approach to produce the 15'000 modules necessary for the CMS Tracker worked very well. A high uniformity between the laboratories has been achieved, with an excellent quality: as of December 2005, the TIB, TID and TOB modules are almost completed, and the production of the TEC ones proceeds rapidly. About 3% of modules are rejected, with about 0.1% of bad strips found on good modules. Integration in a single scientific instrument has already started, as better described in ref. [4].

References

1. The CMS Collaboration, CERN-LHCC/98-6 (1998); The CMS Collaboration, CERN-LHCC/2000-16 (2000).

2. A. Honma *et al.*, CMS NOTE 2002/005.

3. M. Axer *et al.*, CMS NOTE 2001/046.

4. S. Mersi, these proceedings.

Frascati Physics Series Vol. XL (2006), pp. 247–252
Frontier Science 2005, New Frontiers in Subnuclear Physics
Milano, 12-16 September, 2005

MUON RECONSTRUCTION SOFTWARE IN CMS

Gianluca Cerminara
University of Torino and INFN, Torino, Italy

Abstract

The CMS muon system is composed of tracking chambers with trigger capabilities and it plays a key role in the High Level Trigger (HLT). The HLT is fully software implemented, incorporating the functionality of the Level-2 and Level-3 trigger of a more conventional trigger design. To cope with the requirements of this design, a powerful and robust muon reconstruction algorithm has been developed using modern object-oriented techniques. This software is designed to work for both offline reconstruction and for on-line event selection. It reconstructs muons in the muon spectrometer, using regional reconstruction in the three CMS sub-detectors, and links the resulting muon tracks with tracks reconstructed in the silicon tracker. The design and the performance of the CMS muon reconstruction software are presented in the following.

1 Introduction

The Compact Muon Solenoid (CMS) experiment is described in [1]. The tracking is based on an intense (4 T) magnetic field provided by a large superconducting solenoid which allows to measure the bending coordinate independently inside and outside the coil. The iron return yoke of the magnet is instrumented

with a muon spectrometer [2] which is realized with three types of gaseous detectors, all of them used both for tracking and for trigger purposes. Figure 1 shows the longitudinal view of one quarter of the muon system. In the barrel region Drift Tube (DT) chambers are used while in the endcaps Cathode Strip Chambers (CSC) are employed. For redundancy both the barrel and the endcaps are instrumented with Resistive Plate Chambers (RPC).

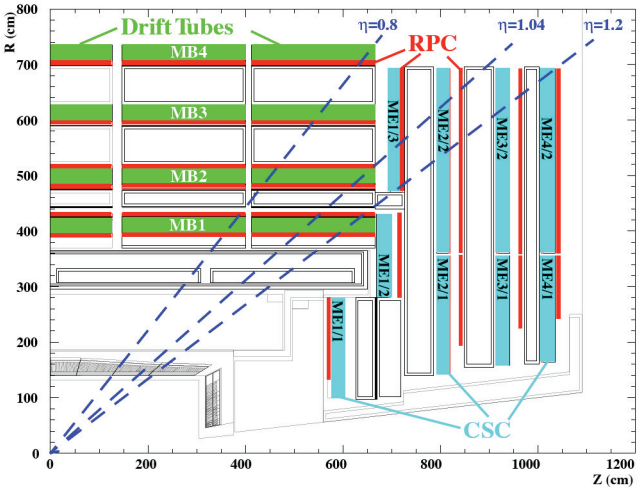

Figure 1: *Longitudinal view of one quarter of the CMS muon system.*

2 The CMS High Level Trigger

CMS adopts an innovative trigger design based on only two physical levels. The Level-1 trigger, implemented on dedicated hardware, only accesses data from the calorimeters and the muon detectors with coarse granularity. The second step of the selection, the High Level Trigger (HLT) [3], is fully implemented in software and will run on a single farm of commercial processors. The goal of the HLT is to reduce the event rate from the maximum Level-1 output ($\sim$ 100 kHz) to about 100 Hz, the maximum rate acceptable for storage given that the event size is of the order of 1 MB.

The HLT does not have an internal architecture of separate trigger levels. However, in order to discard uninteresting events as soon as possible, the selec-

tion is organized in a sequence of logical steps. Each step will progressively use more sophisticated and CPU-time consuming algorithms to reduce the rate. The muon reconstruction and selection is performed in two logical steps: the Level-2, which only uses data from the muon system and the Level-3, which also includes the information from the silicon tracker.

3 Muon Reconstruction Software

The same muon reconstruction algorithms are used in the off-line and HLT reconstruction. The two steps of the HLT are also used in the offline reconstruction where they are called stand-alone (Level-2) and global (Level-3) reconstruction, respectively.

The tracking of a muon candidate in the spectrometer and in the silicon tracker is based on a Kalman filter technique [4]. The algorithm is implemented according to the principle of regional reconstruction, that is the ability to reconstruct an object using only the information coming from a limited region of one (or more) sub-detectors. In the case of the HLT reconstruction, the seeds for the Kalman filter are provided by the muon candidates found by the Level-1 muon trigger, while in the off-line reconstruction, the seeds are built from the segments reconstructed in CSC and/or DT chambers.

3.1 Local Reconstruction

The basic ingredients for track reconstruction are the results of the local pattern recognition in the muon chambers. The primary objects which result from the DT local reconstruction are points in the cell volume: their distances with respect to the wire are computed by converting the drift time to a drift distance. This conversion is based on a time-to-distance parametrization, obtained using a simulation of the cell with GARFIELD [5]. The parametrization takes into account the dependence of the drift velocity from the impact angle of the track and the residual magnetic field. As those quantities are not known at the level of individual hit, an iterative process is implemented. The first step assumes a crude estimate of the impact angle and of the hit position along the wire. The hit is updated after it has been used to fit a 2D R-ϕ or R-Z segment (second step) and after that the two projections are combined to build a 3D segment (third step). The resolution of the reconstructed track segment is almost 100 μm for the position and 1 mrad for the direction.

The CSC chambers are composed by six layers of strips and wires. The bending coordinate is measured clustering together adjacent strips with signals and fitting the charge distribution with a Gatti function [6] to get the cluster centroid. The resolution ranges from 100 μm to almost 200 μm depending on the strip pitch. The other coordinate is obtained from the wire signals, discriminated and read out in bunches to minimize the number of channels. The two projections are associated using a time coincidence and are used to build a three-dimensional track segment with a linear fit.

3.2 Level-2 and Stand-alone Reconstruction

The Level-2 and the stand-alone muon reconstruction use only data from the muon spectrometer. The trajectory is built using a Kalman filter technique starting from a track seed. The hits to be included in the fit are looked for iteratively going from inside out in the muon spectrometer. At each step the state vector (track position, direction and momentum) is extrapolated to the next layer of chambers; local reconstruction is performed on-demand and the track parameters are updated accordingly. A cut on the χ^2 is applied in order to reject bad hits originated by showering, delta rays and pair production. This procedure is iterated until the outermost measurement station in the muon system is reached. A backward Kalman filter is then applied and the track parameters are defined at the innermost muon station. Finally the track is extrapolated to the nominal interaction point and fitted with a vertex constraint.

3.3 Level-3 and Global Reconstruction

A region of interest is identified within the silicon layers of the tracker around the extrapolated track obtained from the stand-alone muon reconstruction. Regional reconstruction is performed using a Kalman filter. The first step is the trajectory building starting from the innermost layer. Then ambiguities between multiple trajectories that may result from the same seed are solved on the basis of the number of hits and the χ^2 of the track fit. Finally, the trajectories are smoothed including also the hits from the muon spectrometer.

4 Performance

The overall efficiency for the reconstruction of single muons with a flat tranverse momentum in the range $5 - 100$ GeV/c is above 97% for the HLT Level-2 and Level-3 reconstruction. In the offline reconstruction the efficiency is higher, around 99%.

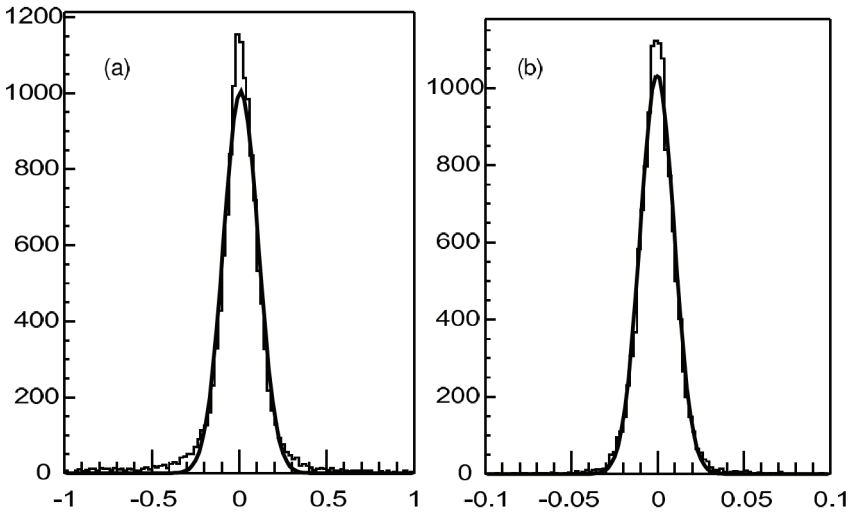

Figure 2: *Resolution on $1/p_T$ for muons reconstructed with the Level-2 (a) and Level-3 (b) reconstruction algorithm in the barrel region of the detector ($|\eta| < 0.8$)* [3] .

Figure 2 shows the resolution on $1/p_T$ for muons from W decays in the central region of CMS. In this region the resolution is about 10% at Level-2 and ten times better, about 1%, at Level-3. The measurement provided by the silicon tracker dominates the p_T resolution for muons with transverse momentum up to ~ 200 GeV/c, while at higher p_T the contribution from the muon system becomes more and more important.

References

1. CMS Collaboration, "CMS Technical Proposal", CERN/LHCC 94-38, (1994).

2. CMS Collaboration, "The Muon Project, Technical Design Report", CERN/LHCC 97-32, (1997).

3. CMS Collaboration, "The Trigger and Data Acquisition Project, Volume II, Data Acquisition & High-Level Trigger Technical Design Report", CERN/LHCC 2002-26, (2002).

4. R. E. Kalman, "A new approach to linear filtering and prediction problems", Transaction of the ASME-Journal of Basic Engineering (1960) 35.

5. R. Veenhof, "Garfield, a Drift Chamber simulation program user's guide", CERN Program Library W5050, (1994).

6. E. Gatti et al., "Analysis of the position resolution in centroid measurements in MWPC", Nucl. Instrum and Meth. 188, 327-346, (1981).

Frascati Physics Series Vol. XL (2006), pp. 223
Frontier Science 2005, New Frontiers in Subnuclear Physics
Milano, 12-16 September, 2005

TEST OF PROTOTYPES AND PERFORMANCE SIMULATION OF THE ALICE SILICON PIXEL DETECTOR

Romualdo Santoro
Dipartimento IA di Fisica dell'Università and INFN, Bari (Italy)

On behalf of the SPD project in the ALICE Collaboration

Abstract

The two innermost layers of the ALICE Inner Tracking System constitutes the Silicon Pixel Detector (SPD). The SPD is designed to provide high spatial precision and high efficiency in a region where the track density could reach 80 $tracks/cm^2$. The SPD is equipped with hybrid silicon pixel detectors. Prototype assemblies with a single readout chip have been tested in high-energy particle beams at the CERN SPS. The performance results at different detector thresholds and track incidence angles are presented. A comparison with the SPD response simulation is also discussed.

1 Introduction

Prototype assemblies of the ALICE SPD have been tested in a 350 GeV/c proton and pion beams at the SPS [1)]. The assembly is an ALICE1 readout chip (8,192 pixel cells of dimensions 50 μm $(r\phi) \times 425$ μm (z)) flip chip bonded to a matrix of silicon diodes (200 μm thick). The experimental setup consisted of the assembly under test placed between two fixed doublets of pixel planes of the same type (see Fig.1). The doublets were used as tracking system with beam tracks passing through the detectors. The spatial position and the

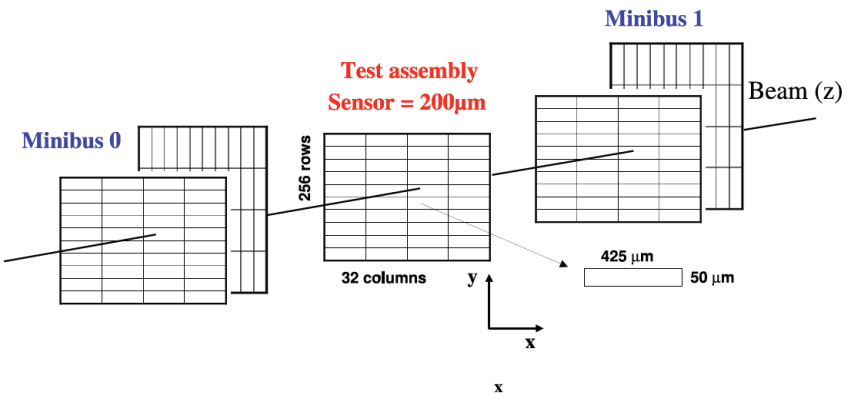

Figure 1: *Schematic view of the experimental setup used in the test beam.*

inclination angle of the assembly under test with respect to the beam line could be changed. Measurements were done at different threshold settings and orientation of the test assembly with respect to the beam line. The analysis method is mainly based on the following steps: a cluster analysis of the pixel hits, the alignment of the transverse position of the planes and the beam track reconstruction by using the two doublets. The reconstructed tracks are then used to estimate the intrinsic spatial precision of the test assembly and its detection efficiency. A detailed description can be found in [2, 3].

2 Performance results

The frequency of different cluster patterns on the test plane, at DAC threshold setting of 200 (corresponding to about 3,000 electrons [4]) and for normal incidence tracks, has been studied. In these conditions most of the clusters are made by a single pixel (68%) or by two pixels (27%) in the y direction, the coordinate along the 50 μm cell side (see Fig.2). This pattern rapidly changes with threshold setting and track incidence angle on the detector, since it is mainly determined by charge sharing and geometrical effects [3].
The spatial precision of the test assembly was estimated from the residuals distribution of the reconstructed tracks on this detector plane.

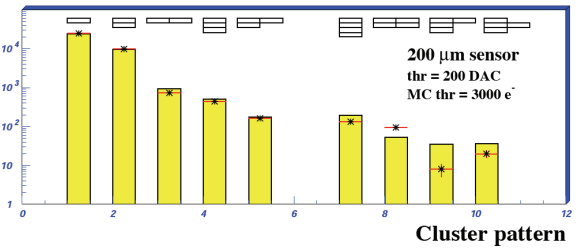

Figure 2: *Comparison of the cluster type distribution between experimental data (marker points) and the MonteCarlo (full histogram) for track at normal incidence. The threshold setting is* 200 *DAC units for the experimental data and* 3000 e^- *for the simulation.*

To disentangle the intrinsic spatial precision of the detector from the widths of the measured residuals distribution, we have taken into account the telescope tracking precision. After subtracting the uncertainty on the telescope prediction, the global detector precision (mixing all cluster patterns) is found to be $\sigma_{pixel}(y) = (\ 11.1 \pm 0.2\ )\ \mu m$, while the corresponding values for the two main cluster patterns separately are found to be:

$$\sigma^{cls1}_{pixel}(y) = (\ 11.5 \pm 0.2\ )\ \mu m \qquad \sigma^{cls2}_{pixel}(y) = (\ 6.8 \pm 0.3\ )\ \mu m \qquad (1)$$

The dependence of the detector performance on global threshold has been investigated in events with tracks at normal incidence. The spatial precision evolution is shown in the left plot of Fig.3, where the increasing DAC value corresponds to decreasing threshold in equivalent electrons (for details see [4]). At lowest threshold setting (high value in DAC units) the spatial precision improves thanks to the increasing of double-y cluster fraction. The minimum is not observed since the perfect balance of single and double-y cluster is not yet reached. At the highest threshold setting (160 DAC units) the precision is close to 50 $\mu m/\sqrt{2}$. In the full range of the threshold ($DAC > 160$) the detector has shown full efficiency ($> 99\%$). For further details see also [3].

Data runs were also taken with the detector under test tilted by 0, 5, 10, 15, 20, 25 and 30 degrees and with threshold DAC set at 185 ($\simeq$ 4000 e^-), 200 ($\simeq$ 3000 e^-) and 210 ($\simeq$ 2000 e^-). The intrinsic spatial resolution as a function of the track incidence angles is shown in the right plot of Fig.3. The precision curves reach the minimum around 5-10 degrees incidence angle, where

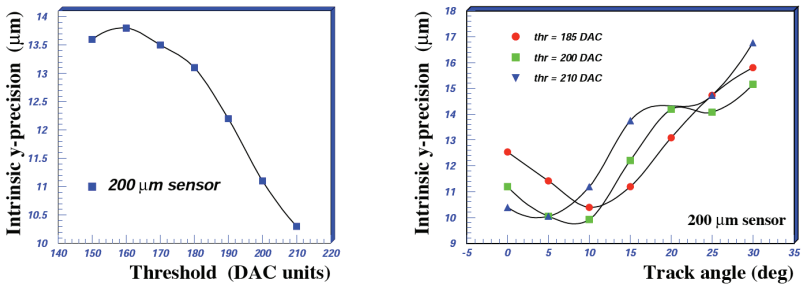

Figure 3: *Left plot: intrinsic spatial precision along the y coordinate for tracks at normal incidence, as a function of the threshold setting. Right plot: intrinsic precision along the y coordinate as a function of track incidence angle at different threshold settings.*

the fractions of single and double-y pixel clusters are roughly equal [3]. The precision degrades with increasing track angle, as expected, since higher cluster typologies are involved.

3 Comparison with the SPD simulation model

In the SPD response simulation the hole-electron cloud, produced by the particle energy loss, drifts according to a Gaussian distribution. As a consequence of the diffusion the generated charge can be shared among several pixel cells. The width of this Gaussian is calculated through the equation $\sigma_{diff} = k\sqrt{l_{dc}}$, where l_{dc} is the mean drift path of the holes (electrons) and $k = \sqrt{2D/v_{dc}}$. Here D is the hole (electron) diffusion coefficient and $v_{dc} = \vec{\mu} \times \vec{\xi}$ is the drift velocity with $\vec{\mu}$ the mobility and $\vec{\xi}$ the electric field determined by the bias voltage and the silicon sensor thickness. The energy assigned to each pixel depends on the energy loss of the incident particle in the pixel cells and the diffusion effect. A software threshold parameter is also implemented in order to determine if a pixel is fired or not.

A detailed comparison of the SPD performance in beam tests with the results obtained from the simulation can be found in reference [5]. In the simulation the kinematical parameters of the incident particles have been set and tuned to reproduce the experimental conditions. The analysis of the simulation has been performed with the same code used for experimental data. The simulation response gives a good description of the detector response; in particular it reproduces spatial precision, efficiency and cluster type distributions as a

function of the threshold and the track incidence angle.
As an example, in Fig.2 we show a comparison of the cluster pattern distributions of the Montecarlo (full histogram) and the data (points), for tracks at normal incidence and for a typical operation threshold setting.

References

1. P. Nilsson *et al.*, Proceedings of the 10^{th} Vienna Conference on Instrumentation, Vienna (Austria), February 2004, NIM A 535 (2004) 424-427.

2. G.E. Bruno *et al.*, ALICE Internal Note, ALICE-INT-2005-007.

3. G.E. Bruno *et al.*, ALICE Internal Note, ALICE-INT-2005-011.

4. P. Riedler *et al.*, Proceedings of the 10^{th} International Workshop on Vertex Detectors, Brunnen (Switzerland), September 2001, Nucl. Instrum. Methods Phys. Res. A501 (2003), 111-118.

5. G.E. Bruno *et al.*, ALICE Internal Note, ALICE-INT-2005-022.

Frascati Physics Series Vol. XL (2006), pp. 259–264
Frontier Science 2005, New Frontiers in Subnuclear Physics
Milano, 12-16 September, 2005

VALIDATION OF GEANT4 BERTINI CASCADE NUCLIDE PRODUCTION

Aatos Heikkinen
Helsinki Institute of Physics, FI-00014 University of Helsinki, Finland

Abstract

We present an investigation to validate Geant4 Bertini cascade nuclide production by proton-induced reactions on various target elements. The production of residual nuclides is calculated in the framework of an intra-nuclear cascade, pre-equilibrium, fission, and evaporation models. Comparisons of Geant4 simulated excitation functions against experimental data are presented.

1 Introduction

Medium-energy nuclear data is useful in many applications, such as accelerator shield design, effects of space radiation on astronauts, accelerator-based nuclear waste transmutation studies, interpretation of reaction products of cosmic ray particles, medical isotopes production, and radiation therapy.

In the last years, the interest to formation of nuclei in the reactions of protons with different targets has increased [1)]. Accumulated new data on fission yields, together with spallation and fragmentation products, are important for understanding the mechanisms of formation of the nuclei, and development of reliable models of intermediate energy nuclear reactions.

In this study we present an investigation to validate Geant4 [2] Bertini cascade nuclide production by proton-induced reactions on various target elements.

2 Bertini intranuclear casade

Bertini cascade implementation in Geant4 is based on INUCL code that implements intra-nuclear cascade, pre-equilibrium, fission, and evaporation models [3]. Bertini cascade and its latest extensions [4] provide inelastic treatment between hadronic bullet particle and target atoms up to 15 GeV energy. Typically, user utilizes Bertini cascade trough physics list, such as QGSP_BERT and LHEP_BERT.

3 Production of residual nuclides

In literature we can find reference [5], which presents experiment and simulation using INUCL code to study radionuclide production in U and Tc irradiated by 0.1-1.6 GeV protons. This reference compares Bertini cascade with other relevant softwares CEM, LAHET, HETC, CASCADE, ALICE, and YIELDSX. Further validations of the Geant4 Bertini Cascade model can be found from [6]. Ref. [7] gives a survey on proton-induced nuclide production from lead and presents measurements of 2000 individual cross-sections and compare them with LAHET code system.

Here, we present a selection of excitation functions induced by 30 MeV - 2.6 GeV protons. A care must be taken when interpreting results below 300 MeV, where some basic assumptions behind intranuclear cascade models may not be valid [3].

A characteristic features of high-energy reactions for excitation function and mass-yield curve are shown in Fig. 1. After an initially steep rise, excitation function levels off and becomes nearly independent of bombarding energy. This is in contrast to a compound-nucleus reaction, where the energy transfer is complete, and excitation function rapidly comes down after maximum.

Typical performance for Bertini cascade simulating yields of residual nuclei products is given in Fig. 2. Also, exitation function for reaction Co-59(p, X)Mn-54 and Co-59(p, X)V-48 are shown.

An example of important isotopes in nuclear waste transmutation in given

in Fig. 3. In this case a hadron-nucleus generator SHIELD was found to have a slightly better agreement [8].

Exitation functions of special interst to underground experiments are shown in Figs. 4. Ge from Ga is quite accurately produced. In the case of F from O Bertini underestimates cross-sections [12].

Neutron induced isotope production is usually treated with Geant4 isotope production model [11], and with an use of evaluated data libraries. Still in some cases Bertini model could be used. An example of isotope production in tungsten target is given in Fig. 5. This picture also demonstrates isotope production at higher 8.1 GeV energy.

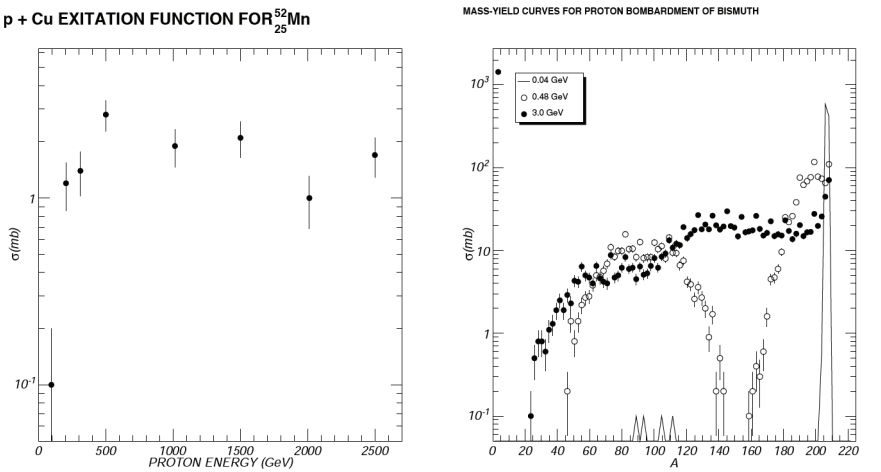

Figure 1: *Left: Geant4 Bertini cascade simulation of energy dependence of the cross section for producing manganese* $^{52}_{25}Mn$ *in the proton bombardment of natural copper. Right: Mass-yield curves for proton bombardement of bismuth target. For the case of 0.48 GeV protons we see spallation products for* $A > 160$ *and fission region for* $A < 140$*. While the energy is increased to the GeV region the clean-cut distinction between these regions vanishes.*

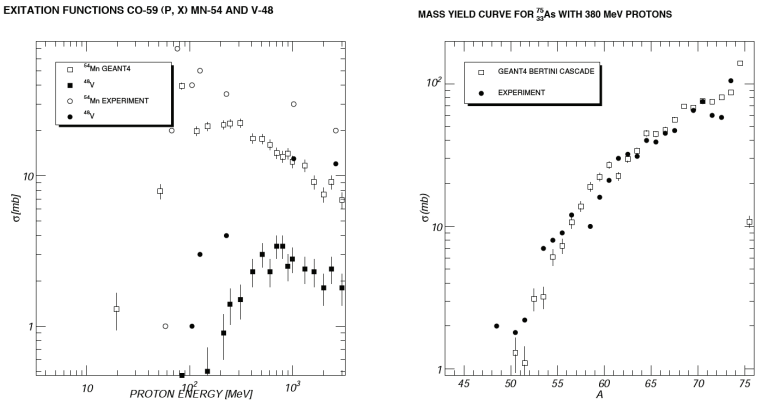

Figure 2: *Left: Bertini cascade models reproducing exitation function. Data from Ref.* [13]. *Right: Yields of residual products nuclei in thin target.*

4 Conclusion

We have given examples of the isotope production of Geant4 Bertini cascade model. In many cases the performance was found to be comparable to codes such as CEM, LAHET, or CASCADE.

References

1. V Aleksandryan *et al.*, Nuclear Physics A 674 (2000) 539–549.

2. Geant4 collaboration, *Geant4 – a simulation toolkit*, Nucl. Instr. and Meth. A 506 (2003), 250–303.

3. A. Heikkinen, N. Stepanov, and J. P. Wellisch, *Bertini intra-nuclear cascade implementation in Geant4*, Proceedings of CHEP03, La Jolla, California 24.-28.3. 2003, `http://arxiv.org/pdf/nucl-th/0306008`.

4. D. Wright and A. Heikkinen, *Adding Kaons to the Bertini Cascade Model*, Proceedings of CHEP04.

5. Yu. E. Titarenko *et al.*, arXiv:nucl-ex/9908012, 19 Aug 1999.

6. A. Heikkinen and T. Lindén, *Validation of the Geant4 Bertini Cascade model and data analysis using the Parallel ROOT Facility on a Linux cluster*, Proceedings of CHEP04.

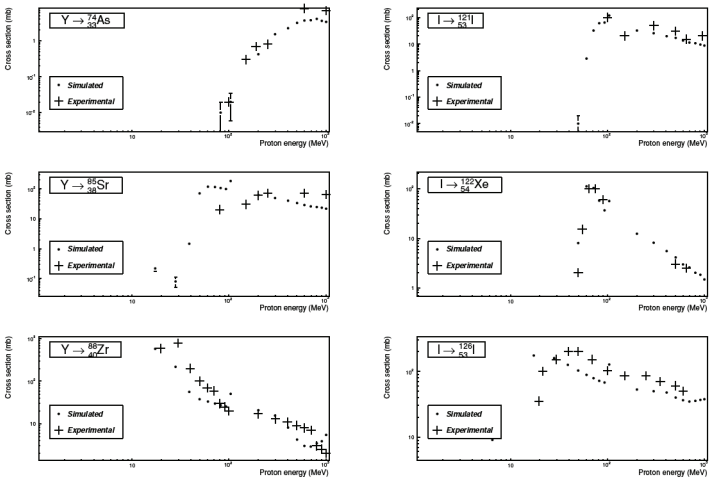

Figure 3: *Comparison of Geant4 calculated exitation functions against experimental data from* [8].

7. M. Gloris *et al.*, *Proton-induced production of residual radionuclides in lead at intermediate energies*, Nucl. Instr. and Meth. A 463 (2001), 593–633.

8. M. Khankhasayev *ed.*, *Nuclear Methods for Transmutation of Nuclear Waste*, Proceedings of the Workshop, Dubna, Russia, 29-31 May, 1996.

9. A. Letourneau *et al.*, *Composite-particle emission in the reaction p + Au at 2.5 GeV*, Nuclear Physics A 712 (2002) 133–166.

10. A. Boudard *et al.*, *A new model for production of fast light clusters in spallation reactions*, Nuclear Physics A 740 (2004) 195–210.

11. J. P. Wellisch, *The Geant4 isotope production model.*

12. H. Münzel *ed.*, *Physics Data, Karlsruhe Charged Particle Reaction Data Compilation*, Index to Vol. 1-5 (1982).

13. Th. Schiekel *et al.*, *Nuclide production by proton-induced reactions on elements ($6 \leq Z \leq 29$) in the energy range from 200 MeV to 400 MeV*, Nucl. Instr. and Meth. B 114 (1996), 91–119.

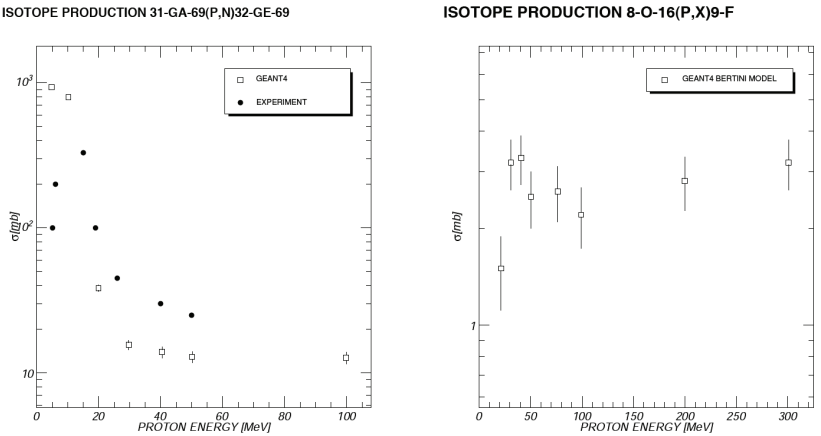

Figure 4: *Left: Here Bertini cascade has reasonable agreement with data* [12]. *Right: At low energies simulated cross-section agrees better with experimental data* [12].

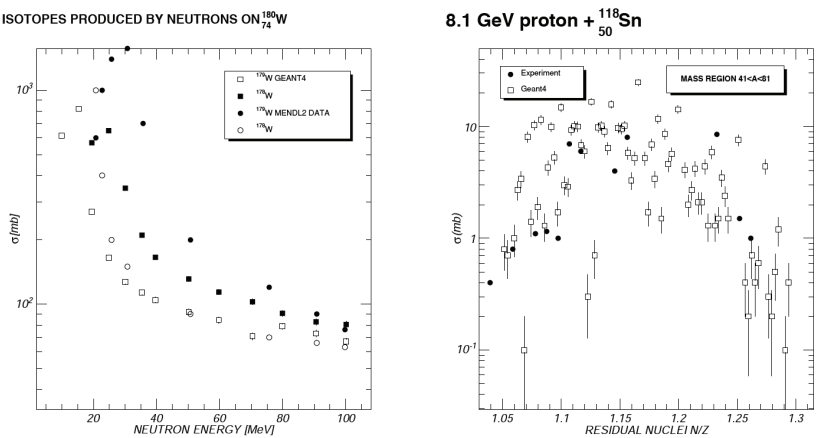

Figure 5: *Left: Example of Bertini cascade neutron induced isotope production. For more detailed treatment for low energy neutrons see Ref.* [11]. *Right: Comparison of Bertini cascade formation of residual nuclei against data from* [1]. *Energy of incoming proton is at the upper limit for Bertini models, yet we see reasonable performance.*

Frascati Physics Series Vol. XL (2006), pp. 265–269
Frontier Science 2005, New Frontiers in Subnuclear Physics
Milano, 12-16 September, 2005

GEANT4 FOR THE MEDICINE

Giovanni Santin
ESA / ESTEC, Noordwijk, The Netherlands,
and RHEA System SA, Belgium

Abstract

Accurate simulations based on the GEANT4 simulation toolkit are made possible by advanced geometry and material functionalities (including voxel based geometries and sources and anthropomorphyc phantom models) and by precise physics models, which offer an outstanding energy validity range down to the electronvolt scale in the electromagnetic domain and up to extreme high energy for hadronic interactions. Object oriented design, open source approach, collaborative development and large user community are instrumental for the continuous upgrade and extension of the toolkit capabilities, key factors for its application in the medical domain. A number of GEANT4-based tools have been created in the recent years for the use in the medical domain. Applications range from detector development and reconstruction techniques in functional imaging to accurate dosimetry in radiation therapy. Examples of such applications are given, including physics studies and realistic device simulations.

1 Introduction

Medical and nuclear physics and biology research topics in the last decades have seen an increasing use of techniques based on Monte Carlo (MC) simulations. Detailed description of the interaction of radiation with matter is

required in a wide range of applications, from functional image reconstruction algorithms to image correction methods, protocol optimisation, new medical device technology development.

MC studies are utilised for investigating the interaction of radiation with both human tissues (such as in dosimetry for therapy applications or radioprotection) and detector devices (for example for the development, validation or calibration of new imaging or dosimetric devices).

Nuclear power plants and medical radiation therapy and imaging facilities are typical examples of ground facilities in which radiation effects to humans are causing increasing concern. Short and long term effects of radiation to astronauts are also a critical factor in the design of human space missions, in particular in the context of exploration programmes. Long exposures to the harsh radiation environment in lightly shielded spacecraft in interplanetary trajectories can have a severe impact to both astronaut health and electronic devices reliability and therefore limit the mission feasibility.

MC studies offer several advantaged with respect to more traditional approaches such as analytical techniques. Detailed 3D geometry models can be used for the description of the propagation of radiation from its source to the human body through all shielding elements. A detailed material description is essential for the optimisation of effect mitigation methods and for the improvement of radiation detector performance.

Application of MC is up to now very limited in patient treatment planning, where protocols require special official approval, and traditional non-MC commercial software tools are normally used despite the superior performances of MC techniques.

Several simulation tools have been applied in the past to the domains described above. In particular, GEANT4 features and performances will be described in the next sections, together with examples of applications to the medical domain.

2 GEANT4 in the medical domain

GEANT4 [1) 2)] is an open source object-oriented toolkit for the simulation of particle transport in matter. It is developed, maintained and still continuously upgraded by a large international collaboration. While initially focussed on

High Energy Physics (HEP) experiments, it is currently used also in domains such as nuclear physics, astrophysics and space science, medical physics and nuclear medicine, radio-protection.

GEANT4 offers a wide set of electromagnetic and hadronic physics models, a good performance of the particle transport in complex 3D geometry models and the possibility of interfacing to external packages such as simulation engines and visualisation and analysis tools.

GEANT4 comprises a very large set of physics processes with a variety of models implementing them. Thanks to the object-orientated software design, complementary or alternative models can be easily developed and integrated, allowing for continuous improvements and evolution of the toolkit.

2.1 Physics development and validation

Simulation of radiation transport for the medicine imposes in particular stringent requirements on the physics description.

The Low Energy Electromagnetic package provice specific models for electrons, photons, hadrons and ions down to energies of the order of 250 eV. A recent development of relevance for the medical domain further extends the electromagnetic processes down to the eV range in liquid water.

Comparisons of GEANT4 electromagnetic models against established references [3) 4)] have demonstrated their accuracy. Verification of physics models and validation of simulation results against data is a pre-requirement for the application of a simulation tool in the medical domain. While this is auspicable already when MC tools are used for detector development, the issue becomes critical for the application of GEANT4 for radiation protection assessment or in radiation therapy protocols.

2.2 GEANT4-based applications

All the features previously described are enabling the application of GEANT4 in various domains. It is worth mentioning its use for radiotherapy, including brachytherapy [5)], hadrontherapy [6) 7)] and external beam treatment.

In recent years these has been a significant synergy with space applications, due in particular to the importance of accurate dosimetry for radiation

protection in space missions and for electronic component and system reliability issues in the space radiation environment [8) 9)].

The application of GEANT4 in the functional imaging domain and in particular to PET and SPECT, has recently dramatically increased, thanks in particular to the GATE application, which is described in the next section.

2.2.1 GEANT4 Application for Tomographic Emission (GATE)

The GEANT4 Application for Tomographic Emission (GATE) [10) 11)] is a versatile and adaptable simulation platform based on GEANT4, designed to answer the specific needs of PET/SPECT applications.

A distinctive feature in GATE is the management of time-dependent phenomena. Source kinetics and geometry movements are kept synchronised for realistic simulations of data acquisitions including patient movement, respiratory and cardiac motions, scanner rotation or changes in multiple activity distributions over time. A dedicated mechanism has been created for the development of complex 3D geometry models via scripting, hence without the need of C++ programming. Voxelised phantoms or patient data can be used for both geometry models and source activity distribution. Realism in the simulations of signals from detectors coupled to electronic systems is addressed by digitiser chains, providing signal processing modules such as discriminators, energy and spatial resolution spread, deadtime [12)], pile-up and coincidence detection algorithms. Image reconstruction of simulated data is made easier through an interface to the external libraries. Recent extensions of the GATE tool include the development of a user interface to the GEANT4 optical photon transport and energy deposition tallying for use in dosimetry applications.

Code development, mantenance and user support are shared among many research groups forming the OpenGATE collaboration [13)].

3 Conclusions and perspectives

Accurate simulations based on the GEANT4 simulation toolkit have been made possible by advanced geometry and material functionalities (including voxel based geometries and sources and anthropomorphyc phantom models) and by precise physics models, which offer an outstanding energy validity range down

to the electronvolt scale in the electromagnetic domain and up to extreme high energy for hadronic interactions. Object oriented design, open source approach, collaborative development and large user community have been instrumental for the continuous upgrade and extension of the toolkit capabilities, key factors for its application in the medical domain. A number of GEANT4-based tools have been created in the recent years for the use in the medical domain. Applications range from detector development and reconstruction techniques in functional imaging to accurate dosimetry in radiation therapy.

References

1. S.Agostinelli et al., Nucl. Instrum. Meth. A **506** (2003) 250-303.
2. J.Allison et al., "GEANT4 developments and applications", IEEE Trans. Nucl. Sci (2006) in press.
3. K.Amako et al., IEEE Trans. Nucl. Sci. **52** (2005) 910-8.
4. F.Carrier et al, Med. Phys. **31** (2004) 484.
5. F.Foppiano et al., Proceedings of the Monte Carlo 2005 Conference, Chattanooga, TN, USA.
6. G.Cirrone et al., IEEE Trans. Nucl. Sci. **52** (2005) 262-5.
7. H.Paganetti et al., Phys. Med. Biol. **49** (2004) N75-N81.
8. T.Ersmark et al., IEEE Trans. Nucl. Sci. **51** 4 (2004) 1378-84.
9. S.Guatelli et al., IEEE Nuclear Science Symposium Conference Record (2004) 2169-73.
10. G.Santin et al, IEEE Trans. Nucl. Sci. **50** (2003) 1516-21.
11. D.Strul et al, Nucl. Phys. B (Proc. Suppl.) **C 125** (2003) 75-9.
12. L.Simon et al., Nucl. Instrum. Meth. A **527** (2004) 190-4.
13. More information at the URL: http://www.opengatecollaboration.org

SESSION VII – COMPUTER SCIENCE

C. Rebbi	Physics and Computers
F. Fogolari	Computers and Bioscience
E. Valente	GARR and the research network
D. Bonacorsi	Running the Italian Tier-1 for CMS using GRID tools
D. Liko	Prototypes for User Analysis on the GRID - the ARDA project
Z. Xie	Pool persistency framework for LHC: new developments and CMS applications
A. Sciabà	The LCG project

Frascati Physics Series Vol. XL (2006), pp. 273
Frontier Science 2005, New Frontiers in Subnuclear Physics
Milano, 12-16 September, 2005

PHYSICS AND COMPUTERS

C. Rebbi
University of Boston, US

Written contribution not received

Frascati Physics Series Vol. XL (2006), pp. 275– 280
Frontier Science 2005, New Frontiers in Subnuclear Physics
Milano, 12-16 September, 2005

COMPUTERS AND BIOSCIENCES

Federico Fogolari
University of Udine, Italy

Abstract

Methods and objectives of biosciences have been changing in the last decades due to the widespread diffusion of computing machines and computer networks. The advancement mostly perceived by biologists is related to the use of databases and publicly available servers for sequence alignment and analysis, but it is foreseeable that modeling and computation will play a relevant role in the study of biological systems. Although the subject is extremely vast, here I will present a survey of applications of computation in the biological sciences.

1 Introduction

Applications of computers are widespread in biological sciences laboratories. The availability of low-cost powerful computing machines has changed completely the way data are acquired, processed, stored, retrieved and analysed. It is almost impossible to deal here with all the applications linked with specific laboratory practice. It is worth mentioning that sequencing of the human and several hundreds genomes sequenced so far would have never been possible, without automated processing and analysis. The large amount of data that

has been created by sequencing projects and the public deposition and sharing policy of the largest biological databanks has made information storage, information retrieval and processing the most evident application of computers and computer networks to biologists. The sequence database Genbank includes now more than 100 Gbases and roughly doubles in size every two years. More and more databases are created and made accessible over the Internet. Such fastly evolving landscape made the Nucleic Acids Research to have the first issue of the year entirely dedicated to biological databases and the first issue of July dedicated to publicly available web servers. From a physicist's point of view however most interesting applications are connected with modeling and computer simulations of biological entities or processes. In the following I will attempt an overview of biological systems and processes and of their computational models and point to some representative references.

2 Modeling biological processes

Following a top-down approach we may describe the main targets of biological studies according to a very schematic table reported hereafter (Table 1).

2.1 Ecological systems, population dynamics

At the highest level is the study of ecological systems where relevant entities are species individuals interacting among themselves and with the environment. Species are typically represented by populations which can be distributed in space and the time evolution of populations is modelled using differential equations [1)]. Protoypical equations are the Lotka-Volterra equations for the predator-prey system whose non-trivial solution displays oscillatory behavior. Simulation of individuals is also possible for restricted environments. Depending on system stochasticity, typically performance of many simulations and analysis is required. Since parameters for complex systems are mostly unknown, these are determined through comparison with observational data. Using such models, for instance, the dynamics of infectious diseases can be simulated and predictions of their impact on population can be performed. The outbreak of AIDS, Creutzfeldt-Jakob disease and SARS epidemics with social and economical consequences renewed the interest and the resonance of model simulation based predictions. Very recently computer simulation studies suggested optimal strategies for containing the expected outbreak of avian flu epidemics [2)].

Table 1: *Biological systems, processes and models.*

Biological system or process	Relevant entities	Represented entities	Modeling methods
Ecological systems, population dynamics	Species individuals, environment	Populations in space and time, environment	Differential equations
Organisms, organs, cells	Cells, cell's compartments, proteins, genes, metabolites, environment	Cells, cell's compartments, molecular concentrations in space and time	Differential equations
Metabolic processes, gene regulatory cycles	Enzymes, metabolites, proteins, genes	Molecular concentrations in space and time	Differential equationsi, graphs
Biomolecular evolution	Species, DNA, proteins, environment	DNA and protein sequences	String algorithms, Hidden Markov Models, Neural networks, statistical methods
Biomolecular dynamics and thermodynamics, biomolecular recognition	DNA, protein and solvent atoms, electrons	Residues, chemical groups, implicit solvent, atoms, electrons	Simplified (lattice) models, Monte Carlo, molecular dynamics, ab-initio methods.

2.2 Organisms, organs, cells

Modeling and simulation of cells, organs and (parts of) organisms is one of the challenging goals of biomedical sciences and engineering. The task requires integration of knowledge from physiological, anatomical, biomechanical and biochemical investigations. Modeling of the heart shows in a paradigmatic way these features. Cardiac myocytes are modelled, as far as membrane potential is concerned, by non-linear ordinary differential equations. Properties of cells are included in anatomically detailed models of the heart through a continumm representation. Finite difference or finite elements methods are then used to solve the (in the range of millions) coupled non-linear partial differential equations. Results achieved, although studies at this level of detail are just starting, have been impressive [3, 4].

Another emerging field of application is the simulation of development where the network of interactions between proteins and genes within and among cells is simulated. Integration of ordinary differential equations governing the time and spatial concentrations of proteins and mRNAs leads to solutions which are compared with experimental observation. The model is thus refined in an iterative way. Model refinement via comparison with experimental data is a constant feature of all simulation approaches discussed here.

Although still far from being predictive, simulation could highlight general features of developmental regulatory interactions [5].

2.3 Gene regulatory cycles, metabolic processes

The complex interplay of genes, transcription factors, other proteins and metabolites constitutes the heart of what is called systems biology [6, 7]. The interest in addressing complex biological behaviors stems from the massive amount of expression data available from DNA microarray experiments, which probe the expression of thousands of genes in a single experiment. On one hand analysis of experimental data requires numerical data processing and data-mining techniques, entailing clusterization of genes whose expression is correlated and classification techniques. On the other hand interactions can be simulated. One approach involves the usage of directed or undirected graphs where each vertex represents a gene and interactions, which can be modeled according to different formalisms, are represented by edges. A more standard approach involves coupled non-linear ordinary differential equations which are used to propagate in time genes, proteins and metabolites concentrations. The prototypical equation for describing molecular interactions is the Michaelis-Menten equation for enzyme-catalysed reactions. Since the parameters are not known (or at least they are incompletely known), the model must be iteratively refined by direct

comparison with known experimental facts. Simulation software packages including most common equations used to describe molecular interactions are available [8].

2.4 Biomolecular evolution

All functions of cells are ultimately performed by proteins whose chemical structure is coded in DNA. The linear and polymeric nature of proteins and DNA allows to represent them as strings (or sequences) of characters. DNA sequences evolve in time according to the neo-Darwinist theory. Similarity between two sequences is mostly due to homology (i.e. descent from a common ancestor sequence). When significant similarity is found it can be inferred that two sequences probably share a common origin, structure and a common or related function. Strings can be compared (aligned) using dynamic programming algorithms, heuristic algorithms based on hash tables or suffix trees. Due to the ever increasing size of sequences databases, alignment is performed by specialized servers, like the NCBI server in the United States or the EBI server in Europe. Sequence alignment, pattern finding and property predictions are performed also by other statistical methods like sequence profiling, and machine learning approaches such as hidden Markov models and neural networks [9].

2.5 Biomolecular dynamics and thermodynamics, biomolecular recognition.

The prediction of structure of proteins and the elucidation of structure-function relationship of proteins is the ultimate goal of structural proteomics or genomics. Structural predictions are typically performed generating structural models for the system (be it a single protein or a biomolecular complex) and selecting the most plausible among them [10]. Selection requires assigning a score to each model. Since the most plausible models are the lowest free energy ones, scoring functions are often assimilated to free energies. The two main approaches use knowledge based (or statistical or empirical) potentials and physical potentials. Computation is typically demanding because of the number of models to be screened and the complexity of both the systems (including thousands of atoms) and the computational model that must include solvation effects. Protein flexibility has consequences on its function. Powerful techniques for molecular dynamics simulation exist which enable simulation of tens to hundreds thousand atoms on PC clusters [11]. Atomic interactions are mostly described using classical forcefields, although ab-initio treatments of small molecular parts is possible. Molecular dynamics is also used for sampling the conformational space close to a given (typically experimental) conformation. These methods complement standard laboratory practice and are playing

an increasing role in structural studies and drug design.

3 Conclusions

Computation and simulation are showing wider landscapes to biological sciences researchers. In the next future a move from proofs-of-principle to predictive applications is foreseeable.

4 Acknowledgements

Support by FIRB (grant RBNE03B8KK) by Italian Ministry for Education, University and Research is gratefully acknowledged.

References

1. S.A. Levin *et al*, Science **275**, 334 (1997).
2. N.M. Ferguson *et al*, Nature **437**, 209 (2005).
3. D. Noble *et al*, Physiol. **19**, 191 (2004).
4. R.L. Winslow *et al*, IBM Systems J. **40**, 342 (2001).
5. G. von Dassow *et al*, Nature **406**, 188 (2000).
6. H. Kitano, Nature **420**, 206 (2000).
7. H. de Jong, J. Comput. Biol. **9**, 67 (2002).
8. K. Takahashi *et al*, Bioinformatics **19**, 1727 (2003).
9. P. Baldi and S. Brunak, Bioinformatics: the machine learning approach. MIT Press (2001).
10. P. Bradley *et al*, Science **309**, 1868 (2005).
11. D. van der Spoel *et al*, J. Comput. Chem. **26**, 1701 (2005).

Frascati Physics Series Vol. XL (2006), pp. 281
Frontier Science 2005, New Frontiers in Subnuclear Physics
Milano, 12-16 September, 2005

GARR AND THE RESEARCH NETWORK

E. Valente
University of Roma, Italy

Written contribution not received

Frascati Physics Series Vol. XL (2006), pp. 283– 286
Frontier Science 2005, New Frontiers in Subnuclear Physics
Milano, 12-16 September, 2005

RUNNING THE ITALIAN TIER-1 FOR CMS USING GRID TOOLS

D. Bonacorsi
(on behalf of INFN-CNAF Tier-1 and CMS experiment)

Abstract

The CMS computing system relies on a distributed infrastructure of Grid resources, services and toolkits, whose building blocks are provided by the Worldwide LHC Computing Grid (WLCG). CMS builds application layers able to interface with few - at most - different Grid flavours (LCG-2, Grid-3, EGEE, NorduGrid, OSG). In the Grid-enabled tiered architecture depicted in the CMS computing model, the Tier-1 centres play a crucial role. As an example, recent CMS activities at the INFN Tier-1 are briefly outlined and discussed.

1 Introduction

The CMS computing model as outlined in the Technical Design Report [1)] is to be seen in preparation for the first year of LHC running (2008). It depicts a hierarchy of computing Tiers relying on WLCG tools, and describes the baseline targets and development strategies for the forthcoming years.

CMS relies on Grid technologies for the *Workload Management* to grant a configure environment for CMS jobs and to ensure submission rates of $\sim$1000 jobs/few-secs and processing reliability at 24/7 with $> 95\%$ job success rate.

The CMS *Data Management* requires a data book-keeping system to tell "what data do exist?" (containing references to parameters, luminosity and data quality info); a data location service to tell "what is the data location?"; a data transfer/placement system which relies (not "trusts") on underlying transfer systems; site local services and local file catalogues for data storage/access.

The CMS Tier-1 centres are ASCC (Taipei), CCIN2P3 (Lyon), FNAL (Chicago), GridKA (Karlsruhe), INFN-CNAF (Bologna), PIC (Barcelona), RAL (Oxford). The Tier-1 functionalities required by CMS are: *i)* scheduled data-processing operations (later-pass reconstruction, AOD extraction, skimming, reprocessing); *ii)* data custody (raw+reco, subsequently produced data); *iii)* disk (fast cache to MSS archives, buffer for data transfer) and MSS management; *iv)* data distribution (import/export from/to CMS Tiers); *v)* analysis/user support to grant data access via WLCG services; *vi)* possible use as a co-located Tier-2 (access to local long-term storage and batch facilities) but the latter with no interference with Tier-1 commitments towards CMS.

To provide such functionalities, a Tier-1 for CMS must accordingly guarantee services (disk/MSS management, WLCG-enabled farming, site security, accounting, database services, user support) and resources (nominal for an average CMS Tier-1 in 2008: WAN >10 Gb/s, CPU 2.5 MSI2k, disk 1.2 PB: 85% for analysis data serving, MSS 2.8 PB: tens of GB lost per PB stored).

In the following, the CMS experience at INFN Tier-1 is outlined.

2 INFN-CNAF Tier-1: Grid-enabled services and resources

The INFN Tier-1 centre, located at CNAF in Bologna, offers computing facilities for the INFN HEP community, and is one of the main nodes of the GARR network. As a multi-experiment Tier-1, it aims to provide a dynamic share of access to resources to all involved experiments. CNAF is a peculiar site from a Grid perspective: it participates in LCG, EGEE and INFN-Grid projects, leading R&D activities, developing middleware prototypes and components, and supporting the use of Grid technologies by experiments. Currently, the INFN Tier-1 CPU power on non-legacy farms is about 2250 CPU slots available as biprocessor boxes with hyper-thread activated, in use by all Tier-1 experiments on a fair-share basis on a monthly time-window. The LCG 2.6.0 middleware is installed, Quattor 1.1.0 is used to manage nodes, the LSF 6.1 scheduler is used: LCG interfacing is fully certified. The set-up of storage re-

sources at CNAF is focussed on robust, load-balanced, redundant solutions to grant proficient and stable data access to distributed users. The disk storage capacity is currently divided into 4 NAS systems (60 TB), and 2 SAN systems (225 TB). The disk access patterns are derived from specific experiments use-cases. Currently CMS uses disk space to host and serve simulated data to the CMS analysis community. CMS uses tapes as a reliable, affordable means for storing large volumes of data and for addressing the Tier-1 data custodial responsibility as required in the CMS computing and analysis model. At CNAF a Castor HSM system operates a Stk L180 tape library (18 TB) and a Stk 5500 tape library (240 TB on 6 IBM LTO-2 drives and 136 TB on 2 9940b drives).

Apart from daily production-quality operations, along its path CMS undertook a large-scale data challenge (DC04) - with the aim of validating its computing and Grid infrastructure on a sufficient number of Tier-0/1/2s - and is also involved in LCG Service Challenges - focussed, sustained testing activities in which existing hw/sw are pushed beyond their current use levels toward those required for running when the LHC experiments come on-line.

The reliability of CMS tools and the stability of Tier-1 Grid-enabled resources emerged as crucial items in CMDS DC04. The preliminary large Pre-Challenge Production (PCP) of simulated events was successfully done using both traditional methods and Grid prototypes (CMS/LCG-0, LCG-1, Grid3). The need for an automatic system for data registration and distribution was fulfilled, also supporting a (reasonable) variety of different data transfer tools (INFN Tier-1 achieved good performance using LCG-2 tools). A key role was played by the central Transfer Management Database (TMDB): this was the embrional PhEDEx (see later). The real-time distributed data analysis at the Tiers acting as nodes in the data distribution topology was demostrated to be possible. The Tier-1 analyzed the reconstructed data as they arrived, fully using LCG-2 components (a dedicated RB/bdII, standard UIs, a CE and the pool of WNs of the official CNAF Grid-enabled farm). At the Tier-2s, 15k jobs were submitted, with a 20 minutes end-reco/job-start time window.

The LCG Service Challenge phase 3 (SC3) focuses on data transfer and data serving in real use-cases, aiming to review (and boost) existing infrastructure/tools. SC3 was organized in two phases: a "throughput" phase focused on Tiers simultaneous data import/export, with MSS involved, while a "service" phase aimed to implement a small scale replica of the overall system, with main

focus on testing a quite complete environment for experiment-specific tests and inputs. The INFN Tier-1 participated to SC3, also with CMS applications. CMS ran the phase 3 of LCG-SC using the PhEDEx tool.

3 Physics Experiment Data Export (PhEDEx)

The PhEDEx system offers a large-scale, reliable, scalable dataset replication. It is currently in use by CMS as official data distribution management system. Basically, it addresses HEP use-cases via a push-pull negotiation: it grants replication, data safety, tape migration/stage via a layered architecture and agnosticism towards the basic transfer mechanisms used. It ensures reliability and replication robustness. More information in [2] and references therein.

4 CMS data analysis

CMS is moving from "controlled" and "fake" analysis efforts (as in DC04) towards "unpredictable" and "real" data access and analysis activities. The INFN Tier-1 stably provides one full LCG site, and a complete support to CMS physics groups. The data samples (80 million of events) for the Physics TDR are distributed at CMS Tier-1s, and Grid allows end-to-end analysis, i.e. jobs are sent to prelocated data. The CMS Remote Analysis Builder (CRAB) tool is used for job preparation, submission and monitoring, and tens of users submit hundreds jobs/day on INFN Tier-1 resources.

References

1. The CMS Computing Project: Technical Design Report, CERN-LHCC-2005-023, 20 June 2005

2. D. Bonacorsi *et al*, PhEDEx: reliable, scalable dataset replication, in: Proc. of this conference

Frascati Physics Series Vol. XL (2006), pp. 287– 296
Frontier Science 2005, New Frontiers in Subnuclear Physics
Milano, 12-16 September, 2005

PROTOTYPES FOR DISTRIBUTED ANALYSIS ON THE GRID - THE ARDA PROJECT

D. Liko, J. Andreeva, J. Herrala, M. Lamanna,
A. Mayer, J. Mosckicki, B. Koblitz, A. Peters, N. Santos
CERN, Geneva, Switzerland
C. Munro
Brunel University, London, U.K.
D. Feichtinger
Paul Scherrer Institute, Villigen, Switzerland

Forschungszentrum Karlsruhe, Karlsruhe, Germany
F. Orellana
University of Geneva, Geneva, Switzerland
T.S. Chen, S. C. Chiu, H.C. Lee, W.L. Ueng
Academica Sinica Grid Computer Center, Taipei, Taiwan
A. Demichev, A. Berejnoy
Moscow State University, Moscow, Russia
V. Galaktionov, V. Pose
Joint Institute for Nuclear Research, Dubna, Russia

Abstract

In collaboration with the four LHC experiments the ARDA [1)] project has developed prototypes for distributed analysis. These prototypes were developed in close interaction with the development of the EGEE [2)] middleware, gLite. In this context, ARDA contributed to the evaluation of new middleware components. A further ARDA contribution is the development of a new metadata catalog, which is now part of next gLite release. Currently the prototypes are still in evolution with the goal to become part of the LCG environment for the LHC users.

1 Introduction

The ARDA project (A Realisation of Distributed Analysis for LHC) was created within the LCG project in 2004 to develop a prototype grid analysis

system for the experiments at the Large Hadron Collider (LHC). The guiding idea behind ARDA is that exploring the opportunities and the problems encountered in using the grid for LHC analysis would provide key inputs for the evolution of gLite the EGEE middleware. Enabling a large, distributed community of individual users and small groups to use the Grid without central control stresses the infrastructure in a radically different way compared to large scale, continuous 'production' activities like generation of simulated data or event reconstruction.

Fostering innovation is a key element: the understanding of analysis activities in the LHC era is still evolving very fast, and so we need to retain flexibility. The patterns observed in the past suggest that the new Grid infrastructure will enable and stimulate new approaches to data handling and analysis with the ultimate goal to enable a large scientific community to maximize the scientific output of the LHC programme. A sound approach to such an evolving infrastructure is to prototype the future systems together with the users, exposing them early to the Grid environment, and discussing the evolution on the basis of their experience.

Testing the Grid under real conditions gives effective feedback to the developers of Grid middleware. During the first phase of EGEE, ARDA played a key role in the testing of the middleware, with its access to 'previews' of gLite components. Progressively this activity moved towards detailed studies of performance issues, but always using the analysis scenario as a guideline. As an example, the experience and requirements of the LHC experiments led ARDA to propose a general interface for metadata access services. Eventually an ARDA prototype called AMGA (ARDA Metadata Grid Application) made its way into the gLite middleware and is now also used by non-HEP applications. The ARDA project is developing prototype for analysis on the grid for the four LHC experiments. These prototypes follow the experiment strategy and are complementary in their approach.

2 Distributed Analysis Prototypes

From the beginning, it was decided to agree with each LHC experiment an a-priori independent prototype activity. It was considered unrealistic to force at an early stage commonality in the use of tools, since each experiment has different physics goals and data organization models. On the other hand, all

different activities hosted in the ARDA team benefit for common experience and cross fertilisation. In this section, a series of examples of the prototype activity with the LHC experiments are given.

2.1 ALICE

The ALICE prototype is an evolution of the early distributed-analysis prototypes made by the experiment using their AliEn system, incorporating features from the PROOF [3] system (Parallel ROOt Facility) and providing the user with access via the ROOT/ALIROOT prompt. Close integration with the standard (local) analysis environment can be obtained only by carefully designing the gateway into the distributed system. An important component, developed within ARDA, is the C Access Library, optimizing the connection to the Grid infrastructure via an intermediate layer that caches the status of the clients (in particular their authorization) and therefore helps to optimize the performance as required for interactive use. Operations like browsing the file catalogue or inspecting a running job can be provided via mechanisms already known to the ALICE users (shell commands and ROOT system).

The ALICE framework provides user analysis in batch and interactive mode. It uses the AliEn grid middleware as a high-level service interface for access to the AliEn file catalogue and distributed computing resources via internal interfaces (LCG, native AliEn). The user interface consists of a grid shell, a QT based GUI and an AliEn grid plug-in to the ROOT framework. The GUI allows the selection of data, the execution of analysis jobs in interactive and batch mode, the retrieval and the storing of results. The PROOF system is used for interactive analysis, which on its own provides a GUI for interactive analysis. ALICE uses a multi-tier PROOF setup to allow analysis of data distributed over several mass storage systems in the same PROOF session. Depending on the data volume to be analyzed the response time for interactive analysis can be few seconds, while for batch analysis it is in the order of several minutes or hours.

2.2 ATLAS

The ATLAS strategy follows a service oriented approach to provide Distributed Analysis capabilities to its users. Based on initial experiences with a dedicated analysis service, the ATLAS production system has been evolved to support

analysis jobs. The ATLAS ARDA group has contributed to the initial system and is now coordinating the overall ATLAS effort.

As the ATLAS production system is based on several grid flavours (LCG, OSG and Nordugrid), analysis jobs are supported by specific executors on the different infrastructures (Lexor, CondorG, Panda and Dulcinea). The implementations of some of these executors in the new schema are currently under test, in particular also in analysis mode [4)].

While submitting jobs to the overall system will provide seamless access to all ATLAS resources, ATLAS support user analysis by submitting directly to the separate grid infrastructures (Panda at OSG, direct submission to LCG and Nordugrid.) A common job definition system is currently under development that will be supported by all systems.

Finally a common user interface project, GANGA, will provide support for the various submission options and will provide a consistent user experience. This project is developed in collaboration with the LHCb experiment and is discussed in more detail in section 2.4.

A point of specific interest is the coexistence of Distributed Analysis by individual ATLAS users with the overall ATLAS production. At this point the effective coexistence of different jobs (long production jobs and relatively short analysis tasks) is still under study and the final model is being worked out. Another fundamental point (and an important contribution of ARDA) is the study and the tuning of the Workload Management System, which would have a major impact for analysis jobs, when the system will have to deal with a increasingly larger number of jobs without degrading the system response time [5)]. These aspects are currently addressed in the context of the ATLAS LCG/EGEE taskforce.

2.3 CMS

The ARDA-CMS activity started with a comprehensive evaluation of gLite and the existing CMS software components. Eventually ARDA focused on providing a full end-to-end prototype called ASAP [6)], prototyping some advanced services such as the Task Monitor and the Task Control. The Task Monitor gathers information from different sources: MonaLisa (mainly providing run time information via the CMS C++ framework COBRA); the CMS production system; Grid-specific information (initially the gLite/LCG logging and

bookkeeping and recently the R-GMA system). The Task Control implements CMS specific strategies, making essential use of the Task Monitor information. The Task Control understands the user tasks (normally a set of jobs) and organizes them in a way which enables the user to delegate several tasks, e.g. the actual submission (the user registers a set of task and then disconnects) and error recovery. Some key components of this very successful prototype, which incorporated a lot of feedback from users, are now being migrated within the official CMS system CRAB (CMS Remote Analysis Builder) in the framework of the CMS-LCG taskforce.

CMS has developed a job generating tool - CMS Remote Analysis Builder (CRAB) - to support user analysis on the Grid. In the CMS workload management model, jobs are sent to the sites where the input data are available.

Though there is an overlap between CRAB and ASAP in the job generation phase, ASAP provides additional functionality by managing tasks for the user on behalf of him. Users only need to call the ASAP job generation command in order to generate a set of jobs, which are combined into a task. The newly created task can be registered in the ASAP Task Manager.

The Task Manager follows the progress of task processing, resubmits failed jobs and generates web pages, which provides physicists the status of all their tasks. Monitoring of the user jobs is based on the Monalisa monitoring system. The functionality of the Task Manager and the Job Monitor was appreciated by the pilot CMS users. These components should be integrated into the final CMS system. Currently ARDA is working on the integration of the Task Manager and the Job Monitor with the CRAB job generation tool.

Another important aspect of Grid usage, both for analysis and production, is to provide a global view of all jobs belonging to a given VO, presenting information about usage, sharing of resources, performance and data distribution issues, failure rates of the Grid and the physics applications, and load balancing between different sites. ARDA is participating in the development of the CMS Dashboard. The CMS dashboard is a tool to show the CMS computing activities, allowing to focus on specific interval of times, sites, group of jobs, sets of data etc..

2.4 LHCb

The ARDA-LHCb prototype activity is focusing on the GANGA [7] system (a joint ATLAS-LHCb project). The main idea behind GANGA is that the physicists should have a simple interface to their analysis programs. GANGA allows preparing the application, to organize the submission and gather the results. The details needed to submit a job on the Grid (like special configuration files) are factorised out and applied transparently by the system. In other words, it is possible to set up an application on a portable PC, then run some higher-statistics tests on a local facility (like LSF at CERN) and finally analyse all the available statistics on the Grid just changing the parameter which identifies the execution back-end.

The complete functionality of GANGA Core is defined in the GANGA Public Interface (GPI). GPI is a python-based, user-centric API that is a key component of the system.

The GPI provides a convenient abstraction layer for job submission and monitoring. Presently GANGA supports several back-ends, namely different version of the LCG/EGEE middleware, the DIRAC system (LHCb production system), the ATLAS production system plus local batch systems and local execution. Any application can be submitted, but the system is optimized to help in the customization of the major applications ATLAS and LHCb users are interested in, namely ATHENA and GAUDI applications. As a result, GANGA provides the same interface for local and grid environment. From the end-user perspective it is very easy to switch between various environments depending on the computing and data access needs (local debugging fully distributed execution of heavy tasks) with the reduced learning overhead.

A graphical user interface, based on the Qt framework, is a part of the new GANGA releases. The GUI integrates scripting and graphical capabilities into a single environment. It also provides an easy and intuitive way of work, especially important for the beginners. The GUI is a GPI overlay and it is a perfect example of how the GANGA Core may be easily embedded in a separate framework. The present architecture envisages the creation of different specialized user interfaces to best cope with specific activities. Although there is a clear value in graphical portals (especially for novice users on one hand and to simplify large repetitive tasks as in large productions), the availability of the 'grid scripting language' provided by the GPI is a real plus provided by

this system (in addition, the usage of the GU produces editable files which can be modified and embedded in other applications).

GANGA is an open-development framework which fully exploits the plug-in architecture. This makes the integration of new applications and backends very easy. Applications, such as Geant4 simulations in medical physics, or the BLAST protein alignment algorithm in biotechnology have been successfully run with GANGA.

3 Contributions to the EGEE middleware

3.1 Evaluation of the Workload Management

In the next generation EGEE workload management system, gLite WMS, new features such as bulk submission and input sandbox sharing are introduced for improving the job processing performance. In order to evaluate the bulk submission feature, all test jobs are submitted in bulk. The job processing performance is represented by the following three inter-periods of job lifecycle: Job submission time: the time interval from issuing job submission command on User Interface (UI) to the end of job submission (i.e. the prompt back on UI). Job dispatching time: the time interval from the job acceptance by Network Server to the completion of job transferring from Resource Broker (RB) to Computing Element (CE). Job finishing time: the time interval from job launching on CE to the end of job lifecycle. The evaluation is performed in the context of the ATLAS LCG/EGEE taskforce on the test environment at INFN-Milan with the installation of gLite 1.4 [5)].

3.2 Evaluations of the Data Management

File Catalogues represent an important component of any Grid system. ARDA focused on the evaluation of the LCG File Catalogue (LFC) and the File and Replica Management Catalogue (FiReMan) [8)] . LFC is a stateful, connection-orientated catalogue written in C while FiReMan uses a service-orientated approach using SOAP for communication and Tomcat as a server.

A series of tests were conducted using a multi-threaded client to imitate many simultaneous connections. Each of the elementary catalogue operations: insert, delete and query were tested with different test parameters such as the number of threads, bulk message size for FiReMan and use of sessions for LFC.

The Oracle and MySQL backends were used and the client and server were connected by a Grid Security enabled SSL connection over a LAN and a WAN.

The LFC catalogue shows very similar performance with both the Oracle and MySQL back-ends. A query rate of 24 with 1 client up to 227 queries/s for 20 clients. The MySQL implementation of the FiReMan catalogue with a bulk size of 1000 can perform 241 queries/s with 1 client up to a maximum of 407 with 50 clients. The Oracle implementation performs much better mainly due to the fact that the application logic is implemented as stored procedures in Oracle rather than in Tomcat. For a single client with a bulk size of 1000 763 queries/s can be obtained up to a limit of 1800 with multiple clients. This relies on the fact that the database will cache the result so that we can effectively measure the overhead the catalogue server imposes on the operation.

3.3 The Grid metadata system AMGA

AMGA [9] (ARDA Metadata Grid Application) is the metadata service within gLite. It can be used to associate key-value pairs as metadata to files stored on the grid as well as to provide simple relational database services on the grid.

AMGA was initially developed by ARDA to be a prototype system for metadata access based on the knowledge obtained from extensive testing of the experiment prototypes of metadata catalogues. Key features of AMGA include a SOAP WebService front-end as well as a TCP streaming interface, bulk operations via TCP streaming or SOAP iterators and several different database back-ends including MySQL, Oracle and PostgreSQL. AMGA can be used as an add-on to the LFC file-catalogue.

Many functionality tests similar to the tests of the experiment metadata solutions were performed with AMGA in order to validate the basic design and stability of the implementation, in particular the behaviour of bulk operations which are done via iterators in the SOAP interface or via TCP streaming. Tests on a wide area network showed very encouraging performance of the streamed operations which allow minimize the impact of the long roundtrip time. We also validated the ACL-based security of AMGA.

4 Collaboration with other sciences

ARDA is a very active contributor to the EGEE project. EGEE benefits from the exchange of ideas with and experience of groups that actively support

scientific communities, notably the LHC experiments and biomedicine. Being capable to map concepts and strategies developed in one particular application domain to other sciences is a powerful indicator of an improved theoretical understanding of Grid techniques. Each application domain can contribute with its specific requirements and knowledge and thus improve the system as a whole. At the beginning, the main field where the ARDA group collaborated with other sciences are in participating to a common testing effort of the gLite middleware. In this phase, there is a major collaboration in the field of grid databases. The AMGA system is being evaluated with encouraging results by several users' group in EGEE, notably the Gilda team (EGEE Generic application support), the biomedical community (Medical Data Management working group) and by Earth Observation groups (ESR and UNOSAT).

5 Conclusions

The different prototype activities in ARDA, together with other activities within the experiments, are converging on a first version of the distributed-analysis systems, which will be used in the first phase of LHC operation. In the second phase of EGEE we expect to streamline this activity to further support the experiments' systems for both production and analysis. This means also continuing to influence the evolution of the middleware and the Grid infrastructure, using larger-scale experience and fostering the contacts with non-HEP scientists established during the first phase.

6 Acknowledgements

We would like thank EGEE middleware developers and the Distributed Analysis teams within the LHC experiments for their excellent collaboration.
This work received support by the Federal Ministry of Education and Research (Bundesministerium fuer Bildung und Forschung), Berlin, Germany.

References

1. A Realisation of Distributed Analysis for LHC, `http://cern.ch/arda`
2. Enabeling Grids for ESciencE, `http://cern.ch/egee`

3. PROOF, The parallel ROOT facility, `http://root.cern.ch/root/PROOF.html`

4. S. Gonzalez de la Hoz et al., *Distributed Analysis Jobs using the ATLAS production system*, this proceedings.

5. ARDA/gLite Middleware Activity, `http://cern.ch/arda`

6. ARDA Support for CMS Analysis Processing, `http://cern.ch/arda`

7. Karl Harrison et al., *GANGA*, this proceedings.

8. C. Munro, *Performance Comparison of the LCG2 and gLite File Catalogues*, Proc. of Advanced Computing and Analysis Techniques (ACAT 05), DESY, Zeuthen, Germany, May 2006.
   C. Munro, B. Koblitz, N. Santos and A. Khan, *Performance Comparison of the LCG2 and gLite File Catalogues*, IEEE Nuclear Science Symposium, October 23 - 29, 2005, Puerto Rico.

9. N. Santos and B. Koblitz, *Metadata Services on the Grid*, Proc. of Advanced Computing and Analysis Techniques (ACAT 05), DESY, Zeuthen, Germany, May 2006.

Frascati Physics Series Vol. XL (2006), pp. 297– 300
Frontier Science 2005, New Frontiers in Subnuclear Physics
Milano, 12-16 September, 2005

POOL PERSISTENCY FRAMEWORK FOR LHC NEW DEVELOPMENTS AND CMS APPLICATIONS

Z. Xie
Princenton University, Princeton, NJ 08544 USA
D.Düllmann, G.Govi, V.Innocente, I.Papadopoulos
CERN, Geneva 23, CH-1211, Switzerland

Abstract

POOL [1)], the persistency framework for LHC, has been successfully used by ATLAS, CMS and LHCb to handle event data during data challenges. It is now in the fourth year of active development. New developments in POOL focus on implementing the storage manager based on relational technologies. The relational backend of POOL(POOL-ORA) is chosen by the CMS experiment for handling conditions data.

1 Introduction

The scope of the POOL(Pool Of persistent Objects for LHC) project is to provide a software framework for object storage for LHC experiments. The system should handle object persistency in a technology-neutral way while preserving the navigational capabilities of the objects. Built on a component-based architecture, POOL components communicate only through abstract interfaces which ensures minimal dependencies between packages. Concrete implementations are loaded on-demand via plugin management. As a result, the experiment framework client code is not aware of the underlying storage technology.

The POOL-API can be divided into three domains. The Storage Service domain is responsible for object I/O and streaming; File Catalog components resolve a logical reference into a physical data source; the Collection domain manages ensembles of objects.

While File Catalog and Collection components are in general built on transactional-safe relational database technologies, Storage Service components are implemented using the file-based ROOT/IO streaming technology. This hybrid implementation of the POOL-API has been established as the baseline for event data handling in three LHC experiments and has been deployed successfully.

To fulfill new requirements from the experiments for non-event data handling and to demonstrate that the system is truly technology neutral, the POOL team has set new development focus on implementing the Storage Service domain with relational technologies. After the first functional release of the RDBMS backend of POOL(POOL-ORA) at the beginning of 2005, it was chosen by the CMS experiment as the baseline technology for conditions data management.

2 The relational backend of POOL(POOL-ORA)

2.1 Domain Decomposition

As shown in Fig.1 POOL-ORA consists of three domains:

- **COmmon Relational Access Layer(CORAL)** defines a vendor independent API for relational database access, data and schema manipulation. Three technology plugins, Oracle, MySQL and SQLite are released together with the API.
- **Object Relational Access(ORA)** implements the object relational mapping mechanism and is responsible for transforming C++ object definitions to relational structures and vice-versa.
- **Relational Storage Service** implements the POOL Storage Service using the Relational Access and the Object Relational Access components.

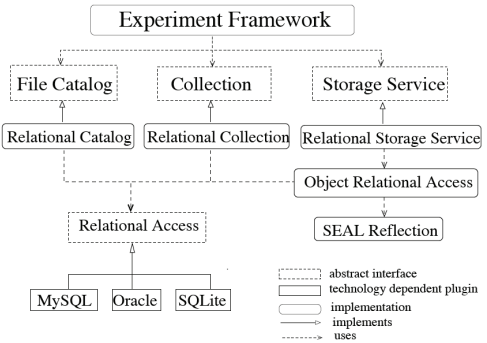

Figure 1: *POOL-ORA in the overall architecture*

2.2 Object Relational Mapping

The tabular representation of data in relational databases is fundamentally different from networks of objects used in object-oriented applications. Object Relational Mapping is one of the solutions to bridge this mismatch. It is, in essence, an automated mechanism to transform data from one representation to another.

In POOL, this transformation is achieved in the Object Relational Access component by implementing the following mapping rules.

- Object id is generated from the Primary Key of the table
- A simple class is mapped to one table
- An embedded class is mapped to subset of table rows of the owning class
- The default rule for class inheritance mapping is "table-per-concrete-class"
- Object association is mapped to table foreign key constraints

The Object Relational Mapping can be annotated with metadata such as association between class/member names to table/column names and types. The mapping metadata is versioned and stored with the object data. Combined information from the SEAL [2)] reflection library and the mapping metadata guides the object streaming at runtime.

3 CMS offline non-event data model with POOL

Non-event data are data whose validities span more than one event, e.g. calibration, alignment and geometry as well as the monitoring data. These data might come from the online system or from the offline processing. While the online system stores the data directly in relational databases, in the CMS offline system, POOL-ORA is used for non-event data access.

The advantage of this choice is that the object-driven nature of the offline software system is not disturbed by using the relational technology while the technology compatibility of the online and the offline database is preserved. Moreover, both event and non-event data are processed in the offline Event-Processing framework via the same POOL API even though the underlying storage technologies are different.

Two typical use cases in data access are: writing/reading data as objects to/from offline applications, reading data in online tables as objects from offline applications. In the former case, there is no need for explicit database schema design; tables are generated automatically and handled by POOL. In the latter case, there is an online to offline transfer procedure to extract and transfer data from the online to the offline database and then a set of tools are used to make the transferred data readable as C++ objects.

CMS is currently implementing the offline conditions data model with POOL-ORA for all its sub-detectors. Large scale deployment and testing are underway with the goal of being ready for the cosmic test next year.

References

1. D. Düllmann *et al*, The LCG POOL Project - General Overview and Project Structure, Proc. CHEP 2003 **MOKT**007, La Jolla, March 24-28 2003.

2. J. Generowicz *et al*, SEAL: Common Core Libraries and Services for LHC Applications, Proc. CHEP 2003 **MOJT**003, La Jolla, March 24-28 2003.

Frascati Physics Series Vol. XL (2006), pp. 301–306
Frontier Science 2005, New Frontiers in Subnuclear Physics
Milano, 12-16 September, 2005

THE LHC COMPUTING GRID

Andrea Sciabà
CERN, Switzerland

Abstract

The LHC experiments will start taking data in about two years and will produce about 15 PB of data each year. The goal of the LHC Computing Grid (LCG) is to provide the infrastructure and the environment for the preparation and the operation of the experiment computing systems. In this contribution, the global architecture, the main services and functionalities, and the challenges to be addressed by the LCG are described.

1 Introduction

The Large Hadron Collider will become operational at CERN in 2007, and the four major experiments (ALICE, ATLAS, CMS, LHCb) will collect an unprecedented amount of data, estimated to be of the order of 15 PB/year. These data will have to be processed, calibrated and analyzed several times, requiring a huge amount of computing and storage resources. In order to meet the computing requirements of the LHC experiments, the LHC Computing Grid project (LCG) was created.

The LHC computing infrastructure follows the Grid paradigm of a federation of etherogeneous computing and storage resources. This model maps very well with the structure of the LHC collaborations (4000+ physicists from 100+ of research institutes worldwide) and was motivated by the impossibility to physically concentrate in a single location all the necessary resources and by the desire to integrate the local resources of the participating institutes [1)]. This implies to have an adequate network between the different sites, a uniform interface to heterogeneous resources and an efficient and fair access to them. The project is developing in two phases: in the first one, a prototype is built and experience is accumulated on how to operate a world-wide Grid, while in the second one, beginning in 2006, the full-scale production service will become operational. As we write, LCG includes approximately 170 sites, 18000 CPUs and 4 PB of storage capacity.

In the following, a description of the current status of the LCG project will be given.

2 The LCG architecture

All the experiments have chosen to implement for their computing system a multi-tiered, hierarchical model, where different sites have different roles as a function of the services offered and the support level. A schematic data flow among tiers is depicted in fig.1 (left).

A single Tier-0, located at CERN, reconstructs the raw experimental data coming from the data acquisition systems and distributes the raw and the reconstructed data according to the experiment policies to each Tier-1 centre.

Each Tier-1 centre supplies a complete range of services (disk and tape storage, computing farms, databases) and support to end users and to a given set of Tier-2 centres. They perform data analysis and reconstruction, and provide archiving for raw, reconstructed and Monte Carlo data.

The primary roles of Tier-2 centres are event simulation and end-user analysis. No archival service is required, but partial copies of specific data samples can be hosted if required.

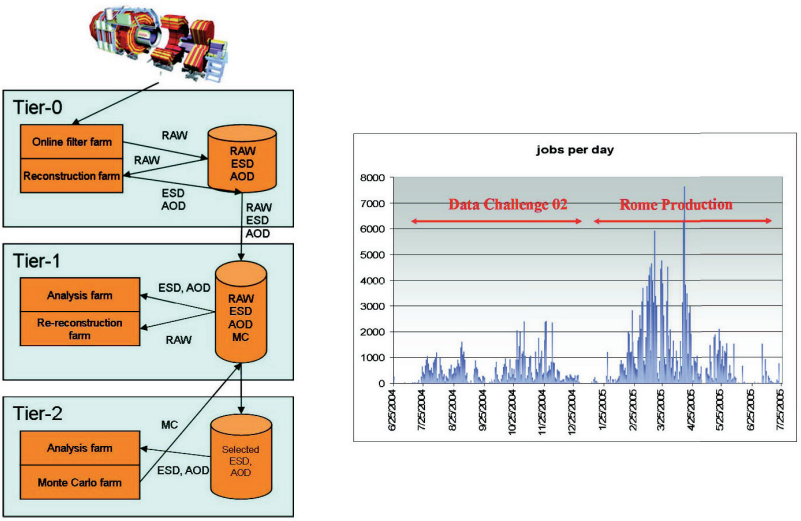

Figure 1: *(left) Data processing flow in the LCG multi-tiered architecture; (right) jobs per day run by ATLAS in LCG in 2004 and 2005.*

3 Overview of the LCG middleware

The middleware adopted by the LCG project is developed by external sources, research projects and institutions. It is currently based on the Virtual Data Toolkit [2)] and the DataGrid middleware [3)]. Other important components include the GLUE information schema [4)], which allows interoperability with other Grids, the dCache storage system [5)], the LCG File catalogue [6)] and the Disk Pool Manager [6)]. The middleware developed by the EGEE project [7)], gLite, is gradually being introduced: the File Transfer Service (FTS) is an example of a gLite service already used in LCG.

Resources in LCG are of two kinds: *computing elements (CE)*, which provide a Grid interface to a whole farm and its batch system, and *storage elements (SE)*, which provide a uniform interface to a disk server or a tape-based mass storage system. An *information system* maintains an updated view of the status of the Grid resources through a hierarchical structure of information providers and publishers. Information about all files stored in the LCG SEs is stored in *file catalogues*, global or local, which associate logical names to physical files. Data are accessed via transfer protocols, like GridFTP [8)],

using reliable file transfer tools (e.g. FTS), or directly via secure POSIX-like protocols [6]. The distribution of jobs to CEs is done in a load-balanced way by a central service, the *resource broker*.

A number of accounting and monitoring systems displays, records and analyzes the information available from the information system, the fabric monitoring and the result of periodic test jobs to give an accurate view of the status of LCG.

4 LCG deployment and operations

In order to integrate the middleware components in a coherent distribution, LCG has set up a thorough testing and certification procedure. If the tests are passed, a candidate release is defined and made available to the experiments for further testing. Then, a distribution for deployment is prepared, adding installation tools, configuration files, release notes and documentation, and is installed world-wide [9].

The operation of the LCG infrastructure is done by a distributed support structure [1], managed together with the EGEE project. It includes continuous site monitoring, problem solving through a multi-level support team, coordination of middleware installation and upgrade, user support and documentation. Regional Operations Centres (ROC) coordinate and support sites in their region, Core Infrastructure Centres (CIC) maintain central services and perform, in rotation, the daily monitoring, while the Operations Management Centre, which is located at CERN, oversees the LCG deployment and provides high level expertise. The User Support Centre (GGUS) coordinates the user support by providing a central portal.

5 LCG and the Experiments

The LHC experiments are performing an increasingly substantial part of their computing activities on LCG resources, from prototyping of their computing models to running standard applications like Monte Carlo production or analysis of simulated data. This strongly helps in identifying the limitations of the system and steers the middleware development based on requirements derived also from actual experience.

In 2004 and 2005, all experiments have performed a series of Data Challenges, simulating the data processing flow during the LHC data taking at a sizeable fraction of the full scale, and Monte Carlo productions [10) 11) 12) 13)]; in fig.1 (right) the number of jobs per day run by ATLAS during data challenges is shown.

These data challenges served multiple purposes: they were milestones towards the final commissioning of the experiment computing systems, but they were also effective in exposing some weaknesses of the system. They showed that site misconfiguration was responsible for a large fraction of the failures (failure rates ranged from 5% to 40% depending on the application), which lead to a big effort being invested in tools to identify and minimize the effects of site problems. Other issues were related to insufficient scalability and reliability of some services (RLS file catalogue, data management tools). An important observation made from such large-scale exercises was that the system still requires a significant human effort to be operated.

In 2005, experiments have been focusing more on using LCG to run user analysis jobs with user-friendly interfaces like CRAB [14)] or Ganga [15)].

The transformation of the LCG in a real production service is happening gradually through Service Challenges, which must attain certain goals in terms of inter-site data transfer and job submission rates and stability of services, both from the point of view of LCG and the experiments. The schedule foresees to have the initial LHC service in stable operation by September 2006, ready for the beginning of the data taking in April 2007.

References

1. LHC Computing Grid – Technical Design Report, LCG-TDR-001 CERN-LHCC-2005-024, 20 June 2005

2. Virtual Data Toolkit, http://vdt.cs.wisc.edu/

3. The DataGrid Project, http://www.edg.org/

4. S. Andreozzi *et al*, Sharing a conceptual model of Grid resources and services, in: Proc. Computing in High Energy Physics – CHEP2003, La Jolla, March 2003

5. P. Fuhrmann, dCache, the commodity cache, in: Proc. 12th NASA Goddard and 21st First IEEE Conference on Mass Storage Systems and Technologies, Washington DC, Spring 2004

6. J.P. Baud, J. Casey, Evolution of LCG-2 Data Management, in: Proc. Computing in High Energy and Nuclear Physics (CHEP), Interlaken, September 2004

7. The EGEE Project, http://www.eu-egee.org/

8. W. Allcock (editor), GridFTP: Protocol Extensions to FTP for the Grid, GGF recommendation GFD.20, March 2003

9. M. Serra *et al*, Building the LCG: from middleware integration to production quality software, in: Proc. Computing in High Energy and Nuclear Physics (CHEP), Interlaken, September 2004

10. L. Goossens *et al*, ATLAS Production System in ATLAS Data Challenge 2, in: Proc. Computing in High Energy and Nuclear Physics (CHEP), Interlaken, September 2004

11. A. Peters, The ALICE Data Challenge 2004 and the ALICE distributed analysis prototype, in: Proc. Computing in High Energy and Nuclear Physics (CHEP), Interlaken, September 2004

12. A. Fanfani *et al*, Distributed Computing Experiences in CMS DC04, in: Proc. Computing in High Energy and Nuclear Physics (CHEP), Interlaken, September 2004

13. J. Closier *et al*, Results of the LHCb experiment Data Challenge 2004, LHCb 2004-088-Offline

14. F. Fanzago *et al*, CRAB: a tool to enable CMS Distributed Analysis, in: these proceedings

15. U. Egede *et al*, Ganga user interface for job definition and management, in: Proceedings of the Fourth UK e-Science All-Hands Meeting, Nottingham, UK, September 2005

SESSION VIII – JOINT ADVENTURES WITH MEDICAL SCIENCE

P. Russo	A review of Detectors for Medicine
S. Rossi	Hadrontherapy in the world
G. Cirrone	The CATANA project
C. Davià	3D silicon detectors for imaging applications
P. Sala	FLUKA for medicine and biology
A. Retico	Lung nodule detection in low-dose and high-resolution CT scans
G. Pittá	MATRIX, an innovative Pixel Ionization Chamber for on-line beam monitoring in hadrontherapy

Frascati Physics Series Vol. XL (2006), pp. 309
Frontier Science 2005, New Frontiers in Subnuclear Physics
Milano, 12-16 September, 2005

A REVIEW OF DETECTORS FOR MEDICINE

P. Russo
University of Naples, Italy

Written contribution not received

Frascati Physics Series Vol. XL (2006), pp. 311
Frontier Science 2005, New Frontiers in Subnuclear Physics
Milano, 12-16 September, 2005

HADRONTHERAPY IN THE WORLD

S. Rossi
CNAO, Pavia, Italy

Written contribution not received

Frascati Physics Series Vol. XL (2006), pp. 313
Frontier Science 2005, New Frontiers in Subnuclear Physics
Milano, 12-16 September, 2005

THE CATANA PROJECT

G. Cirrone
INFN-LNS, Catania, Italy

Written contribution not received

Frascati Physics Series Vol. XL (2006), pp. 315
Frontier Science 2005, New Frontiers in Subnuclear Physics
Milano, 12-16 September, 2005

3D SILICON DETECTORS FOR IMAGING APPLICATIONS

C. Davià
University of Brunel, US

Written contribution not received

Frascati Physics Series Vol. XL (2006), pp. 317–322
Frontier Science 2005, New Frontiers in Subnuclear Physics
Milano, 12-16 September, 2005

FLUKA FOR MEDICINE AND BIOLOGY

P.R. Sala
INFN Milan, Italy
for the FLUKA collaboration
(D. Alloni, F. Ballarini, G. Battistoni, M. Campanella, M. Carboni, F. Cerutti, A . Clivio, A. Empl, A. Fassò, A. Ferrari, E. Gadioli, E. Gadioli-Erba, M.V. Garzelli, E. Giroletti, A. Mairani, A. Mostacci, S. Muraro, A. Ottolenghi, V. Parini, M. Pelliccioni, L.S. Pinsky, J. Ranft, S . Roesler, P. R. Sala, D. Scannicchio, G. Smirnov, S. Trovati, R. Villari, V. Vlachoudis, T . Wilson, N. Zapp)

Abstract

The FLUKA Monte Carlo code is briefly described, and examples of applications to medicine and biology are presented

1 A short description of FLUKA

FLUKA [1)] is a general purpose tool for calculations of particle transport and interactions with matter. It can handle hadronic and electromagnetic particles from thermal energies (for neutrons) up to cosmic ray energies. The highest priority in the design and development of FLUKA has always been the implementation and improvement of sound and modern physical models. Microscopic models are adopted whenever possible, consistency among all the reaction steps and/or reaction types is ensured, conservation laws are enforced

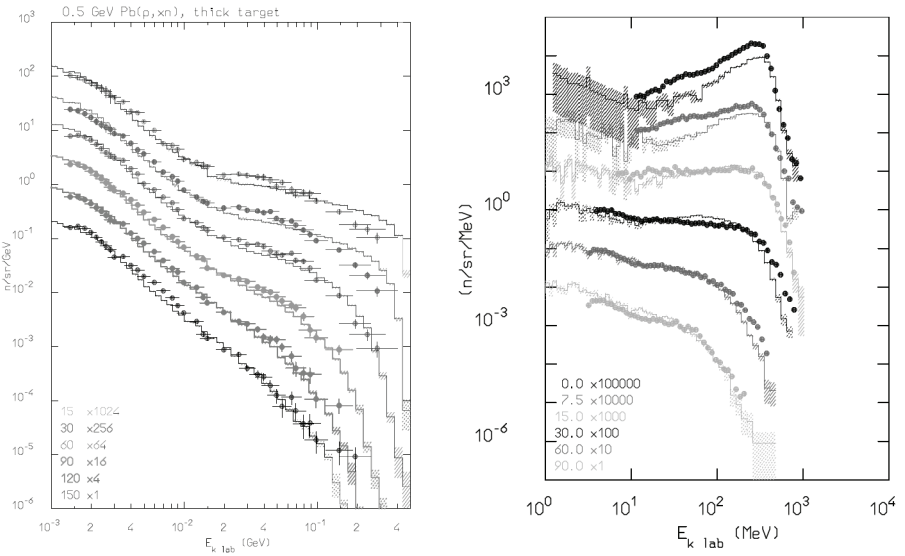

Figure 1: Left: PEANUT results (dashed histogram) and experimental data (symbols) neutron double differential distributions out of stopping length targets for 500 MeV protons on Pb [9]. Right: Modified RQMD results (histograms) and data [10] (dots)for double differential neutron yield by 400 MeV/n Fe ions on a thick Al target.

at each step, results are checked against experimental data at single interaction level. Since detailed descriptions of the FLUKA models and comparison with experimental data are available in the literature [1] and on the FLUKA web page (www.fluka.org), we give here only a short summary.

Hadron-nucleus interaction models depend on projectile energy. The high energy range (> 5 GeV) is treated in the Glauber-Gribov formalism, that couples Glauber multiple scattering to a Dual Parton Model description of hadron-nucleon interactions. Nuclear effects on reaction products are described by a Generalized Intra Nuclear Cascade (GINC) where the formation zone concept plays a fundamental role. At lower energies, the intermediate energy hadronic model of FLUKA , called PEANUT is used. The reaction mechanism is modeled in PEANUT by explicit intranuclear cascade (INC) smoothly joined to statistical (exciton) preequilibrium emission.INC modeling in PEANUT is highly

sophisticated (see fig1). Independently from the original projectile energy, the equilibrium steps of the reaction include evaporation in competition with fission and gamma deexcitation. For light nuclei, a Fermi break-up model is implemented.

Ion-Ion interaction are of great interest for new therapeutic beams. FLUKA implements DPMJET [2] as event generator to simulate nucleus-nucleus interactions at $E > 5$ GeV/n. An interface to a modifies version of the RQMD-2.4 [3] was developed to enable FLUKA to treat ion interactions from ≈ 100 MeV/n up to 5 GeV/n [4]. An example is shown in fig.1. For both generators, de-excitation and evaporation of the excited residual nuclei is performed by calling the FLUKA evaporation module. Work is in progress to implement a Boltzmann Master Equation model for A-A interactions at very low energy [5] and to replace the RQMD interface with a new QMD model [4, 6] developed for FLUKA

Transport and interactions of electromagnetic particles are fully coupled to the hadronic sector, allowing for instance to follow in the same event secondary hadrons from photon nuclear interactions and γ rays from nuclear deexcitation. All electromagnetic processes are simulated with high accuracy, accounting for atomic bonds, polarization, electron-positron differences, actual angular distributions etc.

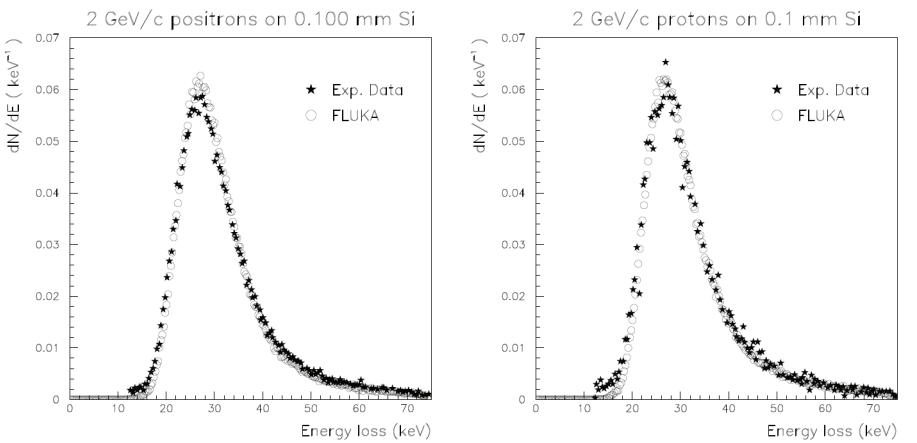

Figure 2: Experimental [11] and calculated energy loss distributions for 2 GeV/c positrons (left) and protons (right) traversing 100μm of Si

An original treatment of multiple Coulomb scattering [7] and of ionization

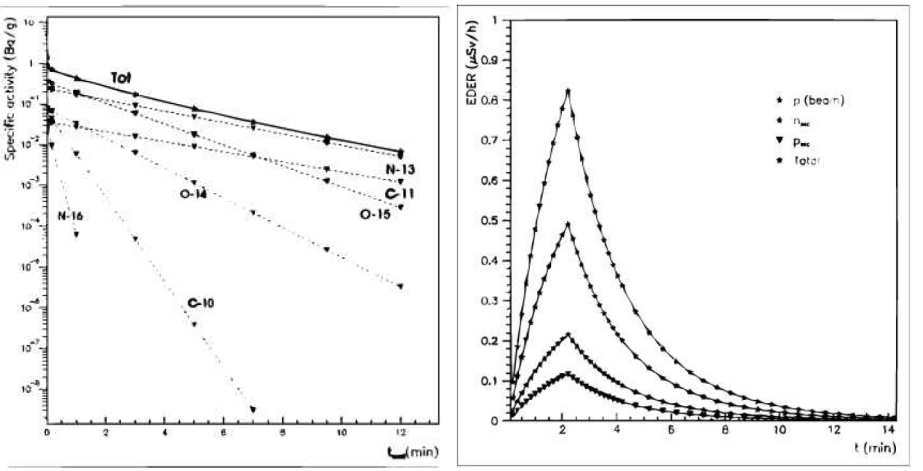

Figure 3: Left: specific activity vs. time after 3 min. irradiation, 400 MeV/n C ion beam. Right: dose rate vs. time during and after irradiation, 250 MeV proton beam.

fluctuations [8] allows the code to handle accurately some challenging problems such as electron backscattering and energy deposition in thin layers (fig.2) even in the few keV energy range. The FLUKA geometrical modeler is based on the Combinatorial Geometry. Recently, the possibility to embed "voxel" regions in the CG has been added.This algorithm was originally developed to allow to use inside FLUKA the human phantoms developed at GSF out of real person whole body CT scans. It was general enough to be coupled with generic CT scans, and applications to automatically assign CT numbers to "organs" have been developed

2 Applications

2.1 Air activation at CNAO

Recent developments in the evaporation model further improved FLUKA performances in predicting residual nuclei production. Activation of air in the future treatment rooms of the CNAO facility is being calculated with FLUKA , both for ion and proton beams. Preliminary examples [12] are reported in fig.3

2.2 Biological dose in therapy and space dosimetry

Dose or LET as calculated by any condensed history Monte Carlo are is not sufficient to fully characterize the radiation effects in biological targets, especially if one takes into account that the DNA linear dimensions are of the order of the nm. A better estimator is the "biological dose", represented by the average number of "Complex Lesions" (CLs) per cell in a given organ or tissue, where Complex Lesions are clustered breaks of the DNA double helix. Their yields per Gy and per cell, which depend on the radiation quality, can be calculated by means of "event-by-event" track structure simulations at the nm level [13] and subsequently integrated on-line into FLUKA. This approach was applied [14] with excellent results to the "real" therapeutic proton beam of the OPTIS facility at PSI.

Astronauts' exposure to the various components of the space radiation field is of great concern for long-term missions, especially for those in deep space such as a possible travel to Mars. Calculations of biological dose in a voxel human phantom have been performed for Galactic Cosmic Rays as well as for Solar Particle Events, in several shielding conditions. While SPE doses decrease dramatically even with a relatively thin shielding, calculated GCR doses are almost independent on shielding thickness [15].

2.3 In-beam positron-emission-tomography

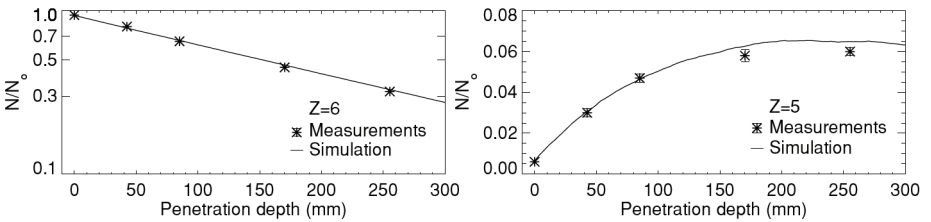

Figure 4: 676 AMeV ^{12}C beam on a water phantom. Left: Carbon ion intensity as a function of depth. Right: Build-up of boron ions as a function of depth. Experimental data from [18, 19].

Fragmentation of therapeutic ion beams is often regarded as an undesirable drawback which deteriorates the selective energy deposition. due to the more frequent electromagnetic energy losses. However, the production of a

minor amount of positron emitting fragments offers the possibility to monitor in-situ and non-invasively the precision of the treatment by means of positron-emission-tomography (PET) [16]. An example of comparison [17] of FLUKA predictions to experimental data for fragmentation of therapeutic ion beams in tissue-like material is shown in fig. 4. Further validation is in progress.

References

1. A. Ferrari et al., CERN-2005-010, INFN/TC_05/11 (2005); A. Fassò et al., Proc. of CHEP2003, eConf C0303241 (2003), arXiv:hep-ph/0306267
2. J. Ranft, Phys. Rev. **D51** (1995) 64.
3. H. Sorge, H. Stöcker, and W. Greiner, Nucl. Phys. **A498**, (1989) 567c.
4. V. Andersen et al.,Adv. Space Res. **34** (2004) 1302.
5. F. Cerutti et al., proceedings of NPDC19, Pavia, 2005.
6. M.V. Garzelli et al. et al., proceedings of NPDC19, Pavia, 2005.
7. A. Ferrari et al., Nucl. Instr. Meth. **B71** (1992) 412
8. A. Fassò et al.,KEK Proceedings **97–5** (1997) 32.
9. S. Meigo et al., JAERI-Conf **95-008** (1995) 213.
10. T. Kurosawa et al., Phys. Rev. **C 62** (2000) 11.
11. J.Bak et al. Nucl. Phys. **B288** (1987) 681.
12. Anna Ferrari and M. Pelliccioni, private communication.
13. A. Ottolenghi et al., Radiat. Environ. Biophys. **34** (1995) 239.
14. M. Biaggi et al., NIM **B 159** (1999) 89.
15. F. Ballarini et al., proceedings of NPDC19, Pavia, 5-9 September 2005
16. W. Enghardt et al., Phys. Med. Biol. **37**, (1992) 2127.
17. H. Aiginger et al., Adv. Space Res. **35** (2005) 214.
18. I. Schall, D. Schardt, H. Geissel et al, Nucl. Instr. Meth. B **117**, 221 (1996).
19. I. Schall, Ph.D. Thesis, Technische Hochschule Darmstadt, 1994.

Frascati Physics Series Vol. XL (2006), pp. 323–326
Frontier Science 2005, New Frontiers in Subnuclear Physics
Milano, 12-16 September, 2005

LUNG NODULE DETECTION IN LOW-DOSE AND HIGH-RESOLUTION CT SCANS

P. Delogu[1,2], M.E. Fantacci[1,2], I. Gori[3],
A. Preite Martinez[1], A. Retico[2] and A. Tata[2]
[1]*Dipartimento di Fisica dell'Università di Pisa,*
Largo Pontecorvo 3, 56127 Pisa, Italy
[2]*Istituto Nazionale di Fisica Nucleare, Sezione di Pisa,*
Largo Pontecorvo 3, 56127 Pisa, Italy
[3]*Bracco Imaging S.p.A.,*
Via E. Folli 50, 20134 Milano, Italy

Abstract

We are developing a computer-aided detection (CAD) system for the identification of small pulmonary nodules in screening CT scans. The main modules of our system, i.e. a dot-enhancement filter for nodule candidate selection and a neural classifier for false positive finding reduction, are described. The preliminary results obtained on the so-far collected database of lung CT are discussed.

1 Introduction

Lung cancer most commonly manifests as non-calcified pulmonary nodules. Computer Tomography (CT) has been shown to be the best imaging modality for the detection of small pulmonary nodules [1)], particularly since the introduction of the helical technology. The amount of images that need to

Figure 1: *Some examples of small pulmonary nodules.*

be interpreted in CT examinations can be very high, especially when multi-detector helical CT and thin collimation are used, thus generating up to about 300 images per scan. In order to support radiologists in the identification of early-stage pathological objects, researchers have recently begun to explore computer-aided detection (CAD) methods in this area.

The First Italian Randomized Controlled Trial that aims to study the potential impact of screening on a high-risk population using low-dose helical CT has started last year. In this framework we are developing a CAD system for small pulmonary nodule identification. The system is based on a dot-enhancement filter and a neural-based module for the reduction of the amount of false-positive (FP) findings per scan.

2 Description of the CAD system

An important and difficult task in the automated nodule detection is the selection of the nodule candidates. Nodules may be characterized by very low CT values and/or low contrast, may have CT values similar to those of blood vessels and airway walls or may be strongly connected to them (see fig. 1).

In order to identify the nodule candidates we modeled nodules with spherical objects and we applied a dot-enhancement filter to the 3D matrix of voxel data. This filter attempts to determine the local geometrical characteristics

of each voxel, by computing the eigenvalues of the Hessian matrix and evaluating a *likelihood* function that was purposely built to discriminate between local morphology of linear, planar and spherical objects, modeled as having 3D Gaussian sections [2]. A simple peak-detection algorithm (i.e. a local maxima detector) is then applied to the filter output to detect the filtered-signal peaks.

Since most FP findings are provided by crossings between blood vessels, we attempted to reduce the amount of FP/scan by applying the procedure we called voxel-based approach (VBA). According to this method, each voxel of a region of interest (ROI) is characterized by the grey level intensity values of its neighborhood. The CT values of the voxels in a 3D neighborhood of each voxel of a ROI are rolled down into vectors of features to be analyzed by a neural classification system. The feed-forward neural network implemented to this purpose assigns each voxel either to the class of voxels belonging to a nodule, or to that of normal voxels. We can evaluate a free response receiver operating characteristic (FROC) curve for our CAD system, by varying the percentage of voxels to be classified as belonging to a nodule in order to assign each ROI either to the class of ROIs containing a nodule or normal ROIs.

3 Results

We tested the CAD system on a dataset of low-dose (screening setting: 120÷140 kV, 20÷80 mA) and high-resolution (reconstructed slice thickness: 1.25 mm) CT scans collected and annotated by experienced radiologists in the framework of the screening trial being conducted in Tuscany (Italy). The database available at present for our tests consists of 20 scans, 8 of which contain 12 internal nodules. Each scan is a sequence of about 300 slices stored in DICOM (Digital Imaging and COmmunications in Medicine) format.

Our preliminary results show that the 3D dot-enhancement filter is characterized by a high sensitivity. In particular, if we keep the first 67 entries of the list of interesting ROIs provided by the filter output for each scan, we achieve a 100% sensitivity to internal nodule detection. In other words, a 100% sensitivity is obtained at a maximum number of 67 FP/scan.

Since the amount of data available for training the neural networks in the VBA method is quite small, we first partitioned our dataset into a train and a test set, then we evaluated the performances of the trained neural network both on the test set and on the whole dataset (train set + test set). The best results

achieved are the following: 87.0% sensitivity and 85.3% specificity on the test set; 88.0% sensitivity and 84.9% specificity on the whole dataset. Once the VBA approach has been applied to each ROI, the rate of FP findings per scan has been reduced from 67 to 14 for a sensitivity of 100% (12 nodules detected out of 12). If the sensitivity value is decreased to 91.7% (11 nodules detected out of 12), a rate of 8.9 FP/scan is obtained.

4 Conclusions

The dot-enhancement pre-processing algorithm has shown a good sensitivity in the identification of nodule candidates, and the VBA was shown to be an effective approach to the problem of false positives reduction. The results obtained so far seem promising, albeit they are preliminary and need to be validated against a larger database. Finally, we are convinced that the methods used are effective, and that there is margin for improvement.

5 Acknowledgments

We acknowledge Dr. L. Battolla, Dr. F. Falaschi and Dr. C. Spinelli of the U.O. Radiodiagnostica 2 of the Azienda Universitaria Pisana, and Prof. D. Caramella and Dr. T. Tarantino of the Diagnostic and Interventional Radiology Division of the Dipartimento di Oncologia, Trapianti e Nuove Tecnologie in Medicina of the Pisa University.

References

1. S. Diederich *et al*, Detection of pulmonary nodules at spiral CT: comparison of maximum intensity projection sliding slabs and single-image reporting, Eur Radiol **11** 1345 (2001).

2. Q. Li, S. Sone and K. Doi, Selective enhancement filters for nodules, vessels, and airway walls in two- and three-dimensional CT scans, Med. Phys. **30**(8) 2040 (2003).

3. P. Delogu *et al*, Preprocessing methods for nodule detection in lung CT, Computer Assisted Radiology and Surgery, Proceedings of the 19$^{\text{th}}$ International Congress and Exhibition, International Congress Series **1281** 1099 (Berlin, Germany, 2005).

Frascati Physics Series Vol. XL (2006), pp. 327–331
Frontier Science 2005, New Frontiers in Subnuclear Physics
Milano, 12-16 September, 2005

MATRIX: AN INNOVATIVE PIXEL IONIZATION CHAMBER FOR ON-LINE BEAM MONITORING IN HADRONTHERAPY

G. Pittá(*), S. Braccini
TERA Foundation, Novara, Italy
(*) Corresponding author. E-mail: Giuseppe.Pitta@tera.it

M. Donetti
CNAO Foundation, Milan, Italy

R. Cirio, A. La Rosa, M.A. Garella,
S. Giordanengo, F. Marchetto, C. Peroni
University and INFN, Turin, Italy

Abstract

The control of beam position and dose delivery are key issues in the treatment of tumours using hadron beams, especially in the case of active dose distribution systems. In this framework, an innovative pixel ionization chamber has been designed and constructed for 2-D control of beam position, shape and intensity. This chamber is characterized by a 21×21 cm^2 sensitive area subdivided in 1024 pixels of 6.5×6.5 mm^2. The 1024 channels are read-out by 8 boards based on 16 TERA06 chips. The sensitivity can be adjusted in the range 100-800 fC. The tested minimum read-out time of the full chamber is 1 ms. After some preliminary measurements with X-rays, tests have been performed on the proton beam of the cyclotron of the Joint Research Centre in Ispra, Italy. In March 2005, MATRIX has been successfully tested on several beam lines for proton-therapy at the Loma Linda University Medical Center, US. The very positive results of these tests are presented.

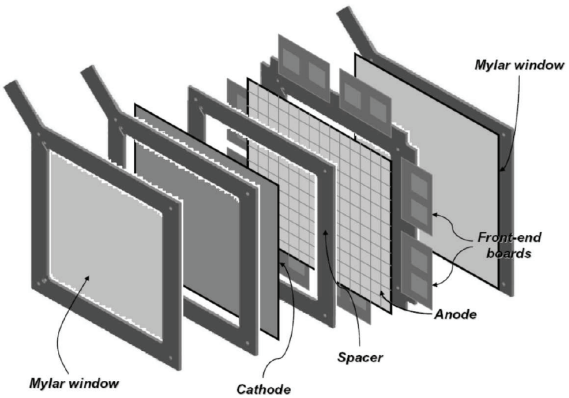

Figure 1: *Schematic view of the MATRIX pixel ionization chamber.*

1 Introduction

Hadrontherapy is a technique of cancer radiation therapy based on the use of proton and carbon ion beams. Due to their characteristic ionization loss, the so called Bragg curve, and due to the fact that being charged they can be precisely directed toward a small target, hadrontherapy allows to conform the dose to the tumour volume much better than conventional X-ray radiotherapy. During a treatment, the on-line control of beam intensity, position and shape is of paramount importance in order to assure the conformity of the dose given to the patient according to the treatment planning specifications. To accurately control the clinical beams during hadrontherapy treatments an innovative pixel ionization chamber, named MATRIX, has been designed and constructed. In this paper the construction and the first beam tests of this detector are described.

2 Design and construction of the chamber

The structure of the chamber is made of five successive fiberglass frames, as shown in Figure 1. The external frames are equipped with glued mylar foils which allow to maintain the planarity of the internal cathodic and anodic electrodes in case a gas is used at non atmospheric pressure. The sensitive volume of the detector corresponds to the air gap between the anode and the cathode foils. MATRIX is designed to have a gap of 5 mm but a different gas volume can be easily obtained by substituting the spacer. The anode and cathode foils are glued to the respective spacers using a non-conductive epoxy araldite. The gluing procedure required the construction of a special tool, designed to

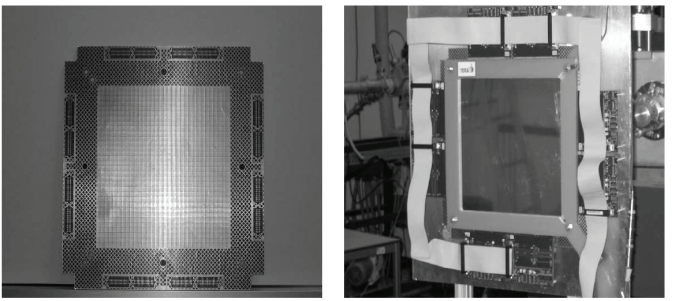

Figure 2: *The top side of the anode with the 1024 pixels (left). The MATRIX chamber fully assembled. The fibreglass frame and the eight electronic boards for the read-out are visible (right).*

obtain a good planarity of the electrodes. The chamber is characterized by a 21×21 cm^2 sensitive area subdivided in 1024 pixels of 6.5×6.5 mm^2. In order to minimize the amount of material traversed by the beam, the anodic electrode is made of a thin 50 μm kapton foil, with a deposition of 17 μm copper on each side. As shown in Figure 2 (left), the pixels are located in one side of the anode foil together with a guard ring and pads for soldering the read-out connector. The other side of the anode foil contains the pixel-pad connections. Metallized holes are used to electrically connect the two sides. The fully assembled MATRIX detector is shown in Figure 2 (right). The 1024 channels are read-out by 8 electronic boards which handle 128 channels each. Each board hosts two VLSI chips, named TERA06, specifically designed for this specific application [1)]. Each chip has 64 independent channels based on a recycling integrator architecture which allows the implementation of a wide dynamic range charge-to-digital converter. Each channel is equipped with a 16-bit digital counter whose output value is proportional to the integrated charge. The sensitivity can be adjusted by varying the quantum of charge, which corresponds to one digital count, in the range between 100 and 800 fC. The maximum frequency of 5 MHz limits the maximum current for each channel to 4 μA. The linearity of the measurement of the charge has been measured to be better than 1% in a wide range. The tested minimum read-out time for all the 1024 channels of MATRIX is 1 ms.

3 Beam tests

Laboratory tests have been performed before the first beam tests. The electronic noise has been measured to be less than one count per channel per second.

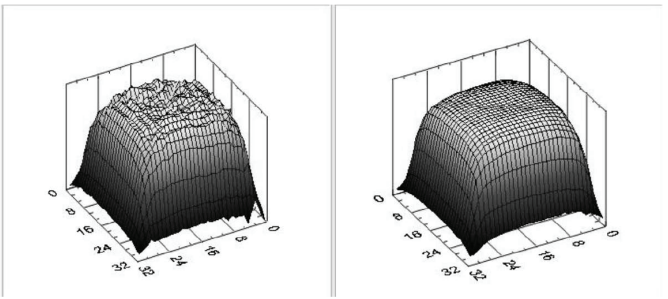

Figure 3: *Two-dimensional representation of the read-out of the MATRIX pixel chamber before (left) and after calibration (right) for a square shaped field.*

The chamber has been irradiated with X-rays in order to verify the correct operation of all the 1024 pixels. For all these tests and the following beam tests the voltage of 400 V has been applied which corresponds to an electric field of 800 V/cm in the sensitive volume. The first beam tests have been performed at the cyclotron of the Joint Research Centre of the European Commission in Ispra (Italy) at the end of 2004. Using a proton beam of 17 MeV and approximately 5 nA, the chamber was irradiated under several conditions and different beam shapes were measured. These first beam tests showed that MATRIX was successfully designed and constructed, fulfilling all the design requirements. In March 2005, several tests have been performed on the clinical beams of the proton-therapy centre of the Loma Linda University Medical Center in California (USA). Figure 3 shows the results of the calibration procedure [2)], based on three different measurements (reference, 90° rotation and one pixel shift). No assumption on the shape of the beam is used for the calibration. MATRIX has been installed in several treatment rooms equipped with horizontal beams or gantries and the full system could be dismounted and put in operation in about 30 minutes. This shows the system is highly reliable and user friendly. The two-dimensional map of several fields has been measured. As an example, a field shaped for the treatment of a prostate cancer is shown in Figure 4 (left). The Bragg peak due to the ionization loss of a 149 MeV proton beam has been measured by interposing layers of water equivalent absorber between the exit window of the accelerator and the chamber, as presented in Figure 4 (right). Several tests have been performed using the read-out speed of 1 ms for the full chamber.

The very positive results of all these beam tests show that MATRIX is an innovative detector that can be successfully used for on-line beam monitoring in hadrontherapy.

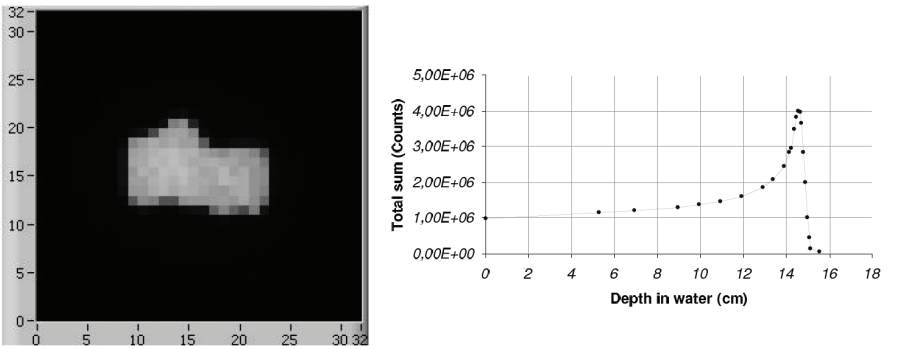

Figure 4: *Two-dimensional map of a field shaped for a prostate cancer treatment (left). The Bragg peak measured for a 149 MeV proton beam (right).*

4 Acknowledgments

We gratefully acknowledge the Monzino Foundation (Milan, Italy) for the financial support of this project. The authors would like to thank U. Amaldi, President of the TERA Foundation, whose ideas are at the basis of MATRIX, G. Dellacasa and his team of the University of Western Piedmont (Alessandria, Italy) for the technical support given during the construction. We sincerely acknowledge the support for the beam tests of the research groups of the Joint Research Centre in Ispra and of the Loma Linda University Medical Center.

References

1. S. Amerio et al., Proceedings of the 7th ICATPP Conference, Como (Italy), 2001, M. Barone et al. Editors, World Scientific, p. 487.

2. S. Amerio et al., Medical Physics, Vol. 31, No. 2, February 2004.

SESSION IX – CONCLUSION SESSION

M. Mazzucato	GRID facilities worldwide
D. Tommasini	LHC
M. Mezzetto	Next generation neutrino beams: Beta Beams

Frascati Physics Series Vol. XL (2006), pp. 335
Frontier Science 2005, New Frontiers in Subnuclear Physics
Milano, 12-16 September, 2005

GRID FACILITIES WORLDWIDE

M. Mazzucato
INFN-Padova, Italy

Written contribution not received

Frascati Physics Series Vol. XL (2006), pp. 337
Frontier Science 2005, New Frontiers in Subnuclear Physics
Milano, 12-16 September, 2005

LHC

D. Tommasini
CERN, Geneva, Switzerland

Written contribution not received

Frascati Physics Series Vol. XL (2006), pp. 339–344
Frontier Science 2005, New Frontiers in Subnuclear Physics
Milano, 12-16 September, 2005

NEXT GENERATION NEUTRINO BEAMS: BETA BEAMS

Mauro Mezzetto
INFN, Sezione di Padova. Via Marzolo 8, 35100 Padova, Italy.

Abstract

Beta Beams aim at producing pure, intense electron neutrino beams from the decay of relativistic radioactive ions. They could be the ideal tool for future neutrino oscillation experiments optimized to discover non zero values of the mixing angle θ_{13} and leptonic CP violation.

The expected performances using a megaton water Čerenkov detector are shown, together with the synergy with a companion neutrino SuperBeam. Recent technical progress and new ideas are underlined.

1 Introduction

Evidence of neutrino oscillations have been discovered both with atmospheric [1)] and solar neutrinos [2)]. They have been recently confirmed by experiments using artificial sources of neutrinos: Kamland [3)] confirmed solar neutrino oscillations by using reactor neutrinos, while K2K [4)] confirmed atmospheric neutrino oscillations by using accelerator neutrinos.

These evidences can be described as two independent oscillations of two flavor neutrinos. At today no evidence has been found of genuine three neutrino oscillations. They would be modulated by the mixing angle θ_{13} and could bring to the discovery of leptonic CP violation, modulated by the $\delta_{\rm CP}$ phase. In particular subleading $\nu_\mu \to \nu_e$ (or $\nu_e \to \nu_\mu$) transitions, could be used for these searches. These transitions are characterized by their smallness, given the present experimental Chooz bound [5] $\sin^2 2\theta_{13} \leq 0.14$. Only in a well controlled, full optimized environment it will be possible to perform these experiments: long baseline (LBL) neutrino beams are the natural candidates.

The present generation of LBL neutrino experiments (K2K , Minos, Opera) has been optimized to confirm the SuperKamiokande result on atmospheric neutrinos and not to detect subleading $\nu_\mu \to \nu_e$ transitions. Second generation experiments, like the already approved T2K [6], and NOνA [7], will extend the sensitivity on $\sin^2 2\theta_{13}$ by more than one order of magnitude with respect to the Chooz limit, but will have very limited sensitivity to $\delta_{\rm CP}$ [8].

A third generation of LBL neutrino experiments will be required to start a sensitive search of leptonic CP violation. These future experiments will push conventional neutrino beams to their ultimate limits (neutrino SuperBeams), or will require new concepts in the production of neutrino beams.

Conventional neutrino beams are generated by secondary particle decays, mainly pions and kaons, producing a multiflavour neutrino beam (ν_e, $\overline{\nu}_\mu$, $\overline{\nu}_e$, besides the main neutrino component, ν_μ) difficult to precisely predict even combining sophisticated MonteCarlo codes and close detector data.

These limits are overcome if the neutrino parents can be collimated and accelerated to a given energy. This can be tempted within the muon or a beta decaying ion lifetime. The first approach brings to the Neutrino Factories [9], the second to the Beta Beams.

2 The baseline Beta Beam

BetaBeams (βB) have been introduced by P. Zucchelli in 2001 [10]. The idea is to generate pure, well collimated and intense ν_e ($\overline{\nu}_e$) beams by producing, collecting, accelerating radioactive ions and storing them in a decay ring in 10 ns long bunches, to suppress the atmospheric neutrino backgrounds. The best ion candidates so far are ^{18}Ne and ^{6}He for ν_e and $\overline{\nu}_e$ respectively. The layout of a Beta Beam is sketched in Fig. 1.

In a neutrino BetaBeam the beam energy depends on the Lorentz γ factor of the parent ion, the ion accelerator can be tuned to optimize the sensitivity of the experiment. The neutrino beam contains a single flavor with an energy spectrum and intensity known a priori. Therefore, unlike conventional neutrino

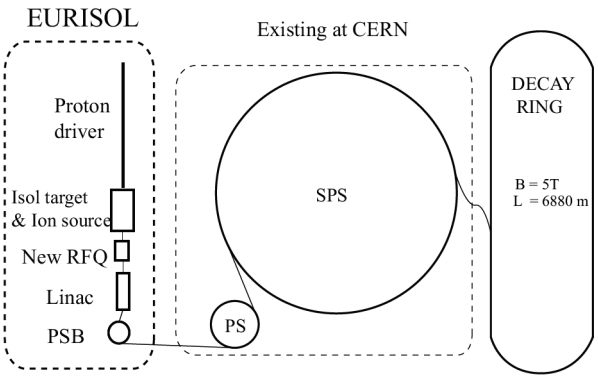

Figure 1: *A schematic layout of the BetaBeam complex. At left, the low energy part is largely similar to the EURISOL project* [11]. *The central part (PS and SPS) uses existing facilities. At right, the decay ring has to be built.*

beams, close detectors are not necessary to normalize the fluxes. Differently from SuperBeams, BetaBeams experiments search for $\nu_e \to \nu_\mu$ transitions, requiring a detector capable to identify muons from electrons. Moreover, since the beam does not contain ν_μ or $\bar{\nu}_\mu$ in the initial state, magnetized detectors are not needed. This is in contrast with the neutrino factories where the determination of the muon sign is mandatory.
A baseline study for a Beta Beam complex (Fig. 1) has been carried out at CERN [12]. The reference βB fluxes are $5.8{\cdot}10^{18}$ ^{6}He useful decays/year and $2.2{\cdot}10^{18}$ ^{18}Ne decays/year if a single ion species circulates in the decay ring.

3 Physics potential

The physics potential has been initially computed in ref. [13, 14] for $\gamma_{^6\mathrm{He}} = 60$, $\gamma_{^{18}\mathrm{Ne}} = 100$ and with a 440 kton water Čerenkov detector at 130 km. The most updated sensitivities for the baseline βB are computed in a scheme where both ions are accelerated at $\gamma = 100$, the optimal setup for the CERN-Frejus baseline of 130 km [15]. The θ_{13} sensitivity curve and the leptonic CP violation discovery potential (LCPV) are shown in Fig. 2 [15]. Effect of degeneracies [16] are sometimes visible for high values of θ_{13}, precisely the region where they can be canceled by a combined analysis with atmospheric neutrinos with the statistics available at the 440 kton detector [17].

BetaBeams require a proton driver in the energy range of 1-2 GeV, 0.5

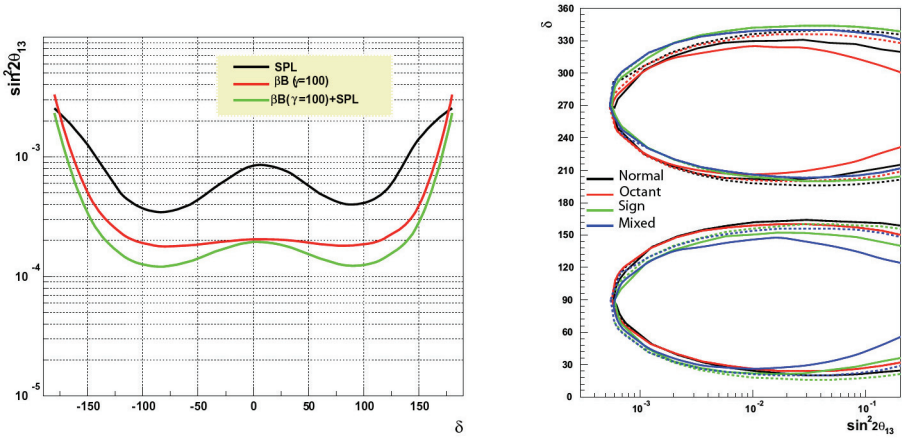

Figure 2: *Left: θ_{13} 90% C.L. sensitivity as function of $\delta_{\rm CP}$ for $\Delta m^2_{23} = 2.5{\cdot}10^{-3}eV^2$, $\mathrm{sign}(\Delta m^2_{23}) = 1$, 2% systematic errors. Right: LCPV discovery potential at $3\sigma(\Delta\chi^2 > 9.0)$ computed for the 4 different options about the true values of $\mathrm{sign}(\Delta m^2_{23})$ and θ_{23}. Each of these options is fitted with all the 4 different choices of the true values, taking the worst case. Dotted curves are computed with the right choice of the true parameters.*

MWatt power. The SPL [18] could be used as injector, at most 10% of its protons would be consumed. This allows a simultaneous βB and SPL-SuperBeam [19] run, the two neutrino beams having similar neutrino energies. The same detector could then be exposed to 2×2 beams (ν_μ and $\overline{\nu}_\mu \times \nu_e$ and $\overline{\nu}_e$) having access to CP, T and CPT violation searches in the same run. This is particularly important because CP and T channels would have different systematics and different backgrounds, allowing for independent checks of the same signal. Furthermore the SPL ν_μ and $\overline{\nu}_\mu$ beams would be the ideal tool to measure signal cross sections in the close detector.

With this combination of neutrino beams a sensitivity to $\sin^2 2\theta_{13} \geq 2 \cdot 10^{-3}$ (90%CL) exploiting a CP violation discovery potential at 3 σ if $\delta_{\rm CP} \geq 18°$ and $\theta_{13} \geq 0.55°$ [20].

4 Extensions of the BetaBeam concept

BetaBeam capabilities for the maximum values of γ available with the SPS, $\gamma^6\mathrm{He} = 150$ have been computed in ref. [21].

Performances for ions accelerated at higher energies than those allowed by SPS have been firstly computed in ref. [22] and subsequently in ref. [21, 23, 24].

These studies assume that the same ion fluxes of the baseline scenario can be maintained. However, this is not the case if the number of stored bunches is kept constant in the storage ring. Studies are in progress at CERN in order to define realistic neutrino fluxes as a function of γ [25]. Performances of these higher energy Beta Beams would be anyway extremely interesting, as discussed in ref. [21, 24]

It is worth noting that if a high intensity Beta Beam with $\gamma \sim 300 \div 500$ (requiring a higher energy accelerator than SPS, like the Super-SPS [26]) can be built, a 40 kton iron calorimeter located at the Gran Sasso Laboratory will have the possibility to discover a non vanishing δ_{CP} if $\delta_{\rm CP} > 20^\circ$ for $\theta_{13} \geq 2^\circ$ (99% C.L.) and measure the sign of Δm^2_{23} [27].

A very recent development of the Beta Beam concept is the possibility to have monochromatic, single flavor neutrino beams thanks to the electron capture process [28, 29]. A suitable ion candidate exists: ^{150}Dy, whose performances have been already delineated [28].

References

1. Y. Fukuda *et al.*, Phys. Rev. Lett. **81** (1998) 1562 [arXiv:hep-ex/9807003].
2. S. R. Ahmad et al., nucl-ex/0204008. S. N. Ahmed *et al.*, Phys. Rev. Lett. **92** (2004) 181301 [arXiv:nucl-ex/0309004].
3. K. Eguchi *et al.*, Phys. Rev. Lett. **90** (2003) 021802 [arXiv:hep-ex/0212021]. T. Araki *et al.*, Phys. Rev. Lett. **94** (2005) 081801 [arXiv:hep-ex/0406035].
4. E. Aliu *et al.*, Phys. Rev. Lett. **94** (2005) 081802 [arXiv:hep-ex/0411038].
5. M. Apollonio *et al.*, Eur. Phys. J. C **27** (2003) 331, [arXiv:hep-ex/0301017].
6. Y. Itow *et al.*, arXiv:hep-ex/0106019.
7. D. S. Ayres *et al.*, arXiv:hep-ex/0503053.
8. P. Huber *et al*, arXiv:hep-ph/0403068.
9. S. Geer, Phys. Rev. D57 (1998) 6989; A. De Rujula, M.B. Gavela and P. Hernandez, Nucl. Phys. B547 (1999) 21; A. Blondel et al., Nucl. Instrum. Methods Phys. Res., A 451 (2000) 102; J. J. Gomez-Cadenas and D.A. Harris, "Physics opportunities at neutrino factories," Ann. Rev. Nucl. Part. Sci. 52 (2002) 253 and the annual proceedings of the International Nufact Workshop. M. Apollonio *et al.*, arXiv:hep-ph/0210192.
10. P. Zucchelli, Phys. Lett. B **532** (2002) 166.

These studies assume that the same ion fluxes of the baseline scenario can be maintained. However, this is not the case if the number of stored bunches is kept constant in the storage ring. Studies are in progress at CERN in order to define realistic neutrino fluxes as a function of γ [25]. Performances of these higher energy Beta Beams would be anyway extremely interesting, as discussed in ref. [21, 24]

It is worth noting that if a high intensity Beta Beam with $\gamma \sim 300 \div 500$ (requiring a higher energy accelerator than SPS, like the Super-SPS [26]) can be built, a 40 kton iron calorimeter located at the Gran Sasso Laboratory will have the possibility to discover a non vanishing δ_{CP} if $\delta_{\rm CP} > 20^\circ$ for $\theta_{13} \geq 2^\circ$ (99% C.L.) and measure the sign of Δm^2_{23} [27].

A very recent development of the Beta Beam concept is the possibility to have monochromatic, single flavor neutrino beams thanks to the electron capture process [28, 29]. A suitable ion candidate exists: ^{150}Dy, whose performances have been already delineated [28].

References

1. Y. Fukuda *et al.*, Phys. Rev. Lett. **81** (1998) 1562 [arXiv:hep-ex/9807003].
2. S. R. Ahmad et al., nucl-ex/0204008. S. N. Ahmed *et al.*, Phys. Rev. Lett. **92** (2004) 181301 [arXiv:nucl-ex/0309004].
3. K. Eguchi *et al.*, Phys. Rev. Lett. **90** (2003) 021802 [arXiv:hep-ex/0212021]. T. Araki *et al.*, Phys. Rev. Lett. **94** (2005) 081801 [arXiv:hep-ex/0406035].
4. E. Aliu *et al.*, Phys. Rev. Lett. **94** (2005) 081802 [arXiv:hep-ex/0411038].
5. M. Apollonio *et al.*, Eur. Phys. J. C **27** (2003) 331, [arXiv:hep-ex/0301017].
6. Y. Itow *et al.*, arXiv:hep-ex/0106019.
7. D. S. Ayres *et al.*, arXiv:hep-ex/0503053.
8. P. Huber *et al*, arXiv:hep-ph/0403068.
9. S. Geer, Phys. Rev. D57 (1998) 6989; A. De Rujula, M.B. Gavela and P. Hernandez, Nucl. Phys. B547 (1999) 21; A. Blondel et al., Nucl. Instrum. Methods Phys. Res., A 451 (2000) 102; J. J. Gomez-Cadenas and D.A. Harris, "Physics opportunities at neutrino factories," Ann. Rev. Nucl. Part. Sci. 52 (2002) 253 and the annual proceedings of the International Nufact Workshop. M. Apollonio *et al.*, arXiv:hep-ph/0210192.
10. P. Zucchelli, Phys. Lett. B **532** (2002) 166.

11. `http://www.ganil.fr/eurisol/`

12. B. Autin *et al.*, arXiv:physics/0306106. M. Benedikt, S. Hancock and M. Lindroos, Proceedings of EPAC 2004, http://accelconf.web.cern.ch/AccelConf/e04.

13. M. Mezzetto, J.Phys. G **29** (2003) 1781 [arXiv:hep-ex/0302007]. J. Bouchez, M. Lindroos and M. Mezzetto, AIP conference proceedings, **721** (2003) 37 [arXiv:hep-ex/0310059]. M. Mezzetto, Nucl. Phys. Proc. Suppl. **143** (2005) 309 [arXiv:hep-ex/0410083].

14. A. Donini *et al*, Nucl. Phys. B **710** (2005) 402 [arXiv:hep-ph/0406132].

15. M. Mezzetto, arXiv:hep-ex/0511005.

16. V. Barger, D. Marfatia and K. Whisnant, Phys. Rev. D **65** (2002) 073023 [arXiv:hep-ph/0112119].

17. P. Huber, M. Maltoni and T. Schwetz, Phys. Rev. D **71** (2005) 053006 [arXiv:hep-ph/0501037].

18. B. Autin *et al.*, CERN-2000-012

19. J. J. Gomez-Cadenas *et al.*, Proceedings of "Venice 2001, Neutrino telescopes", vol. 2*, 463-481, arXiv:hep-ph/0105297. A. Blondel *et al.*, Nucl. Instrum. Meth. A **503** (2001) 173. M. Mezzetto, J. Phys. G **29** (2003) 1771 [arXiv:hep-ex/0302005]. J. E. Campagne and A. Cazes, arXiv:hep-ex/0411062.

20. M. Mezzetto, Nucl. Phys. Proc. Suppl. **149** (2005) 179.

21. J. Burguet-Castell *et al*, arXiv:hep-ph/0503021.

22. J. Burguet-Castell *et al.*, Nucl. Phys. B **695** (2004) 217 [arXiv:hep-ph/0312068].

23. F. Terranova *et al*, Eur. Phys. J. C **38** (2004) 69 [arXiv:hep-ph/0405081].

24. P. Huber et al., arXiv:hep-ph/0506237.

25. M. Lindroos, proceedings of Nufact 05, to be published.

26. O. Bruning *et al.*, CERN-LHC-PROJECT-REPORT-626.

27. A. Donini *et al*, arXiv:hep-ph/0511134.

28. J. Bernabeu *et al*, hep-ph/0505054

29. J. Sato, hep-ph/0503144.

D. Bonacorsi	PhEDEx: reliable, scalable dataset replication
M. Caselle	Assembly procedure of the ALICE silicon pixel detector module
A. Citterio	IDRA: an innovative centre for diagnostic and protontherapy
F. Fanzago	CRAB, a tool to enable CMS distributed analysis
S. Gonzalez	Distributed analysis jobs with the ATLAS production system
K. Harrison	Ganga user interface for job definition and management
A. Retico	An Automatic System to Discriminate Malignant from Benign Massive Lesions in Mammograms
A. Sciabà	Monte Carlo production in LCG
P. Solevi	The role of low doses in radiotherapy
A. Tata	A multi-scale approach to the computer-aided detection of microcalcification clusters in digital mammograms

Frascati Physics Series Vol. XL (2006), pp. 347–348
Frontier Science 2005, New Frontiers in Subnuclear Physics
Milano, 12-16 September, 2005

PhEDEx RELIABLE, SCALABLE DATASET REPLICATION

D. Bonacorsi
(on behalf of INFN-CNAF Tier-1 and CMS experiment)

Abstract

High Energy Physics experiments need to perform tasks as ensuring data safety, large-scale dataset replication, tape migration/stage of datasets. PhEDEx is designed for data distribution management and allows the Compact Muon Solenoid (CMS) experiment at the Large Hadron Collider (LHC) to manage large scale production transfer of data. It provides a scalable infrastructure for managing these operations by automating many low level operations and without imposing constraints on choice of Grid or other distributed technologies.

1 Architecture for a reliable replication management

PhEDExs primary concern is reliability. Experience shows that many existing replication tools and services are unreliable at high loads. To counter this, the PhEDEx system was developed. A PhEDEx distribution infrastructure comprises a set of *nodes*, operating independently as logical entities given the task of hosting *software agents* [1]. Such agents are persistent stateless processes, responsible for undertaking specific tasks: they exchange information about system state through a central 'blackboard', which contains dataset-replica mappings and locations, dataset subscriptions and allocations, replica set metadata

(size, checksums, ...), transfer states. The PhEDEx system does not impose any constraint on the basic transfer mechanism: for CMS, PhEDEx currently couples standalone resources with LCG, OSG and NorduGrid infrastructures. All PhEDEx components form a series of logical layers, each improving the scalability and reliability of replication operations.

2 Scalability tests, deployment and replication reliability

On a dedicated testbed, tests of scalability [2] showed that PhEDEx is capable of 200k routing decisions per hour and up to 30k replication operations per hour. On a real playground, PhEDEx has been in production use with simulated data for over a year for CMS (see e.g. [3]), and now: *i)* it links 8 regional centres and 16 smaller sites in production topology; *ii)* it handles 110 TB, replicated on average twice; *iii)* it exhibits sustained rates of 1 TB per day per Tier-1 on standard Internet; *iv)* it deploys the blackboard as a high-availability Oracle database; *v)* Storage Resource Manager (SRM) provides standard a interface to storage; *vi)* srmcp, globus-url-copy, lcg-cp, dccp, rfcp are used for replication. As well as providing a day-to-day production service for CMS, PhEDEx takes part in Service Challenges, i.e. focussed, sustained testing activities in which existing hardware and software are pushed beyond their current use levels toward the levels required for running when the LHC experiments come on-line.

References

1. T. Barrass *et al*, Software agents in data and workflow management, in: Proc. CHEP04, Interlaken, 2004. See also http://www.fipa.org

2. T. Barrass, V. Innocente, L. Tuura, Replaying a data challenge to optimise resource usage, in: Proc. CHEP04, Interlaken, 2004

3. D. Bonacorsi *et al*, Towards the operation of the INFN Tier-1 for CMS: lessons learned from CMS DC04, in: Proc. ACAT05, DESY Zeuthen, 2005

Frascati Physics Series Vol. XL (2006), pp. 349–351
Frontier Science 2005, New Frontiers in Subnuclear Physics
Milano, 12-16 September, 2005

ASSEMBLY PROCEDURE OF THE ALICE SILICON PIXEL DETECTOR MODULE

M Caselle
INFN, Bari, Italy
on behalf of the SPD project in the ALICE Collaboration

Abstract

The assembling procedure of the half-stave detector modules of the ALICE Silicon Pixel Detector (SPD), is described. The assembly essentially requires attaching the bump bonded detector components (ladders and multi-chip module) to the pixel bus, a multi-layer aluminium-polyimide laminate, and in wire bonding the complete detector module. A full electrical characterization and qualification test of the module is also performed.

1 Half-stave components and attachment technique

The half-stave is the basic building block of the ALICE SPD [1)]. It is an assembly of several components:
- ladders: array of five pixel ASICs bump bonded to a silicon sensor;
- multi-chip-module (MCM): a very compact, low mass copper-polyimide laminate on which several auxiliary ASICs and an optical module are mounted;
- pixel bus: an multi-layer aluminium-polyimide laminate for power distribution and signal interconnect;
- grounding foil: a single-side aluminium-polyimide 50 μm thick foil that acts

as spacer and electrical screen.
The component attachment takes place in two steps. The Eccobond-45 adhesive has been chosen for its good mechanical strength and high elasticity coefficient. The first step consists in attaching the ladders and the MCM components to the grounding foil. After a micrometric alignment of the two ladders and the MCM with respect to each other, the adhesive is deposited on the grounding foil, then ladder 1, 2 and MCM are placed in sequence. The second step consists in attaching the ladders and the MCM to the pixel bus. A good attachment between pixel bus, ladders and MCM is very crucial for the following wire-bonding step: it must ensure that the adhesive is uniformly distributed underneath the pixel bus bonding pads without flowing onto the ladders and the MCM bonding pads. The handling of the components and the attachment steps are carried out on a Mitutoyo coordinate measuring machine equipped with positioners, vacuum suction lifting tools and precision adhesive dispensers. Automated procedures have been developed for the various steps.

2 Wire-bonding process

The wire-bonding is based on a solid phase welding process, where the two metallic materials (the wire and the pad surface) are brought into contact such that electron sharing or interdiffusion of atoms takes place, resulting into the formation of the wire-bond. The wire-bonding technique used for ALICE SPD consists of an ultrasonic aluminium wedge bonding with a 25 μm diameter wire. The main parameters of the process are: Bonding Force (BF), UltraSonic bonding Time (USTime) and UltraSonic Power (USPower). A protocol has been developed to determine the acceptable ranges of parameters. The settings depend on the wire type, pad metallization, substrate, etc. Therefore, for each type of the half-stave components a series of bonding test has been performed. Destructive pull tests (Standard MIL-STD-883E method 2011) have also been carried out to evaluate the bond strength. The results of the pull test are particularly important to assess the quality and the reliability of the bonding with respect to main bond failure mechanisms [2)].
The next step consists in the optimization of the Bond Process Control (BPC). The BPC is very important since it allows to maintain a stable process also under critical local conditions, such as: non homogeneous wire composition, variation of surface properties and contaminations. The BPC is based on the

use of a sensor which measures the deformation of the wire during the bonding and automatically adjusts USPower and USTime in order to obtain a suitable process and reduce fluctuations in the bond strength.
Another important issue is the loop of the wire-bonding. There are ten different loops each optimized according to the space available for the half-stave mounting on the carbon fibre sector. A visual inspection is carried on to check the loop height and shape, the position and size of the bonds within the pads. Each half-stave contains more than 1,100 wire-bondings distributed on seven layers. A detail of the final assembly for one pixel chip is shown in Figure 1.

At the end of the assembly phase a complete electrical characterization and

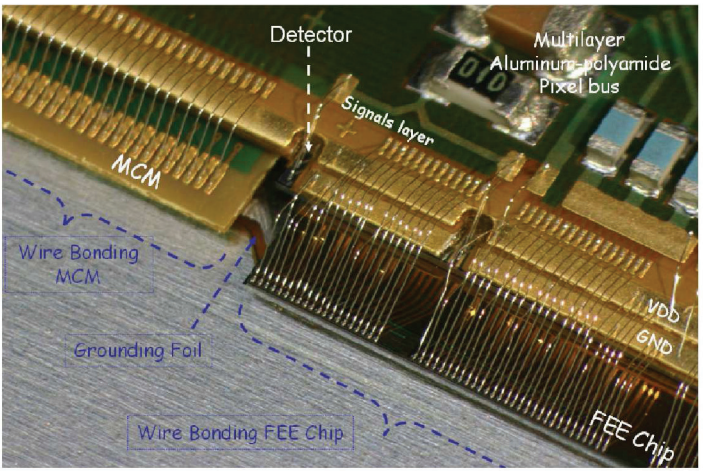

Figure 1: *Half-stave and components.*

qualification test takes place in order to verify the good quality of the assembly and provide a feedback to the assembly procedure.

References

1. ITS Technical Design Report, CERN-LHCC 99-12, 1999.

2. Charles A. Harper, *Electronic Packaging and Interconnection Handbook*, Mc Craw-Hill handbook, IV edition, 2005.

Frascati Physics Series Vol. XL (2006), pp. 353–355
Frontier Science 2005, New Frontiers in Subnuclear Physics
Milano, 12-16 September, 2005

IDRA: AN INNOVATIVE CENTRE FOR DIAGNOSTIC AND PROTONTHERAPY

Alessandro Citterio[1]
Università degli Studi di Milano-Bicocca, Milano - Italy
TERA Foundation, Novara - Italy

Ugo Amaldi, Sonia Allegretti, Paolo Berra, Faiza Bourhaleb, Saverio Braccini, Massimo Crescenti, Arianna Giuliacci (*), Gabriele Fagnola, Peter Pearce, Sandro Toncelli, Cesare Tronci, Mario Weiss, Riccardo Zennaro
TERA Foundation, Novara - Italy
(*)*also Politecnico di Torino, Torino - Italy*

Ettore Rosso, Balazs Szeless
CERN, Geneva, Switzerland

Abstract

The IDRA project (fig.1) - the *Institute for Diagnostic and RAdiotherapy* - consists of a 30 MeV commercial cyclotron for the production of isotopes for PET, SPECT and other radionuclides for diagnostic and therapy combined with a proton linac for the treatment of deep seated tumours. A 3 GHz Side Coupled Linac named LIBO (LInac BOoster) post-accelerates the 30 MeV protons from the cyclotron up to 210 MeV in a length of 16.6 metres. The combination of a cyclotron and a linac has been dubbed "cyclinac".

An accelerating module of LIBO is composed of a biperiodic chain of accelerating and coupling cells and houses 2 permanents quadrupoles. Two accelerating units are powered by a dual klystron solid state modulator (DKSSM).This modular structure can be repeated to increase the final energy in successive steps (65 MeV for ocular tumours, 160 MeV for pediatric tumours, 210 MeV

[1]Corresponding author. E-mail: Alessandro.Citterio@cern.ch.

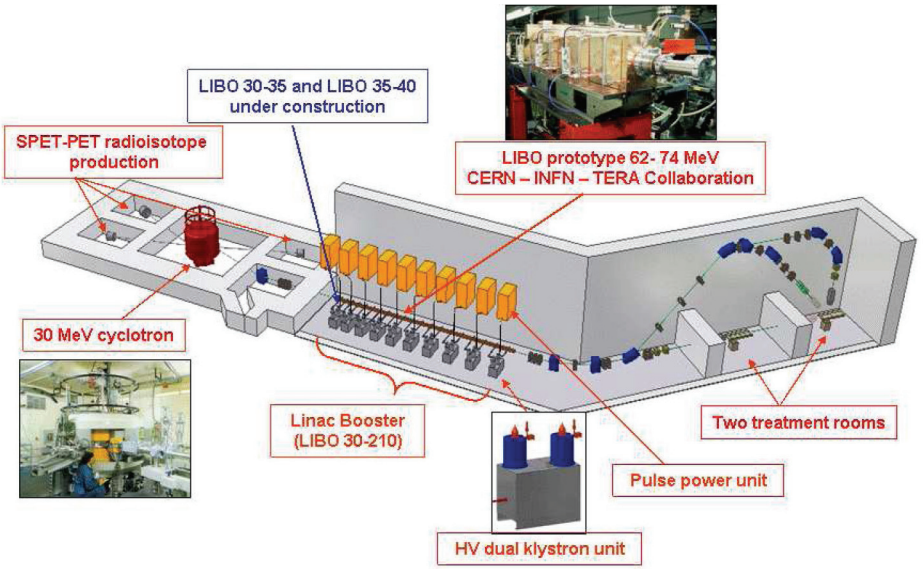

Figure 1: *A comprehensive overview of IDRA including the 30 MeV commercial cyclotron, the solid target rooms for the production of radioisotopes, LIBO, the beam transfer lines, and the two treatment rooms.*

for all the deep seated tumours). A "full" LIBO 30-210 is composed of 20 modules supplied by 10 DKSSM.

The LIBO basic structure proof-of-principle fully succeeded in 2000. A prototype was built in the framework of a scientific collaboration among CERN, INFN and TERA [1)]. During the full power tests a maximum field of 27 MV/m was reached, much larger than the nominal value of 15.7 MV/m; the beam was accelerated from 62 MeV to 73 MeV at the cyclotron of Laboratori Nazionali del Sud of INFN [2)].

By the end of year 2005, TERA will complete the first two modules of LIBO 30-210 with the aim of engineering, reducing the cost and relaxing the tolerances. These modules will accelerate protons from 30 to 40 MeV. The work is done in collaboration with two industrial partners responsible of the mechanical production and the brazing of the cells.

The design of IDRA includes also a comprehensive study of the transfer lines, the beam optics for different settings of the machine, the development of the

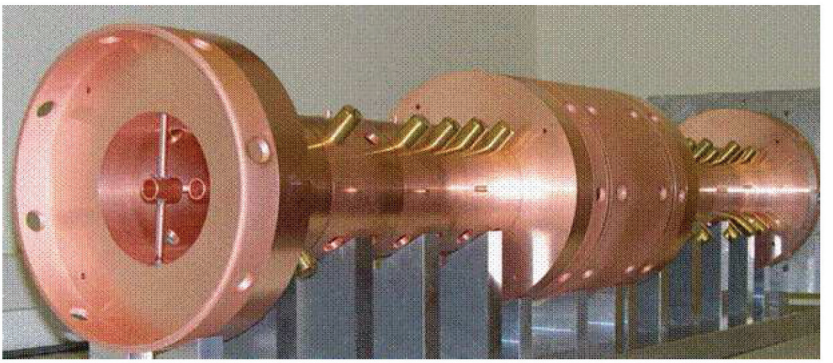

Figure 2: *The 1 GHz model of CLUSTER, which has been constructed and tested. Resonating mode distributions and accelerating field shape have showed good agreement between computed and measured values.*

delivery system and the specifications of the magnets.

Most recently, TERA developped the design of a new linac structure called CLUSTER (Coupled cavity Linac USing Transverse Electric Radial fields), that enables, compared to LIBO, larger gradients with similar power consumption. In a cyclinac structure, CLUSTER can use as injector a small commercial proton cyclotron with an output energy of only 10-15 MeV.

This innovative linac has very high shunt impedence at low and medium beam energy. A proof-of-principle low-power prototype has been built and successfully tested (fig.2). The design of a 1.5 GHz CLUSTER structure, capable to accelerate protons from 15 to 66 MeV, is under study. This structure could inject the beam without losses into a 3 GHz LIBO that starts from 66 MeV and post-accelerates the beam up to 210 MeV.

References

1. U. Amaldi *et al*, LIBO-A linac-booster for protontherapy: construction and tests of a prototype, NIM **A521**, 512 (2004).

2. C. De Martinis *et al*, Beam tests on a proton linac booster for hadrontherapy, Proceedings of the European Particle Acceleration Conference, EPAC, Paris, pp. 2727-2729 (2002).

Frascati Physics Series Vol. XL (2006), pp. 357–362
Frontier Science 2005, New Frontiers in Subnuclear Physics
Milano, 12-16 September, 2005

CRAB, A TOOL TO ENABLE CMS DISTRIBUTED ANALYSIS

Federica Fanzago, Stefano Lacaprara, Nikolai Smirnov
INFN Padova, Italy
Spiga Daniele
Università of Perugia and INFN, Italy
Giovanni Ciraolo
Università of Firenze and INFN, Italy
Marco Corvo
CERN, Meyrin, Switzerland
Nicola De Filippis
Università of Bari and INFN, Italy
Alessandra Fanfani
Università of Bologna and INFN, Italy

Abstract

The CMS experiment will produce a large amount of data (few PBytes each year) that will be distributed over many computing centres spread in the countries participating to the CMS collaboration. To access and analyse data available at remote sites, physicists will use the grid infrastructure.
CMS is developing a user friendly tool, CRAB (Cms Remote Analysis Builder), whose aim is to simplify the creation and the submission of analysis jobs into the grid environment. Its purpose is to hide the grid infrastructure complexity to final users, so that they can access remote data as easily as in a local environment. Data discovery, resources availability, status monitoring and output retrieval of submitted jobs are fully handled by CRAB.
In this report we will explain how CRAB is interfaced with other CMS/grid services, the experience gained during production and future developments.

1 Introduction

CMS (Compact Muon Solenoid) [1] is one of the four particle physics experiments that will collect data at LHC (Large Hadron Collider) starting in 2007 at CERN, Switzerland.
This experiment will produce a large amount of data (few PBytes each year) that will be stored in many computing centres (Tiers) in the countries partecipating to the CMS collaboration and made available for analysis to world-wide distributed physicists [2].
CMS will use a distributed architecture based on grid infrastructure to ensure remote resources availability and to assure remote data access to authorized user (belonging to CMS Virtual Organization).
Tools for accessing distributed data and resources, provided by the European LHC Computing Grid (LCG) [3] and the American Open Science Grid (OSG) [4], are under evaluation.

2 Distributed analysis chain and CRAB role

Data analysis in a distributed environment is a complex computing task. It assumes to know which data are available, where they are stored and how to access them. It is also needed to understand which resources are able to comply with user analysis job requirements. The CMS collaboration is developing some tools, interfaced with available grid services, to achive these purposes.
They include:

- installation of CMS software via grid on remote resources [5]
- data transfer service to move and manage a large flow of data among Tiers [6]
- data validation system to ensure data consistency and readiness [7]
- data location system to keep track of data available in each site and to allow data discovery. Now it is composed by a central database located at CERN (RefDB) containing information about what kind of data have been produced; a local database (PubDB) in each Tier with information about where data are stored (which local Storage Element - SE) and the

protocol to access them; local POOL catalogs with physical data location on SE [2)]

- A friendly interface to simplify the creation and the submission of analysis jobs to grid environments: **CRAB** (**C**MS **R**emote **A**nalysis **B**uilder). Its purpose is to allow users with no knowledge of grid infrastructure to run their analysis code on data available at remote sites as easily as in a local environment hiding grid infrastructure details [8)]

- job monitoring and logging-bookkeeping system to keep trace of submitted jobs and to identify grid middleware or user application problems

3 CRAB

The aim of CRAB is to simplify the work of final users to create and submit analysis job to the grid. CRAB is written in python and have to be installed to the User Interface (UI), the user access point to the grid. Users develop their analysis code in an interactive environment and decide which data to analyze. They have to provide to CRAB:

- Data parameters: keywords to select a given dataset, as found on RefDB web page, total number of events to be accessed and number of events for each job

- Analysis executable (which is in general user specific) and corresponding parameter cards

- Output file name and how to manage them (return file on UI or store into SE)

Data discovery, resources availability, job creation and submission, status monitoring and output retrieval are fully handled by CRAB.
Specifically, CRAB queries RefDB and local PubDB to discover the location of data to be analyzed and uses these information as job requirements. The grid workload management system match correct resources according to these requirements.
CRAB creates a wrapper of the analysis executable which will be run on remote resources, including CMS environment setup and output management,

like final copy to a grid SE, if required.
CRAB splits the analysis into a number of jobs according to user provided information about events. The user executable is sent to remote resource via input sandbox, together with the job, as tgz archive.
Jobs are submitted using grid workload management command and monitored querying the grid logging and bookkeeping system.

4 CRAB current usage

In the last month (15 August-12 September 2005) have been submitted about 50000 jobs whose weekly rate increased from 6000 to 15000 jobs.
About 210 different datasets are used at least once and the most accessed was required by 15000 jobs. Jobs have been submitted from 25 UI using 40 remote sites storing data.
The job success rate is about 75%, where success means that jobs arrive to remote sites and produce outputs, while the remnant 25% aborts due to site setup problem or grid services failure.

5 CRAB future development

5.1 CRAB job splitting

Up to now the criteria for job splitting is based on events. A user decides the total number of events to analyze and how many events for each jobs and CRAB creates a number of jobs according to this information. By policy, only complete dataset are stored in a site.
In the future the core splitting mechanism will be based on "event-collection" (today this correspond to a "run"), the smallest unit of events that a user is able to select. A job will be configured with the proper set of event-collections contained in given file-blocks, where file-blocks are the packaging units used in data transfer that can contain more than one event-collection.

5.2 CRAB data location and discovery system

Today the data location is based on RefDB, local PubDB and local POOL catalog, as explained in section 2. In the future will be used a "three catalogues system" [2]:

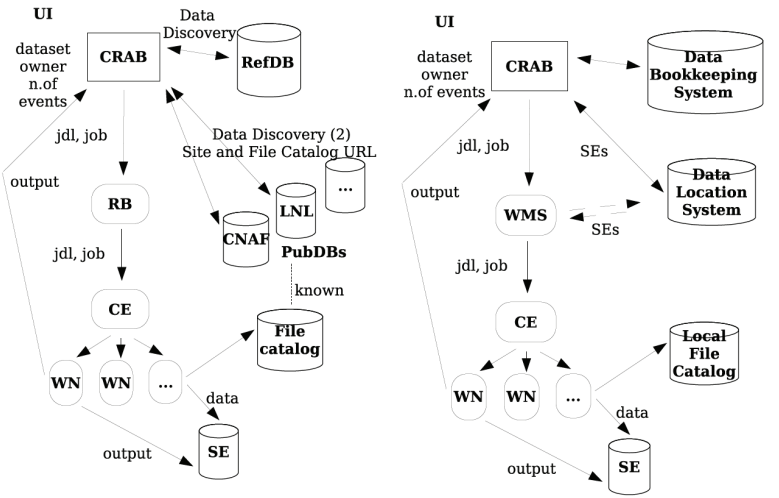

Figure 1: *The current and future data discovery system*

- Dataset Bookkeeping System (DBS) : which data exists. It contains CMS-specific description of event data.
- Data Location Service (DLS): where data are located. It allows to find replicas of a given set of data (file-block) in the distributed grid computing system. It maps file-blocks to Storage Elements where the data are located.
- Local File Catalogue: physical location of data on the SE

CRAB will be modified to use the new catalog and splitting model.

6 Conclusion

The CMS collaboration is developing CRAB, a tool to simplify the creation and the submission of analysis jobs in a distributed environment, based on grid infrastructure. A big effort has been done to understand user needs in order to realize a friendly tool and to use in the best way services provided by grid. The tool has been successfully used by many CMS collaborators to analyze

remote data otherwise not accessible. As CMS analysis framework and grid middleware evolve, CRAB has adapt to cope with these changes and always guarantee its usability and thus remote data access to users.

References

1. The CMS experiment: http://cmsdoc.cern.ch
2. C-TDR - Computing Technical Design Report, CERN-LHCC-2005-023, June 2005
3. LCG Project: http://lcg.web.cern.chLCG and LCG Technical Design Report, CERN-LHCC-2005-024, June 2005
4. OSG project: http://www.opensciencegrid.org
5. XCMSI project: http://cern.ch/cms-xcmsi
6. Tim Barras *et al*, Software agents in data and workload management, presented at CHEP2004, http://www.chep2004.org
7. N. De Filippis, Data Validation tools for CMS analysis, CMS Note 2005/XXX in preparation
8. CRAB project: http://cmsdoc.cern.ch/cms/ccs/wm/www/Crab

Frascati Physics Series Vol. XL (2006), pp. 363–365
Frontier Science 2005, New Frontiers in Subnuclear Physics
Milano, 12-16 September, 2005

DISTRIBUTED ANALYSIS JOBS WITH THE ATLAS PRODUCTION SYSTEM

Santiago González, Dietrich Liko, Armin Nairz, Gregor Mair,
Frederik Orellana, Luc Goossens
CERN, European Organization for Nuclear Research, Geneva, Switzerland
Silvia Resconi, Alessandro de Salvo
INFN, Istituto Nazionale di Fisica Nucleare, Italy

Abstract

The ATLAS production system has been successfully used to run production of simulation data at an unprecedented scale. Up to 10000 jobs were processed by the system in one day. The experiences obtained operating the system on several grid flavors was essential to perform a user analysis using grid resources.

1 Introduction

According to the ATLAS Computing Model [1)], the expected volume of data recorded for offline reconstruction and analysis will be of the order of 10 PB (10^{15} bytes), after reduction of the data by the online trigger processor farms. Therefore, in 2002 a series of Data Challenges (DC's) was planned with the purpose of the validation of the Computing Model, including the complete software suite, to ensure the correctness of the technical choices.

2 ATLAS Production Sytem

In order to handle the task of ATLAS DC's an automated production system [2] was designed (see figure 1). All jobs are defined and stored in a central database. A supervisor agent picks them up, and sends their definition as an XML message to the various executors. Executors are specialised agents, able to convert the XML job description into a GRID specific language. All the data management operations are performed through calls to a central service, Don Quijote (DQ) [3].

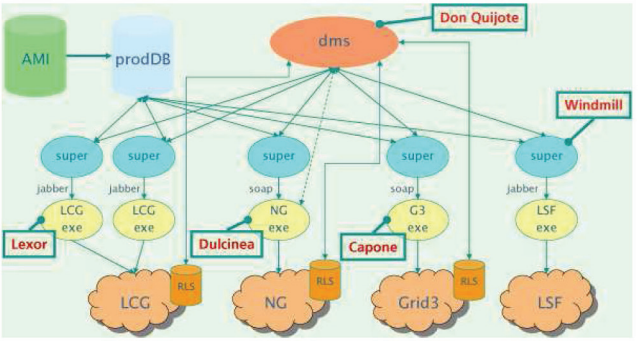

Figure 1: *ATLAS production sytem.*

3 Setup for distributed analysis

While it is possible to run analysis jobs through the production system, not all funcionalities to support distributed analysis are currently available. Important aspects for user analysis had to be implemented in a specialised version of an executor:

- new syntax for input datasets;
- submission of jobs to sites where the data is already available;
- shipping of customized user algorithms;
- storage of user results.

A Graphical User Interface (GUI) [4] was used to define jobs and monitor the current status.

4 Experience running the Analysis

A generical analysis transformation was created to run over different user analysis algorithms. Several dataset were used. Using the GUI, hundreds of jobs were created with 100 input files each one. These jobs were submitted with an instance of supervisor-executor and they ran in different sites. Each job produced three output files (ntuple, histrogram and log) stored at CASTOR (CERN, IFIC-Valencia, Taiwan).

5 Conclusions

The ATLAS production system has been used to submit physics analysis jobs. The work is profiting in a natural way from the investment in the production system for ATLAS big productions. Only limited resources were needed to perform the necessary modifications to run these jobs.

References

1. ATLAS Collaboration, Computing Technical Design Report - TDR (CERN-LHCC-2005-022) (2005).
2. L. Goossens, Production System in ATLAS DC2, CHEP04, Interlaken, contr. no. 501 (2004).
3. http://uimon.cern.ch/twiki/bin/view/Atlas/DonQuijote
4. http://uimon.cern.ch/twiki/bin/view/Atlas/AtCom3

Frascati Physics Series Vol. XLI (2006), pp. 501-514
Frontier Science 2005, New Frontiers in Subnuclear Physics
Milano, 12-16 September, 2005

GANGA USER INTERFACE FOR JOB DEFINITION AND MANAGEMENT

U. Egede[1], K. Harrison[2], R.W.L. Jones[3], D.Liko[4], A.Maier[4], J.T. Moscicki,[4], G.N. Patrick[5], A. Soroko[6], C.L. Tan[7]

[1] *Department of Physics, Imperial College London, UK*
[2] *Cavendish Laboratory, University of Cambridge, UK*
[3] *Department of Physics, University of Lancaster, UK*
[4] *CERN, Geneva, Switzerland*
[5] *Rutherford Appleton Laboratory, Chilton, Didcot, UK*
[6] *Department of Physics, University of Oxford, UK*
[7] *School of Physics and Astronomy, University of Birminhgam, UK*

Abstract

Details are presented of the GANGA job definition and management system. This is being developed in the context of the ATLAS and LHCb experiments, to simplify for end-user physicists the task of analysing large volumes of data using distributed computing resources.

1 Introduction

GANGA [1] is a component-based system providing a user interface for job definition and management in a distributed environment. It is being developed in the context of two high-energy physics experiments, ATLAS [2] and LHCb [3], whose specific needs it addresses, but offers possibilities for extension and customisation that make it potentially interesting for a wide range of user communities. It is implemented in Python [4].

tion and decay in high-energy proton-proton interactions at the Large Hadron Collider (LHC) [5], due to start operation at CERN, Geneva, in 2007. Both experiments will require processing of data volumes of the order of petabytes per year, and will rely on computing resources distributed across multiple locations. The experiments' data-processing applications, including simulation, reconstruction and physics analysis, are all based on the GAUDI/ATHENA C++ framework [6]. This provides core services, such as message logging, data access, histogramming; and allows run-time configuration via options files. These can be written in Python, or using a value-assignment syntax similar to that of C++, and may have considerable complexity.

Several possibilities for exploiting distributed computing resources, and for processing distributed data, have been developed using Grid technologies. These include systems from national and international projects, such as LCG (LHC Computing Grid) [7], EGEE (Enabling Grids for e-Science) [8], OSG (Open Science Grid) [9], GridPP (UK Computing for Particle Physics) [10] and NorduGrid [11]; and experiment-specific solutions, such as DIAL [12] in ATLAS and DIRAC [13] in LHCb. The situation for the user is confusing, in that different sites hosting data of interest may have adopted different systems, requiring different commands and job descriptions, and all of the systems continue to evolve. Also, a user will often wish to run test jobs on local resources, where debugging is simpler, before submitting to remote sites, and will prefer not to have to do different things in the two cases.

GANGA provides a single frontend for submission to multiple backends, shielding the user from the uncertainties and technical complications associated with data processing in a distributed environment. This paper outlines the design of GANGA, and illustrates the system's use.

2 Ganga design

GANGA has an extensible architecture (Fig. 1), with the main functionality divided among three components:

- the Application Manager deals with defining the task to be performed within a job, including the application to be run, the values to be assigned to any configurable parameters, and the data to be processed;

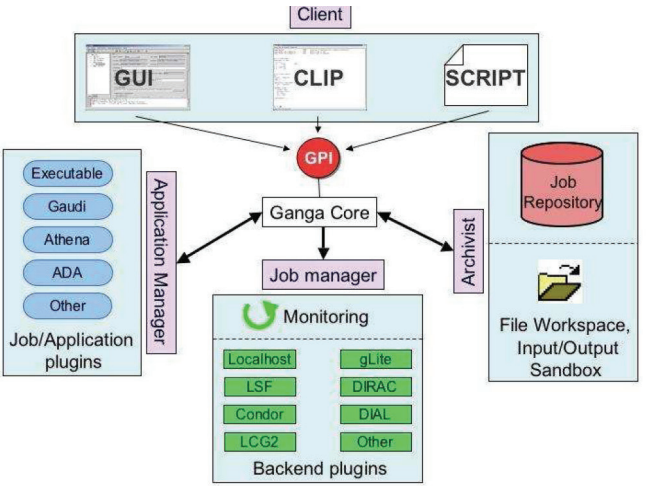

Figure 1: Schematic representation of the GANGA architecture. The main functionality is divided between Application Manager, Job Manager and Archivist, and is accessed by the Client through the GANGA Public Interface (GPI). The client can run the Graphical User Interface (GUI), the Command-Line Interface In Python (CLIP) or GPI scripts.

- the Job Manager creates a wrapper script for running the specified application, performs job submission to a chosen processing system (backend), monitors the job progress, and retrieves output files when the job completes;
- the Archivist provides a repository for storing job information, and manages GANGA's workspace, and keeping track of the locations of input and output files.

The above components communicate with one another through the GANGA core, and their functionality is made available through the GANGA Public Interface (GPI). Users access the GPI through a fourth GANGA component, the Client, which provides a Graphical User Interface (GUI), a shell – the Command-Line Interface In Python (CLIP) – and the possibility to run GPI scripts.

Different types of application and backend are supported by the Application Manager and Job Manager through plug-in classes. These define each application and backend in terms of its own schema, placing in evidence the

configuration properties and their meanings. Users can easily add new plug-in classes, or suppress the loading of unwanted classes, so that GANGA can readily be extended or customised to meet the requirements of different user communities.

3 Using Ganga

3.1 Configuration

GANGA has default parameters and behaviour that can be redefined at startup using one or more configuration files, which use the syntax understood by the standard Python ConfigParser module. Configuration files can be introduced at the level of system, group or user, with each successive file processed able to override settings from preceding files.

One important feature of the configuration files is that they allow selection of the Python packages that should be initialised when GANGA starts, and consequently of the modules, classes, objects and functions that are made available through the GPI. The configuration files also allow modification of the default values to be used when creating objects from plug-in classes, and permit actions such as choosing the log level for messaging, specifying the location of the job repository, and changing certain visual aspects of GANGA.

3.2 GPI and CLIP

The GANGA Public Interface (GPI) is designed as a high-level, user-friendly Python API for job manipulation, and can be used in scripting. GANGA's Command-Line Interface in Python (CLIP) is intended as an extension to the GPI, with enhanced support for interactive operations at the Python prompt. In the current implementation, CLIP and GPI are identical, but at a later stage CLIP may add features such as higher-level shortcuts and a property-aliasing mechanism.

From CLIP, or after GPI has been imported into a script, the user has access to functionality determined by the configuration file(s) used. For example, an LHCb user at CERN might have a setup that would load the plug-ins for the LHCb simulation, reconstruction and analysis applications, for the local LSF batch system, for LCG and for DIRAC. An ATLAS user might, instead, load the plug-ins for submitting jobs to DIAL, and objects for accessing the DIAL

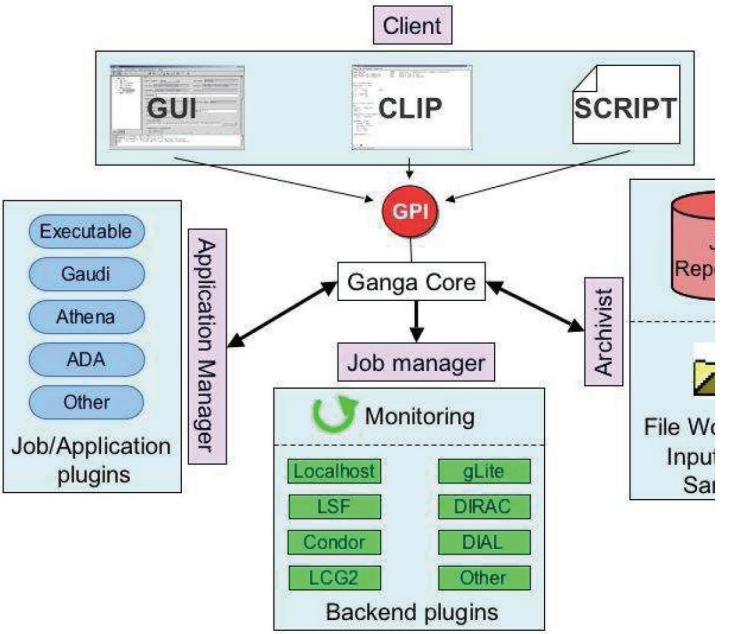

Figure 2: Example job submission using CLIP. Here, the user wishes to run the LHCb analysis application, DaVinci [14], on the experiment's own distributed processing system, DIRAC. The user selects the version number for the application (v12r11), specifies the options file to be used (DVHLTCore.opts), and accepts the default values for the DIRAC backend. Submission is then a one-line command.

catalogues for dataset selection. CLIP and the GPI additionally make available an object for interacting with the job repository, allowing examination of the stored jobs.

With CLIP or GPI, a user needs give only a few commands to be able to set application properties and submit a job to run the application on a Grid backend (Fig. 2). The output, when ready, is retrieved automatically. The user is protected from the technicalities of the submission and output-retrieval operations, and is spared from working directly with shell scripts and description files, which, even for fairly simple jobs, can be tens or hundreds of

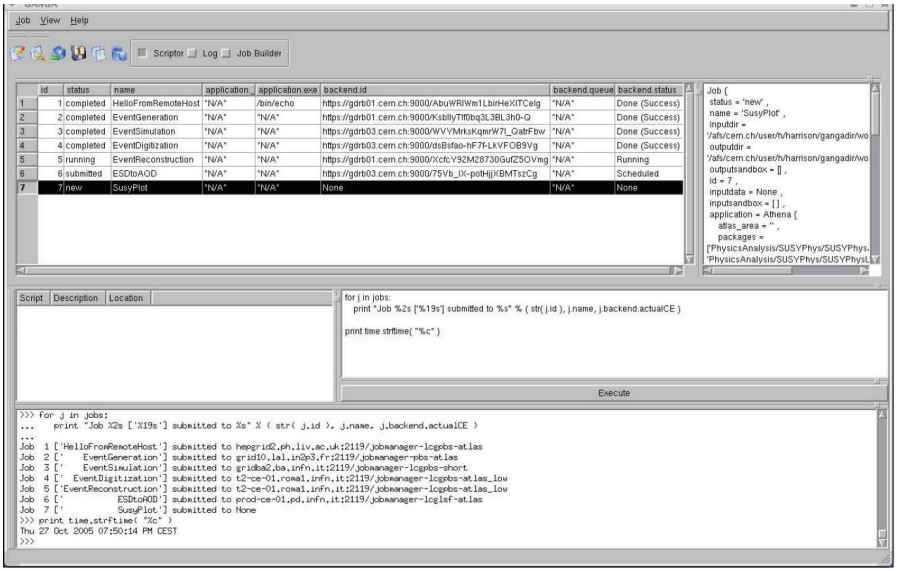

Figure 3: Screenshot of the GANGA GUI, showing: the monitoring panel (top left), the job-description panel (top right), the scriptor panels (middle), and the execution panel (bottom). Here, the monitoring panel reports the status of jobs submitted to LCG to perform various steps in the ATLAS data processing, and the scriptor has been used to print information on where the jobs were sent.

.

3.3 GUI

A GUI (Fig. 3), to further simplify user tasks, is being developed using the PyQt [15] graphics toolkit. The GUI includes:

- a monitoring panel, which shows the status of user jobs, and provides access to job definitions;
- a log panel, where message from GANGA are directed;
- a job-builder panel, for job creation and modification;
- scriptor and execution panels, which allow the user to run Python scripts and GPI commands, maximising flexibility when working inside the GUI.

By default, panels are shown together in a single window, but the panels are dockable, and can be resized and placed according to the tastes of the individual user.

Job submission through the GUI involves creating a job of the required type (accomplished with a few mouse clicks), filling in application and backend properties in the job-builder panel, then clicking on the "Submit" button.

4 Summary and outlook

GANGA has been developed in Python as a frontend for job definition and management, providing a single, easy-to-use interface for running and monitoring user-defined applications on a variety of local batch queues and Grid-based systems, hiding Grid technicalities. The main functionality is divided between an Application Manager, which deals with application setup, a Job Manager, which deals with job submission and monitoring, and an Archivist, which deals with job storage and workspace management. Functionality is made available through the GANGA Public Interface (GPI), and is accessed using the GANGA Client. The Client provides a Graphical User Interface (GUI), a Command-Line Interface in Python (CLIP), and the possibility to run GPI scripts.

GANGA specifically addresses the needs of the ATLAS and LHCb high-energy physics experiments for running applications performing large-scale data processing on globally distributed resources. As it handles different applications and backend processing systems using plug-in classes, which are easily added, and it offers significant configuration possibilities at startup, GANGA can readily be extended and customised to meet the requirements of other user communities.

Work in progress focuses on ensuring the availability of all plug-in classes required for the applications and backends of interest to ATLAS and LHCb, and on further developing the GUI. Trial users have been positive in their response to GANGA, which they have used successfully to submit jobs to both local and remote systems. Longer-term development efforts will be guided by feedback from an increasingly large user group.

5 Acknowledgements

We are pleased to acknowledge support for the work on GANGA from GridPP in the UK and from the ARDA group at CERN. GridPP is funded by the UK Particle Physics and Astronomy Research Council (PPARC). ARDA is part of the EGEE project, funded by the European Union under contract number INFSO-RI-508833.

1. http://ganga.web.cern.ch/ganga/
2. ATLAS Collaboration, Atlas - Technical Proposal, CERN/LHCC94-43 (1994);
   http://atlas.web.cern.ch/Atlas/
3. LHCb Collaboration, LHCb - Technical Proposal, CERN/LHCC98-4 (1998);
   http://lhcb.web.cern.ch/lhcb/
4. G. van Rossum and F. L. Drake, Jr. (eds.), Python Reference Manual, Release 2.4.1 (Python Software Foundation, 2005);
   http://www.python.org/
5. LHC Study Group, The LHC conceptual design report, CERN/AC/95-05 (1995);
   http://lhc-new-homepage.web.cern.ch/lhc-new-homepage/
6. P. Mato, GAUDI - Architecture design document, LCHb-98-064 (1998);
   http://proj-gaudi.web.cern.ch/proj-gaudi/welcome.html
7. http://lcg.web.cern.ch/lcg/
8. http://egee-intranet.web.cern.ch/egee-intranet/gateway.html
9. http://www.opensciencegrid.org/
10. http://www.gridpp.ac.uk/
11. http://www.nordugrid.org/
12. D. Adams *et* al., DIAL - Distributed Interactive Analysis of Large datasets, in: Proc. 2003 Conference for Computing in High Energy and Nuclear Physics, (La Jolla, California, USA, 2003);
    http://www.usatlas.bnl.gov/~dladams/dial/
13. V. Garonne, A. Tsaregorodtsev and I. Stokes-Rees, DIRAC: A Scalable Lightweight Architecture for High Throughput Computing, in: Proc. 5th IEEE/ACM International Workshop on Grid Computing (Pittsburg, USA, 2004);
    http://lbnts2.cern.ch/
14. http://lhcb-comp.web.cern.ch/lhcb-comp/Analysis/
15. http://www.riverbankcomputing.co.uk/pyqt/

Frascati Physics Series Vol. XL (2006), pp. 377–380
Frontier Science 2005, New Frontiers in Subnuclear Physics
Milano, 12-16 September, 2005

AN AUTOMATIC SYSTEM TO DISCRIMINATE MALIGNANT FROM BENIGN MASSIVE LESIONS IN MAMMOGRAMS

P. Delogu[1,2], M.E. Fantacci[1,2], P. Kasae[3] and A. Retico[2]
[1] *Dipartimento di Fisica dell'Università di Pisa, Largo Pontecorvo 3, 56127 Pisa, Italy*
[2] *Istituto Nazionale di Fisica Nucleare, Sezione di Pisa, Largo Pontecorvo 3, 56127 Pisa, Italy*
[3] *The Abdus Salam International Center for Theoretical Physics, Strada Costiera 11, P.O. Box 563, I-34100 Trieste, Italy*

Abstract

Evaluating the degree of malignancy of a massive lesion on the basis of the mere visual analysis of the mammogram is a non-trivial task. We developed a semi-automated system for massive-lesion characterization with the aim to support the radiological diagnosis. A dataset of 226 masses has been used in the present analysis. The system performances have been evaluated in terms of the area under the ROC curve, obtaining $A_z = 0.80 \pm 0.04$.

1 Introduction

Breast cancer is still one of the most common forms of cancer among women, despite a significant decrease has occurred in the breast cancer mortality in the last few decades [1)]. Mammography is widely recognized as the most reliable technique for early detection of this pathology. However, characterizing the

massive lesion malignancy by means exclusively of a visual analysis of the mammogram is an extremely difficult task and a high number of unnecessary biopsies are actually performed in the routine clinical activity. Computerized methods have recently shown a great potential in assisting radiologists in the malignant vs. benign decision, by providing them with a second opinion about the visual diagnosis of the lesion.

2 Method

The computer-aided diagnosis (CADi) system we present is based on a three-stage algorithm: 1) a segmentation technique identifies the contour of the massive lesion on the mammogram; 2) several features, based on size and shape of the lesion, are computed; 3) a neural classifier analyzes the features and outputs a likelihood of malignancy for that lesion. The segmentation method is a gradient-based one: it is able to identify the mass boundaries inside a physician-located region of interest (ROI) image. The algorithm is based on the maximization of the local variance along several radial lines connecting the approximate mass center to the ROI boundary [2]. The critical points maximizing the local variance on each radial line are interpolated, thus a rough mass shape is identified. The procedure is iterated for each point inside the approximate mass, resulting in a more accurate identification of the mass boundary. The main advantage of this segmentation technique is that no free parameters have to be fitted on the dataset to be analyzed, thus it can in principle be directly applied to datasets acquired in different conditions without any ad-hoc modification. Sixteen features are computed for each segmented mass, some of them being more sensitive to the shape and some to the texture of the lesion. They are: area, perimeter, circularity, mean and standard deviation of the normalized radial length, radial distance entropy, zero crossing, maximum and minimum axes, mean and standard deviation of the variation ratio, convexity; mean, standard deviation, skewness and kurtosis of the grey-level distribution. The features are analyzed by a multi-layered feed-forward neural network trained with the error back-propagation algorithm. The classifier performances are evaluated according to the 5×2 cross validation method.

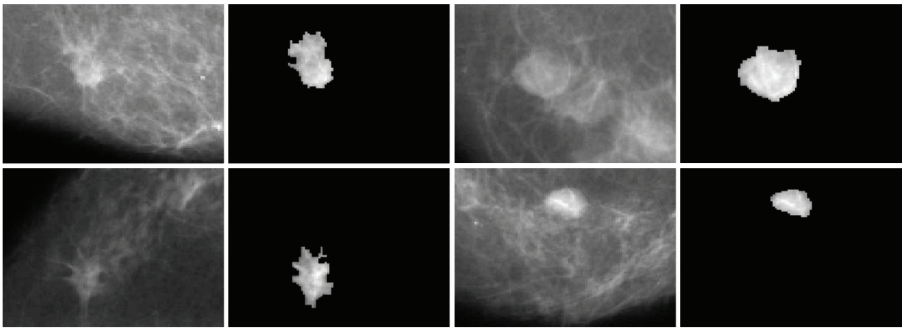

Figure 1: *Examples of malignant (left) and benign (right) segmented masses.*

3 Results

In this work we present the results obtained on a dataset of 226 massive lesions (109 malignant and 117 benign) extracted from a database of mammograms collected in the framework of a collaboration between physicists from several Italian Universities and INFN Sections, and radiologists from several Italian Senological Centers [3]. Despite the boundaries of the masses are usually not very sharp, our segmentation procedure leads to an accurate identification of the mass shapes both in malignant and benign cases, as shown in fig. 1. The performances of the neural network in classifying the features extracted from each mass have been evaluated in terms of the sensitivity and the specificity on the test sets: the average values obtained are 78.1% and 79.1% respectively. The discriminating capability of the system has been evaluated also in terms of the receiver operating characteristic (ROC) analysis (see fig. 2) [4]. The estimated area under the ROC curve is $A_z = 0.80 \pm 0.04$.

4 Conclusions

Mass segmentation plays a key role in CADi systems to be used for supporting radiologists in the malignant vs. benign decision. We developed a robust technique based on edge detection to segment mass lesions from the surrounding normal tissue. The results so-far obtained in the classification of malignant and benign masses indicate that the segmentation procedure we developed provides

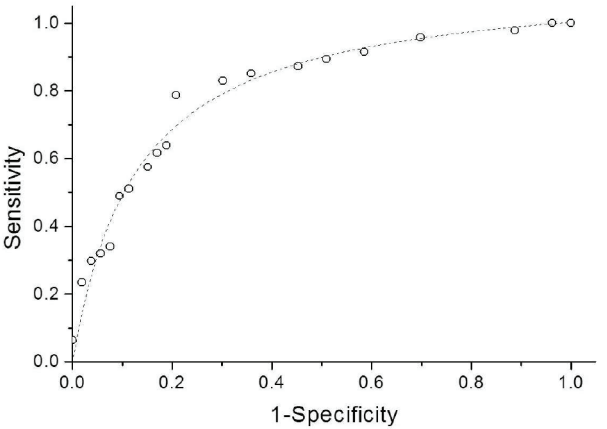

Figure 2: *ROC curve.*

an accurate approximation of the mass shapes and that the features we took into account for the classification have a good discriminating power.

5 Acknowledgments

We are grateful to Dr M. Tonutti from Cattinara Hospital (Trieste, Italy) for her essential contribution to the present analysis. We acknowledge Dr S. Franz from ICTP (Trieste, Italy) for useful discussions.

References

1. S.H. Landis *et al*, Cancer statistics, 1999. Ca-Cancer J Clin **49**(1), 8 (1999).

2. D.R. Chen *et al*, Diagnosis of Breast Tumors with Sonographic Texture Analysis using Wavelet Transform and Neural Networks, Ultrasound Med Biol **28**(10), 1301 (2002).

3. R. Bellotti *et al*, The MAGIC-5 Project: Medical Applications on a Grid Infrastructure Connection, IEEE NSS Conf Rec **3**, 1902–1906 (2004).

4. C.E. Metz, ROC methodology in radiologic imaging, Invest Radiol **21**(9), 720 (1986).

Frascati Physics Series Vol. XL (2006), pp. 381–384
Frontier Science 2005, New Frontiers in Subnuclear Physics
Milano, 12-16 September, 2005

MONTE CARLO PRODUCTION IN LCG

Simone Campana
Andrea Sciabà
CERN, Switzerland

Abstract

An important part of the computing activities performed by the LHC experiments is production of Monte Carlo events. With the advent of the LHC Computing Grid, an increasing part of it is done using the LCG distributed computing infrastructure. In this contribution, we briefly describe the experiment MC production frameworks and how they are interfaced to the Grid.

1 Introduction

Monte Carlo production is one of the must crucial computing activities for high energy physics experiments, as it is a fundamental tool for studying the performance of the detector and the physics analyses. In the LHC era, it is becoming necessary to move from a number of disconnected computing centers to a more integrated Grid infrastructure, like the LHC Computing Grid [1)].

The LCG middleware provides a set of services consisting of:
a) a Workload Management System, responsible for the management and monitoring of user jobs;
b) a Data Management System, allowing users to move files in and out of the Grid, to replicate them among different Storage Elements, and to locate them;
c) an Information System, providing information about the Grid resources and their status;
d) an Accounting System, and various monitoring services.

In order to make the most efficient use of the large amount of computing, storage and network resources in LCG, all the LHC experiments have built, or adapted, their Monte Carlo production tools to the Grid environment, taking care of job definition, submission and monitoring, and trying to make the system as robust and fault tolerant as possible.

In general, Monte Carlo production involves different steps: generation, simulation, digitization (with or without mixing of pile-up events) and reconstruction. These steps may differ greatly in terms of processing time and file size required to create a single event.

In general, Monte Carlo datasets are defined in a *parameter database* (number of events, run number, MC generator parameters, etc). This information is retrieved by a specific experiment component, which creates the job definition, submits the job to the LCG, retrieves the output upon completion and, if the job fails, resubmits the job.

2 ALICE

ALICE has developed since a long time a proprietary Grid-like system called AliEn [2]. AliEn uses a *pull* model to distribute jobs to remote sites: the AliEn *computing elements* pull jobs from a job queue managed by a central AliEn server whenever they are ready to process a new job. In the case of LCG, the whole Grid is seen as a single AliEn CE through an appropriate interface to LCG, which takes care of the job submission and handling. The generated files are stored in LCG storage elements and registered in both the LCG file catalog and the AliEn file catalog, so that they can be accessed in the future also by pure AliEn resources. A significant Monte Carlo production was performed on LCG during the Alice Data Challenge 04: the activity was divided in two phases, namely an event generation phase and an event reconstruction phase

to which LCG contributed with a statistic of about 25% and 10% respectively.

3 ATLAS

The ATLAS Monte Carlo production has been carried on three different Grid infrastructures: LCG, NorduGrid and Grid3/OSG. ATLAS jobs are defined in a central database holding Grid-neutral information about tasks to be executed. A *supervisor* agent distributes jobs to Grid-specific agents called *executors*, follows up their status and validates them in case of success or flags them for resubmission. The executor itself offers an interface to the underlying Grid middleware. The data management relies on Grid-specific tools and the ATLAS Data Management System through its Don Quijote service (high-level data management across different Grids). The job monitoring is also performed through Grid-specific tools even though an effort to uniform the monitoring for the different Grid flavors is currently being carried on. Since Data Challenge 02 (July 2004) ATLAS productions have been performed completely in a Grid environment. MC production for the Rome Physics workshop in LCG represented a significant improvement compared to DC2: 380000 jobs submitted to the LCG system, 1400000 files stored on LCG storage elements (45 TB). Jobs were uniformly distributed around the different sites, depending on their amount of computing resources.

4 CMS

The CMS Monte Carlo production system is based on McRunJob [3]. McRunJob was developed initially in the D0 collaboration and then adopted also by CMS to run productions on local computing farms. More recently, it has been interfaced to Grid infrastructures like LCG and OSG.

Datasets to be produced are defined in RefDB, the CMS dataset bookkeeping database, and assigned to a *regional center*, which can be a local farm or a whole Grid. LCG jobs are made resilient against errors in file transfers by packing output files in a single zip file, by using backup storage elements and by waiting some time between retries.

The produced files are copied by the jobs on LCG storage elements, from where they are automatically harvested by PhEDEx, the CMS data movement tool [4], and copied where they are needed.

Digitization jobs using with event pile-up require that a sample of minimum bias events is stored at the site storage element, and each job copies locally a randomly chosen set of files from the minimum bias sample.

So far, 11.4 million events have been generated, 9.3 simulated, 8.5 digitized and 2 reconstructed on LCG.

5 LHCb

The LHCb Monte Carlo production is managed through DIRAC (Distributed Infrastructure with Remote Access Control) [5]. As in the case of AliEn, DIRAC relies on the "pull" philosophy in order to assign jobs to resources: submitted jobs are stacked in a queue managed by the job management service, and agents running at each DIRAC site request new jobs to this service when they detect that there are free resources available. On LCG, agents are started as Grid jobs and pull a job to the worker node where they are running on: therefore, in some sense, each worker node is a DIRAC site. During its Data Challenge in 2005, LHCb has run successfully up to 5000 concurrent jobs on LCG hitting the limit of the available resources and producing in average 10 millions of events/day. Now, almost all of its Monte Carlo production is done on LCG.

References

1. A. Sciabà, The LCG Project, in these proceedings
2. S. Bagnasco *et al*, AliEn – EDG Interoperability in ALICE, in Proc. Computing in High Energy Physics – CHEP2003, La Jolla, March 2003
3. P. Garcia-Albia, J.M. Hernández, Implementation of Monte Carlo Production in LCG-2, CMS NOTE 2005/019
4. T. Barrass *et al*, PhEDEX: Reliable, scalable dataset replication, in these proceedings
5. A. Tsaregorodtsev *at al*, DIRAC – The Distributed MC Production and Analysis for LHCb, LHCb 2004-083-Offline

Frascati Physics Series Vol. XL (2006), pp. 383–386
Frontier Science 2005, New Frontiers in Subnuclear Physics
Milano, 12-16 September, 2005

THE ROLE OF LOW DOSES IN RADIOTHERAPY

Paola Solevi
Università degli studi di Milano, Via G. Celoria 16, 20133 Milano
Emanuela Mariani, Andrea Crespi, Gian Stefano Gardani,
Chiara Julita, Gianluca Montanari, Roberto A. Perego
A.O. San Gerardo di Monza, Via Pergolesi 33, 20052 Monza (MI)
Università di Milano Bicocca, Via Cadore 48, 20052 Monza (MI)

Abstract

Biological studies and epidemiological data demonstrate that high doses of ionizing radiation (IR) clearly produce deleterious consequences in humans, including cancer induction. Estimates of various damages at cellular level induced at low doses are generally based on linear back-extrapolation from data at higher doses. However a large amount of recent studies seems to suggest a possible deviation from linearity due to different effects. All these effects are linked to unrepaired or misrepaired Double Strand Breaks (DSBs), which are the most relevant lesions by which IR causes cancer and ereditary desease. The method of foci is able to explore the DSBs induction and repair down to mGy, contributing to understand the cellular kinetics at very low doses. The study is implemented in a IMRT exposure scenario.

1 Overview of the effects

A low dose can be defined by a microdosimetric or biological approach and an upper limit of 200 mGy is given by the incidence of mortality for solid tumors induced by low LET ionizing radiation [1)]. In this range genomic instability, bystander effect and adaptive response modulate cell answer. It was observed that pre-exposing cells to a low dose of radiation appeared to protect these cells from the effects of a second larger dose. This effect is known as adaptive response. The term genomic instability refers to a phenomenon whereby radiation exposure appears to induce instability in individual cells that is trasmitted to their progeny, leading to a persistent enhancement in the rate at which genetic changes arise in the descendants of irradiated cell after many generations of replication. A bystander effect is suggested by the evidence that damage signals may be trasmitted from irradiated to non-irradiated cells in a population, leading to the occurrence of biological effects in cells that receive no radiation exposure. Several studies involving both *in vivo* and *in vitro* assays have shown that trasmissible genomic instability may arise in bystander cells and that the bystander effect may be modulated by an adaptive response. When considered as a whole, the emerging results with these three phenomena raise the possibility that the dose response at low doses of ionizing radiation is uncertain and a simple extrapolation from high dose effects may not be appropriate [2)].

2 Low dose scenario in IMRT

Intensity modulated radiation therapy (IMRT) in external beams radiation therapy is one of the latest conformal therapy techniques used in tumor treatments. IMRT employs non-uniform beam intensity, individually optimized, to deliver highly conformal radiations to the target while minimizing doses to normal tissues and critical organs [3)].

At the San Gerardo Hospital in Monza, the beam intensity modulation via a multi-leaf collimator (MLC) is achieved by means of a static segmented approach, also known as step and shoot approach, using a sequence of multiple and fixed field shapes. Moving from three-dimensional conformal radiation therapy (3DCRT) to IMRT, more fields are involved and, as a consequence, a larger volume of normal tissue is exsposed to lower doses and normal tissue cells experience a series of radiation "pulses". Also some critical sites far from

target could receive a very low dose of IR due to scattered radiation or leakages of the beam. The latter is of particular importance in IMRT because the delivery of a specified dose to the target from modulated field will require the accelerator to be energized for a longer time [4]. To discriminate between the two contributions, we simulated a single fraction of 2Gy, delivered by 3DCRT and IMRT techniques, of a prostate cancer treatment. Using a Rando anthropomorphic phantom, we placed an ionization chamber (1cc, type 23331) at the tyroid location (54 cm distant from target). A dose of 2.7 mGy and 1.4 mGy was detected respectively in the modulated technique and in the standard one. The difference, even if small, is probably due to leakage radiation as expected. At so low doses, the lack of knowledge on cellular response could result in an underestimation of second cancer in far sites too. Available Normal Tissue Complication Probability (NTCP) models drop to zero at doses smaller than Gy. The Lyman NTCP model is the most applied in radiation oncology and it is based on the assumption of a sigmoidal dose-response curve taking into account the volume effect depending on the architecture of the organ, serial or parallel distribution of biological functions [5] [6]. But this model is not based on radiobiology and so it is unable to take into account the most relevant effects at low doses.

3 The method of foci

One of the earliest steps in the cellular response to DSBs is the phosphorylation of serine 139 of H2AX. Using a specific antibody (γ-H2AX), discrete nuclear foci can be visualized at sites of DSBs, either induced by exogenous agents such as IR or generated endogenously during programmed DNA rearrangments. The method has a sensibility down to 1.2 mGy with 0.1 foci per cell, respect to a background level of 0.05 foci per cell [7]. Thanks to the one-one relation existing between number of DSBs and foci, combined to the sensibility of the method, γ-H2AX assay has the potential to serve as a dosimetric scale for exposition to very low doses of IR.
This technique will be implemeted at the Department of Medicine of the University of Milano-Bicocca.

4 Perspectives

The kinematics of DSBs induction and repair, combined with different fractionated dose delivering, can help in discriminating between different radiotherapy techniques. In particular the IMRT is characterized by a longer application and "pulsed" fields, resulting in a strong dependence on the time factor.
The cellular response at low doses is affected by different mechanisms (genomic instability, bystander effect and adaptive response), perhaps resulting in a underestimation of the damage. In this case, the necessity of a NTCP model strongly linked to DSBs and working at low doses is clear. Such a model can be implemented and verified by Monte-carlo computational tools adapted to simulate interaction of radiation with biological targets.

References

1. UNSCEAR Report, Annex **G**, (2000).
2. ICRP Report, (2004)
3. G.A. Ezzell *et al*, Med. Phys. **30**, 2089 (2003).
4. E.J. Hall *et al*, Int. J. Rad. Onc. Biol. Phys. **56-1**, 83 (2003).
5. J.T. Lyman, Radiat. Res. **104**, S13 (1985).
6. E.D. Yorke, Report of IMRT subcommittee of AAPM radiation therapy committee, 77 (2003).
7. K. Rothkamm et M. Lobrich, PNAS **100-9**, 5057 (2003).

Frascati Physics Series Vol. XL (2006), pp. 389–392
Frontier Science 2005, New Frontiers in Subnuclear Physics
Milano, 12-16 September, 2005

A MULTI-SCALE APPROACH TO THE COMPUTER-AIDED DETECTION OF MICROCALCIFICATION CLUSTERS IN DIGITAL MAMMOGRAMS

P. Delogu, M.E. Fantacci, A. Retico, A. Stefanini and A. Tata
Dipartimento di Fisica dell'Università e INFN di Pisa,
Largo Pontecorvo 3, 56127 Pisa, Italy

Abstract

A computer-aided detection (CADe) system for the identification of microcalcification clusters in digital mammograms has been developed. It is mainly based on the application of wavelet transforms for image filtering and neural networks for both the feature extraction and the classification procedures. This CADe system is easily adaptable to different databases. We report and compare the FROC curves obtained on the private database we used for developing the CADe system and on the publicly available MIAS database. The results achieved on the two databases show the same trend, thus demonstrating the good generalization capability of the system.

1 Introduction

Microcalcifications appear as small bright circular or slightly elongated spots embedded in the complex normal breast tissue imaged in a mammogram. Es-

pecially when they are grouped in clusters, microcalcifications can be an important early indication of breast cancer. Computer-aided detection (CADe) systems can improve the radiologists' accuracy in the interpretation of mammograms by alerting them to suspicious areas of the image containing possibly pathological signs.

The main problem one has to deal with, in developing a CADe system for mammography, is the strong dependence of the method, of the parameters and of the performances of the system on the dataset used in the set-up and testing procedures. The approach we adopted for our CADe system is mainly based on the exploitation of the properties of the wavelet analysis and the artificial neural networks. The use of wavelets in the pre-processing step, together with the implementation of an automatic neural-based procedure for the feature extraction, allows for a plan generalization of the analysis scheme to databases characterized by different acquisition and storing parameters.

2 CADe scheme

The CADe scheme can be summarized in the following main steps:

- INPUT: digitized mammogram;
- Pre-processing of the mammogram: identification of the breast skin line and segmentation of the breast region with respect to the background; application of a wavelet-based filter in order to enhance the microcalcification signal;
- Feature extraction: decomposition of the breast region in several $N \times N$ pixel-wide sub-images to be processed each at a time; automatic extraction of the features from each sub-image;
- Classification: clustering of the processed sub-images into two classes, i.e. those containing microcalcification clusters and the normal tissue[1];

[1]In this paper the tissue not containing microcalcification clusters is referred as normal breast tissue, i.e. in our notation this class of tissue can even accommodate regions of mammograms affected by the presence of different pathologies, such as opacities, massive lesions, etc.

- OUTPUT: merging of contiguous or partially overlapping sub-images and visualization of the final output by superimposing rectangles indicating suspicious areas to the original image.

3 Tests and results

The CADe system was set up and tested on a private database of mammograms collected in the framework of the INFN (Istituto Nazionale di Fisica Nucleare)-founded CALMA (Computer-Assisted Library for MAmmography) project [1]. The digitized images are characterized by a 85μm pixel pitch and a 12-bit resolution, thus allowing up to 4096 gray levels. The dataset used for training the CADe consists of 305 mammograms containing microcalcification clusters and 540 normal mammograms. The system performances on a test set of 140 CALMA images (70 with microcalcification clusters and 70 normal images) have been evaluated in terms of the FROC analysis [2] as shown in fig. 1. In particular, as shown in the figure, a sensitivity value of 88% is obtained at a rate of 2.15 FP/im.

In order to test the generalization capability of the system, we evaluated the CADe performances on the publicly available MIAS database [3]. Being the MIAS mammograms characterized by a different pixel pitch (50 μm instead of 85 μm) and a less deep dynamical range (8 bit per pixel instead of 12) with respect to the CALMA mammograms, we had to define a tuning procedure for adapting the CADe system to the MIAS database characteristics. A scaling of the wavelet analysis parameters allows the CADe filter to generate very similar pre-processed images on both datasets. The remaining steps of the analysis, i.e. the characterization and the classification of the sub-images, have been directly imported from the CALMA CADe neural software. The performances the rescaled CADe achieves on the images of the MIAS database have been evaluated on a set of 42 mammograms (20 with microcalcification clusters and 22 normal) and are shown in fig. 1. As can be noticed, a sensitivity value of 88% is obtained at a rate of 2.18 FP/im.

4 Conclusions

The implementation of the wavelet transform in the preprocessing step of the analysis and the use of an auto-associative neural network for the automatic

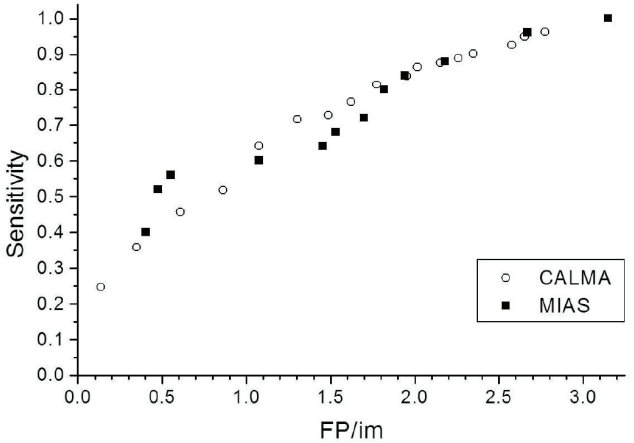

Figure 1: *FROC curve obtained on the CALMA dataset (140 mammograms) and on the MIAS dataset (42 mammograms).*

feature extraction make our CADe system tunable to different databases. The main advantage of this procedure is that this scalable CADe system can be tested even on very small databases, i.e. databases not allowing for the learning procedure of the neural networks to be properly carried out. The strong similarity in the trends of the FROC curves obtained on the CALMA and on the MIAS databases provides a clear evidence that the CADe system we developed can be applied to different databases with no decrease in the detection performance.

References

1. U. Bottigli *et al*, Search of microcalcification clusters with the CALMA CAD station, The International Society for Optical Engineering (SPIE) **4684** 1301 (2002).

2. D. Chakraborty, Free-response methodology: Alternative analysis and a new observer-performance experiment, Radiology **174**(3) 873 (1990).

3. J. Suckling *et al*, The mammographic images analysis society digital mammogram database, Excerpta Medica, International Congress Series **1069** 375 (1994).

Participants

Duccio Abbaneo	CERN Duccio.abbaneo@cern.ch
Cristina Adorisio	Università della Calabria Cristina.adorisio@cern.ch
Guido Altarelli	CERN Guido.altarelli@cern.ch
Mariagrazia Alviggi	Università di Napoli "Federico II" Mariagrazia.alviggi@na.infn.it
Nicola Amapane	INFN Torino Nicola.amapane@to.infn.it
Silvia Amerio	Università and INFN di Trento Silvia.Amerio@tn.infn.it
Azzurra Autieri	Università di Napoli "Federico II" Azzurra.autieri@na.infn.it
Giuseppe Avolio	Università della Calabria Giuseppe.avolio@cern.ch
Giuseppe Bagliesi	INFN Pisa Giuseppe.bagliesi@pi.infn.it
Alessandro Ballestrero	INFN Torino ballestrero@to.infn.it
Lucia Barbone	Università and INFN di Bari Lucia.barbone@ba.infn.it
Luciano Maria Barone	Università di Roma "La Sapienza" Luciano.barone@roma1.infn.it
Franco Bedeschi	INFN Pisa bed@fnal.gov
Massimiliano Bellomo	Università di Pavia Massimiliano.bellomo@pv.infn.it
Leonardo Benucci	INFN Pisa Leonardo.benucci@pi.infn.it
Umberto Berzano	Università di Pavia Umberto.berzano@pv.infn.it
Michela Biglietti	INFN Napoli Michela.biglietti@na.infn.it
Halina Bilokon	INFN LNF Halina.bilokon@lnf.infn.it

Tommaso Boccali	SNS/INFN Pisa Tommaso.boccali@pi.infn.it
Matteo Cacciari	LPTHE UPMC Parigi Matteo.cacciari@cern.ch
Vincenzo Canale	Università di Napoli “Federico II” Vincenzo.canale@na.infn.it
Paolo Capiluppi	Università and INFN Bologna Paolo.capiluppi@bo.infn.it
Mario Caprio	Università di Napoli “Federico II” Mario.caprio@na.infn.it
Gianpaolo Carlino	INFN Napoli Gianpaolo.carlino@na.infn.it
Leonardo Carminati	Università and INFN Milano Leonardo.carminati@mi.infn.it
Rino Castaldi	INFN Pisa Rino.castaldi@pi.infn.it
Andrea Castro	Università di Bologna Andrea.castro@bo.infn.it
Ariella Cattai	CERN Ariella.cattai@cern.ch
Donatella Cavalli	INFN Milano Donatella.cavalli@mi.infn.it
Nicola Cavallo	INFN Napoli Nicola.cavallo@na.infn.it
Fabio Cerutti	INFN LNF Fabio.cerutti@lnf.infn.it
Vitaliano Chiarella	INFN LNF Vitaliano.Chiarella@lnf.infn.it
Gianni Chiefari	Università di Napoli “Federico II” Giovanni.chiefari@na.infn.it
Gabriele Chiodini	INFN Lecce Gabriele.chiodini@le.infn.it
Massimiliano Chiorboli	Università di Catania Massimiliano.chiorboli@ct.infn.it
Anna Cimmino	Università di Napoli Anna.cimmino@na.infn.it

Claudia Ciocca	Università and INFN di Bologna Claudia.ciocca@bo.infn.it
Manuela Cirilli	CERN Manuela.cirilli@cern.ch
Francesco Conventi	Università di Napoli "Federico II" Francesco.conventi@na.infn.it
Davide Costanzo	Lawrence Berkeley Laboratory Davide.costanzo@cern.ch
Giovanni Crosetti	Università della Calabria crosetti@fis.unical.it
Susanna Cucciarelli	CERN Susanna.cucciarelli@cern.ch
Mariarosaria DAlfonso	INFN Pisa Mariarosaria.dalfonso@pi.infn.it
Giancarlo DAmbrosio	INFN Napoli Giancarlo.dambriosio@na.infn.it
Riccardo de Asmundis	INFN Napoli Riccardo.deasmundis@na.infn.it
Nicola De Filippis	Università and INFN di Bari Nicola.defilippis@ba.infn.it
Alberto De Min	Università and INFN di Milano Alberto.demin@mi.infn.it
Mauro De Palma	Università di Bari Mauro.depalma@ba.infn.it
Guido De Zorzi	Università di Roma "La Sapienza" Guido.dezorzi@roma1.infn.it
Vittorio Del Duca	INFN Torino Vittorio.delduca@to.infn.it
Massimo Della Pietra	Università di Napoli "Federico II" Massimo.dellapietra@na.infn.it
Domenico Della Volpe	Università di Napoli "Federico II" Domenico.dellavolpe@na.infn.it
Natale Demaria	INFN Torino Natale.demaria@to.infn.it
Marcella Diemoz	INFN Roma I Marcella.diemoz@roma1.infn.it

Alessandro Di Mattia	INFN Roma I Alessandro.dimattia@roma1.infn.it
Carlo Dionisi	Università di Roma "La Sapienza" Carlo.dionisi@roma1.infn.it
Fabrizio Fabbri	INFN Bologna Fabrizio.fabbri@bo.infn.it
Francesco Fabozzi	INFN Napoli Francesco.fabozzi@na.infn.it
Speranza Falciano	INFN Roma I Speranza.falciano@roma1.infn.it
Pamela Ferrari	CERN Pamela.ferrari@cern.ch
Roberto Ferrari	INFN Pavia Roberto.ferrari@pv.infn.it
Lorenzo Fo	Scuola Normale Superiore Pisa Lorenzo.foa@pi.infn.it
Stefano Frixione	INFN Genova Stefano.frixione@ge.infn.it
Guido Gagliardi	INFN Genova Guido.gagliardi@ge.infn.it
Fabrizio Gasparini	Università di Padova Fabrizio.gasparini@pd.infn.it
Ugo Gasparini	INFN Padova Ugo.gasparini@pd.infn.it
Paolo Gauzzi	Università di Roma "La Sapienza" Paolo.gauzzi@roma1.infn.it
Simone Gennai	INFN e SNS Pisa Simone.gennai@pi.infn.it
Andrea Giammarco	Scuola Normale Superiore Pisa Andrea.giammarco@pi.infn.it
Fabiola Gianotti	CERN Fabiola.gianotti@cern.ch
Edoardo Gorini	Università di Lecce Edoardo.gorini@le.infn.it
Claudio Grandi	INFN Bologna Claudio.grandi@bo.infn.it

Mario Greco	Università Roma III Mario.greco@roma3.infn.it
Paolo Iengo	INFN Napoli Paolo.iengo@na.infn.it
Fabio Iervolino	Università di Napoli "Federico II" Fabio.iervolino@na.infn.it
Vincenzo Izzo	Università di Napoli "Federico II" Vincenzo.izzo@na.infn.it
Stefano La Caprara	Università and INFN di Padova Stefano.lacaprara@pd.infn.it
Laura La Rotonda	Università della Calabria larotonda@fis.unical.it
Francesco La Cava	Università di Roma "La Sapienza" Francesco.lacava@roma1.infn.it
Paolo Lariccia	Università di Perugia Paolo.lariccia@pg.infn.it
Ignazio Lazzizzera	INFN di Trento lazi@tn.infn.it
Franco Ligabue	Scuola Normale Superiore Franco.ligabue@pi.infn.it
Luca Lista	INFN Napoli Luca.lista@na.infn.it
Egidio Longo	Università di Roma "La Sapienza" Egidio.longo@roma1.infn.it
Claudio Luci	Università di Roma "La Sapienza" Claudio.luci@roma1.infn.it
Lamberto Luminari	INFN Roma I Lamberto.luminari@roma1.infn.it
Boris Mangano	Scuola Normale Superiore Pisa Boris.mangano@pi.infn.it
Michelangelo Mangano	CERN Michelangelo.mangano@cern.ch
Stefano Marcellini	INFN Bologna Stefano.marcellini@bo.infn.it
Anna Teresa Meneguzzo	Università di Padova Anna.meneguzzo@unipd.it

Lorenzo Menici	Università di Roma "La Sapienza" Lorenzo.menici@roma1.infn.it
Evelin Meoni	Università della Calabria meoni@fis.unical.it
Paolo Meridiani	Università di Roma "La Sapienza" Paolo.meridiani@roma1.infn.it
Leonardo Merola	Università di Napoli "Federico II" Leonardo.merola@na.infn.it
Agostino Migliaccio	Università di Napoli "Federico II" Agostino.migliaccio@na.infn.it
Ernesto Migliore	Università and INFN di Torino Ernesto.migliore@to.infn.it
Aleandro Nisati	INFN Roma I Aleandro.nisati@roma1.infn.it
Pasquale Noli	Università di Napoli "Federico II" Pasquale.noli@na.infn.it
Maria Margherita Obertino	Università di Torino Margherita.obertino@cern.ch
Marco Paganoni	Università Bicocca and INFN di Milano Marco.paganoni@mib.infn.it
Fabrizio Palla	INFN Pisa Fabrizio.palla@pi.infn.it
Pierluigi Paolucci	INFN Napoli Pierluigi.paolucci@na.infn.it
Riccardo Paramatti	INFN Roma Riccardo.paramatti@roma1.infn.it
Andrea Parenti	Università and INFN di Padova Andrea.parenti@pd.infn.it
Francesca Pastore	INFN Roma I Francesca.pastore@roma1.infn.it
Sergio Patricelli	Università di Napoli "Federico II" Sergio.patricelli@na.infn.it
Andrea Perrotta	INFN Bologna Andrea.perrotta@bo.infn.it
Davide Piccolo	INFN Napoli Davide.piccolo@na.infn.it

Giovanni Polese	Università di Napoli "Federico II" Giovanni.polese@na.infn.it
Giacomo Polesello	CERN Giacomo.polesello@cern.ch
Guy Umberto Poloni	Università di Milano Guy.poloni@mi.infn.it
Antonino Pullia	Università Bicocca and INFN di Milano Antonino.pullia@mib.infn.it
Stefano Ragazzi	Università Bicocca and INFN di Milano Stefano.ragazzi@mib.infn.it
Francesco Ragusa	Università di Milano Francesco.Ragusa@mi.infn.it
Riccardo Ranieri	Università and INFN di Firenze Riccardo.ranieri@fi.infn.it
Marco Rescigno	INFN Roma I Marco.rescigno@roma1.infn.it
Adele Rimoldi	Università di Pavia Adele.rimoldi@pv.infn.it
Andrea Rizzi	Scuola Normale Superiore Pisa Andrea.rizzi@sns.it
Gigi Rolandi	CERN Gigi.rolandi@cern.ch
Lucio Rossi	CERN Lucio.rossi@cern.ch
Matteo Sani	Università and INFN di Firenze Matteo.sani@fi.infn.it
Pietro Santarelli	Università di Napoli "Federico II" Pietro.santorelli@na.infn.it
Francesca Sarri	INFN Pisa Francesca.sarri@pi.infn.it
Carlo Schiavi	Università and INFN di Genova Carlo.schiavi@ge.infn.it
Crisostomo Sciacca	Università di Napoli "Federico II" Crisostomo.sciacca@na.infn.it
Lucia Silvestris	INFN Bari Lucia.silvestris@ba.infn.it
Stefania Spagnolo	Università di Lecce Stefania.spagnolo@le.infn.it

Tommaso Tabarelli de Fatis	Università Bicocca and INFN di Milano defatis@mib.infn.it
Roberto Tenchini	INFN Pisa Roberto.tenchini@pi.infn.it
Guido Tonelli	Università di Pisa Guido.tonelli@pi.infn.it
Ezio Torassa	INFN Padova Ezio.torassa@pd.infn.it
Andrea Ventura	INFN Lecce Andrea.ventura@le.infn.it
Valerio Vercesi	INFN Pavia Valerio.vercesi@pv.infn.it
Ilaria Villella	INFN Napoli Ilaria.villella@na.infn.it
Iacopo Vivarelli	Scuola Normale Superiore Pisa Iacopo.vivarelli@pi.infn.it
Marcel Vos	INFN Pisa Marcel.vos@pi.infn.it
Marco Zanetti	INFN Padova Marco.zanetti@pd.infn.it

FRASCATI PHYSICS SERIES VOLUMES

Volume I
Heavy Quarks at Fixed Target
Eds.: S. Bianco and F.L. Fabbri
Frascati, May 31–June 2, 1993
ISBN—88–86409–00–1

Volume II – Special Issue
Les Rencontres de Physique de la Vallée d'Aoste – Results and Perspectives in Particle Physics
Ed.: M. Greco
La Thuile, Aosta Valley, March 5 –11, 1995
ISBN—88–86409–03–6

Volume III
Heavy Quarks at Fixed Target
Ed.: B. Cox
University of Virginia, Charlottesville
October 7–10, 1994, 11
ISBN—88–86409–04–4

Volume IV
Workshop on Physics and Detectors for DAΦNE
Eds.: R. Baldini, F. Bossi, G. Capon, G. Pancheri
Frascati, April 4–7, 1995
ISBN—88–86409–05–2

Volume V – Special Issue
Les Rencontres de Physique de la Vallée d'Aoste – Results and Perspectives in Particle Physics
Ed.: M. Greco
La Thuile, Aosta Valley, March 3–9, 1996
ISBN—88–86409–07–9

Volume VI
Calorimetry in High Energy Physics
Eds.: A. Antonelli, S. Bianco, A. Calcaterra, F.L. Fabbri
Frascati, June 8–14, 1996
ISBN—88–86409–10–9

Volume VII
Heavy Quarks at Fixed Target
Ed.: L. Kőpke
Rhinefels Castle, St. Goar, October 3–6, 1996
ISBN—88–86409–11–7

Volume VIII
ADONE a milestone on the particle way
Ed.: V. Valente 1997
ISBN—88–86409–12–5

Volume IX – Special Issue
Les Rencontres de Physique de la Vallée d'Aoste – Results and Perspectives in Particle Physics
Ed.: M. Greco
La Thuile, Aosta Valley, March 2–8, 1997
ISBN–88–86409–13–3

Volume X
Advanced ICFA Beam Dynamics
Workshop on Beam Dynamics Issue for e^+e^- Factories
Eds.: L. Palumbo, G. Vignola
Frascati, October 20–25, 1997
ISBN—88–86409–14–1

Volume XI
Proceedings of the XVIII International Conference on Physics in Collision
Eds.: S. Bianco, A. Calcaterra, P. De Simone, F. L. Fabbri
Frascati, June 17–19, 1998
ISBN—88–86409–15–X

Volume XII – Special Issue
Les Rencontres de Physique de la Vallée d'Aoste – Results and Perspectives in Particle Physics
Ed.: M. Greco
La Thuile, Aosta Valley, March 1–7, 1998
ISBN—88–86409–16–8

Volume XIII
Bruno Touschek and the Birth of thee$^+ e^-$
Ed.: G. Isidori
Frascati, 16 November, 1998
ISBN—88–86409–17–6

Volume XIV – Special Issue
Les Rencontres de Physique de la Vallée d'Aoste – Results and Perspectives in Particle Physics
Ed.: M. Greco
La Thuile, Aosta Valley, February 28–March 6, 1999
ISBN—88–86409–18–4

Volume XV
Workshop on Hadron Spectroscopy
Eds.: T. Bressani, A. Feliciello, A. Filippi
Frascati, March 8 2 1999
ISBN—88–86409–19–2

Volume XVI
Physics and Detectors for DAΦNE
Eds.: S. Bianco, F. Bossi, G. Capon, F.L. Fabbri, P. Gianotti, G. Isidori, F. Murtas
Frascati, November 16 –19, 1999
ISBN—88–86409–21–4

Volume XVII – Special Issue
Les Rencontres de Physique de la Vallée d'Aoste – Results and Perspectives in Particle Physics
Ed.: M. Greco
La Thuile, Aosta Valley, February 27 March 4, 2000
ISBN—88–86409–23–0

Volume XVIII
LNF Spring School
Ed.: G. Pancheri
Frascati 15–20 May, 2000
ISBN—88–86409–24–9

Volume XIX
XX Physics in Collision
Ed.: G. Barreira
Lisbon June 29–July1st. 2000
ISBN—88–86409–25–7

Volume XX
Heavy Quarks at Fixed Target
Eds.: I. Bediaga, J. Miranda, A. Reis
Rio de Janeiro, Brasil, October 9–12, 2000
ISBN—88–86409–26–5

Volume XXI
IX International Conference on Calorimetry in High Energy Physics
Eds.: B. Aubert, J. Colas, P. Nédélec, L. Poggioli
Annecy Le Vieux Cedex, France, October 9–14, 2000
ISBN—88–86409–27–3

Volume XXII – Special Issue
Les Rencontres de Physique de la Vallée d'Aoste – Results and Perspectives in Particle Physics
Ed.: M. Greco
La Thuile, Aosta Valley, March 4–10, 2001
ISBN—88–86409–28–1

Volume XXIII
XXI Physics in Collision
Ed.: Soo–Bong Kim
Seoul, Korea, June 28 30, 2001
ISBN—88–86409–30–3

Volume XXIV
International School of Space Science – 2001 Course on: Astroparticle and Gamma–ray Physics in Space
Eds.: A. Morselli, P. Picozza
L'Aquila, Italy, August 30 September 7, 2000
ISBN—88–86409–31–1

Volume XXV
TRDs for the 3rd Millennium Workshop on Advanced Transition Radiation Detectors for Accelerator and Space Applications
Eds. N. Giglietto, P. Spinelli
Bari, Italy, September 20–23, 2001
ISBN—88–86409–32–X

Volume XXVI
KAON 2001 International Conference on CP Violation
Eds.: F. Costantini, G. Isidori, M. Sozzi
Pisa Italy, June 12th 17th, 2001
ISBN—88–86409–33–8

Volume XXVII – Special Issue
Les Rencontres de Physique de la Vallée d'Aoste – Results and Perspectives in Particle Physics
Ed.: M. Greco
La Thuile, Aosta Valley, March 3–9, 2002
ISBN—88–86409–34–6

Volume XXVIII
Heavy Quarks at Leptons 2002
Eds.: G. Cataldi, F. Grancagnolo, R. Perrino, S. Spagnolo
Vietri sul mare (Italy), May 27th June 1st, 2002
ISBN—88–86409–35–4

Volume XXIX
Workshop on Radiation Dosimetry: Basic Technologies, Medical Applications, Environmental Applications
Ed.: A. Zanini
Rome (Italy), February 56, 2002
ISBN—88–86409–36–2

Volume XXIX – Suppl.
Workshop on Radiation Dosimetry: Basic Technologies, Medical Applications, Environmental Applications
Ed.: A. Zanini
Rome (Italy), February 56, 2002
ISBN—88–86409–36–2

Volume XXX – Special Issue
Les Rencontres de Physique de la Vallée d'Aoste –
Results and Perspectives in Particle Physics
Ed.: M. Greco
La Thuile, Aosta Valley, March 9–15, 2003
ISBN—88–86409–39–9

Volume XXXI
Frontier Science 2002 – Charm, Beauty and CP,
First International Workshop on Frontier Science
Eds.: L. Benussi, R. de Sangro, F.L. Fabbri, P. Valente
Frascati, October 6–11, 2002
ISBN—88–86409–37–0

Volume XXXII
19th International Conference on x–ray and Inner–Shell Processes
Eds.: A. Bianconi, A. Marcelli, N.L. Saini
Universitá di Roma La Sapienza June 24–28, 2002
ISBN—88–86409–39–07

Volume XXXIII
Bruno Touschek Memorial Lectures
Ed.: M. Greco, G. Pancheri
Frascati, May 11, 1987
ISBN—88–86409–40–0

Volume XXXIV – Special Issue
Les Rencontres de Physique de la Vallée d'Aoste –
Results and Perspectives in Particle Physics
Ed.: M. Greco
La Thuile, Aosta Valley, February 29 – March 6, 2004
ISBN—88–86409–42–7

Volume XXXV
Heavy Quarks And Leptons 2004
Ed.: A. López
San Juan, Puerto Rico, 1–5 June 2004
ISBN—88–86409–43–5

Volume XXXVI
DAΦNE 2004: Physics At Meson Factories
Eds.: F. Anulli, M. Bertani, G. Capon, C. Curceanu–Petrascu,
F.L. Fabbri, S. Miscetti
Frascati, June 7–11, 2004
ISBN—88–86409–53–2

Volume XXXVII
Frontier Science 2004, Physics and Astrophysics in Space
Eds.: A. Morselli, P. Picozza, M. Ricci
Frascati, 14–19 June, 2004
ISBN—88–86409–52–4

Volume XXXVIII
II Workshop Italiano sulla Fisica di ATLAS e CMS
Eds.: Gianpaolo Carlino and Pierluigi Paolucci
Napoli, October 13 – 15, 2004
ISBN—88–86409–44–3

Volume XXXIX – Special Issue
Les Rencontres de Physique de la Vallée d'Aoste –
Results and Perspectives in Particle Physics
Ed.: M. Greco
La Thuile, Aosta Valley, February 27 – March 5, 2005
ISBN—88–86409–45–1